

Influence of the newly identified Mos10 interaction partner Vps68
on ESCRT-III function

**Dissertation zur Erlangung des Doktorgrades
der Naturwissenschaften
(Dr. rer. nat.)**

**Fakultät
Naturwissenschaften
Universität Hohenheim**

Institut für Lebensmittelwissenschaft und Biotechnologie

Vorgelegt von
Sören Alsleben
aus Mülheim an der Ruhr

Stuttgart, 2021

1. Gutachter: Prof. Dr. Ralf Kölling
Institut für Lebensmittelwissenschaften und Biotechnologie
Fachgebiet für Hefegenetik und Gärungstechnologie
2. Gutachter: Prof. Dr. Armin Huber
Institut für Biologie
Fachgebiet Biochemie
- Dekan: Prof. Dr. Uwe Beifuss

Eingereicht am: 06.12.2021

Tag der mündlichen Prüfung: 22.02.2022

Die vorliegende Arbeit wurde am 17.12.2021 von der Fakultät der Naturwissenschaften der Universität Hohenheim als „Dissertation zur Erlangung des Grades eines Doktors der Naturwissenschaften“ angenommen.

TABLE OF CONTENT

LIST OF FIGURES	7
LIST OF FIGURES (SUPPLEMENTARY).....	8
LIST OF TABLES	10
LIST OF TABLES (SUPPLEMENTARY).....	10
ABBREVIATIONS.....	11
1 INTRODUCTION	14
1.1 Clathrin-mediated endocytosis.....	15
1.2 Endomembrane system.....	16
1.3 The ESCRT machinery.....	18
1.3.1 ESCRT-0	20
1.3.2 ESCRT-I.....	20
1.3.3 ESCRT-II	21
1.3.4 ESCRT-III.....	22
1.3.5 Vps4	26
1.4 ESCRT functions.....	26
1.4.1 Cytokinesis	27
1.4.2 Virus budding.....	28
1.4.3 The nuclear envelope (NE)	29
1.4.4 Autophagy	29
1.4.5 Exosomes & Microvesicles.....	30
1.4.6 Other functions.....	30
1.5 Aim of this thesis	31
2 MATERIAL AND METHODS	32
2.1 Strains and media.....	32
2.1.1 Bacteria strains	32
2.1.2 E. coli growth conditions	32

2.1.3	Yeast strains	32
2.1.4	Yeast growth conditions	36
2.2	Plasmids.....	37
2.3	Designed oligonucleotides	38
2.4	Materials	44
2.4.1	Chemicals and solutions.....	44
2.4.2	Facilities and consumables.....	46
2.4.3	Software	48
2.5	Molecular biological methods	49
2.5.1	PCR (Polymerase chain reaction)	49
2.5.2	Colony Test PCR.....	49
2.5.3	Agarose gel electrophoresis	49
2.5.4	Isolation of DNA fragments	50
2.5.5	Calculating DNA concentration	50
2.5.6	Enzymatic Digestion	50
2.5.7	SDS PAGE	50
2.5.8	Coomassie staining.....	51
2.5.9	Silver staining for mass spectrometry	51
2.5.10	Western Blot analysis.....	52
2.6	Microbiological methods.....	53
2.6.1	<i>S. cerevisiae</i> genomic DNA extraction (for Western Blot).....	53
2.6.2	Yeast transformation	54
2.6.3	<i>E. coli</i> transformation.....	55
2.7	Antibody Purification	55
2.7.1	Protein expression in <i>E. coli</i>	55
2.7.2	Lysing <i>E. coli</i> cells	56
2.7.3	Protein purification from <i>E. coli</i> cells	57
2.7.4	Protein Dialysis	57

2.7.5	Affigel purification.....	57
2.7.6	Antibody purification	58
2.8	Cell fractionation.....	58
2.8.1	Sucrose Gradient	58
2.8.2	Flotation	59
2.8.3	Differential centrifugation.....	60
2.9	Protein purification from yeast cells.....	60
2.9.1	Co-Immunoprecipitation	60
2.9.2	Crosslinking experiment	61
2.9.3	AEKTA purification.....	62
2.10	Cycloheximide chase	63
2.11	Fluorescence microscopy	64
2.12	SILAC Experiments.....	64
3	RESULTS.....	65
3.1	Finding interacting partners of ESCRT-III subunit Mos10	65
3.1.1	IMAC purification of His-tagged Mos10.....	66
3.1.2	AEKTA purification of His-tagged Mos10.....	67
3.1.3	AEKTA purification of His-tagged Mos10 with SILAC	74
3.1.4	Improved batch purification by sedimentation and SILAC	77
3.1.5	Purification of untagged Mos10.....	81
3.1.6	The first set of potential Mos10 interacting partners	85
3.1.7	Tagged Mos10 purification via IP.....	88
3.1.8	The second set of potential Mos10 interacting partners.....	91
3.1.9	ESCRT-III interacting partners of Mos10.....	94
3.2	Influence of <i>VPS68</i> deletion on ESCRT-III	95
3.2.1	IP and Co-IP in WT.....	95
3.2.2	IP and Co-IP in the $\Delta vps68$ strain RKY3222.....	97
3.2.3	Effect of VPS68 deletion on the intracellular ESCRT-III protein distribution....	99

3.3	Cell-fractionation	102
3.3.1	Differential centrifugation experiments	102
3.3.2	Flotation	105
3.3.3	Sucrose Gradients.....	106
3.4	Perturbations in endocytic cargo degradation and transport.....	110
3.5	Synchronized ESCRT-III assembly.....	113
3.6	Linking ESCRT-III to non-endosomal functions.....	115
3.6.1	Potential association of ESCRT-III with nucleic acids.....	115
3.6.2	P-bodies and stress markers	119
4	DISCUSSION.....	122
4.1	The Mos10 crosslinking pattern.....	122
4.2	Choosing a proper tag.....	124
4.3	Choosing suitable Mos10 interaction candidates	125
4.4	Influence of <i>VPS68</i> deletion.....	126
4.5	Non-endosomal functions	128
5	LITERATURE	130
6	SUPPLEMENTARY MATERIAL.....	149
	SUMMARY.....	188
	ZUSAMMENFASSUNG.....	190
	DANKSAGUNG	192
	APPENDIX.....	193
	CURRICULUM VITAE.....	194

LIST OF FIGURES

Figure 1: Phagocytosis pathway, adapted from “INTRACELLULAR DIGESTION”(De Duve, 1963).	14
Figure 2: Clathrin-mediated vesicle formation, adapted from the poster (Lu et al., 2016).	15
Figure 3: Endomembrane trafficking in mammals and yeast, adapted from (Day et al., 2018).....	17
Figure 4: Scheme of the ESCRT machinery assembly, adapted from (Teis et al., 2009).	19
Figure 5: The ESCRT-III proteins in yeast, redrawn from (Schoneberg et al., 2017).....	22
Figure 6: ESCRT-III open and closed conformational structure, adapted from (McCullough et al., 2018).	24
Figure 7: Membrane fission by ESCRT-III exchange, adapted from (McCullough and Sundquist, 2020).	25
Figure 8: Summary of ESCRT-III mediated cellular processes, adapted from (McCullough et al., 2018).....	27
Figure 9: Identification of Mos10 interacting partners by a characteristic WB pattern.	66
Figure 10: AEKTA purification of Mos10-6His from <i>S. cerevisiae</i> culture with Ni-NTA column.....	68
Figure 11: Isocratic AEKTA purification of Mos10-6His using a Ni-NTA column.....	69
Figure 12: WB results of a gradient AEKTA purification of Mos10-6His using a Ni-NTA column.	71
Figure 13: Gradient AEKTA purification of Mos10-6His using a Ni-NTA column Coomassie staining.	72
Figure 14: Lane intensity distribution of Coomassie-stained SDS PAGE.	73
Figure 15: AEKTA purified samples for MS analysis.	73
Figure 16: Validating crosslinker induced WB pattern of 6His tagged Mos10 with Arg auxotrophy in YNB.....	75
Figure 17: WB results of the Mos10-6His AEKTA purification using a Ni-NTA column with SILAC.	76
Figure 18: Crosslinking pattern sub-division by differential centrifugation.	78
Figure 19: Mos10-6His purification with Ni ²⁺ - and Co ²⁺ -NTA column with P13 separation.....	79
Figure 20: SILAC samples for MS analysis from batch Mos10-6His purification.	80
Figure 21: Autoinduction media used for Mos10-6His heterologous expression in <i>E. coli</i>	82
Figure 22: Testing antibody sera against native Mos10 extract.	83
Figure 23: Crosslinking pattern of native Mos10 by α -Mos10 immunoprecipitation.	84
Figure 24: Purification of potential Mos10-6His interacting partners by α -13myc immunoprecipitation.	86
Figure 25: Identification of co-immunoprecipitated Mos10-6His by potential interacting partners.	87
Figure 26: Crosslinking pattern of crosslinked Mos10-6His and 13myc tagged interacting partners.....	88
Figure 27: Evaluating Mos10 affinity tags for immunoprecipitation compared to IMAC.....	89
Figure 28: Purification of Mos10-sfGFP by α -GFP antibodies on WB and silver-stained gel for MS.....	90
Figure 29: Purification of potential Mos10 interacting partners by α -13myc immunoprecipitation.	92
Figure 30: Identification of co-immunoprecipitated Mos10 by potential interacting partners.....	93
Figure 31: Comparison of Mos10-6His specific IMAC WB patterns of ESCRT-III single deletions.	95
Figure 32: Molar fraction of ESCRT-III proteins in ESCRT-III complexes in the WT strain RKY1558.	96
Figure 33: Simplified ESCRT-III complex composition based on the co-IP in WT strain RKY1558.....	97
Figure 34: Difference between the co-immunoprecipitated values of strains RKY1558 and RKY3222.....	98
Figure 35: Co-IP values of strain Δ vps68 RKY3222 in comparison to the WT strain RKY1558.	98
Figure 36: Intracellular distribution of ESCRT-III proteins by fluorescence microscopy.	100
Figure 37: Vps68-mCherry induced localization shift of Mos10-sfGFP.	101
Figure 38: Reverse Vps68 and Mos10 tagging to visualize protein distribution.....	102

Figure 39: ESCRT-III distribution in the WT strain RKY 1558 with and without Triton X-100 treatment.	103
Figure 40: Sedimentation comparison between WT strain RKY1558 and Vps68 deletion strain RKY3222.	104
Figure 42: Flotation comparison between WT strain RKY1558 and Vps68 deletion strain RKY3222.....	105
Figure 43: Flotation comparison between the WT strain RKY1558 and the $\Delta snf7$ strain RKY2790.....	106
Figure 44: ESCRT-III distribution fractionation by sucrose density gradient separation.	107
Figure 45: Gradient of tagged Mos10 in WT and $\Delta vps68$ background in comparison with marker proteins.	109
Figure 46: Cycloheximide chases of Ste6 in WT strain RKY1558 and $\Delta vps68$ strain RKY3222.	111
Figure 47: Classifying Vps68 deletion by established Class D & E protein null mutations.	112
Figure 48: Perturbation of CPS cargo sorting by Vps68 deletion.	113
Figure 49: Heat-induced alteration of ESCRT-III assembly and disassembly by a Vps27 variant.....	114
Figure 50: ESCRT-III distribution on sucrose density gradients after pre-incubation.....	116
Figure 51: Flotation experiment with WT strain RKY1558 with and without incubation.....	117
Figure 52: Sucrose gradients of N- & C-terminally tagged Did2 in comparison with marker proteins.....	118
Figure 53: C- & N-terminal tagging of Did2 by GFP/sfGFP.....	119
Figure 54: Heat and sodium azide-induced stress granule formation visualized by Pub1-sfGFP.....	120
Figure 55: Heat and sodium azide-induced replication stress visualized by Dcp2-sfGFP.....	120
Figure 56: Heat and sodium azide-induced mRNA stress visualized by Nmd2-sfGFP.	121

LIST OF FIGURES (SUPPLEMENTARY)

Figure S 1: Color Pre-stained Protein Standard, Broad Range (11–245 kDa).	149
Figure S 2: Gradient AEKTA purification protocol of Mos10-6His from RKY2999 with Ni-NTA column.	151
Figure S 3: SDS PAGE of gradient Mos10-6His AEKTA purification using a Ni-NTA column and SILAC. ..	152
Figure S 4: Ni ²⁺ - vs. Co ²⁺ -NTA column assay for purifying crosslinked Mos10-6His.....	152
Figure S 5: SILAC Experiment with mixed “light” and “heavy” RKY2998 and RKY2999 purification.....	153
Figure S 6: Analyzing antibody sera efficiency against native Mos10 extract.	155
Figure S 7: Comparison of WT and $\Delta Mos10$ purification on SDS PAGE with Coomassie and silver staining.	155
Figure S 8: Samples for MS once stained with Coomassie and once with silver staining.	156
Figure S 9: Graphing electrophoresis results of WB bands.	156
Figure S 10: Crosslink pattern of Mos10-13myc OD 1 and OD 4 cultures.	157
Figure S 11: IP of potential Mos10 interacting partners with a GFP-tag and Co-IP of Mos10.....	160
Figure S 12: IP of potential Mos10 interacting partners with a sfGFP-tag and Co-IP of Mos10.....	161
Figure S 13: IMAC purification of WT (RKY1558) strain with RKY2889 (Mos10-6His) control sample.	162
Figure S 14: IMAC purification of RKY2889 (Mos10-6His).....	162
Figure S 15: IMAC purification of RKY3228 (Mos10-6His + $\Delta chm7$).	163
Figure S 16: IMAC purification of RKY2788 (Mos10-6His + $\Delta did2$).	163
Figure S 17: IMAC purification of RKY2789 (Mos10-6His + $\Delta ist1$).	164
Figure S 18: IMAC purification of RKY2790 (Mos10-6His + $\Delta snf7$).	164
Figure S 19: IMAC purification of RKY2841 (Mos10-6His + $\Delta vps2$).....	165
Figure S 20: IMAC purification of RKY2893 (Mos10-6His + $\Delta vps20$).....	165

Figure S 21: IMAC purification of RKY2830 (Mos10-6His + $\Delta vps24$).....	166
Figure S 22: IP and Co-IP of all ESCRTs in WT strain. RKY1558.....	166
Figure S 23: Total amount of protein co-immunoprecipitated by ESCRT-III IP in WT strain RKY1558.....	169
Figure S 24: IP and Co-IP of all ESCRTs in VPS68 deletion strain RKY3222.....	169
Figure S 25: Total amount of protein co-immunoprecipitated by ESCRT-III IP in $\Delta vps68$ strain RKY3222....	172
Figure S 26: Differential centrifugation experiment without Triton X-100 in the WT strain RKY 1558.....	173
Figure S 27: Differential centrifugation experiment with Triton X-100 in the WT strain RKY 1558.....	173
Figure S 28: Western Blots of differential centrifugation of WT strain RKY1558 in triplets.	174
Figure S 29: Protein distribution in the $\Delta vps68$ strain RKY 3221 with and without Triton X-100 treatment. ...	175
Figure S 30: Differential centrifugation experiment without TX-100 in the $\Delta vps68$ strain RKY 3221.....	175
Figure S 31: Differential centrifugation experiment with TX-100 in the $\Delta vps68$ strain RKY 3221.....	176
Figure S 32: Sedimentation comparison between RKY1558 and RKY3222 with Triton X-100 treatment.....	176
Figure S 33: Western Blots of differential centrifugation results from the $\Delta vps68$ strain RKY 3221.	177
Figure S 34: Summary of the flotation results from the WT strain RKY1558.....	177
Figure S 35: Summary of the flotation results from the $\Delta vps68$ strain RKY3222.....	178
Figure S 36: Summary of the flotation results from the $\Delta snf7$ strain RKY2790.....	178
Figure S 37: Summary of the flotation results from the WT strain RKY1558 after incubation.....	179
Figure S 38: WB results of the flotation experiments of WT strain RKY1558.....	180
Figure S 39: WB results of the flotation experiments of $\Delta snf7$ strain RKY2790.....	180
Figure S 40: Flotation results regarding WT incubation, Dpm1 marker protein, and Vps68 deletion.....	181
Figure S 41: Sucrose gradient incubated Did2 WB results of RNaseA treated cells.	181
Figure S 42: ESCRT-III proteins sucrose profiles in the Vps68 deletion strain RKY3222.	182
Figure S 43: ESCRT-III proteins sucrose profiles in the Vps68 deletion strain RKY3222 after incubation.	183
Figure S 44: WB results of the sucrose gradient from the WT strain RKY1558.	184
Figure S 45: WB results of the sucrose gradient from the WT strain RKY1558 after incubation.	184
Figure S 46: WB results of the sucrose gradient from the $\Delta vps68$ strain RKY3222.....	185
Figure S 47: WB results of the sucrose gradient from the $\Delta vps68$ strain RKY3222 after incubation.....	185
Figure S 48: Sucrose profiles of marker and tagged proteins.....	186
Figure S 49: Evaluating Vps68 induced alterations in ER-PM tethering visualized by Ist2- & Tcb1-sfGFP.....	187
Figure S 50: Alterations in Mos10-sfGFP distribution by Vps68 and Vps55 single and double deletions.....	187

LIST OF TABLES

Table 1: The ESCRT nomenclature in yeast and metazoans (Hurley, 2010).	18
Table 2: <i>Escherichia coli</i> (<i>E. coli</i>) strains.	32
Table 3: <i>Saccharomyces cerevisiae</i> (<i>S. cerevisiae</i>) strains.	32
Table 4: Constructed <i>S. cerevisiae</i> strains according to (Longtine et al., 1998).	33
Table 5: Constructed <i>S. cerevisiae</i> strains using various techniques.	36
Table 6: Plasmid register.	37
Table 7: Synthesized oligonucleotides register.	38
Table 8: Chemicals and solutions register.	44
Table 9: Facility register.	46
Table 10: Consumables register.	47
Table 11: Software register.	48
Table 12: PCR protocol for Q5 polymerase.	49
Table 13: PCR protocol for OneTaq.	49
Table 14: Pipetting scheme for the SDS PAGE separating gel.	50
Table 15: Pipetting scheme for the SDS PAGE stacking gel.	51
Table 16: Antibody list.	53
Table 17: Transformation mixture.	55
Table 18: Autoinduction medium according to Studier.	56
Table 19: Table of used sucrose solutions.	59
Table 20: Testing Buffer conditions according to Affi-Gel 15 manufactures guidelines.	83
Table 21: Selected crosslinking partners of Mos10.	85
Table 22: Extended set of Mos10 crosslinking partners.	91
Table 24: Half-life of CPS in WT and Vps68 depleted strain.	111

LIST OF TABLES (SUPPLEMENTARY)

Table S 1: CSM Single Drop-out media (-Trp left; -His right).	149
Table S 2: Corresponding sample concentrations of the gradient purification.	150
Table S 3: Mos-6His to Ni-NTA binding condition test.	154
Table S 4: Calculation of the unknown protein bands sized of the established crosslinking pattern partner.	157
Table S 5: MS Results overview (ESCRT-III in bold).	158
Table S 6: Co-IP Overview in WT strain.	167
Table S 7: Co-IP Overview in $\Delta vps68$ strain RKY3222.	170
Table S 8: ESCRT-III molecules per cell.	172

ABBREVIATIONS

AAA	ATPases associated with a variety of cellular activities
ALIX	ALG-2 interacting protein X
APS	Ammonium persulfate
Bro	BCK1-like resistance to osmotic shock
BSA	Bovine serum albumin
CCP	Clathrin-coated pit
CCV	Clathrin-coated vesicle
CHMP	Chromatin modifying protein
CME	Clathrin-mediated endocytosis
CPY	Carboxypeptidase Y
CTD	C-terminal domain
DAPI	4,6-Diamidino-2-Phenylindol
dH ₂ O	Distilled water
Did	Doa4-independent degradation
DMSO	Dimethyl sulfoxide
DNA	Deoxyribonucleic acid
Doa	Degradation of anti-2
DSP	Dithiobis[succinimidylpropionate]
DSS	Disuccinimidyl suberate
DTT	Dithiothreitol
EAP	ELL-associated protein
EDTA	Ethylenediaminetetraacetic acid
EE	Early endosome
EGFR	Epidermal growth factor receptor
ER	Endoplasmic reticulum
ESCRT	Endosomal sorting complex required for transport
Et al	Et alii
FYVE	Fab1, YOTB, Vac1, EFA1
GAT	GGA and TOM (target of myb)
GGA	Golgi-localized, gamma ear-containing ADP ribosylation factor-binding protein
GLUE	GRAM-like ubiquitin binding in EAP45
GTP	Guanosine triphosphate
HEPES	4-(2-hydroxyethyl)-1-piperazineethanesulfonic acid
HRS	Hepatocyte growth factor-regulated tyrosine kinase substrate
Hse	Has symptoms of class E mutants; resembles Hrs, STAM, East
ILV	Intraluminal vesicle
IMAC	Immobilized metal affinity chromatography
IP	Immunoprecipitation

Ist	Increased sodium tolerance
LB	Lysogeny broth
LE	Late endosome
MAPB	MVB12-associated b-prism domain
MIM	MIT-interacting motif
MIT	Microtubule interacting and trafficking
MOPS	3-(<i>N</i> -morpholino)propanesulfonic acid
Mos	More of Ste6
MVB	Multivesicular body
MWCO	Molecular weight cut-off
NE	Nuclear envelope
NHS	N-hydroxysuccimide
NPC	Nuclear pore complex
NSF	<i>N</i> -ethylmaleimide sensitive fusion protein
NTA	Nitrilotriacetic acid
NZF	Np14 zinc finger
OD	Optical density
PAGE	Polyacrylamide Gel Electrophoresis
PBS	Phosphate-buffered saline
PCR	Polymerase chain reaction
PEG	Polyethylenglykol
pH	Potentia Hydrogenii
pI	Isoelectric point
PI3P	Phosphatidylinositol 3-phosphate
PM	Plasma membrane
PMSF	Phenylmethylsulfonyl fluoride
PPxY	proline-proline-x-tyrosine
PRD	proline-rich domain
PVC	Prevacuolar compartment
PVE	Prevacuolar endosome
rpm	Rounds per minute
RT	Room temperature
SD	Synthetic defined
SDS	Sodium Dodecyl Sulfate
SH3	src homology-3
SILAC	Stable isotope labeling with amino acids in cell culture
SN	Supernatant
SNAP	Soluble NSF attachment protein
SNARE	SNAP Receptor
Snf	Sucrose non-fermenting
ssDNA	Single-stranded DNA

STAM	Signal transducing adaptor molecule
TAE	Tris base acetic acid and EDTA
TCA	Trichloroacetic acid
TEMED	Tetramethylethylenediamine
TGN	<i>Trans</i> -Golgi Network
ts	Temperature-sensitive
TSG	Tumor suppressor gene
Ub	Ubiquitin
UEV	unusual E2 variant
UIM	Ubiquitin-interacting motif
UV	Ultraviolet
V	V-shaped ubiquitin and the signal binding central domain of Bro1 and ALIX
VHS	Vps27, HRS, STAM
VPS/Vps	Vacuolar protein sorting
Vta	Vps twenty associated
WH	Winged-helix
WT	Wild type
YNB	Yeast nitrogen base
YPD	Yeast extract peptone dextrose
TSG101	Tumor susceptibility gene 101

Names of measurement units are abbreviated following the SI base unit system, and proteinogenic amino acids are referred to either by their single or multiple letter code.

1 INTRODUCTION

Microorganisms are microscopic scaled and unicellular organisms considered one of the earliest life-forms on earth (Schopf et al., 2018). Grouped into archaea, bacteria, and eukaryotes, microorganisms are highly abundant in the earth's ecosphere, which drives their dispersal into vastly diverse environments (Finlay and Clarke, 1999). As ubiquitously found species, the ability to sense and adapt to continually changing environments is essential for all microorganism domains, necessitating common stress responses (Mosesso et al., 2019).

Thus, despite morphological diversities in the cellular organization that differ in the three domains, a unifying characteristic is the possession of a cell enwrapping biological membrane. This cell membrane, also known as a plasma membrane, serves as a natural barrier for directed interactions between the cell's interior and the environment. Inflammation studies discovered the phenomenon of intracellular digestion in which products coming from the environment are internalized and digested inside the cell (Ambrose, 2006). This active motion and absorption of foreign particles as a protective response and the underlying mechanism against an external agent was initially named phagocytosis (Mechnikov, 1908).

The advent of electron microscopy led to more profound insight into intracellular digestion morphology by a putative cascade-like membrane remodeling pathway. In this pathway, distinct membrane-enclosed compartments drift from the plasma membrane to the cell interior (Figure 1). By endocytic invagination of the plasma membrane, a compartment called phagosome has formed that harbors extracellular cargo material and is supplementarily enriched by internal cell products targeted for degradation. The pathway proceeds to the fusion of the phagosome with the digestive vacuole/lysosome to release the cargo material targeted for hydrolyzation, thus concluding the intracellular digestion cascade.

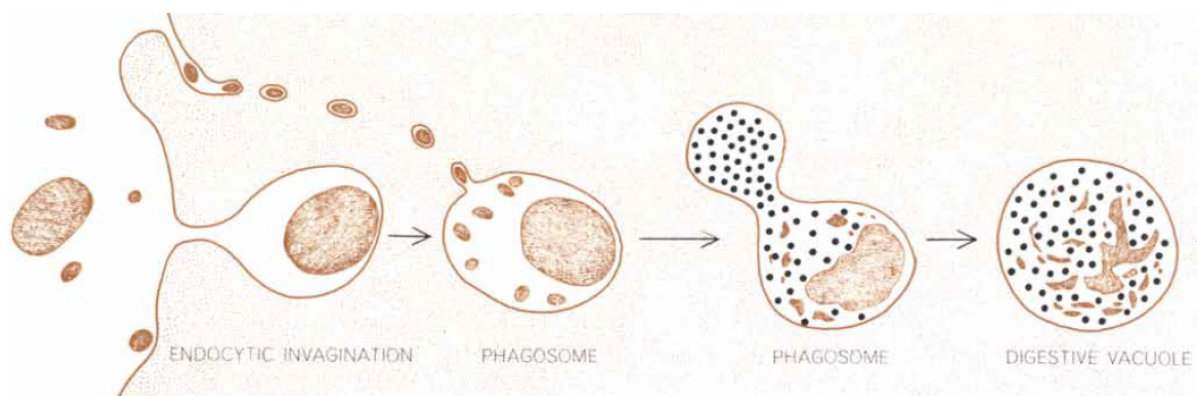


Figure 1: Phagocytosis pathway, adapted from "INTRACELLULAR DIGESTION"(De Duve, 1963).

Scheme of external cargo uptake by endocytic invagination into phagosomes delivered to the digestive vacuole.

1.1 Clathrin-mediated endocytosis

Engulfing molecules, bacteria, and other external resources by de novo generation of internal membranes from the plasma membrane lipid bilayer is generally referred to as endocytosis (De Duve, 1963). Many different co-existing routes of endocytic uptake into the cell's interior exist and ensure a precise regulation of the interactions between the environment and the cell (Hoeller et al., 2005). These individual pathways create endosomal compartments with distinct lumina and surfaces given the cell the possibility of delivering cargoes to different intracellular destinations (Doherty and McMahon, 2009).

Postulated over 40 years ago, one essential and best-characterized endocytic pathway in yeast comprises clathrin-coated vesicles and is specified as clathrin-mediated endocytosis (CME) (Goldstein et al., 1979). CME involves the chronological assembly and disassembly of many associated proteins and cellular structures for cargo uptake at the plasma membrane (Figure 2).

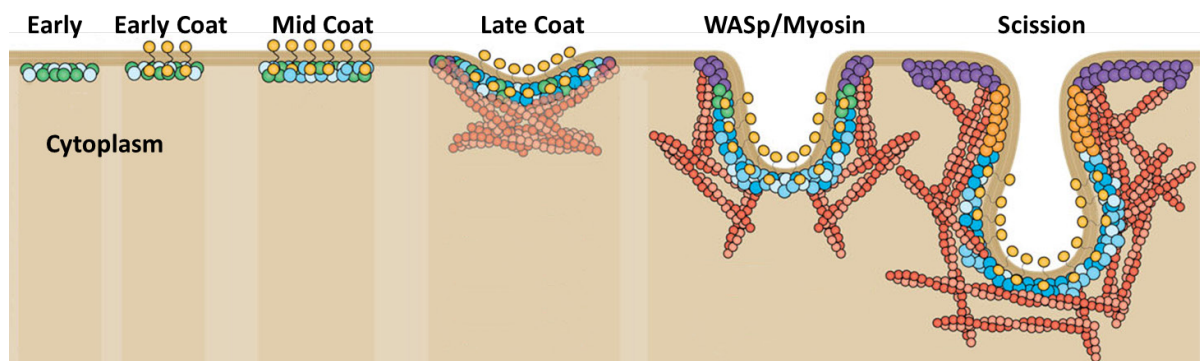


Figure 2: Clathrin-mediated vesicle formation, adapted from the poster (Lu et al., 2016).

Chronological pathway of membrane deformation and scission; Early protein in green, early coat in bright blue, mid-coat in blue, late coat in dark blue, WASp/Myosin in purple, actin in orange, and cargo in yellow

Clathrin-mediated endocytosis can be sub-divided into clustering coat proteins and cargo at the endocytic site, membrane deformation, and membrane scission to release a membrane enwrapped vesicle (Conibear, 2010). Initially, early proteins and furrow plasma membrane domains named eisosomes assemble at the putative organizing sites, followed by the accumulation of cargo molecules for endocytosis (Walther et al., 2006).

CME uptake and vesicle formation is regulated via cascade-like phosphorylation of almost all endocytic proteins and the ubiquitylation of the cytosolic domains of endocytic cargo (Haglund and Dikic, 2012). The coating-protein clathrin functions as a molecular scaffold for vesicular uptake by self-assembling into cage-like, polyhedral lattices on and around the plasma membrane called clathrin-coated pit (CCP) (Roth and Porter, 1964). The clathrin-coat and the

membrane bilayer are linked together by four subunits of the heterotetrameric adaptor complex AP2 (Kirchhausen et al., 2014). The subsequent WASp/Myosin protein complex recruitment promotes actin polymerization, pulling the coated plasma membrane towards the cell's interior and allowing the matured clathrin-coated pit to commit invagination. Bringing the two membrane bilayers in close proximity activates scission effectors like the GTPase dynamin to pinch off the vesicle from the plasma membrane (Weinberg and Drubin, 2012). The fully matured clathrin-coated vesicle (CCV) sheds the clathrin coat before associated actin cables transport and fuse the endocytic vesicle to accepting organelles of the endomembrane system (Toshima et al., 2006).

1.2 Endomembrane system

The endomembrane system consists of a combination of intracellular sorting organelles like the early, late, and recycling endosomes, the *trans*-Golgi network (TGN), vesicles, and the lysosome. Traffic between these organelles form branched and often bi-directional routes to sort, recycle and degrade cargo material (Scott et al., 2014).

The early endosome serves as the initial sorting organelle in mammalian cells which membrane composition and volume mainly derives and constantly regenerates from fused endocytic vesicles (Murphy, 1991). Upon vesicle fusion, cargo material gradually dissociates from the corresponding receptor allowing the receptor molecules to detach from the EE and recycle back to the plasma membrane via the *trans*-Golgi network and the recycling endosome (Delic et al., 2013). Proteins exported from the endoplasmic reticulum (ER) likewise pass by the TGN, sorted for endosomal or plasma membrane delivery. The exchange of material between the TGN and the recycling endosome serves as a critical nexus between the endocytic and secretory pathways in endosomal trafficking (Maxfield and McGraw, 2004). Cargo material targeted for degradation and cell material for lysosomal maintenance remains associated with the EE, which maturation process involves changes in the lipid composition, acidity, and membrane markers (Huotari and Helenius, 2011). Membrane markers, including Rab proteins, vesicle coats, tethering molecules, and proteins of the SNARE family, characterize each endomembrane compartment (Cai et al., 2007). Tethering factors and Rab proteins mediate docking of vesicles to the proper target endomembrane, whereas membrane-bound soluble *N*-ethylmaleimide-sensitive-factor (NSF) attachment receptor (SNARE) proteins mediate vesicle fusion (Wang et al., 2017). Specific target-SNAREs (t-SNAREs) on the membrane interact with vesicle-SNAREs (v-SNAREs) to form a structured SNAREpin harboring a hydrophobic coiled-coil

structure to bring the organelles in close proximity for membrane fusion (Sollner et al., 1993). Conversion of Rab GTPases drives endosome maturation, crucial for sorting endocytic cargo and receptors after membrane fusion. In mammalian cells, the early endosome's development to the late endosome (LE) is advanced by exchanging the Ras-related protein Rab5 with Rab7a (Rink et al., 2005). Rab7a recruitment implements LE maturation, enabling lysosomal targeting and concluding the endocytic pathway (Hesketh et al., 2018).

In contrast, yeast's putative minimal endomembrane system functions like an endosomal shuttling model rather than by endosomal maturation, in which the TGN serves as an early and recycling endosome (Skjeldal et al., 2021) (Figure 3). Yeast expression of the early endosome marker Rab5 homologs Vps21 and Ypt52 colocalize with a joint prevacuolar compartment (PVC) marker protein (Day et al., 2018). Cargo material targeted for degradation in the yeast vacuole is exchanged via vesicles from the TGN to the prevacuolar endosome (PVE), resembling the mammalian's late endosome in yeast (Grissom et al., 2020).

Maturation of the early endosome or PVE involves membrane invagination and budding towards the endosome's lumen, processing cargo into intraluminal vesicles (ILVs) (Luzio et al., 2007). Mature endosomal compartments feature a round morphology, harboring numerous ILVs, forming a multivesicular body (MVB) located close to the cell nucleus (Mellman, 1996). MVB undergoes transient fusion ("kiss and run") with the lysosome in which proteases and lipases drive the hydrolyzation of the mono- or polyubiquitinated target proteins marked for degradation (Haglund and Dikic, 2012). Recognition of ubiquitin added to the target protein and proper cargo sorting into forming ILVs is mediated by the endosomal sorting complex required for transport (ESCRT) (Hurley, 2010).

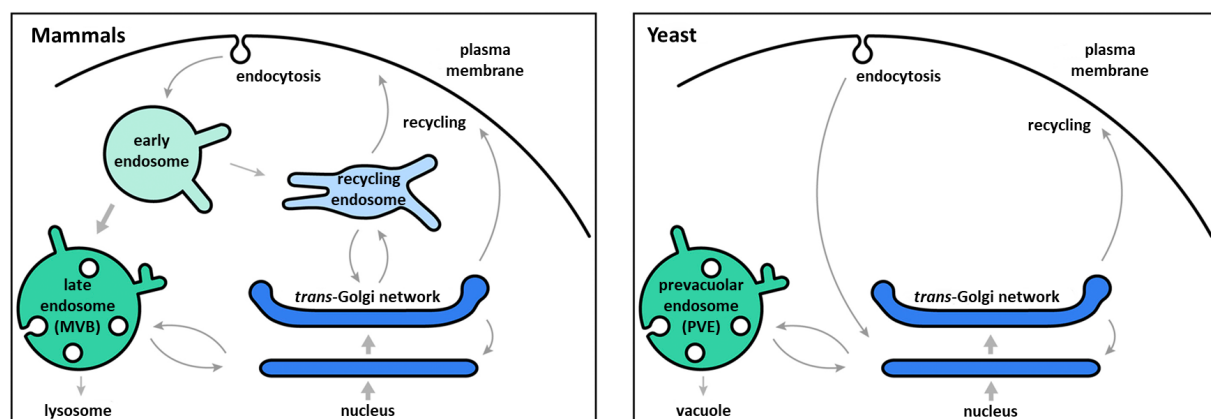


Figure 3: Endomembrane trafficking in mammals and yeast, adapted from (Day et al., 2018).

In mammalian cells, endocytic and secretory pathways include early, late, and recycling endosomes, which communicate with the TGN through bidirectional traffic. In yeast cells, endocytosed cargo is sorted in the TGN, recycled back to the PM, or transported to the PVE for degradation.

1.3 The ESCRT machinery

Genetic screens in yeast led to the identification of mutants secreting vacuolar proteins, like the well-documented soluble vacuolar glycoprotein carboxypeptidase Y (CPY), usually sorted from the TGN to the vacuole, out of the cell (Stevens et al., 1986). Proteins initiating the absence of a sorting signal are identified as vacuolar protein sorting (vps) associated proteins, which mutants also commence defects in sorting several other cargo proteins (Robinson et al., 1988, Rothman et al., 1989). Miss sorting of cargo proteins like CPY into morphological distinct prevacuolar compartments led to a further classification into class A-F phenotypes. Fourteen genes grouped into the phenotypic class E show a miss localization of transmembrane proteins onto the vacuole membrane processed by an exaggerated endosome classified as a class E compartment (Raymond et al., 1992). Class E Vps proteins form the highly conserved ESCRT (endosomal sorting complex required for transport) machinery consisting of ESCRT-0, -I, -II, and -III, and the AAA-ATPase Vps4 (Leung et al., 2008) (Table 1).

Table 1: The ESCRT nomenclature in yeast and metazoans (Hurley, 2010).

Complex	Yeast Protein	Metazoan protein	Domains and motifs
ESCRT-0	Vps27	VPS27/Hrs/HGS	VHS, UIM, GAT, FYVE
	Hse1	HSE1/STAM1, 2	VHS, UIM, GAT, SH3
ESCRT-I	Vps23/Stp22	VPS23/TSG101	UEV, PRD, coiled-coil
	Vps28	VPS28	Vps28 CTD, coiled-coil
	Vps37/Sm2	VPS37A, B, C, D	Coiled coil
	Mvb12	MVB12A, B/UBAP1(L)	MAPB, UBD, coiled-coil
ESCRT-II	Vps22/Snf8	VPS22/EAP30	WH, coiled-coil
	Vps25	VPS25/EAP20	WH, PPxY
	Vps36	VPS36/EAP45	GLUE, NZF1, 2, WH
ESCRT-III	Chm7	CHMP7	MIM1, 2
	Did2/Chm1/Vps46	DID2A, B/CHMP1A, B	MIM1
	Ist1	IST1	MIM1, 2
	Mos10/Chm5/Vps60	VPS60/CHMP5	MIM1
	Snf7/Vps32	SNF7A, B, C/CHMP4A, B, C	MIM2
	Vps2/Chm2/Did4	VPS2A, B/CHMP2A, B	MIM1
	Vps20/Chm6	VPS20/CHMP6	MIM2
	Vps24	VPS24CHMP3	Weak MIM1
Vps4-Vta1	Vps4	VPS4A, B/SKD1	AAA, MIT
	Vta1	VTA1/LIP5	MIT
Bro1/ALIX	Bro1/Vps31	ALIX/AIP1	Bro1, V, PRD

Although found highly conserved amongst all eucaryotes, the ESCRT machinery and the vps proteins were first characterized in yeast for the essential role in ILV formation and MVB biogenesis (Bryant and Stevens, 1998). Early electron microscopy elucidated MVB biogenesis and structure with ILV's without an associated function (Palade, 1955). Later on, the discovery of MVB's limiting membrane invagination with contemporaneous cargo receptor uptake, such as the epidermal growth factor receptor (EGFR), into the formed vesicle, linked the MVB to the endocytic pathway (Felder et al., 1990). Here, the interplay between all four ESCRT complexes with the AAA-ATPase Vps4 leads to the detection and assembly of endocytic cargo on the endosomal membrane destined for degradation in the vacuole (Saksena et al., 2007). Selective cargo detection and incorporation into ILVs is initiated by the post-translational modification of the target protein with ubiquitin (Ub) (Katzmann et al., 2001, Piper and Lehner, 2011). A single Ub is covalently attached to the cargo by the lysine residue 63 (K63), which sufficiently targets the protein substrate for Ub-binding protein recognition. (Stringer and Piper, 2011). The modification leads to signal termination by segregating the still active receptor domain from the cytoplasmic downstream signaling molecule. The interplay between the attached Ub and ESCRT's containing ubiquitin-binding domains (UBD) concludes receptor inactivation (Katzmann et al., 2002). To accomplish ILV biogenesis, most Ub is removed from the cargo by ESCRT proteins which assemble into a piece of complex multi-subunit machinery with membrane deforming and constricting abilities, as depicted in Figure 4. Each ESCRT complex is recruited in a cascade-like manner to consecutively fulfill a distinct function leading to membrane invagination and luminal vesicle abscission (Piper and Katzmann, 2007).

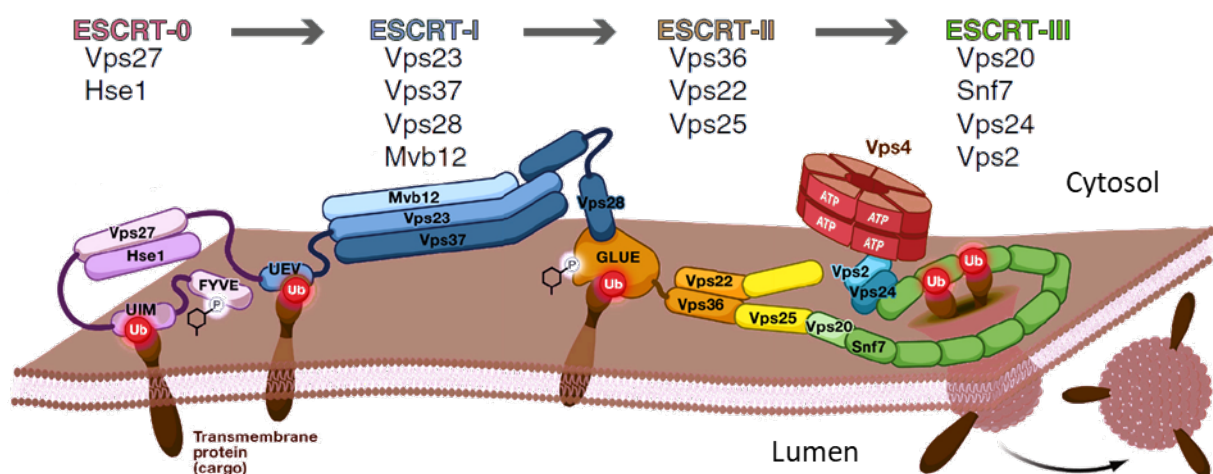


Figure 4: Scheme of the ESCRT machinery assembly, adapted from (Teis et al., 2009).

Sequentially recruitment of the ESCRT machinery for incorporation of transmembrane proteins into ILVs. The machinery consists of cargo recognition by ESCRT-0, recruiting ESCRT-I and ESCRT-II, and subsequent assembly and oligomerization of ESCRT-III proteins before vesicle abscission and ESCRT disassembly by Vps4.

1.3.1 ESCRT-0

The primer of ESCRT machinery recruitment is the ESCRT-0 complex required to sort plasma membrane proteins and receptors into the endocytic pathway for MVB biogenesis. The complex is responsible for binding and clustering ubiquitinated cargo at the putative membrane locus for ILV formation, further recruiting clathrin, ubiquitin ligases, and de-ubiquitinating enzymes to the specific endosomal membrane (Meister et al., 2017).

ESCRT-0 complex development comprises a 1:1 heterodimer of Vps27 and Hse1 in yeast and Hrs and STAM1, 2 in metazoa (Ren et al., 2007). The none transient complex exists in a cytosolic persistent state, recruited and dislodged to and from the endosomal membrane upon request (Prag et al., 2007). Vps27 and Hse1 contain an N-terminal ubiquitin-binding VHS (Vps27, HRS, STAM) domain, followed by an FYVE (Fab1, YOTB, Vac1, EFA1) domain in Vps27 (Ren and Hurley, 2010). The FYVE domain of Vps27 and the metazoa homolog Hrs1 bind phosphatidylinositol 3-phosphate (PI3P) to guide the ESCRT-0 complex to the target endomembrane (Raiborg et al., 2001, Stahelin et al., 2002). Additional to the FYVE domain, Vps27 contains two ubiquitin-interacting motifs (UIM) for binding up to five Ub moieties attached to the target cargo and thus commencing ESCRT-0 governed Ub cargo clustering (Swanson et al., 2003). Vps27 interacts with clathrin, which polymerizes into a flat bi-layered membrane coat, limiting ESCRT-0 distribution on the local Ub cargo cluster (Raiborg et al., 2006). The protein Hse1 (or STAM1) contains a VHS domain for membrane targeting and cargo recognition and an SH3 (src homology-3) domain to recruit de-ubiquitinating enzymes such as UBPY or Ub ligases like Rsp5 to the local protein cluster (Kato et al., 2000). The constitutively assembled ESCRT-0 heterodimer shapes into an antiparallel coiled-coil structure through an elongated, rigid core, mediated by SNARE structural like GAT domains (Ren et al., 2009). The overall unstructured C-terminus of Vps27 holds a short PTAP motif for binding the ESCRT-I subunit Vps23, thus enhancing ESCRT recruitment (Katzmann et al., 2003).

1.3.2 ESCRT-I

The role of ESCRT-I, much like ESCRT-0, is to ensure clustering of ubiquitinated cargo and generating ILV's by recognizing target membranes, thus further bridging ESCRT-0 to the upstream ESCRT machinery (Morita et al., 2011). The ESCRT-I subunits Vps23, Vps28, Vps37, and Mvb12 form a rigid long, cytosolic persistent heterotetramer in a 1:1:1:1 ratio with two contiguous but distinct core complexes (Curtiss et al., 2007).

The first sub-complex consists of Vps23, Vps37, and Mvb12, which form a rod-shaped stalk with an antiparallel coiled-coil structure, whereas Vps23, Vps28, and Mvb12 form a fanned cap

headpiece complex of three pairs of antiparallel helices (Kostelansky et al., 2007). Vps23 (human tumor susceptibility gene 101 or TSG101 in humans) contains one N-terminal ubiquitin E2 Variant (UEV) domain for binding ubiquitinated cargo like the UIM of Vps27 and a PTAP motif for bilateral binding and connecting ESCRT-0 to ESCRT-I (Chu et al., 2006). Targeting ESCRT-I to the midbody connecting the two daughter cells during cytokinesis, Vps23 harbors a GPPX₃Y motif after the UEV domain spaced by a pro-rich linker sequence (Carlton and Martin-Serrano, 2007). The ESCRT-I subunit Vps37 contains an N-terminal basic helix mediating membrane binding of the complex, and the subunit Mvb12 has an additional C-terminal UBD for Ub cargo binding (Oestreich et al., 2007). Vps28 core region linked to a C-terminal four-helix bundle domain (CTD) is responsible for ESCRT-I co-assembly with ESCRT-II in a 1:1 super complex at the ESCRT-0 locus (Gill et al., 2007).

1.3.3 ESCRT-II

ESCRT-II functions as an essential partner of ESCRT-I in MVB biogenesis and bud formation since overexpression of ESCRT-II bypasses ESCRT-I presence during MCB cargo sorting (Babst et al., 2002b). Like the ESCRT-0 and ESCRT-I complex, ESCRT-II is constitutively assembled to form a stable hetero-oligomeric complex in the cytoplasm. Partly involved in Ub cargo binding, the pivotal role of ESCRT-II is the bridging of ESCRT-I to ESCRT-III (Wang and Hong, 2006). Thus, the ESCRT-I and ESCRT-II super complex indirectly promotes membrane budding by recruiting ESCRT-III to induce local membrane deformation. ESCRT-II modulates the ordered assembly of ESCRT-III into a ring-like polymer with a defined diameter to mediate cargo capture and vesicle formation (Henne et al., 2012). The Y-shaped ESCRT-II complex consists of a 1:2:1 heterotetramer of Vps22 (ELL-associated protein of 30 kDa, or EAP30 in metazoa), Vps36 (EAP45), and two units of Vps25 (EAP20). Vps22 and Vps36 resemble the core complex of ESCRT-II, where each subunit consists of a tandem winged-helix motif to stabilize the sub complex and is flexibly associated with Vps25 (Teo et al., 2004). Vps22 promotes membrane targeting by a basic helix motif at the N-terminus of the protein (Im and Hurley, 2008). The N-terminus of Vps36 contains a variant pleckstrin homology (PH) domain named “GLUE” (GRAM-like ubiquitin binding in EAP45) domain that mediates binding preferred to PI3P and Vps28 of ESCRT-I (Slagsvold et al., 2005). The GLUE domain harbors two Np14 zinc finger (NZF) domains by which the NZF1 acts as the locus for the Vps28-CTD of ESCRT-I and NZF2 interacts with a single Ub moiety of clustered cargo (Alam et al., 2004). Both Vps25 subunits are essential for MVB sorting by interacting with Vps20 of ESCRT-III and thereby promoting ESCRT-III assembly (Hierro et al., 2004).

1.3.4 ESCRT-III

The ESCRT-III complex resembles the heart of the ESCRT system as the central membrane scission machinery. Only ESCRT-III and Vps4 homologs are conserved in all life domains for catalyzing cell division (Lindas et al., 2008). The complex is considered to be the most ancient remodeling complex found in archaea and lokiarchaeota, a phylum seen as the missing link between archaea and eukaryotes, to possibly participate in prokaryotic to eukaryotic transition by the inside out model (Baum and Baum, 2014, Spang et al., 2015).

The ESCRT-III complex in budding yeast consists of Vps20, Snf7, Vps24, Vps2 and Did2, Ist1, Vps60 (Mos10), and Chm7, the latter four considered as ESCRT-III associated or ESCRT-III-like proteins in previous works (Babst et al., 2002a). The human genome encodes twelve ESCRT-III proteins corresponding to the eight yeast homologs comprising several isoforms named CHMPs (chromatin-modifying protein) (Bertin et al., 2020). All ESCRT-III subunits contain diverse sequences, unified by an identical domain organization with an asymmetrical charge distribution (Lata et al., 2009).

ESCRT-III proteins commonly harbor six α -helices that reside within the positively charged N-terminal region comprising $\alpha 1 - \alpha 2$ followed by an acidic C-terminal, electronegatively charged domain of $\alpha 3 - \alpha 6$ (Schoneberg et al., 2017) (Figure 5).

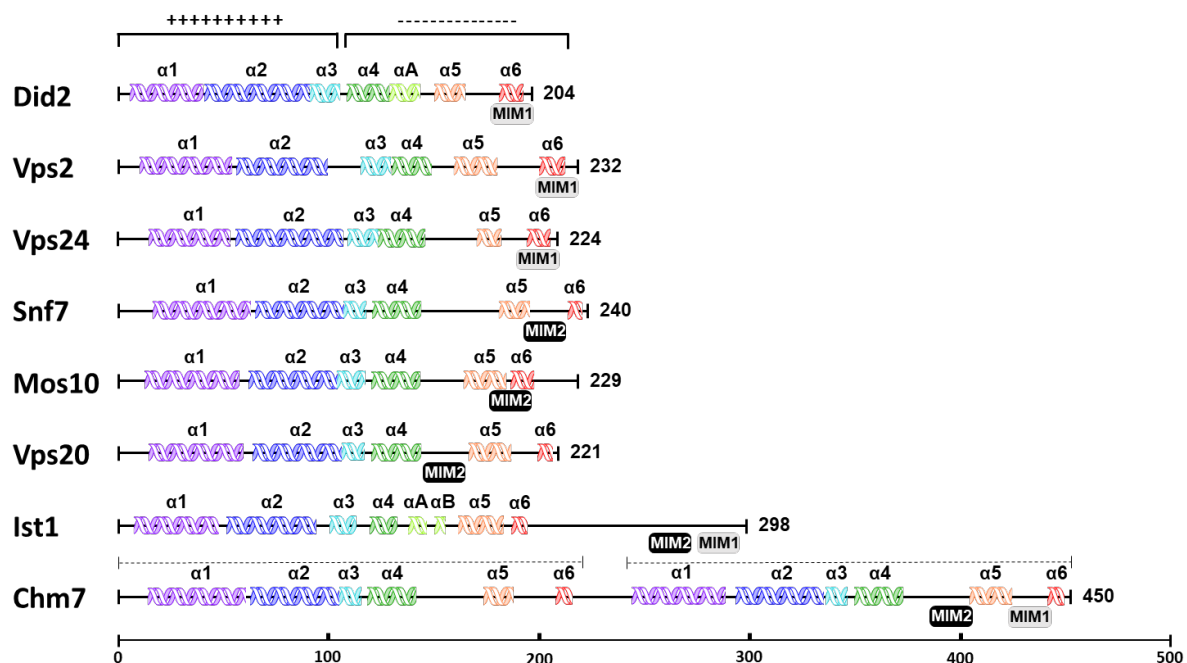


Figure 5: The ESCRT-III proteins in yeast, redrawn from (Schoneberg et al., 2017).

All eight ESCRT-III complex-associated proteins are schemed with the secondary structure, motifs, and charge. The length of the black line describes the number of amino acids per protein, thus the total protein size. Secondary α -helices are colored as follows: $\alpha 1$ in purple, $\alpha 2$ in blue, $\alpha 3$ in cyan, $\alpha 4$ in green, αA and αB in bright green, $\alpha 5$ in orange, and $\alpha 6$ in red. The C-terminal MIM1 and MIM2 domains are highlighted in black and grey boxes.

All ESCRT-III subunits are related 200 to 240 amino acid large proteins besides Ist1 that contains an elongated N-terminal domain and Chm7, which appears to be twice as large as the other members with an ESCRT-III domain in the C-terminal half (Bauer et al., 2015, Horii et al., 2006). The C-terminus of all ESCRT-III proteins contains a MIT (microtubule-interacting and transport)-interacting motif (MIM) for mediating successional Vps4 binding. Did2, Vps2, and Vps24 carry a MIM1 domain at the C-terminus, whereas Snf7, Mos10, and Vps60 contain a MIM2 domain. The enlarged ESCRT-III subunits Ist1 and Chm7 contain both motifs (Kieffer et al., 2008, Stuchell-Brereton et al., 2007). MIM1 contains a sequence-conserved amphipathic helix (D/E)xxLxxRLxxL(K/R) motif, critical for Vps4 recruitment by Vps24, and MIM2 is a proline-rich sequence for selective ESCRT-III recognition by the MIT domains of Vps4 (Obita et al., 2007, Shestakova et al., 2010). Vps20 carries a myristoylation site at the N-terminus important for targeting the protein to the membrane (Yorikawa et al., 2005). The positively charged N-terminus of Vps2 and Vps24 further promotes the association of ESCRT-III to the membrane (Scott et al., 2005). The lack of a PI3P binding or Ub-cargo recognition domain leads to the ability of ESCRT-III to perform remodel function and catalyze membrane fission on all cellular membranes like the PM, endosomal or nuclear envelope (Schoneberg et al., 2017). The ESCRT-III subunit Snf7 carries an N-terminal ANCHR (N-terminus containing hydrophobic residues motif) domain acting as a high-affinity anchor for MVB sorting (Buchkovich et al., 2013). Snf7 also contains a Bro1 binding site at the C-terminus for ESCRT-III disassembly and promoting de-ubiquitination of cargo before entering the ILV by recruiting the ubiquitin hydrolase Doa4 (Richter et al., 2007, Wemmer et al., 2011). All considered core complex subunits of ESCRT-III consisting of Vps20, Snf7, Vps24, and Vps2 contain an N-terminal lipid interacting domain to allow for the assembly and oligomerization on the lipid surface for membrane budding and scission.

For the assembly of the ESCRT-III complex, many ESCRT-III subunits interconvert between two conformations, namely the closed, monomeric conformation in the cytoplasm and an open conformation for polymerization at the membrane (McCullough et al., 2015). Crystal structures of Vps24 revealed an asymmetric, antiparallel, N-terminal region comprising the $\alpha 1$ and $\alpha 2$ helices, which form a 70 Å rigid hairpin followed by two short helices (Lata et al., 2009). The crystal structure of the ESCRT-III subunit IST1 reveals the closed state to be organized by an N-terminal helical hairpin followed by $\alpha 3$ and $\alpha 4$ linker connected to the regulatory $\alpha 5$ domain (McCullough et al., 2018) (Figure 6). The entire N-terminal conserved region of the $\alpha 1$ - $\alpha 4$ core functions as the structural scaffold of ESCRT-III filament biogenesis, whereas the C-terminal $\alpha 5$ - $\alpha 6$ part governs autoinhibitory and regulatory roles (Shim et al., 2007).

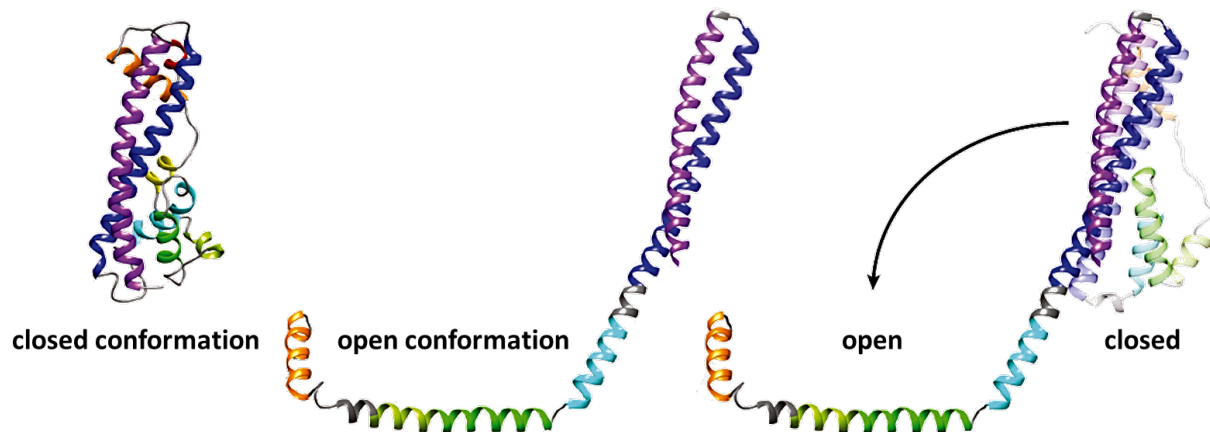


Figure 6: ESCRT-III open and closed conformational structure, adapted from (McCullough et al., 2018).

The secondary structure of IST1 and CHMP1B (Did2 in yeast) consists of five conserved helices following the color scheme in Figure 5. The crystal structure reveals (from left to right) the open IST1 and closed CHMP1B conformation and the superposition of both conformations in a light and dark shade.

The closed conformation defines a folded back $\alpha 5$ helix against the closed end of the $\alpha 1 - \alpha 2$ helical hairpin to maintain the protein in a soluble, inactive state in the cytoplasm. The Vps24 protein crystallizes as an antiparallel dimer by which the $\alpha 5$ helix mediates intermolecular contact between neighboring monomers hardening the regulatory character of the C-terminal domain of ESCRT-III members (Bajorek et al., 2009). Snf7 and CHMP1B (Did2 in yeast) structurally rearrange into a continuous elongated $\alpha 2 - \alpha 3$ helix after converting into the open conformation (McMillan et al., 2016). CHMP1B and IST1 form co-polymers of two distinct strands with an inner strand of open CHMP1B and an outer strand of IST1 in a close conformation tightly associated in a 1:1 ratio (Nguyen et al., 2020).

Elucidating the structural composition and ambivalent conformation of ESCRT-III subunits allows for predictive ESCRT-III assembly and putative functions within the ILV formation and abscission. Each subunit is present as a cytosolic monomer that transiently assembles on membranes into the active ESCRT-III complex, unlike the heteropolymers ESCRT-0, -I, and -II that exists in persistent complexes (Saksena et al., 2009). Nucleation of ESCRT-III requires the ESCRT-II subunit Vps25, where a single Vps25 arm at the Y-shaped structure is sufficient to promote ESCRT-III assembly, although the complex lacks functional formation capability (Teis et al., 2010). Functional ESCRT-III assembly is thereby initiated by the interaction of the N-terminal half of two Vps20 to ESCRT-II via the WH2 domain of two Vps25 (Im et al., 2009). Tightly associated with the membrane, Vps20 turns into the nucleator of Snf7 oligomerization, which converts from the inactive, closed conformation to the activated, open state to induce filament formation. Vps24 caps Snf7 filamentation, which recruits Vps2 and eventually Vps4

to recycle the complex (Teis et al., 2008). *In vitro* experiments revealed that Snf7, Vps24, and Vps2 are sufficient to form polymers like short helical and non-helical filaments, rings, spirals, and tube structures, some with the capacity to deform membranes (Hanson et al., 2008). The cited conventional pathway of sequential ESCRT-III assembly was recently refined to a dynamic self-assembly pathway of continuous ESCRT-III/Vps4 exchange catalyzed by ATP hydrolysis, further including the ESCRT-III-like proteins Did2 and Ist1 (Pfitzner et al., 2020) (Figure 7). While Vps20 induced filament formation by oligomerization of Snf7 leads to spiral structures with buckle properties regarding growth and elasticity, no tubular protrusions could be observed (Chiaruttini et al., 2015). Buckling transition from a flat spiral to a cylindrical structure is promoted by a secondary filament or second layer of recruited Vps2-Vps24 to rigidify the polymer and form a helical tube (Mierzwa et al., 2017, Moser von Filseck et al., 2020). The second layer reduces spiral-induced stress in the flat structure by twisting the filaments, further promoted by Vps24 to Did2 exchange forming conical spirals (Harker-Kirschneck et al., 2019). For the third layer, Vps2 exchanges to Ist1 to form the Did2-Ist1 fission complex able to reduce membrane tube constricted to 4.8 nm which is in the range required for membrane fission like in the dynamin induced fission of CCV by a super-constricted complex of 3.7 nm (Sundborger et al., 2014). Dynamic ESCRT-III subunit assembly and disassembly requires Vps4 ATPase activity and is ATP-driven since subunit-turnover was found to be Vps4/ATP induced (Pfitzner et al., 2020). ESCRT-III filament depolymerization by Vps4/ATP occurs in the order Vps2-Vps24 to Snf7, Vps2-Did2 and finally removing Did2-Ist, forming a unidirectional stepwise pathway *in vitro* (McCullough and Sundquist, 2020).

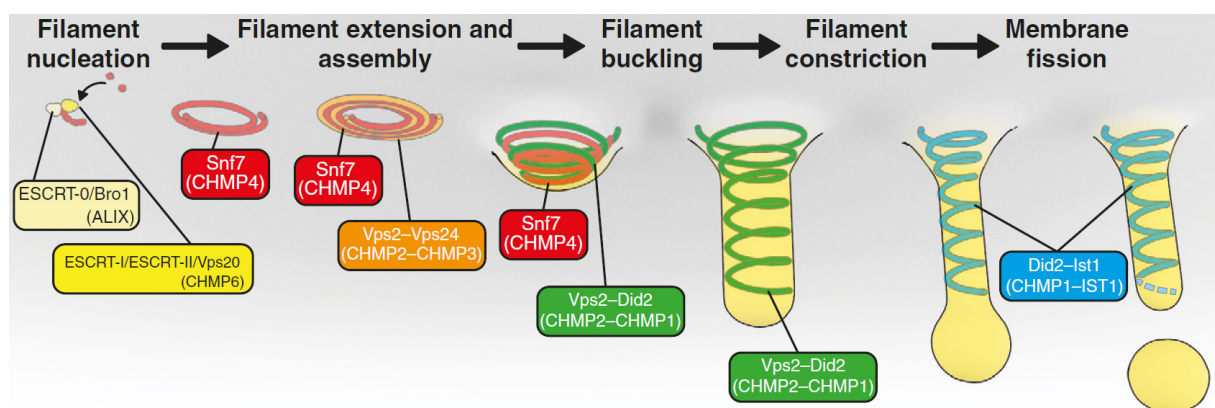


Figure 7: Membrane fission by ESCRT-III exchange, adapted from (McCullough and Sundquist, 2020).

Schematic stepwise filament formation by Snf7, nucleated by the ESCRT-0 to Vps20 cascade. The dynamic exchange of ESCRT-III subunits Snf7, Vps2-Vps24, and Did2-Ist1 for progressive membrane invagination and fission. The endosomal membrane is shaded in grey, and the lighter grey shading represents the endosomal lumen, while the cytoplasm is depicted in yellow.

1.3.5 Vps4

The AAA (ATPase associated with a variety of cellular activities) ATPase Vps4 mediates ESCRT-III re-assembly and recycling by being the thermodynamic force of the late ESCRT machinery (Babst et al., 1998). The enzyme submits the dynamic exchange of ESCRT-III subunits in and out of the filaments by hydrolyzing ATP for harnessing energy (Monroe and Hill, 2016). The structural form of Vps4 resembles a hexameric ring capable of unfolding individual ESCRT-III subunits by guiding these through the central pore in an ATP-dependent manner (Monroe et al., 2017, Yang et al., 2015). Interaction of Vps4 is mediated by the N-terminal microtubule interacting and trafficking motif (MIT) domain that interacts with the C-terminal MIM domains of ESCRT-III proteins (Stuchell-Brereton et al., 2007). Coordinated interaction with the MIT domain of Vps4 within the stepwise assembly and disassembly of ESCRT-III filaments biogenesis is crucial for ILV formation (Adell et al., 2014). After the N-terminal domain, the core ATPase mediates the hexamerization and ATP hydrolysis while the C-terminal β -domain of Vps4 binds the ATPase activator LIP5 (Vta1) (Han et al., 2017).

LIP5/Vta1 functions as a co-factor of Vps4 by stabilizing the hexameric ring structure of Vps4 by bridging adjacent ESCRT-III subunits and thus further promoting ESCRT-III lattice association (Xiao et al., 2008). Recruitment of Vps4 is promoted by contact between the Vps4-MIT domain with the Vps2 MIM1 domain, thus leading to Vps4 oligomerization to an active ATPase (Azmi et al., 2008). After the Vps4/ATP induced stepwise depolymerization cascade of individual layers at the fission locus, each ESCRT-III subunit converts to the inactive, autoinhibited state, and Vps4 resets to the mobile, monomeric state (Su et al., 2017).

1.4 ESCRT functions

The principal biochemical function of ESCRTs is to induce membrane bending and constrictions to narrow down membrane necks for scission events (Hurley and Hanson, 2010). Elucidating profound functions of the ESCRT machinery led to the incorporation of the ESCRT family into the endosomal system, hence the primary involvement of the ESCRT machinery in ILV formation during MVB biogenesis (Wideman et al., 2014). Therefore, the ESCRT system could be directly linked to moderate endosomal functions for selectively sorting ubiquitinated cargo proteins in vesicles for vacuolar targeting and degradation (Katzmann et al., 2001). Besides the pivotal role in MVB biogenesis, consequent studies revealed a variety of non-endosomal functions mediated by the ESCRT machinery, broadening the role of ESCRTs in cellular processes (Figure 8). Hence, “ESCRTs are everywhere” (Hurley, 2015).

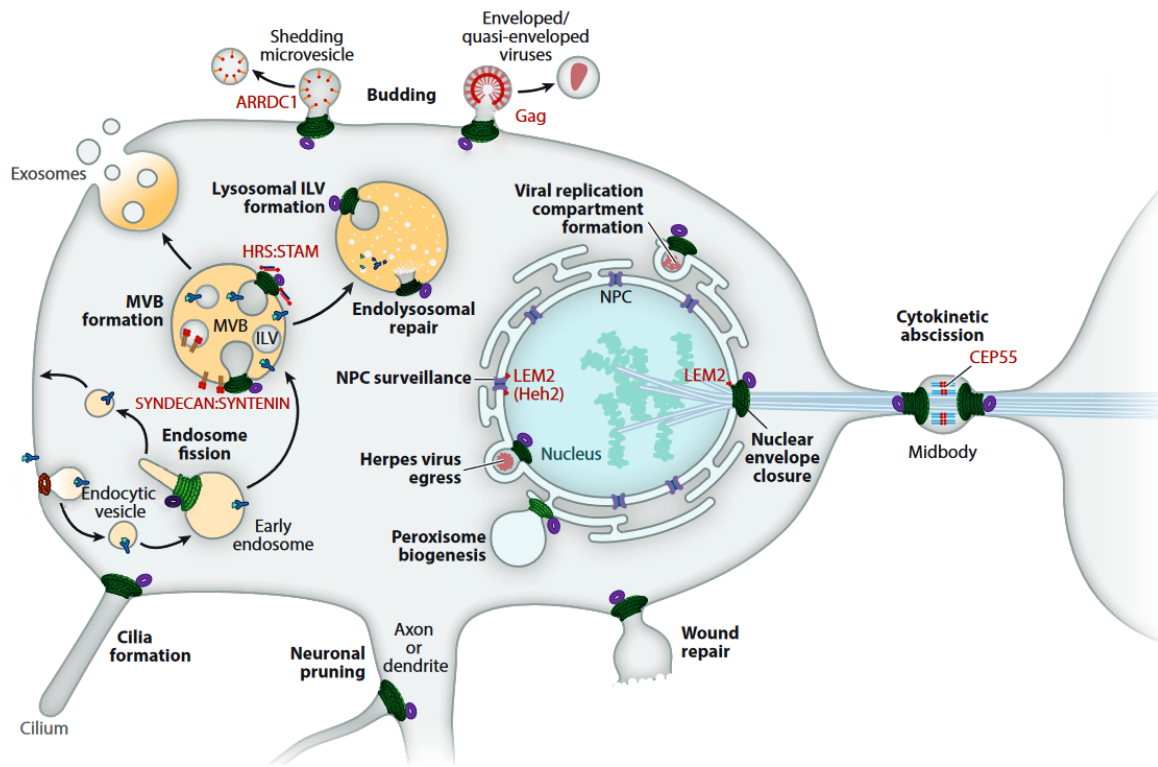


Figure 8: Summary of ESCRT-III mediated cellular processes, adapted from (McCullough et al., 2018).

Schematic illustration of known ESCRT-III mediated functions in membrane remodeling, ESCRT spiral filaments depicted as green helices. ESCRT dependent cellular functions are labeled in bold, cellular organelles in regular font, and compartments specific adapter proteins in red.

1.4.1 Cytokinesis

An example of a fundamental cellular process involving the deformation of membranes to form tubular structures is cytokinesis. Cytokinesis describes the progress of cell division in which a daughter cell emerges connected by an intracellular bridge with a midbody ring at the center (Guizetti et al., 2011). Cytokinesis progression factors recruited to the midbody arms alongside the midbody ring govern final abscission, whereas failure in abscission function promotes diseases like tumorigenesis and chromosomal instability (Lens and Medema, 2019). One of the most ancient function of ESCRTs was to catalyze membrane cleavage in cell division found in archaea involving ESCRT-III and Vps4 homologs (Samson et al., 2008).

The centrosomal protein CEP55 of 55 kDa functions as the compartment-specific targeting factor accumulated at the midbody to recruit ESCRT-I TSG101 (VPS23) and associated protein ALIX to the midbody via a GPPx3Y motif (Lee et al., 2008). Both proteins nucleate for ESCRT-III assembly at the midbody ring in which ALIX bridges to CHMP4B (Snf7 in yeast) via the Bro1 domain and TSG101 engages ESCRT-II to recruit CHMP4B-CHMP6 (Vps20 in yeast) (Goliand et al., 2014, Tang et al., 2016). All MVB biogenesis essential ESCRT-III subunits are also present in cytokinesis, bound to the membrane via the microtubule interacting

and trafficking domain containing 1 (MITD1) protein, to induce filament polymerization (Hadders et al., 2012, Lee et al., 2012). These cell-cortex-associated helical filaments on both sides of the midbody ring are continuously remodeled by VPS4 (Schoneberg et al., 2018). VPS4 recruits CHMP1B, which then engages the AAA-ATPase spastin to induce microtubule severing, leading to the physical separation of the daughter cells and thus concluding cell abscission (Yang et al., 2008).

1.4.2 Virus budding

Successful viral infection involves associating the virus to the PM of the host cell, cellular uptake, and uncoating the viral genome to initiate viral gene expression (Votteler and Sundquist, 2013). Various membrane compartments are hijacked to mediate viral maturation inside the host cell, including the associated ESCRT machinery (Scourfield and Martin-Serrano, 2017). Entering the host cell by fusion with the cells PM or taken up by receptor-mediated endocytosis without damaging the integrity of the host cell membrane ensures translocation of the viral genome into the cytoplasm (Tuthill et al., 2006). Gaining access to the cytoplasm and associating with the ER is crucial for viruses exploited to the endosomal system not to be recycled back to the PM, while ESCRT subunits like TSG101 are considered to be necessary for correct endosomal trafficking of viral particles (Kumar et al., 2018, Lozach et al., 2011). Each virus family can take different cellular membranes and thus separate compartments hostage to generate new viral replication origins for a new viral life cycle. The ESCRT machinery is further involved in forming compartments for viral replication at the nucleus-ER region, where the proviral DNA is replicated and egress into the cytosol (Tabata et al., 2016). Pathogenic viruses like Ebola, hepatitis C and the human immunodeficiency virus-1 (HIV-1) preferable take control of the host's ESCRT machinery to release infectious material from the infected cell by budding at the PM to remove matured enveloped viruses (Miller and Krijnse-Locker, 2008). In the case of HIV-1 viral budding, the UEV domain of TSG101 interacts with a P(T/S)AP motif sitting in the p6 region of ubiquitinated viral Gag protein HIV-1, thus directly binding to ESCRT-I (Garrus et al., 2001). Gag contains a second p6 motif YPX(n)L for binding ALIX via the V domain, required for ALIX-dependent viral budding via CHMP4B nucleation (Strack et al., 2003). Membrane cleavage during viral budding is mediated by the ESCRT-III and Vps4 machinery recruited to the budding site prior to virion release (Baumgartel et al., 2011). The ESCRT-III subunits CHMP2 and CHMP4 extrude helical tubes from the PM, whereas CHMP2 and CHMP1 mediate VPS4 recruitment to catalyze membrane scission and enveloped virus release (Carlson and Hurley, 2012).

1.4.3 The nuclear envelope (NE)

The nuclear envelope resembles a specialized double membrane around the nucleus for separating the genome from the cytoplasm, connected via nuclear core complexes (NPCs) regulating passage in and out of the nucleus (Robijns et al., 2018). The ESCRT-III machinery coordinates the ordered sealing of the nuclear envelope, which breaks down during mitosis to facilitate chromosome capture by the mitotic spindle. Assembly and association of CHMP2A, CHMP3B, CHMP4B, and VPS4 are required to mediate the re-sealing process (Olmos et al., 2015). NPC quality surveillance and NE sealing by ESCRT-III involve a distinct recruiting pathway, not mediated by the canonical ESCRT bridging factors. Recruitment of ESCRT-III subunits was linked directly to the nucleus-specific targeting factor CHMP7 (Chm7 in yeast) (Vietri et al., 2015). Chm7 contains an N-terminal ESCRT-II-like domain characterized by the WH domain similar to EAP20 and a C-terminal ESCRT-III-like domain similar to CHMP6 (Vps20 in yeast) (Bauer et al., 2015). At the nuclear envelope, Chm7 works as an assembly factor with the nuclear envelope LEM domain 2 (LEMD2) protein (Heh1 in yeast) to maintain NPC assembly (Webster et al., 2016). Interaction between CHMP7 and LEMD2 ensures nuclear envelope integrity and inhibits unwanted polymerization of ESCRT-III at the NE (Gu et al., 2017). However, executing membrane fission to seal the nuclear envelope after spastin-induced microtubule severing requires the regulated assembly of ESCRT-III and VPS4 distributed and coordinated by additional regulator factors (Ventimiglia et al., 2018).

1.4.4 Autophagy

Autophagy is the process of degrading, not endocytosed, intracellular material by the lysosome mediated by the autophagosome, a double-membrane structure formed by the ER, PM, or mitochondria (Takahashi et al., 2018). Microautophagy describes the degradation of intracellular debris by the lysosome, whereas macroautophagy is utilized by the cell as a defense mechanism against intracellular pathogens or degrading damaged organelles (Sahu et al., 2011). In macroautophagy, cytosolic portions are engulfed and fused with the lysosome to adapt to starvation and remove toxic protein aggregates (Nakatogawa et al., 2009). Coordinated interaction between the MVB pathway and autophagy-mediated by ESCRTs ensures survival during starvation by recycling amino acids from selective degradation of proteins (Muller et al., 2015). Autophagosome biogenesis involves ESCRT-III and VPS4, which mediate double-membrane coating and sealing and govern the autophagosome with the lysosome (Zhen et al., 2020). Atg17, which controls autophagy initiation, recruits ESCRT-III subunits and VPS4 to the nascent autophagosome to catalyze autophagosome closure (Zhou et al., 2019).

1.4.5 Exosomes & Microvesicles

Exosomal compartments are small extracellular vesicles derived from ILVs containing proteins, DNA, and RNA to grant intercellular communication (Thery, 2011). Intracellular traffic of protein leads to degradation in the lysosome/vacuole, recycling to the cytoplasmic protein pool, or secreted release in exosomes centrally routed by ILV biogenesis (Raiborg and Stenmark, 2009). The interaction between ALIX initiates the formation of exosomes via the V domain and the dimeric adaptor protein syntenin-1. Syntenin-triggered clustering of the proteoglycan syndecan bridges the ESCRT machinery engagement to the syndecan-syntenin-Alix complex for exosome biogenesis (Baietti et al., 2012).

ESCRT-III induced deforming of the PM also shapes extracellular vesicles named microvesicles that play a role in intercellular signaling and removal of damaged PM (Matussek et al., 2014). The driving force of microvesicle formation is the arrestin domain-containing protein 1 (ARRDC1), which requires TSG101 and VPS4 ATPase to induce microvesicle release (Nabhan et al., 2012).

1.4.6 Other functions

The continuously extending field of ESCRT functions includes neuronal pruning in which unnecessary neuronal branches are selectively removed by ESCRT-I, ESCRT-III, and VPS4 (Loncle et al., 2015). Further implications are found in linking ESCRT indirectly to dendritic arborization neuron pruning mediated by RAB5 in *Drosophila* (Zhang et al., 2014). Other studies discovered rapid recruitment of CHMP4B due to plasma membrane lesions while closing the wounded membrane also included CHMP1A, CHMP2A, CHMP2B, CHMP3, and VPS4B (Jimenez et al., 2014, Scheffer et al., 2014). ALIX induces ESCRT-III association to the PM recruited to the PM lesion site by binding to TSG101 in a Ca^{2+} dependent manner (Sun et al., 2015).

Lysosomes, essential cellular compartments, are harboring an acidic, proton-rich environment suitable for acidic hydrolysis to degrade proteins, receptors, macromolecules, and pathogens but hazardous for the cell in the event of lysosomal membrane rupture (Papadopoulos and Meyer, 2017). The recruitment of TSG101 and ALIX is crucial for ESCRT-III induced membrane repair at the damaged lysosomal locus (Radulovic et al., 2018). The sheer endless pantheon of ESCRT functions further involves endosomal fission events, cilia formation, endosomal membrane repair, peroxisome biogenesis, neurodegenerative diseases, and cancer (Allison et al., 2013, Jung et al., 2020, Li et al., 1998, Mast et al., 2018, Skibinski et al., 2005, Skowyra et al., 2018).

1.5 Aim of this thesis

This thesis aimed to investigate new endosomal functions of ESCRT-III subunits, mainly focusing on Mos10 (Vps60). The recently extended mechanism of ESCRT-III assembly by dynamic exchange of ESCRT-III subunits mediated by Vps4 led to the incorporation of the former ESCRT-III associated proteins Did2 and Ist1 into the ESCRT-III core complex family. Chm7 was identified to perform on the nuclear membrane exerting specialized functions in nuclear membrane repair and nuclear envelope reformation (Olmos et al., 2016). Still, endosomal or non-endosomal functions of Vps60/CHMP5 are waiting to be elucidated since the protein still “remains poorly characterized” (Remec Pavlin and Hurley, 2020). Vps60 was found to be not essential for Vps2 recruitment to the endosome but was suggested to be required for MVB sorting since *vps60Δ* shows a sorting defect (Kranz et al., 2001, Losko et al., 2001). A putative link might be the stimulation of Vps4 activity in later stages of ESCRT-III polymerization by interacting with the MIT motifs of Vta1, acting as an adaptor to facilitate ESCRT-III subunits Vps20 and Mos10 to Vta1 interaction (Shiflett et al., 2004, Yang et al., 2012, Yeo et al., 2003).

I, therefore, searched for new interacting partners of Mos10 to link the ESCRT-III subunit to a specific compartment or pathway for elucidating the unknown potential of the protein. Also, functionality within the ESCRT-III complex was investigated to extend the established complex to additional endosomal functions.

2 MATERIAL AND METHODS

2.1 Strains and media

2.1.1 Bacteria strains

Table 2: *Escherichia coli* (*E. coli*) strains.

Strain	Genotype	Reference
BL21(DE3)	F ⁻ <i>ompT gal dcm lon hsdS_B(r_B⁻m_B⁻) λ(DE3 [<i>lacI lacUV5-T7p07 ind1 sam7 nin5</i>]) [<i>malB</i>⁺]_{K-12}(λ^S)</i>	(Wood, 1966)
DH5αF'	F'(Φ 80 (Δ <i>lacZ</i>) M15) Δ(<i>lacZYA-argF</i>) <i>U169 recA1 endA1 hsdR17 rk⁻mk⁺ supE44 thi-1 gyrA relA1</i>	Gibco BRL, Gaithersburg MD, USA (Woodcock et al., 1989)
XL1-Blue	F' ⁺ ::Tn10 proA+B+ <i>lacIq</i> Δ(<i>lacZ</i>)M15/ <i>recA1 end1 gyrA96</i> (Nalr) <i>thi hsdR17 (rk⁻mk⁺) supE44 relA1 lac</i>	(Bullock, 1987)
RKB2311	BL21(DE3) + pRK1854	R. Kölling, Hohenheim

2.1.2 *E. coli* growth conditions

E. coli cells were grown in LB-media (lysogeny broth) consisting of 1 % (w/v) tryptone, 0.5 % yeast extract, and 0.5 % NaCl at 37 °C and shaking at 100 rpm. Growth plates contained an additional 2 % agar. For selective pressure, 100 µg/ml ampicillin (or kanamycin) was added to the autoclaved media to ensure the growth of cells that harbor and maintain the plasmids for protein overexpression containing the ampicillin (or kanamycin) resistance gene.

2.1.3 Yeast strains

Table 3: *Saccharomyces cerevisiae* (*S. cerevisiae*) strains.

Strain	Alias	Genotype	Reference
RKY827	JD53	MATα <i>ura3-52 his3-Δ200 leu2-3, 112 trp1-Δ63 lys2-801 ssd1-d2</i>	J. Dohmen., Köln
RKY1452	RKY1558	<i>Mos10-13myc::kan</i>	R. Kölling, Hohenheim
RKY1558 (Wildtype)	JD52	MATα <i>ura3-52 his3-Δ200 leu2-3, 112 trp1-Δ63 lys2-801 ssd1-d2</i>	J. Dohmen., Köln
RKY1832	RKY1558	<i>Mos10-ProteinA::kan</i>	R. Kölling, Hohenheim
RKY1882	ZLY2-1A	MATα <i>ura3 his3 leu2 trp1 lys2 ypt6-2::URA3</i>	(Luo and Gallwitz, 2003)
RKY1920	RKY1558	Δ <i>vps21::LEU2</i>	A. Pawelec, Düsseldorf
RKY1922	RKY1558	Δ <i>bro1::kan</i>	A. Pawelec, Düsseldorf
RKY2100	RKY1558	Δ <i>rim20::kan</i>	R. Kölling, Hohenheim
RKY2788	RKY1558	Δ <i>did2</i>	(Brune et al., 2019)

Strain	Alias	Genotype	Reference
RKY2789	RKY1558	<i>Δist1</i>	(Brune et al., 2019)
RKY2790	RKY1558	<i>Δsnf7</i>	(Brune et al., 2019)
RKY2830	RKY1558	<i>Δvps24</i>	(Brune et al., 2019)
RKY2841	RKY1558	<i>Δvps2</i>	(Brune et al., 2019)
RKY2844	RKY1558	<i>Δchm7 Δdid2 Δist1 Δmos10 Δsnf7 Δvps2 Δvps20 Δvps24</i>	(Brune et al., 2019)
RKY2889	RKY1558	<i>MOS10-6His::His3</i>	R. Kölling, Hohenheim
RKY2892	RKY1558	<i>Δmos10</i>	(Brune et al., 2019)
RKY2893	RKY1558	<i>Δvps20</i>	(Brune et al., 2019)
RKY2998	RKY1558	<i>Δarg4</i>	L. Mücke, Hohenheim
RKY2999	RKY2889	<i>Δarg4</i>	L. Mücke, Hohenheim
RKY3136	RKY1558	<i>IST2-sfGFP::kan</i>	R. Kölling, Hohenheim
RKY3139	RKY1558	<i>TCB1-sfGFP::kan</i>	R. Kölling, Hohenheim

Table 4: Constructed *S. cerevisiae* strains according to (Longtine et al., 1998).

Strain	Alias	Genotype	Template	Primer
RKY2923	RKY1558	<i>DCP2-sfGFP::kan</i>	pRK1693	3199+3200
RKY2924	RKY1558	<i>NMD2-sfGFP::kan</i>	pRK1693	3203+3204
RKY2925	RKY1558	<i>PUB1-sfGFP::kan</i>	pRK1693	3191+3192
RKY2926	RKY2844	<i>NMD2-sfGFP::kan</i>	pRK1693	3203+3204
RKY2935	RKY2844	<i>DCP2-sfGFP::kan</i>	pRK1693	3199+3200
RKY3110	RKY2844	<i>PUB1-sfGFP::kan</i>	pRK1693	3191+3192
RKY3111	RKY2892	<i>DCP2-sfGFP::kan</i>	pRK1693	3199+3200
RKY3112	RKY2892	<i>NMD2-sfGFP::kan</i>	pRK1693	3203+3204
RKY3113	RKY2892	<i>PUB1-sfGFP::kan</i>	pRK1693	3191+3192
RKY3114	RKY2889	<i>ALD5-13myc::kan</i>	pFA6a-13myc-kanMX6	3504+3505
RKY3115	RKY2889	<i>EFT1-13myc::kan</i>	pFA6a-13myc-kanMX6	3508+3509
RKY3116	RKY2889	<i>GET3-13myc::kan</i>	pFA6a-13myc-kanMX6	3451+3452
RKY3117	RKY2889	<i>PRE6-13myc::kan</i>	pFA6a-13myc-kanMX6	3512+3513
RKY3118	RKY2889	<i>SSC1-13myc::kan</i>	pFA6a-13myc-kanMX6	3516+3517
RKY3119	RKY2889	<i>VPS68-13myc::kan</i>	pFA6a-13myc-kanMX6	3520+3521
RKY3152	RKY1558	<i>EXO84-GFP::kan</i>	pFA6a-GFP-kanMX6	3641+3642
RKY3153	RKY1558	<i>LEU1-GFP::kan</i>	pFA6a-GFP-kanMX6	3645+3646
RKY3154	RKY1558	<i>OAC1-GFP::kan</i>	pFA6a-GFP-kanMX6	3649+3650
RKY3155	RKY1558	<i>TPS1-GFP::kan</i>	pFA6a-GFP-kanMX6	3653+3654
RKY3156	RKY1558	<i>DNF2-GFP::kan</i>	pFA6a-GFP-kanMX6	3657+3658
RKY3157	RKY1558	<i>YGR130c-GFP::kan</i>	pFA6a-GFP-kanMX6	3661+3662
RKY3158	RKY1558	<i>YCK2-GFP::kan</i>	pFA6a-GFP-kanMX6	3665+3666
RKY3159	RKY1558	<i>PAN1-GFP::kan</i>	pFA6a-GFP-kanMX6	3669+3670

Strain	Alias	Genotype	Template	Primer
RKY3160	RKY1558	<i>TOM71-GFP::kan</i>	pFA6a-GFP-kanMX6	3673+3674
RKY3161	RKY1558	<i>COG8-GFP::kan</i>	pFA6a-GFP-kanMX6	3677+3678
RKY3162	RKY1558	<i>MSS1-GFP::kan</i>	pFA6a-GFP-kanMX6	3681+3682
RKY3163	RKY1558	<i>PTR2-GFP::kan</i>	pFA6a-GFP-kanMX6	3685+3686
RKY3164	RKY1558	<i>MNN5-GFP::kan</i>	pFA6a-GFP-kanMX6	3689+3690
RKY3165	RKY1558	<i>ALD5-GFP::kan</i>	pFA6a-GFP-kanMX6	3504+3505
RKY3166	RKY1558	<i>PRE6-GFP::kan</i>	pFA6a-GFP-kanMX6	3512+3513
RKY3167	RKY1558	<i>VPS68-GFP::kan</i>	pFA6a-GFP-kanMX6	3520+3521
RKY3168	RKY1558	<i>EXO84-sfGFP::kan</i>	pRK1693	3641+3642
RKY3169	RKY1558	<i>LEU1-sfGFP::kan</i>	pRK1693	3645+3646
RKY3170	RKY1558	<i>OAC1-sfGFP::kan</i>	pRK1693	3649+3650
RKY3171	RKY1558	<i>TPS1-sfGFP::kan</i>	pRK1693	3653+3654
RKY3172	RKY1558	<i>DNF2-sfGFP::kan</i>	pRK1693	3657+3658
RKY3173	RKY1558	<i>YGR130c-sfGFP::kan</i>	pRK1693	3661+3662
RKY3174	RKY1558	<i>YCK2-sfGFP::kan</i>	pRK1693	3665+3666
RKY3175	RKY1558	<i>PAN1-sfGFP::kan</i>	pRK1693	3669+3670
RKY3176	RKY1558	<i>TOM71-sfGFP::kan</i>	pRK1693	3673+3674
RKY3177	RKY1558	<i>COG8-sfGFP::kan</i>	pRK1693	3677+3678
RKY3178	RKY1558	<i>MSS1-sfGFP::kan</i>	pRK1693	3681+3682
RKY3179	RKY1558	<i>PTR2-sfGFP::kan</i>	pRK1693	3685+3686
RKY3180	RKY1558	<i>MNN5-sfGFP::kan</i>	pRK1693	3689+3690
RKY3181	RKY1558	<i>ALD5-sfGFP::kan</i>	pRK1693	3504+3505
RKY3182	RKY1558	<i>PRE6-sfGFP::kan</i>	pRK1693	3512+3513
RKY3183	RKY1558	<i>VPS68-sfGFP::kan</i>	pRK1693	3520+3521
RKY3184	RKY1558	<i>EXO84-13myc::kan</i>	pFA6a-13myc-kanMX6	3641+3642
RKY3185	RKY1558	<i>LEU1-13myc::kan</i>	pFA6a-13myc-kanMX6	3645+3646
RKY3186	RKY1558	<i>OAC1-13myc::kan</i>	pFA6a-13myc-kanMX6	3649+3650
RKY3187	RKY1558	<i>TPS1-13myc::kan</i>	pFA6a-13myc-kanMX6	3653+3654
RKY3188	RKY1558	<i>DNF2-13myc::kan</i>	pFA6a-13myc-kanMX6	3657+3658
RKY3189	RKY1558	<i>YGR130c-13myc::kan</i>	pFA6a-13myc-kanMX6	3661+3662
RKY3190	RKY1558	<i>YCK2-13myc::kan</i>	pFA6a-13myc-kanMX6	3665+3666
RKY3191	RKY1558	<i>PAN1-13myc::kan</i>	pFA6a-13myc-kanMX6	3669+3670
RKY3192	RKY1558	<i>TOM71-13myc::kan</i>	pFA6a-13myc-kanMX6	3673+3674
RKY3193	RKY1558	<i>COG8-13myc::kan</i>	pFA6a-13myc-kanMX6	3677+3678
RKY3194	RKY1558	<i>MSS1-13myc::kan</i>	pFA6a-13myc-kanMX6	3681+3682
RKY3195	RKY1558	<i>PTR2-13myc::kan</i>	pFA6a-13myc-kanMX6	3685+3686
RKY3196	RKY1558	<i>MNN5-13myc::kan</i>	pFA6a-13myc-kanMX6	3689+3690
RKY3197	RKY1558	<i>ALD5-13myc::kan</i>	pFA6a-13myc-kanMX6	3504+3505
RKY3198	RKY1558	<i>PRE6-13myc::kan</i>	pFA6a-13myc-kanMX6	3512+3513

Strain	Alias	Genotype	Template	Primer
RKY3199	RKY1558	<i>VPS68-13myc::kan</i>	pFA6a-13myc-kanMX6	3520+3521
RKY3200	RKY2802	<i>MOS10-6His::kan</i>	pRK1760	323+324
RKY3201	RKY2788	<i>MOS10-6His::kan</i>	pRK1760	323+324
RKY3202	RKY2789	<i>MOS10-6His::kan</i>	pRK1760	323+324
RKY3203	RKY2790	<i>MOS10-6His::kan</i>	pRK1760	323+324
RKY3204	RKY2841	<i>MOS10-6His::kan</i>	pRK1760	323+324
RKY3205	RKY2893	<i>MOS10-6His::kan</i>	pRK1760	323+324
RKY3206	RKY2830	<i>MOS10-6His::kan</i>	pRK1760	323+324
RKY3209	RKY1558	<i>MOS10-3HA::kan</i>	pFA6a-3HA-kanMX6	323+324
RKY3210	RKY2998	<i>MOS10-sfGFP::kan</i>	pRK1693	323+324
RKY3211	RKY2998	<i>DID2-sfGFP::kan</i>	pRK1693	1175+574
RKY3212	RKY2998	<i>VPS2-sfGFP::kan</i>	pRK1693	2714+582
RKY3213	RKY1558	<i>CHM7-sfGFP::kan</i>	pRK1693	1439+1284
RKY3214	RKY1558	<i>DID2-sfGFP::kan</i>	pRK1693	1175+574
RKY3215	RKY1558	<i>IST1-sfGFP::kan</i>	pRK1693	2719+2720
RKY3216	RKY1558	<i>MOS10-sfGFP::kan</i>	pRK1693	323+324
RKY3217	RKY1558	<i>SNF7-sfGFP::kan</i>	pRK1693	332+333
RKY3218	RKY1558	<i>VPS2-sfGFP::kan</i>	pRK1693	2714+582
RKY3219	RKY1558	<i>VPS20-sfGFP::kan</i>	pRK1693	415+440
RKY3220	RKY1558	<i>VPS24-sfGFP::kan</i>	pRK1693	1910+1911
RKY3221	RKY1558	<i>MOS10-sfGFP::His3</i>	pRK1694	323+324
RKY3222	RKY1558	$\Delta vps68::kan$	pFA6a-kanMX6	3767+3768
RKY3223	RKY2844	$\Delta vps68::kan$	pFA6a-kanMX6	3767+3768
RKY3224	RKY3216	$\Delta vps68::His3$	pFA6a-His3MX6	3767+3768
RKY3225	RKY3216	<i>VPS68-13myc::His3</i>	pFA6a-13myc-His3MX6	3520+3521
RKY3226	RKY3221	<i>VPS68-mCherry::kan</i>	pRK1100	3520+3521
RKY3227	RKY3222	<i>CHM7-sfGFP::His3</i>	pRK1694	1439+1284
RKY3228	RKY1558	$\Delta chm7::kan$	pFA6a-kanMX6	1283+1284
to	RKY1558	$\Delta chm7::kan$	pFA6a-kanMX6	1283+1284
RKY3233	RKY1558	$\Delta chm7::kan$	pFA6a-kanMX6	1283+1284
RKY3251	RKY1558	<i>SNF7p-GFP-DID2::kan</i>	pRK1699	3839+3840
RKY3252	RKY827	$\Delta vps68::His3$	pFA6a-His3MX6	3767+3768
RKY3253	RKY1882	$\Delta vps68::His3$	pFA6a-His3MX6	3767+3768
RKY3254	RKY3139	$\Delta vps68::His3$	pFA6a-His3MX6	3767+3768
RKY3255	RKY3136	$\Delta vps68::His3$	pFA6a-His3MX6	3767+3768
RKY3256	RKY2100	$\Delta vps68::His3$	pFA6a-His3MX6	3767+3768
RKY3257	RKY3222	<i>IST1-sfGFP::His3</i>	pRK1694	2719+2720
RKY3258	RKY3207	$\Delta vps68::His3$	pFA6a-His3MX6	3767+3768
RKY3259	RKY1558	$\Delta vps55::kan$	pFA6a-kanMX6	3771+3773

Strain	Alias	Genotype	Template	Primer
RKY3260	RKY3222	$\Delta vps55::His3$	pFA6a-His3MX6	3771+3773
RKY3261	RKY3224	$\Delta vps55::TRP1$	pFA6a-TRP1	3771+3773
RKY3262	RKY1558	<i>MOS10-mCherry::His3</i>	pRK1099	323+324
RKY3263	RKY1558	<i>SNF7p-GFP-VPS68::kan</i>	pRK1699	3790+3791
RKY3264	RKY3263	<i>MOS10-mCherry::His3</i>	pRK1099	323+324
RKY3265	RKY1558	<i>SNF7p-GFP-VPS55::kan</i>	pRK1699	3786+3787

Table 5: Constructed *S. cerevisiae* strains using various techniques.

Strain	Alias	Construct	Template
RKY3034	RKY2892	CRISPR/cas9, ARG4 deletion ($\Delta arg4$): fragment A P#628+3354, fragment B P#627+3355 repair fragment: P#3356+3359	YCpLac33 YCpLac33 RKY2998
RKY3207	RKY1558	pRK327 cut with <i>BamHI/EcoRV</i> for $\Delta vps27::kan$	pRK327
RKY3208	RKY3207	A) VPS27-ts23 fragment: P#3627+3628 B) His3 fragment: P#3629+3630 for <i>vps27-ts23::His3</i>	pRCP20 pFA6a-His3MX6

2.1.4 Yeast growth conditions

Yeast strains were cultivated in YPD media consisting of 1 % (w/v) yeast extract, 2 % peptone, and 2 % glucose, which was autoclaved separately and added afterwards, at 30 °C and shaking at 100 rpm. Growth plates contained an additional 2 % agar. As a test for petiteness (loss of mitochondrial DNA), cells were tested on media containing non-fermentable carbon sources like 2 % glycerol/ethanol instead of glucose (Lipinski et al., 2010).

For selective growth conditions, yeast strains with an integrated kanamycin resistance cassette were grown in YPD medium with 200 µg/ml of G418 (geneticin), added to the autoclaved media after letting it cool down to below 50 °C. A single drop-out media was used for yeast strains containing cassettes to overcome histidine or tryptophan auxotrophy. The media consists of 0.67 % yeast nitrogen base (YNB) without amino acids, 2 % glucose, and either 770 mg/l of -His drop-out or 740 mg/l of -Trp drop-out media from Formedium (product composition see Table S 1). Alternatively, yeast strains were grown in 0.67 % YNB, and each essential amino acid was added individually, which showed more insufficient growth than the single drop-out media. If not further indicated, all yeast strains were incubated at 30 °C, whereas “*ts*” strains (temperature-sensitive) were incubated at temperatures below 25 °C to ensure optimal growth. New media and a new flask were used for temperature shifts, which were both previously correctly tempered to ensure the desired temperature upkeep.

2.2 Plasmids

Table 6: Plasmid register.

Plasmid	Reference	Description
pACT2	BD Clontech	<i>GAL4-AD</i> vector for yeast two-hybrid-system
pET-30a	Novagen	Vector for n-terminal His tagging
pFA6a-13myc-His3MX6	(Longtine et al., 1998)	Template for c-terminal protein tagging with 13myc under <i>S. pombe HIS5⁺</i> selection marker control
pFA6a-13myc-kanMX6	(Longtine et al., 1998)	Template for c-terminal protein tagging with 13myc under <i>KanMX4</i> selection marker control
pFA6a-3HA-His3MX6	(Longtine et al., 1998)	Template for c-terminal protein tagging with 3HA under <i>S. pombe HIS5⁺</i> selection marker control
pFA6a-GFPS65T-kanMX6	(Longtine et al., 1998)	Template for c-terminal protein tagging with GFP under <i>KanMX4</i> selection marker control
pFA6a-His3MX6	(Longtine et al., 1998)	Template for gene deletion under <i>S. pombe HIS5⁺</i> selection marker control
pFA6a-kanMX6	(Longtine et al., 1998)	Template for gene deletion under <i>KanMX4</i> selection marker control
pFA6a-Trp1	(Longtine et al., 1998)	Template for gene deletion under <i>Trp</i> selection marker control
pRCP20	(Piper et al., 1995)	VPS27 ts-23 integration plasmid
pRK327	S. Losko, Hohenheim	Template for <i>vps27</i> gene deletion under <i>KanMX4</i> selection marker control
pRK329	R. Kölling, Hohenheim	<i>GAL4-DB</i> vector for yeast two-hybrid-system
pRK1099	R. Kölling, Hohenheim	pFA6a-3mcherry-His3MX6; Template for c-terminal protein tagging with mcherry under <i>S. pombe HIS5⁺</i> selection marker control
pRK1100	R. Kölling, Hohenheim	pFA6a-mcherry-kanMX6; Template for c-terminal protein tagging with mcherry under <i>KanMX4</i> selection marker control
pRK1266	(Bauer et al., 2015)	2 μ Chm7-mCherry URA3
pRK1405	T. Brune, Hohenheim	2 μ -Vector for HXT7p-yEGFP-CPS1 fusion expression with <i>TRP1</i> -selection marker
pRK1651	(Bauer et al., 2015)	2 μ Did2-mCherry URA3
pRK1652	(Bauer et al., 2015)	2 μ Ist1-mCherry URA3
pRK1653	(Bauer et al., 2015)	2 μ Mos10-mCherry URA3
pRK1654	(Bauer et al., 2015)	2 μ Snf7-mCherry URA3
pRK1655	(Bauer et al., 2015)	2 μ Vps2-mCherry URA3
pRK1656	(Bauer et al., 2015)	2 μ Vps20-mCherry URA3
pRK1657	(Bauer et al., 2015)	2 μ Vps24-mCherry URA3
pRK1693	T. Brune, Hohenheim	pFA6a-sfGFP-kanMX6; Template for c-terminal tagging with sfGFP under <i>KanMX4</i> selection marker control

Plasmid	Reference	Description
pRK1694	T. Brune, Hohenheim	pFA6a-sfGFP-His3MX6; Template for c-terminal protein tagging with sfGFP under <i>S. pombe HIS5⁺</i> selection marker control
pRK1699	R. Kölling, Hohenheim	pFA6a-kanMX6-SNF7p-GFP; Template for n-terminal protein tagging with GFP under <i>KanMX4</i> selection marker control
pRK1760	R. Kölling, Hohenheim	pFA6a-6His-kanMX6; Template for c-terminal protein tagging with 6His under <i>KanMX4</i> selection marker control
pRK1785	S. Becker, Hohenheim	2 μ -Vector for Ste6-sfGFP fusion expression with <i>TRP1</i> -selection marker
pRK1854	R. Kölling, Hohenheim	6His-Mos10 <i>KanMX4</i> expression vector
pYM51	(Janke et al., 2004)	Template for c-terminal tagging with eqFP611 under <i>KanMX4</i> selection marker control
YEplac112	(Gietz and Sugino, 1988)	2 μ -Vector with <i>TRP1</i> -selection marker
YEplac195	(Gietz and Sugino, 1988)	2 μ -Vector with <i>URA3</i> -selection marker

2.3 Designed oligonucleotides

Table 7: Synthesized oligonucleotides register.

Oligo	Sequence (5'→3')	Description
#323	TTAGATACTGAAGACAAAAATAAGCTT TAGAAAGCGCTCAGcggatccccgggtaattaa	Primer F2 MOS10 for c-terminal tagging
#324	AGAAAAATTCTGAATATGCAACTTTGTG TGCTTTTTGTTTgaattcgagctcggttaaac	Primer R1 MOS10 for c-terminal tagging
#332	TGAAAAAGCATTAAAGAGAACTACAAGC AGAAATGGGGCTTcggatccccgggtaattaa	Primer F2 SNF7 for c-terminal tagging
#333	ACCTTTTTTTTTCTTTCATCTAAACCGC ATAGAACACGTgaattcgagctcggttaaac	Primer R1 SNF7 for c-terminal tagging
#415	CATCCCTTTATTTTAAATTTGAAGCTA CATACAGACATgaattcgagctcggttaaac	Primer R1 VPS20 for c-terminal tagging
#440	GGAGAGATCAGACACTAAGGAACCTTTA GCATTACTATCCcggatccccgggtaattaa	Primer F2 VPS20 for c-terminal tagging
#574	AACGTAATGATGAACTAAAAATGCATGA CCTGTTAGCATGgaattcgagctcggttaaac	Primer R1 DID2 for c-terminal tagging
#582	TATAGTATAGACCTATTATTCATTAAATA TACTCAGAGCGgaattcgagctcggttaaac	Primer R1 VPS2 for c-terminal tagging
#627	AACGACCGAGCGCAGCGAGT	YCpLac33 upstream the polylinker pUC
#628	GGAGAAAATACCGCATCAGG	YCpLac33 downstream the polylinker pUC
#1175	GAAGACAAACTTGCACAAAGACTAAGA GCATTGAGGGGCcggatccccgggtaattaa	Primer F2 DID2 for c-terminal tagging
#1283	CACCACCAAAGCCAGCCAAATAGTATCT CACTGTATCTGAcggatccccgggtaattaa	Primer F1 CHM7 deletion

Oligo	Sequence (5'→3')	Description
#1284	TATTTATACATATATATTTATTTATTAGT CACTCAGTTTCGgaattcgagctcgtttaaac	Primer R1 CHM7 deletion
#1439	TAATGAGATAAGAAAAATCATGATGGA AGAACAACCACGTcggatccccgggtaattaa□	Primer F2 CHM7 for c-terminal tagging
#1910	GGTAAATGAAATGCGTGAAAGGCTGAG AGCTTTGCAAAACCGGATCCCCGGGTTA ATTAA	Primer F2 VPS24 for c-terminal tagging
#1911	ACTTATTTATTTATTTTCTTTGTACAGTC ACAGTAACACTgaattcgagctcgtttaaac	Primer R1 VPS24 for c-terminal tagging
#2714	TGACTTGCAAGCTCGGTTGAACACTTTG AAGAAGCAGACTcggatccccgggtaattaa	Primer F2 VPS2 for c-terminal tagging
#2719	AGATGAGTTGAAGAAACGGTTTGACGCT TTACGCAGAAAacggatccccgggtaattaa	Primer F2 IST1 for c-terminal tagging
#2720	AAATATGTGGTTAATTAACCATACATAT AAATTATTATCTgaattcgagctcgtttaaac	Primer R1 IST1 for c-terminal tagging
#3191	TGAGCAACAACAGCAACAGCAGCAACA GCAGCAACAACAacggatccccgggtaattaa	Primer F2 PUB1 for c-terminal tagging
#3192	ATTCTTTCTTTTTGTTTCATTCCTTTTC TTCATAATATgaattcgagctcgtttaaac	Primer R1 PUB1 for c-terminal tagging
#3193	GGTAATATTCCGCACT	Primer T1 PUB1 for c-terminal tagging
#3194	AGCCTTCAGAAAATACGTT	Primer T2 PUB1 for c-terminal tagging
#3199	TTCAGGGTCTAATGAATTATTAAGCATT TGCATAGGAAGcggatccccgggtaattaa	Primer F2 DCP2 for c-terminal tagging
#3200	CATTTACAGTGTGTCTATAAAACGTATA ACACTTATTCTTgaattcgagctcgtttaaac	Primer R1 DCP2 for c-terminal tagging
#3201	ACGTCAATGAAACGCAAC	Primer T1 DCP2 for c-terminal tagging
#3202	CCAGTAATAGCCTCGATG	Primer T2 DCP2 for c-terminal tagging
#3203	AAACAAGATTA AAAAGATTGTTTTAAAA CGTTCTTTTCGACcggatccccgggtaattaa	Primer F2 NMD2 for c-terminal tagging
#3204	ATATAGTAAAAATTTAAAGAACTATATT CGCAAAAGAATCgaattcgagctcgtttaaac	Primer R1 NMD2 for c-terminal tagging
#3354	TTTGTAATGTGTGTAGCCTaaagtcccattcgc cac	sgRNA ARG4 fragment A rev
#3355	AGGCTACACACATTTACAAAgtttagagctaga aatagcaag	sgRNA ARG4 fragment B fw
#3356	CAAAGAAAATACGGTACTTGC	ARG4 repair fragment A fw
#3357	CATAACGTCGCCATCTGGTTTGCCTTAGT CTTGTTAT	ARG4 repair fragment A rev
#3358	CAGATGGCGACGTTATG	ARG4 repair fragment B fw
#3359	TTTGTGATGTACCAAGGCTA	ARG4 repair fragment B rev
#3400	AGAATCATCTTGCTCGG	VPS27 sequencing primer pos. 1847
#3401	GTGGAGTTTCTGCCAA	VPS27 sequencing primer pos. 2586
#3402	ATAGAAATGAACGGCAAG	VPS27 sequencing primer pos. 3230
#3451	TACTGATGGCAAAGTCATTTATGAGTTA GAAGATAAGGAAcggatccccgggtaattaa	Primer F2 GET3 for c-terminal tagging

Oligo	Sequence (5'→3')	Description
#3452	TTATATGTCGATGTATCTATTTATGGTA TTCAGGGGCTTgaattcgagctcgtttaaac	Primer R1 GET3 for c-terminal tagging
#3453	TTCCTACGATATGGACGTT	Primer T1 GET3 for c-terminal tagging
#3454	TGGGCTTACTTCGTT	Primer T2 GET3 for c-terminal tagging
#3455	GTCTTCAAAAAGGAGCAAGAACAACA AACTGAGCAAGCTcggatccccgggtaattaa	Primer F2 PAB1 for c-terminal tagging
#3456	TAAGTTTGTTGAGTAGGGAAGTAGGTGA TTACATAGAGCAgaattcgagctcgtttaaac	Primer R1 PAB1 for c-terminal tagging
#3457	CCAAGAAATGCCAACGA	Primer T1 PAB1 for c-terminal tagging
#3458	GCCGTTAATAATGAGACCT	Primer T2 PAB1 for c-terminal tagging
#3504	AACAAAATCTGTCAGAATTGCCATTGAC AAGCCAATTCGTcggatccccgggtaattaa	Primer F2 ALD5 for c-terminal tagging
#3505	ACATACCTTCAATGAGCAGTCAACTCGG GCCTGAGTACTgaattcgagctcgtttaaac	Primer R1 ALD5 for c-terminal tagging
#3506	GTCAAGCCAACAGTGTTC	Primer T1 ALD5 for c-terminal tagging
#3507	CTCTGGCACTTGATCTACC	Primer T2 ALD5 for c-terminal tagging
#3508	GGAAGAAGTTCAGGCTGGCAAGAATAT TACGACAAATTGcggatccccgggtaattaa	Primer F2 EFT1 for c-terminal tagging
#3509	GGTTTGCTTTACAGAACCACCTTTTCTC ATTTAGACTTCgaattcgagctcgtttaaac	Primer R1 EFT1 for c-terminal tagging
#3510	GTTGGCTGATCCAAAGATCC	Primer T1 EFT1 for c-terminal tagging
#3511	GTAATACTACCTCAGGACCG	Primer T2 EFT1 for c-terminal tagging
#3512	AGAGCAGCAAGAGCAGGACAAAAGAA AAAATCTAACCATcggatccccgggtaattaa	Primer F2 PRE6 for c-terminal tagging
#3513	TATTTTATATAGTTTTATGCCCAATATA TATCGCCGTTTgaattcgagctcgtttaaac	Primer R1 PRE6 for c-terminal tagging
#3514	ATATACTCTTCGTGGTCCGC	Primer T1 PRE6 for c-terminal tagging
#3515	ATGGGCATATAGGCGTATGG	Primer T2 PRE6 for c-terminal tagging
#3516	ACAACAACGGCAACAATGCCGAATCTGG TGAAACTAAGCAcggatccccgggtaattaa	Primer F2 SSC1 for c-terminal tagging
#3517	TAACATTGTGGTAGTAATTTATTAACAG GAATTTGCTTTTgaattcgagctcgtttaaac	Primer R1 SSC1 for c-terminal tagging
#3518	GAAGGTAAGGTTGACAAGGC	Primer T1 SSC1 for c-terminal tagging
#3519	TTCCATCATAACCGTCTGGG	Primer F2 SSC1 for c-terminal tagging
#3520	CCAAAATGTTGAAGATGAATATTCATAT TCTTTGACGCTCcgatccccgggtaattaa	Primer F2 VPS68 for c-terminal tagging
#3521	GATCGCCTTAATTGGCCTCGAAAATATT GGTCAACTTAACgaattcgagctcgtttaaac	Primer R1 VPS68 for c-terminal tagging
#3522	TTATCGTCAGATGGTGGTGC	Primer T1 VPS68 for c-terminal tagging
#3523	AGGTGTTGACGTATGATGCC	Primer T2 VPS68 for c-terminal tagging
#3627	TAATATGCACGGAGCCTACC	pRCP20 VPS27 ts upstream prom. region
#3628	CGAGGCAAGCTAAACAGATCTGTATAAG TTGCGTAACAAGC	pRCP20 VPS27 ts downstream term. region
#3629	GATCTGTTAGCTTGCCTCG	pFA6a-His3MX6 upstream prom. Region

Oligo	Sequence (5'→3')	Description
#3630	ATGAATATTCACCTTAAAACTAGTTTA ATGACAGAAATATCGTTTAACTGGATG GCGG	pFA6a-His3MX6 downstream term. Region
#3641	ATTGGACGAGTTTATCAAAAAGAACAGT GATAAAATTCGcggatccccgggtaattaa	Primer F2 EXO84 for c-terminal tagging
#3642	TCATATATATTGAAGTGAGGTTTATTTTC TGTGATCTTGTgaattcgagctcgttaaac	Primer R1 EXO84 for c-terminal tagging
#3645	AGCTGTTACAACACTTTTCGATAAAGTC CACCAGGATTGcggatccccgggtaattaa	Primer F2 LEU1 for c-terminal tagging
#3646	CATGTTATTGACGCCAGGTTTGGACGTT GTTTTTCACTGTgaattcgagctcgttaaac	Primer R1 LEU1 for c-terminal tagging
#3649	ACTAGTTTATTCGATAGAGTCGAGAGTT TTAGGCCATAATcggatccccgggtaattaa	Primer F2 OAC1 for c-terminal tagging
#3650	CAATGAATGAACTTCAAACCTCGGAGT TTGTTATGGGAAGaattcgagctcgttaaac	Primer R1 OAC1 for c-terminal tagging
#3651	TGTTGCCGTCGTTATGAACC	Primer T1 OAC1 for c-terminal tagging
#3652	TTGTGGCCATTTGGTACTGG	Primer T2 OAC1 for c-terminal tagging
#3653	TACATCATCAAGCTCAACAAGCTCCTCT GCCACCAAAAACcggatccccgggtaattaa	Primer F2 TPS1 for c-terminal tagging
#3654	GGACCAGGAATAGACGATCGTCTCATTT GCATCGGGTTCaattcgagctcgttaaac	Primer R1 TPS1 for c-terminal tagging
#3655	ATCCTGAGTGAGTTCACAGG	Primer T1 TPS1 for c-terminal tagging
#3656	AAAGAAGACGTAAGGGCTCC	Primer T2 TPS1 for c-terminal tagging
#3657	TCATGCAGAGACGCTGCTCAGCCAGCGC AGCAGGGACCGTcggatccccgggtaattaa	Primer F2 DNF2 for c-terminal tagging
#3658	TTGGTATACATAGTACAAAAGGAAGAAAA AAATTGTAATCAaattcgagctcgttaaac	Primer R1 DNF2 for c-terminal tagging
#3659	AGAGAAATGTGGTTACGCGG	Primer T1 DNF2 for c-terminal tagging
#3660	ATATTACGTCTCCGGCTTCG	Primer T2 DNF2 for c-terminal tagging
#3661	CTTGTATGAATATCATACTGAGGAAGAC GTCATGTATGCCcggatccccgggtaattaa	Primer F2 YGR130c for c-terminal tagging
#3662	GGTGGGATATTCCTTGAACAAAAGTGGGA ATATTATTTTTTgaattcgagctcgttaaac	Primer R1 YGR130c for c-terminal tagging
#3663	AAAGACTCGAAGATGAGCGC	Primer T1 YGR130c for c-terminal tagging
#3664	AGAGAGTCCATCTTACTCGG	Primer T2 YGR130c for c-terminal tagging
#3665	CAAATCATCGAAAGGTTTTTTCAGTAAG CTAGGATGCTGTcggatccccgggtaattaa	Primer F2 YCK2 for c-terminal tagging
#3666	TGGTGGGAATGATTACAAAAACCTCCT CCGTTTTCTATTgaattcgagctcgttaaac	Primer R1 YCK2 for c-terminal tagging
#3667	TCAAGCACAAGCCAAAGTGC	Primer T1 YCK2 for c-terminal tagging
#3668	AGTACACAATAACGCCGACG	Primer T2 YCK2 for c-terminal tagging
#3669	AATCCACCTGCAGGTATTCCTCCACCCC CACCCCTTCCaaggatccccgggtaattaa	Primer F2 PAN1 for c-terminal tagging
#3670	ATTAGTATACATACGTATCTATAGAAAG CAAATTAATCTgaattcgagctcgttaaac	Primer R1 PAN1 for c-terminal tagging

Oligo	Sequence (5'→3')	Description
#3671	GATGGCTTTCAAGAACCTCC	Primer T1 PAN1 for c-terminal tagging
#3672	ATGAGGATCAACGGTCAACG	Primer T2 PAN1 for c-terminal tagging
#3673	GGAGCTAACATTAGCTCGTTATAGGGCT AAAGGCATGCTTcggatccccgggtaattaa	Primer F2 TOM71 for c-terminal tagging
#3674	TAACTAAAAGTATATATTTGACCAATAC CTGACATATCTTgaattcgagctcgtttaaac	Primer R1 TOM71 for c-terminal tagging
#3675	GCCTGTGAATTAGATCCACG	Primer T1 TOM71 for c-terminal tagging
#3676	ACGCGTCAAGATTGGTTTGC	Primer T2 TOM71 for c-terminal tagging
#3677	TGACAAGAGAGCAGAACTGGCCTCTAAA TATATATACTCCcggatccccgggtaattaa	Primer F2 COG8 for c-terminal tagging
#3678	CGATCGTCATTTTAAAAATACATAGTGA GCCAATATTATAgaattcgagctcgtttaaac	Primer R1 COG8 for c-terminal tagging
#3679	CTGTTCAATCCGTCCTTTCGCG	Primer T1 COG8 for c-terminal tagging
#3680	CTCCTCCTCATGAAATAGGG	Primer T2 COG8 for c-terminal tagging
#3681	AATCTTAGATTTCAGTGTTCAGCAAATTTT GTATAGGAAAACggatccccgggtaattaa	Primer F2 MSS1 for c-terminal tagging
#3682	CAATTTTCTTTTATTTATATACACGATGA TTGTAAGTAACTAGGgaattcgagctcgtttaaac	Primer R1 MSS1 for c-terminal tagging
#3683	AGACTCGGATCAAAGTACCC	Primer T1 MSS1 for c-terminal tagging
#3684	AGTGGTGCCAACATTGATGC	Primer T2 MSS1 for c-terminal tagging
#3685	ATTAGAACCAATGGAAAGTCTAAGATCC ACCACCAAATATcggatccccgggtaattaa	Primer F2 PTR2 for c-terminal tagging
#3686	AAAAAAAAAAAAAAAAAAGACAGTAAG TTAATTAACGCgaattcgagctcgtttaaac	Primer R1 PTR2 for c-terminal tagging
#3687	TTTACAAGGCTGGTCCATGG	Primer T1 PTR2 for c-terminal tagging
#3688	ATACAGTGAGCCTGAAGAGG	Primer T2 PTR2 for c-terminal tagging
#3689	TCTGGAGAGCACACACAAAGAAGCTATG GGGAGAAAAACcggatccccgggtaattaa	Primer F2 MNN5 for c-terminal tagging
#3690	ATGGCGAGTTATTATTAATTATTATAGT TAATCACTTCAgaattcgagctcgtttaaac	Primer R1 MNN5 for c-terminal tagging
#3691	CGCAGCAGAAAGTTAAAGCC	Primer T1 MNN5 for c-terminal tagging
#3692	TTAAACCGTTCACCAAGCGC	Primer T2 MNN5 for c-terminal tagging
#3730	GATCAGTGGACAATCCTACG	Primer T1 EXO84 for c-terminal tagging
#3731	AGCCATAGCTTCTTTGTCCC	Primer T2 EXO84 for c-terminal tagging
#3732	TGGTTCTTCCAGAGAACACG	Primer T1 LEU1 for c-terminal tagging
#3733	CCTGCATGCATTAACAAGGG	Primer T2 LEU1 for c-terminal tagging
#3767	TTATCCCCAACTACAAGATCAATTAGAA AATCACATCATCcgatccccgggtaattaa	Primer F1 VPS68 deletion
#3768	GATCGCCTTAATTGGCCTCGAAAATATT GGTCAACTTAACgaattcgagctcgtttaaac	Primer R1 VPS68 deletion
#3769	GAAGTGCATTCTCTTCTGG	Primer T1 VPS68 deletion
#3770	GCCATCTCTGGATTAGTTGC	Primer T2 VPS68 deletion
#3771	TTTCAAAAAGATTTCAACGAAGATGAT TCCCTTTTTGGTcggatccccgggtaattaa	Primer F2 VPS55 for c-terminal tagging

Oligo	Sequence (5'→3')	Description
#3772	GTTGGCTTAGTCTGTTGAGGGGATGAGT AATTGTTATATAgaattcgagctcgtttaa	Primer R1 VPS55 for c-terminal tagging
#3773	AAAAGGCAAAGAATCTTAATACATAAA ATCCCAGACGGTTCggatccccgggtaattaa	Primer R1 VPS55 deletion
#3774	CTGTTTCCTCGCATTAAGCG	Primer T1 VPS55 c-terminal tagging/deletion
#3775	CACAGAATGGTTGTACGACC	Primer T2 VPS55 c-terminal tagging/deletion
#3786	AAAAGGCAAAGAATCTTAATACATAAA ATCCCAGACGGTgaattcgagctcgtttaa	Primer F4 VPS55 for n-terminal tagging
#3787	AAATAATCTTTGTCAATGGTGACACTTT GAATTCCATCATttgtatagttcatccatgc	Primer R5 VPS55 for n-terminal tagging
#3788	TTAGATGGGCTTTCACCTC	Primer T1 VPS55 for n-terminal tagging
#3789	TATGATAAGACCACCGAT	Primer T2 VPS55 for n-terminal tagging
#3790	TTATCCCCAACTACAAGATCAATTAGAA AATCACATCATCgaattcgagctcgtttaa	Primer F4 VPS68 for n-terminal tagging
#3791	AGGGGAAGCGAAATAAGCTAACATGAT CATCTGCCTCCATttgtatagttcatccatgc	Primer R5 VPS68 for n-terminal tagging
#3792	TTTCATAAAGAAGGCAAG	Primer T1 VPS68 for n-terminal tagging
#3793	CCATAAAACAACGCAAC	Primer T2 VPS8 for n-terminal tagging
#3794	ACACCAGTGCTACTAATGCG	Primer T1 CHM7 for c-terminal tagging
#3795	GGTGGTGATTCAATGACTCC	Primer T2 CHM7 for c-terminal tagging
#3796	CTGTTGAAGTTGGCATCACG	Primer T1 DID2 for c-terminal tagging
#3797	GATGAGCATTGGATGACTCC	Primer T2 DID2 for c-terminal tagging
#3798	GGAACAGCTTGTCAAAGAGC	Primer T1 IST1 for c-terminal tagging
#3799	GCCGAGAATAATAGAGCAGC	Primer T2 IST1 for c-terminal tagging
#3800	TGCCATGAAGGCTCAATACG	Primer T1 MOS10 for c-terminal tagging
#3801	TATCTCTTAGCTCCTGCTCC	Primer T2 MOS10 for c-terminal tagging
#3802	GGAGATGAAATAAGCGACGC	Primer T1 SNF7 for c-terminal tagging
#3803	CATTAGTGGTGCTCAAAGGG	Primer T2 SNF7 for c-terminal tagging
#3804	TTTGATGGGTCAACGACAGG	Primer T1 VPS2 for c-terminal tagging
#3805	TACAAGAAAGCTAGGGAGGG	Primer T2 VPS2 for c-terminal tagging
#3806	GAAGCTTAGTCGGAACAAGC	Primer T1 VPS20 for c-terminal tagging
#3807	AGGAGAAATTCACCTCGAGG	Primer T2 VPS20 for c-terminal tagging
#3808	ATCAAATGGCTGACAGTGCG	Primer T1 VPS24 for c-terminal tagging
#3809	TCAGATCATGGATCCTGAGC	Primer T2 VPS24 for c-terminal tagging
#3810	gatcATGGAGGCAGATGATCATGTTAGCTT ATTTTCGCTTCCCCTTCAAGATTCCCACCT TTCGTGGTATAAGAAAAGGTGGGtag	Y2H Vps68 1-26 fw new
#3811	tcgactaCCCACCTTTTCTTATAACCACGAAA GGTGGGAATCTTGAAGGGGAAGCGAAA TAAGCTAACATGATCATCTGCCTCCAT	Y2H Vps68 1-26 rev new
#3812	gatcTCTAGATATTCCAATGCATCAGATGT TCATGTTACGtag	Y2H Vps68 48-59 fw new

Oligo	Sequence (5'→3')	Description
#3813	tcgactaCGTAACATGAACATCTGATGCATT GGAATATCTAGA	Y2H Vps68 48-59 rev new
#3814	gatacAATTCTATTGAAAAGAATAGATTATT GCAGGGAGCTTTATCGTCAGATGGTGGT GCCTTCGGTAGTGGTGTAGGCGATTTAG ATTCAAGCATGGCATGGCAAGCTCGAAC Ctag	Y2H Vps68 77-113 fw new
#3815	tcgactaGGTTCGAGCTTGCCATGCCATGCT TGAATCTAAATCGCCTACACCACTACCG AAGGCACCACCATCTGACGATAAAGCTC CCTGCAATAATCTATTCTTTTCAATAGAA TT	Y2H Vps68 77-113 rev new
#3816	gatacAAATTTTTAGTCAAGGATTACAATAC CTATCCAACCTTTGGGGATGGGAtag	Y2H Vps68 136-151 fw new
#3817	tcgactaTCCCATCCCCAAAGTTGGATAGGT ATTGTAATCCTTGAATAAAAAATTT	Y2H Vps68 136-151 rev new
#3818	gatacAAAATGTTGAAGATGAATATTCATA TTCTTTGACGCTCtag	Y2H Vps68 172-184 fw new
#3819	tcgactaGAGCGTCAAAGAATATGAATATTC ATCTTCAACATTTTG	Y2H Vps68 172-184 rev new
#3839	CTACTTTGAAAGTATAGGAAGTCAGACA TCGCACTGAGAAgaattcgagctcgtttaaac	Primer F4 DID2 for n-terminal tagging
#3840	AAAGAGTGTTTTCCAAACCTGCTGCAGA ATTACGTGACATttgtatagttcatccatgc	Primer R5 DID2 for n-terminal tagging
#3841	CACTGCCATTTATCTGGT	Primer T1 DID2 for n-terminal tagging
#3842	CATGCCATTTTCGTCAGC	Primer T2 DID2 for n-terminal tagging
#3866	AGGGGAAGCGAAATAAGCTAACATGAT CATCTGCCTCCATttgtacaattcgccattcct	Primer R5 VPS68 for n-terminal sfGFP tagging
#3867	AAAGAGTGTTTTCCAAACCTGCTGCAGA ATTACGTGACATttgtacaattcgccattcct	Primer R5 DID2 for n-terminal sfGFP tagging
#3893	AGATTGGTTGAAACACAGTTATAAACTC TTCAAGGCAATTgaattcgagctcgtttaaac	Primer F4 MOS10 for n-terminal sfGFP tagging
#3894	CATGGCTCTTTTTGTTCCCATATCCGAAA ATCCTGTTCAttgtacaattcgccattcct	Primer R5 MOS10 for n-terminal sfGFP tagging
#3895	ACTAAGTGGACTAAGTCCCG	Primer T1 MOS10 for n-terminal tagging
#3896	ACTAAGTGGACTAAGTCCCG	Primer T2 MOS10 for n-terminal tagging

2.4 Materials

2.4.1 Chemicals and solutions

Table 8: Chemicals and solutions register.

Description	Supplier
Acrylamide Rotiphorese® Gel 30 (37.5:1), Lot 248272238	Carl Roth (Karlsruhe, Germany)
Ammonium peroxydisulphate (APS), Lot 393201798	Carl Roth (Karlsruhe, Germany)

Description	Supplier
Bacto™ Agar	Becton, Dickinson, and Company (Sparks, USA)
Benzamidine hydrochloride hydrate 97 %, Lot 20H7704	Sigma Aldrich (San José, USA)
Bromphenol blue	Merck (Darmstadt, Germany)
1-Butanol (C ₄ H ₁₀ O)	Carl Roth (Karlsruhe, Germany)
Dimethylsulfoxide (DMSO), Lot 266245732	Carl Roth (Karlsruhe, Germany)
Dithiobis (succinimidyl propionate) (DSP), Lot SC239197	Thermo Scientific (Waltham, USA)
1,4-Dithiothreitol (DTT) ≥ 99 %, Lot 277260643	Carl Roth (Karlsruhe, Germany)
DNaseA, RNase free Lot. 00771398	Thermo Scientific (Waltham, USA)
dNTP Mix (10mM)	Thermo Scientific (Waltham, USA)
Ethanol ≥ 99.5 %, Lot 277260243	Carl Roth (Karlsruhe, Germany)
Ethylenediaminetetraacetic acid (EDTA) (C ₁₀ H ₁₆ N ₂ O ₈)	Carl Roth (Karlsruhe, Germany)
D(+)-Glucose, Lot 288273364	Carl Roth (Karlsruhe, Germany)
Glycerol ROTIPURAN® ≥ 99.5 %, Lot 5132075	Carl Roth (Karlsruhe, Germany)
Glycine PUFFERAN ≥ 99.9 %, Lot 514223084	Carl Roth (Karlsruhe, Germany)
Immersion oil x899.4	Carl Roth (Karlsruhe, Germany)
Protino Ni-NTA Agarose, Lot 1807/001	Macherey-Nagel (Düren, Germany)
Nickel (Meister et al.)sulphate · 6H ₂ O T111.1	Carl Roth (Karlsruhe, Germany)
Nonfat dried milk powder, Lot R8528	AppliChem (Darmstadt, Germany)
OneTaq® DNA Polymerase	New England Biolabs (Massachusetts, USA)
Optiprep Density Gradient Medium, Lot. 01556	Axis Shield (Dundee, Scotland)
Bacto™ Peptone, Lot 8023900	Becton, Dickinson, and Company (Sparks, USA)
1,10-Phenanthroline monohydrate, Lot 88H1313	Sigma Aldrich (San José, USA)
Phenylmethanesulfonylfluoride (PMSF) ≥ 98.5 %, Lot 010M1972	Sigma Aldrich (San José, USA)
Ponceau S, Lot 083K3643	Sigma Aldrich (San José, USA)
Color Prestained Protein Standard, Broad Range (11–245 kDa)	New England Biolabs (Massachusetts, USA)
Protein A Sepharose™ CL-4B, Lot 10043746/ 10254134	GE Healthcare (Chicago, USA)
Q5® High-Fidelity 2X Master Mix	New England Biolabs (Massachusetts, USA)
RNaseA, DNase free, Lot. 00781705	Thermo Scientific (Waltham, USA)
SILAC L-Arg, Lot. 201604102	Silantes GmbH (München, Germany)
SILAC L-Lys, Lot. 211604102	Silantes GmbH (München, Germany)
Silver nitrate, Lot. 6207.1	Carl Roth (Karlsruhe, Germany)
Sodium chloride, Lot 307261327	Carl Roth (Karlsruhe, Germany)
Sodium dihydrogen phosphate dihydrate (NaH ₂ PO ₄ · 2H ₂ O), Lot 419645	Merck (Darmstadt, Germany)
Sodium dodecyl sulfate (SDS) ≥ 99.5 %, Lot 195228353	Carl Roth (Karlsruhe, Germany)
Tetramethylethylenediamin (TEMED), Lot 068267753	Carl Roth (Karlsruhe, Germany)
Trichloroacetic acid (TCA) ≥ 99 %, Lot 19786920	Carl Roth (Karlsruhe, Germany)
TRIS base PUFFERAN® ≥ 99.9 %, Lot 464221491	Carl Roth (Karlsruhe, Germany)

Description	Supplier
Triton X-100 (t-Octylphenoxy polyethoxyethanol), Lot 10K0192	Sigma-Aldrich (San José, USA)
Tween®20, Lot 407263603	Carl Roth (Karlsruhe, Germany)
Western blot substrate Signal Fire™ ECL Reagent, Lot 12	Cell signaling technology Inc. (Danvers, USA)
WesternBright™ ECL HRP substrate (Peroxide, Lot 180124-56, ECL, Lot 180124-57)	Advansta Inc. (San José, USA)
Western Blotting Substrate Lumi-Light, Lot 32701200	Roche Diagnostics GmbH (Mannheim, Germany)
Bacto™ Yeast Extract, Lot 2101361	Becton, Dickinson, and Company (Sparks, USA)

2.4.2 Facilities and consumables

Table 9: Facility register.

Description	Supplier
AEKTA Start	GE Healthcare (Chicago, USA)
Analytical scale: MC1 Analytic AC 210 S	Sartorius AG (Göttingen, Germany)
AXIO Imager M1	Carl Zeiss AG (Oberkochen, Germany)
Benchmark PlateFuge Mini Centrifuge	Benchmark Scientific (NJ, USA)
Branson 450 Digital Sonifier w/ Probe	Marshall Scientific (Hampton, USA)
Cassette Cooler	GE Healthcare (Chicago, USA)
Cell density rotor 40	Thermo Scientific (Waltham, USA)
Centrifuge Avanti™ J-30.50 Ti + rotor JA-10 (500 ml bottles)	Beckman Coulter Inc. (Brea, USA)
Centrifuge MEGA STAR 1.6R (falcon tubes)	VWR (Radnor, USA)
Centrifuge Tabletop 5424 (micro reaction tubes)	Eppendorf AG (Hamburg, Germany)
Density Meter DMA 4100M	Anton Paar (Graz, Austria)
FastPrep®-24 cell disrupter	MP Biomedicals (Santa Ana, USA)
Freezer - 20°C	Liebherr (Biberach/Riß, Germany)
Freezer Ultra-low temperature C340 Premium (-70 °C)	New Brunswick Scientific (Edison, USA)
Freezer Ultra-low temperature H86G-400.1 (-70 °C)	EWALD (Bad Nenndorf, Germany)
French Press Cellular Press	American Instrument Company (USA)
Glass plate SE6102, 18x16 cm	GE Healthcare (Chicago, USA)
Glass plate SE6102D, 18x16 cm	GE Healthcare (Chicago, USA)
Heating Block, Thermo shaker TS 100	A. Hartenstein (Wuerzbrug, Germany)
Heraeus Function line	Thermo Scientific (Waltham, USA)
Hoshizaki Ice Machines	Ice machine (Vienna, Austria)
Imaging system (Ponceau S): GelStick	Intas Science Imaging Instruments (Göttingen, Germany)
Imaging system (Western blot): LAS-3000 mini	Fujifilm (Tokyo, Japan)
Magnetic stirrer FB 15045	Thermo Scientific (Waltham, USA)
MaxQ™ 6000	Thermo Scientific (Waltham, USA)

Description	Supplier
Microliter syringe 0-100 µl, 710 RN SYR (SDS-PAGE loading)	Hamilton Bonaduz AG (Bonaduz, Switzerland)
MINI hybridization unit, model OV1/OV2	Biometra (Göttingen, Germany)
Model EP-1 Econo Pump	Bio-Rad (Hercules, USA)
Peristaltic Pumps, Single-Channel, P-1	VWR (Radnor, USA)
pH meter: HI 221 Calibration check Microprocessor	Hanna Instruments (Woonsocket, USA)
Pipets: PIPETMAN Classic™ 2-20 µl, 20-200 µl, 100-1000 µl	Gilson Inc. (Middleton, USA)
Power supply model 1000/500 (for SDS-PAGE)	Bio-Rad (Hercules, USA)
Power supply PS3002 (for SDS-PAGE)	GibcoBRL, Life technologies (Carlsbad, USA)
Power supply Voltcraft VLP-1602 PRO (for Western blot)	CEI Conrad International (New Territories, Hong Kong)
Scale 474-42	Kern & Sohn (Balingen, Germany)
SE 400 vertical unit for SDS-PAGE	GE Healthcare (Chicago, USA)
Shaker Unimax 1010 (Western blot incubation)	Heidolph Instruments (Schwabach, Germany)
Thermo-Shaker TS-100 (95 °C)	A. Hartenstein (Würzburg, Germany)
Spectrophotometer genesis 10 S UV-Vis	Thermo Scientific (Waltham, USA)
Thermostat MA, 50 °C + Water bath	Julabo GmbH (Seelbach, Germany)
Tube rocker M48720-33	Thermo Scientific (Waltham, USA)
Ultracentrifuge M120 SE + S45A-0292 Tube Rotor & S525T-0117 Swing Rotor	Sorvall® /Thermo scientific (Waltham, USA)
Unichromat 19307	UniEquip (Freital Germany)
UV lamp VL-6.MC	Biotech (Madrid, Spain)
UV visualizer	Intas Science Imaging Instruments GmbH (Göttingen, Germany)
Variomag Mono Magnetic stirrerV	VWR (Radnor, USA)
Vibrax VXR basic	IKA (Staufen, Germany)
Vortex-Genie 2	Scientific Industries (Bohemia, USA)
WB system Amersham	GE Healthcare (Chicago, USA)
30 °C shaker	Infors AG (Bottmingen, Switzerland)

Table 10: Consumables register.

Description	Supplier
Amersham™ Protran™ 0.45 µm Nitrocellulose Blotting membranes	GE Healthcare (Chicago, USA)
Centrifugation bottle assembly (500 ml PC bottle, stopper, cap)	Beckman Coulter® Life Sciences (Brea, USA)
Centrifuge tubes, 15 ml	Greiner Bio-One (Kremsmünster, Austria)
Centrifuge tubes, 50 ml	Greiner Bio-One (Kremsmünster, Austria) / neoLab Migge GmbH (Heidelberg, Germany)
Glass beads; SiLibeads type S 0.40-0.60 mm	Sigmund Lindner GmbH (Warmensteinach, Germany)

Description	Supplier
Glass pipets 1,2,5,10,20 ml	Hirschmann® Laborgeräte GmbH & Co. KG (Eberstadt, Germany)
Glassware: Erlenmeyer flasks (300 ml, 500 ml), Fernbach flasks (1800 ml), Test tubes thick-/thin-walled (100x16mm, 160x16mm)	Duran® Group (Wertheim, Germany)
Microreaction tubes 1.5 / 2 ml	SARSTEDT (Nümbrecht, Germany)
Parafilm® M	Sigma Aldrich (San José, USA)
Pipet tips; 0-200 µl / 100-1000 µl	SARSTEDT (Nümbrecht, Germany)
Protein A Sepharose™	GE Healthcare (Uppsala, Sweden)
Rotilabo® single-use cells, PS Semi-micro, 1.6 ml	Carl Roth (Karlsruhe, Germany)
Specialty Tips/Gel Loading Pipet Tips Fisherbrand 1-200 µl	Thermo Fisher Scientific (Waltham, USA)
Sorval® PA Thinwall tube (5 ml)	Kendro Laboratory products Thermo Scientific (Ashville, USA)
Test tubes heavy-walled (100 x 16 mm Ø)	Duran Group (Mainz, Germany)
Test tubes thin-walled (100 x 15/16 mm Ø)	Duran Group (Mainz, Germany)
Test tubes with straight rim	Duran Group (Mainz, Germany)
Tuberculin, Omnifix® F syringe (1 ml)	B. Braun AG (Melsungen, Germany)
Whatman® cellulose chromatography papers, grade 3MM	GE Healthcare (Chicago, USA)

2.4.3 Software

Table 11: Software register.

Software	Supplier
Adobe® Photoshop® Elements 15	Adobe Systems (San José, USA)
Amplify4 1.0	https://engels.genetics.wisc.edu/amplify/
Gel Analyzer 2010a	gelanalyzer.com
ImageJ 1.52a	imagej.net
LAS-3000 Pro	Fujifilm (Tokyo, Japan)
Microsoft Office 2019	University Hohenheim
NEB Tm calculator	https://tmcalculator.neb.com/#!/main
Serial Cloner2.6.1	https://serial-cloner.de.softonic.com/
SnapGeneViewer 5.2.3	https://www.snapgene.com/
Tapforms5	https://www.tapforms.com/
Unicorn 1.1/1.2	GE Healthcare (Chicago, USA)
XnView MP 0.97.1	https://www.xnview.com/
ZEN Pro 2.3 SP1	Carl Zeiss (Oberkochen, Deutschland)

2.5 Molecular biological methods

2.5.1 PCR (Polymerase chain reaction)

Standard PCR with Q5 polymerase was performed to amplify DNA sequences from plasmid sources following the manufactures guide (Table 12). An annealing temperature of 60 °C was being determined for all primers used for the amplification of DNA sequences according to the Longtine et al. method referring to the NEB Tm calculator (Longtine et al., 1998).

Table 12: PCR protocol for Q5 polymerase.

Cycle step	Temperature [°C]	Time [s]	Cycles
Initial denaturation	98	30	x1
Denaturation	98	5	}x35
Annealing	60	10	
Elongation	72	20/kb	
Final Elongation	72	120	x1
Hold	16	∞	

2.5.2 Colony Test PCR

Template DNA was isolated from yeast cells by diluting a colony from a freshly streaked out plate into 40 µl of distilled water and placing the tube into a block heater for 5 min at 95 °C. Prior usage, the tube was vortexed, and 1 µl solution was taken for colony PCR. Colony PCR was performed using the OneTaq 2x MasterMix following the manufactures guide (Table 13).

Table 13: PCR protocol for OneTaq.

Cycle step	Temperature [°C]	Time [s]	Cycles
Initial denaturation	95	120	x1
Denaturation	95	15	}x35
Annealing	55	30	
Elongation	68	60/kb	
Final Elongation	68	600	x1
Hold	16	∞	

2.5.3 Agarose gel electrophoresis

For a 1 % agarose gel 2 g agarose were dissolved in 200 ml boiling distilled water and 2 ml 50x TAE were added to create a 0.5x TAE (20 mM Tris [pH 8], 10 mM NaOAc, 1 mM EDTA)

agarose solution. Ethidium bromide to a final concentration of 0.5 µg/ml was added to the solution, letting it cool down until solidifying in a tray used for agarose gel electrophoresis. DNA samples were stained with 10 % (v/v) marker solution (0.2 % bromophenol blue in 75 % glycerol). Agarose gel was running for 1 h at 200 V in 0.5x TAE/0.5 µg/ml EtBr running buffer with 0.5 µg λ-DNA cut with *EcoRI/HindIII* as a standard ladder.

2.5.4 Isolation of DNA fragments

DNA bands were identified and cut out from the agarose gel using a UV lamp, and the Qiagen gel extraction Kit applied further purification following the manufactures guide.

2.5.5 Calculating DNA concentration

After running an agarose gel, the results were recorded using gel documentation. DNA concentration was calculated by comparing the signal intensity of the separated DNA fragments to the signal intensity of the standard λ-DNA marker.

2.5.6 Enzymatic Digestion

Restriction digestion was performed by mixing 1 Unit of restriction enzyme with 1 µg of DNA and incubating the mixture for 2 - 3 h or overnight according to the manufactures suggested temperature.

2.5.7 SDS PAGE

Proteins were separated under denaturing conditions using the Sodium Dodecyl Sulfate-Polyacrylamide Gel Electrophoresis (SDS-PAGE). For the separating gel, 15 - 16 ml of a 7.5 % or 10 % solution were pipetted between the two glass plates in the scaffold (Table 14).

Table 14: Pipetting scheme for the SDS PAGE separating gel.

Separation gel	7.5 %		10 %		Vol.
	1 Gel	2 Gels	1 Gel	2 Gels	
dH ₂ O	10	20	8.3	16.6	ml
1.5 M Tris, pH 8.8	5	10	5	10	ml
Bis-/Acrylamide 30 %	5	10	6.7	13.4	ml
10 % SDS	200	400	200	400	µl
TEMED	40	80	40	80	µl
10 % APS	50	100	50	100	µl

The freshly poured gel was overlaid by 500 μ l ethanol, and polymerization occurred for 30 min at room temperature. After incubation, the alcohol layer was removed and air dried while the stacking gel solution was prepared (Table 15).

Table 15: Pipetting scheme for the SDS PAGE stacking gel.

Stacking gel	5 %		Vol.
	1 Gel	2 Gels	
dH ₂ O	7	14	ml
1 M Tris, pH 6.8	1.25	2.5	ml
Bis-/Acrylamide 30 %	1.7	3.4	ml
10 % SDS	100	200	μ l
TEMED	20	40	μ l
10 % APS	25	50	μ l

The gel scaffold was filled with approximately 6 ml of stacking gel solution, and a comb was inserted to create the gel pockets. Usually, polymerization of the stacking gel was carried out over a more extended period than 30 min to ensure stable, polymerized pockets for sample loading. After loading the protein solutions and the Color Pre-stained Protein Standard (Broad Range 11–245 kDa) (Table S 1) into the pockets, either 240 V for 3 h or 50 V overnight at 35 mA per gel were applied until the blue loading front ran into the running buffer (25 mM Tris, 192 mM glycine, 0.1 % SDS).

2.5.8 Coomassie staining

After removing the SDS PAGE gel from glass plates, the gel was covered with Coomassie staining solution (0.1 % Coomassie R250, 10 % acetic acid, 40 % methanol) and put into a microwave for up to 1 min until almost boiling. The gel was then incubated for 10 - 15 min on a shaker at room temperature. Afterwards, the Coomassie stain was discarded and recycled while the gel was cleaned off of the stain in distilled water until no further staining of water was visible. An excess of de-stain solution (20 % methanol, 10 % acetic acid) with some tissue paper was carefully placed in the container to the gel and microwaved again until boiling. The gel was repeatedly incubated with new tissue paper until the gel was fully de-stained.

2.5.9 Silver staining for mass spectrometry

For silver staining, clean glass bowls, fresh double distilled water, freshly prepared solutions, and powder-free gloves were used to ensure gel samples applicable for mass spectrometry.

After removing SDS PAGE gel from glass plates, the gel was fixed for 1 h at room temperature in 100 ml 30 % ethanol and 10 % acetic acid solution while shaking mildly. The gel was washed four times for 10 min in double-distilled water. Afterwards, the gel was incubated in 100 ml 0.8 M Na-thiosulfate for 1 min, washed twice in double-distilled water for again 1 min, and then stained in 100 ml 12 mM silver nitrate for 30 min while the bowl is being covered with aluminum foil. The stained gel is briefly washed in double-distilled water and then transferred to a fresh glass bowl with 100 ml developer solution (2 % glucose, 100 mM boric acid, 150 mM NaOH) for up to 30 min. It is crucial to regularly check staining intensity to ensure sufficient but not exceeding protein bands staining. Staining was then stopped in 100 ml 330 mM tris-base and 2 % acetic acid solution for 30 min while gently shaking. The silver-stained gel was washed with double distilled water before being applied for mass spectrometry analysis.

2.5.10 Western Blot analysis

Western blot analysis was carried out onto a nitrocellulose membrane by transferring the separated proteins from the SDS PAGE from the gel matrix to the membrane. Two Whatman cellulose chromatography papers were placed on the frame for tight stacking, and the gel was carefully transferred from between the glass plates onto the upper paper. The nitrocellulose membrane was applied to the gel, and the stack was topped with two additional pieces of Whatman paper before removing bubbles and closing the frame. The frame was placed in the blot tank containing western blot buffer (192 mM glycine, 25 mM Tris, 20 % methanol), and blotting was done overnight at 30 V or for 3 h at 60 V, allowing the proteins to migrate from the gel onto the membrane. After blotting, the membrane was removed from the frame and washed in dH₂O to remove the blotting buffer. Successful transfer of proteins was checked by applying 50 ml of Ponceau S solution (0.2 % Ponceau S, 3 % trichloroacetic acid [TCA]) over the membrane and incubating for 1 min at room temperature. After removing the Ponceau S solution, the membrane was washed with deionized water to remove unspecific staining and reveal stained proteins. The stained blot was documented at the gel imaging system and then fully de-stained with tap water for about 30 min. Prior blot development, unspecific binding sites were blocked in the membrane by blocking solution (1x PBS pH 7.4 [150 mM NaCl, 10 mM NaH₂PO₄], 0.05 % Tween 20, 1 % non-fat-dried milk) for 30 min at room temperature on the rocker. Per gel 4 ml primary antibody solution in blocking buffer was applied (antibody dilution see Table 16) and incubated for 90 min at room temperature on the rocker. Afterwards, the membrane was washed three times for 5 min in 50 ml PBS/Tween 20 (1x PBS pH 7.4, 0.05 % Tween 20) washing solution. The primary antibody was detected by incubating the

membrane with the appropriate secondary antibody in a 1:5000 dilution in 50 ml washing solution for 60 min at room temperature on the rocker. All used secondary antibodies are coupled with a horse reddish peroxidase that can react with luminol. Luminol in its di-anionic state reacts with O₂ and emits light detected by a camera. The incubated membrane was then washed two more times in washing buffer. A 1:1 mixture of 3 ml from each luminol solution was added to the membrane and incubated for 1 min. Luminescence pictures were taken with the LAS-3000 mini.

Table 16: Antibody list.

Primary-antibody epitope	Antigen [kDA]	Dilution	Secondary antibody
α -Alp	64	1:500	α -Mouse
α -Chm7 (K109 H2)	52.8	1:250	α -Rabbit
α -c-myc (9E10)	18.6	1:1000	α -Mouse
α -Did2 (K120 H2)	23.1	1:500	α -Rabbit
α -Dpm1	30	1:500	α -Mouse
α -haemagglutinin (HA)	3.5	1:500	α -Mouse
α -Ilv2 (K15)	75	1:1000	α -Rabbit
α -Ist1 (K117 H2)	37.5	1:500	α -Rabbit
α -Mos10 (K12 H2)	25.8	1:1000	α -Rabbit
α -Pep12	33	1:1000	α -Rabbit
α -Pma1	99	1:1000	α -Rabbit
α -sfGFP	27	1:2000	α -Rabbit
α -Snf7 (K43 H2)	27	1:2000	α -Rabbit
α -Ste6	145	1:200	α -Rabbit
α -Vps2 (K83 H2)	26.3	1:1000	α -Rabbit
α -Vps20 (K123 H2)	25.6	1:200	α -Rabbit
α -Vps24 (K76 H2)	26.2	1.1000	α -Rabbit

2.6 Microbiological methods

2.6.1 *S. cerevisiae* genomic DNA extraction (for Western Blot)

A yeast colony was picked from a freshly streaked out plate and inoculated in 3 ml YPD, incubating overnight at 30 °C and 100 rpm. The stationary cells are diluted in 20 ml fresh YPD and grown for about 2 h. After measuring the OD₆₀₀, about 4 OD cells were harvested at

3000 rpm for 2 min at room temperature in a Duran tube. The cells were washed in 5 ml NaN₃, and the pellet was resuspended in 100 µl lysis buffer (50 mM HEPES pH 7.5, 0.3 M Sorbitol, 10 mM NaN₃ + 1:100 E-Mix [0.017 g PMSF/ml + 10 µl PB Mix/ml] and 1:1000 P-Mix). After adding glass beads to create a slurry solution, the mixture was vortexed for 5 min in the vibrax at 4 °C. To the lysate, 150 µl of 2x SDS sample buffer with 100 mM DTT was added, and the Duran tube was placed in a water bath for 15 min at 50 °C. The liquid was taken off the glass beads and stored at -20 °C for further use.

2.6.2 Yeast transformation

Yeast transformation was performed according to Gietz et al. using the lithium acetate method (Gietz and Schiestl, 2007). 3 ml YPD were inoculated with a single yeast colony from a freshly streaked out plate and grown overnight at 30 °C and 100 rpm on a shaker. The yeast culture was diluted in 50 ml fresh YPD and grew an additional 4 h to reach exponential growth (OD₆₀₀ around 1). Since the transformation mixture contained 50 µl ssDNA, the appropriate number of cells to be harvested was calculated. It was estimated that the UV/Vis spectrometer measures an OD₆₀₀ to cell ratio of

$$OD_{600} \text{ of } 1 \approx 3 * 10^7 \text{ cells/ml}$$

and that the optimal DNA to cell ratio for a transformation mixture would be

$$\begin{aligned} \text{ssDNA of } 37.5 \text{ } \mu\text{l for } 1 * 10^8 \text{ cells} \\ \equiv 50 \text{ } \mu\text{l for } 1.33 * 10^8 \text{ cells.} \end{aligned}$$

Combining the two equations leads to the following term that was used for all transformations

$$\frac{1.33 * 10^8 \text{ cells}}{OD_{600} \text{ (measured)} * 3 * 10^7 \frac{\text{cells}}{\text{ml}}} = \text{Volume [ml]}.$$

The appropriate volume of yeast cell culture was harvested at 3000 g for 2 min at room temperature and washed once with 5 ml dH₂O. In the meantime, a 1 ml aliquot of ssDNA in TE-buffer (10 mM Tris-Cl [pH 8], 1 mM EDTA) was boiled for 5 min at 95 °C and chilled on ice water. A transformation mix stock solution was prepared for each yeast transformation (plus one additional sample) (Table 17).

Table 17: Transformation mixture.

Compound	Volume [μl]
PEG 4000 (50 % (w/v))	240
LiAc 1.0 M	36
Single stranded carrier DNA (2.0 mg/ml)	50
Total volume	336
Plasmid or PCR amplified DNA	1 - 2 or 45

The transformation mixture was added to the yeast cell pellet, and the plasmid or PCR mixture was added and vortexed until no further cell debris or pellets were visible. The entire solution was incubated for 40 min at 42 °C in a shaker at 100 rpm. After incubation, the cells were harvested at 3000 g for 2 min at room temperature. The pellet was resuspended in 200 μ l sterile water and distributed on a YPD plate so that half of the plate was covered with the entire solution and the other half contained a smeared outcrop. After incubation overnight at 30 °C, the plate was replicated on a replica plate containing either G418 as a kanamycin marker or single drop-out media for -His or -Try auxotrophy and incubated for 3 - 4 days at 30 °C.

2.6.3 *E. coli* transformation

75 μ l of competent BL21(DE3) *E. coli* cells were thawed on ice before 1 - 2 μ l plasmid DNA was added and subsequently incubated on ice for 45 min. Cells were then heat shocked at 42 °C for 45 s in a pre-heated water bath and chilled on ice again. Adding 500 μ l LB-Medium to the solution and incubating the cells for 90 min at 37 °C while shaking in an incubator ensures antibiotic resistance development. 200 μ l solution were pipetted on antibiotic-containing LB agar plates and incubated overnight at 37 °C.

2.7 Antibody Purification

2.7.1 Protein expression in *E. coli*

One colony of *E. coli* cells containing a plasmid for protein overexpression was incubated in 10 ml LB/Kan (10 μ l of 30 mg/ml stock solution) or LB/Amp (20 μ l stock solution) in a 100 ml Erlenmeyer flask overnight at 37 °C, shaking at 100 rpm. The saturated overnight culture was diluted 1:50 in 1-liter auto-induction media/kan (1 ml stock solution) or media/amp (2 ml stock solution) according to Studier (Studier, 2014) (Table 18).

Table 18: Autoinduction medium according to Studier.

Autoclave:	/ 1 l
Phosphate buffer (pH 7.2)	7.5 g Na ₂ HPO ₄ · 2 H ₂ O 3 g KH ₂ PO ₄
Tryptone	20 g
Yeast Extract	5 g
NaCl	5 g
50 % w/v glucose	1 ml (0.05 %)
Filter sterilize	
60 % v/v glycerol	10 ml (0.5 %)
10 % w/v lactose	20 ml (0.2 %) or 2 g powder

The culture was incubated at 37 °C and 100 rpm until an OD₆₀₀ of 0.6 - 0.8 was reached. 1 ml sample was taken out, which served as a non-induced control (NC). The temperature was set to 25 °C allowing the culture to cool down slowly, and after reaching the set temperature, another 1 ml sample was taken as an induced control (IC) while the rest of the culture was incubating overnight. The cell culture was harvested at 4000 g in 370 ml Beckmann tubes in a JA10 rotor for 10 min. The cell pellets were combined in a 50 ml Falkontube and either immediately used or stored at -80 °C.

2.7.2 Lysing *E. coli* cells

The pre-cooled piston, cylinder, and valves were prepared for French press lysis following the manufactures guide. The frozen cell pellet in 50 ml Falkontube was thawed on ice for about 15 min and weighted. The pellet was then resuspended in 10 ml/1 g wet weight of lysis buffer (20 mM NaH₂PO₄, 1 M NaCl + 1:100 E-Mix, 1:1000 P-Mix, 1:1000 RNase A, 1:1000 DNase I, 5.8 mM MgCl₂) up to 40 ml before applying it to French press. Cells were lysed by pushing the solution with the help of the piston through the cylinder with a constant pressure of 900 psi into a new Falkontube on ice. The needle valve and knob were constantly adjusted to remain lysate flow at around 900 psi pressure. The cell solution was treated by French press until visibly less turbid, while lysing success was also checked under a light microscope. As a control, 50 µl cell lysate (CL) was taken out and stored for SDS PAGE. The cell lysate solution was centrifuged at 10.000 g and 4 °C for 20 - 30 min in Beckmann tubes (max 40 ml) using the JA 30.50Ti rotor. The supernatant was carefully transferred into a new tubed and chilled on ice while a 50 µl sample was taken out that served as a cell supernatant (CS) control.

2.7.3 Protein purification from E. coli cells

The amount of Qiagen Ni²⁺-NTA resin (or similar product) needed for protein purification depends on the amount of protein in the culture, whereas less resin is typically better in terms of purity. According to the manual of most Ni²⁺-NTA resin, the binding capacity should be in the 50 mg/ml range. His tagged proteins were purified using a 50 % slurry Ni-NTA agarose bead solution stored in ethanol equilibrated in lysis buffer, freshly prior use. For 1 l cell culture, 4 ml 50 % slurry solution was used corresponding to 2 ml bead resin for binding up to 100 mg His tagged proteins. Protein binding was accomplished by combining the Ni²⁺-NTA resin slurry to the lysate in a tube and incubating the mixture for 1 h at 4 °C while gently shaking on a rocker. As an alternative, the Ni²⁺-NTA agarose solution was filled into a syringe, and the lysate solution was force pumped through the resin to ensure binding overnight at 4 °C. Afterwards, the resin was centrifuged for 5 min at 700 g to pellet the bead. The supernatant was retained and served as a flowthrough sample (**FT**). The Ni²⁺-NTA resin was washed three times with wash buffer (lysis buffer + 20 mM imidazole), and each washing step flowthrough was also collected (**W1-W3**). Protein was eluted with elution buffer (lysis buffer + 250 mM imidazole) for a total of four times each time with one column volume of the applied resin (**E1-E4**). All samples were checked on an SDS PAGE to verify protein purification and assess each elution step's purity.

2.7.4 Protein Dialysis

Dialysis membranes (SpectraPor1 = MWCO 8 kDa) were cut in 10 cm long (1 ml: 7 cm) pieces for purified protein dialysis. The membranes were first soaked for 30 min in dH₂O before clamps were attached to form membrane tubes. Samples were loaded into dialysis membrane tubes and placed into dialysis buffer (100 mM MOPS, 300 mM NaCl) 100x sample volume (1 l for 10 ml). The entire bucket was stirred at low speed in the cold room for three times 1 h and then overnight, exchanging the dialysis buffer during each step. After dialysis, the protein was retained for assaying binding, and a sample was stored that served as a dialysis control (**Dia**).

2.7.5 Affigel purification

Depending on the application, affigel-10 or affigel-15 were used to bind the antigen. Affigel-10 is best for binding proteins near or below their isoelectric point, while affigel-15 is better for binding proteins near or above their isoelectric point. For coupling at or close to neutral pH, affigel-10 is better for proteins with a pI of 6.5 to 11.0, while affigel-15 is better for proteins with a pI less than 6.5. According to the affigel resin manufactures guide, the binding capacity

should be in the 30 mg/ml range, for which mostly 1 - 2 ml 50 % slurry solution of affigel was used. The resin was washed with two column volumes of ice-cold dH₂O and once with the specific buffer used for protein binding that should be equal to the used dialysis buffer (0.1 M MOPS pH 7.4 + 300 mM NaCl). It is crucial that the entire preparation process does not exceed 20 min before protein coupling and that the gel bed was kept wet at all times. Purified and dialyzed proteins were mixed with prepared affigel and incubated while agitating on a rocker for 4 h at 4 °C. For affigel blocking, 0.1 ml 1 M ethanolamine HCl (pH 8) per ml gel was used and allowed to block for 1 h at 4 °C. The gel was transferred to a new column and washed with dH₂O or coupling buffer until the gel was free of reactants (detected by OD₂₈₀, Bradford Assay).

2.7.6 Antibody purification

The affigel coupled protein resin was washed with three column volume elution buffer (3.5 M MgCl₂ in 1x PBS pH 7.4) and subsequently washed with three column volumes of 1x PBS pH 7.4. The gel was then blocked with one column volume of 1 mg/ml BSA in 1x PBS pH 7.4 solution for 30 min at room temperature. Crude antibody serum was allowed to thaw on ice and was applied to the gel as a 50 ml antibody solution as a 1:10 solution of 5 ml cleared antibodies in 45 ml 1x PBS pH 7.4. A peristaltic pump was used for binding antibodies to the affigel associated proteins in the cold room. With a set speed of 1 ml/min, the entire antibody solution was pumped about 2 - 3 times through the column over the gel to ensure sufficient binding. Afterwards, the gel was washed with 10 column volumes of BSA/PBS solution, and the bound antibodies were eluted with 4 - 5 column volumes of elution buffer. Each one-column volume of eluant was collected individually and immediately dialyzed in 100x volume of 1x PBS pH 7.4 at 4 °C in dialysis membranes. The gel was washed with 10 column volumes of 1x PBS pH 7.4 and stored at 4 °C soaked in 10 mM sodium acetate in 1x PBS pH 7.4.

2.8 Cell fractionation

2.8.1 Sucrose Gradient

For a sucrose density gradient, 50 OD₆₀₀ cells of an exponential cell culture were harvested in Falkontubes for 5 min at 4000 g by centrifugation and washed in 5 ml NaN₃ utilizing Duran tubes. The pellet was resuspended in 200 µl SPBS10 buffer consisting of 1x PBS pH 7.4 and 10 % w/w sucrose (see Table 19) with the additional proteinase inhibitors (1:100 E-Mix; 1:1000 P-Mix). The cells were then lysed in a vibrax at 4 °C for 5 min at full speed via glass beads. Additional 400 µl SPBS10 were added, and approximately 500 µl lysate was transferred to an

Eppendorf tube. The lysate was centrifuged for 10 min at 4 °C at 2500 rpm to remove cell debris. For better comparison to other experiments, sucrose gradients were performed using 1x PBS pH 7.4 as a standard buffer solution by adding different sucrose amounts (Table 19).

Table 19: Table of used sucrose solutions.

Solution	[% mas]	Density [kg/m³]	[g] Total/200 ml	[g] Sucrose/200 ml
SPBS10	10	1.0381	207.6	20.8
SPBS20	20	1.0810	216	43.2
SPBS36	36	1.1562	230.8	83.1
SPBS53	53	1.244	248.8	131.8

The % mas corresponds to the equation: $\% mas = \frac{270 * \% (\frac{wt}{vol})}{270 + \% (\frac{wt}{vol})}$

To ensure identical buffer conditions, the appropriate amount of sucrose was weighted and dissolved in dH₂O and filled up with 20x PBS pH 6.3 buffer solution. The solutions were filter sterilized through a 0.45 µm filter and stored at 4 °C. Before using 1 mM of DTT was added to all solutions. Sucrose gradient was performed in an ultra-centrifuge that required special centrifugation tubes with a volume of 5 ml. Carefully 1.7 ml of each SPBS solution beginning with SPBS53, then SPBS36 and SPBS20 were added to ensure a layer-like filling of the tube. The tube was sealed by Parafilm and stored horizontally for approximately 3 h at 4 °C to cultivate a continuous gradient. After preparing the cell lysate and ensuring a constant gradient, 400 µl of the gradient was carefully removed and replaced with 400 µl of lysate solutions in the upright centrifugation tube. The ultracentrifuge was loaded with four balanced centrifugation tubes in a swinging rotor, running for 16 h at 4 °C at 100,000 g (37,000 rpm on “avg.” setting for the Rotor number 28 at slowest acceleration and deceleration). After centrifugation, 18 fractions of 280 µl each were carefully pipetted from top to bottom of the gradient. Each fraction was mixed with 280µl of 2x SDS sample buffer with 100 mM DTT and heated for 5 min at 95 °C.

2.8.2 Flotation

For a flotation experiment, 20 OD₆₀₀ cells of an exponential cell culture were harvested in Falkontubes for 5 min at 4000 g by centrifugation and washed in 5 ml NaN₃ utilizing Duran tubes. The pellet was resuspended in 200 µl 1x PBS pH 7.4 buffer with the additional proteinase inhibitors (1:100 E-Mix; 1:1000 P-Mix). The cells were then lysed in a vibrax at 4 °C for 5 min

at full speed via glass beads. Additional 200 μ l 1x PBS pH 7.4 were added, and approximately 300 μ l lysate was transferred to an Eppendorf tube. The lysate was centrifuged for 5 min at 4 $^{\circ}$ C and 2500 rpm to remove cell debris. 175 μ l of cleared lysate supernatant was transferred to 350 μ l of a 60 % OptiPrepTM solution for a final OptiPrepTM concentration of 40 %. Carefully a second layer of 840 μ l 30 % OptiPrepTM solution (420 μ l 60 % OptiPrepTM + 420 μ l 1xPBS pH 7.4) was placed on top of the first layer. The second layer was coated with 140 μ l 1xPBS pH 7.4, and the entire gradient was applied to ultra-centrifugation for 2 h at 4 $^{\circ}$ C, spinning at 100,000 g (Discovery M120SE Micro-Ultracentrifuge; Rotor: S45A = 45,000 rpm, set to slowest acceleration and deceleration). After centrifugation, six fractions of 250 μ l each were carefully removed from the gradient from top to bottom, mixed with 2x SDS sample buffer with 100 mM DTT, and boiled for 5 min at 95 $^{\circ}$ C.

2.8.3 Differential centrifugation

For differential centrifugation, 20 OD₆₀₀ cells of an exponential cell culture were harvested in Falkontubes for 5 min at 4000 g by centrifugation and washed in 5 ml NaN₃ utilizing Duran tubes. The pellet was resuspended in 200 μ l 1x PBS pH 7.4 buffer with the additional proteinase inhibitors (1:100 E-Mix; 1:1000 P-Mix). The cells were then lysed in a vibrax at 4 $^{\circ}$ C for 5 min at full speed via glass beads. Additional 600 μ l 1x PBS pH 7.4 were added, and approximately 700 μ l lysate was transferred to an Eppendorf tube. The lysate was either directly applied for differential centrifugation or was incubated with different additives to study various perturbation effects. Afterwards, the lysate was centrifuged for 15 min at 4 $^{\circ}$ C and 13,000 rpm. The pellet was retained, and the supernatant was transferred to a new tube and applied to ultracentrifugation at 100,000 g for 1 h at 4 $^{\circ}$ C. After centrifugation, the new pellet and supernatant were put on ice, and all three samples (pellet from 13,000 rpm spin (P13) and supernatant and pellet from 100,000 g spin (S100 & P100) were brought to the same volume. After intense mixing to ensure sufficient pellet resuspension in 1x PBS pH 7.4 buffer before 2x sample buffer with 100 mM DTT was applied, and the solution was boiled for 5 min at 95 $^{\circ}$ C.

2.9 Protein purification from yeast cells

2.9.1 Co-Immunoprecipitation

For Co-Immunoprecipitation (Co-IP) experiments, 50 OD₆₀₀ cells of an exponential cell culture were harvested in Falkontubes for 5 min at 4000 g by centrifugation and washed in 5 ml 1x PBS pH 7.4 utilizing Duran tubes. The pellet was resuspended in 200 μ l PBS pH 7.4 containing

1:1000 E-Mix, further named PBS+, and lysed in a vibrax at 4 °C for 5 min at full speed via glass beads. Additional 600 µl PBS+ were added, and approximately 700 µl lysate solution was transferred to an Eppendorf tube. DSP (dithiobis[succinimidylpropionate]) was used for protein crosslinking. The reagent contains a homo-bifunctional N-hydroxysuccinimide ester (NHS ester) crosslinker that reacts with primary amines with an additional eight-carbon spacer arm cleavable by reducing agents, thus enabling a non-permanent crosslinking. Because of the lipophilic nature, DSP was dissolved in DMSO (Dimethyl sulfoxide) (10 mg/200 µl for 125 mM), and 1:50 dilution was applied to the lysate for a final crosslinker concentration of 2.5 mM. The solution was incubated for 1 h at 4 °C on a rocker. The crosslinking reaction was stopped by quenching with 100 mM Tris-HCl (1 M, pH 8.0 stock solution) since it contains a primary amine, and membranes were dissolved by 1 % Triton X-100 (20 % stock solution). The reaction was incubated for 15 min at 4 °C on a rocker and then centrifuged for 10 min at 2500 rpm in the cold room. The supernatant was carried over to a new tube, and a small amount of approximately 50 µl was taken as an input control, and immediately 50 µl of 2x SDS sample buffer with 100 mM DTT was added and heat-treated for 5 min at 95 °C. The supernatant was incubated with 10 µl antibody solution for 1 h at 4 °C on a rocker. Afterwards, 80 µl of a 50 % slurry protein A solution in 1x PBS pH 7.4 was added and again incubated for 1 h at 4 °C on a rocker to allow protein A antibody binding. The solution was repeatedly washed with 1 ml pre-chilled PBS+ with slow centrifugation of 100 g for 30 s at room temperature. After three washing steps, the protein A beads were pelleted at full speed for 30 s and resuspended in 100 µl PBS+ and 100 µl 2x SDS sample buffer without DTT after removing the supernatant. The beads were boiled for 5 min at 95 °C, and the supernatant was afterwards transferred to a fresh tube. DTT to 50 mM final concentration was added, and the solution was again heat-treated for 5 min at 95 °C. Sequential boiling led to more negligible amounts of cleaved-off antibodies while high yields of crosslinked co-immunoprecipitated proteins were maintained.

2.9.2 Crosslinking experiment

For Crosslinking experiments, 40 OD₆₀₀ cells of an exponential cell culture were harvested in Falkontubes for 5 min at 4000 g centrifugation and washed in 5 ml 1x PBS pH 7.4 or dH₂O utilizing Duran tubes. The pellet was resuspended in 200 µl PBS containing 1:1000 E-Mix, further named PBS+, and lysed in a vibrax at 4 °C for 5 min at full speed via glass beads. Additional 600 µl PBS+ were added, and approximately 700 µl lysate solution was transferred to an Eppendorf tube. For protein crosslinking, DSS (disuccinimidyl suberate) was used. The reagent contains a homo-bifunctional N-hydroxysuccinimide ester (NHS ester) crosslinker that

reacts with primary amines for permanent protein crosslinking. Because of its lipophilic nature, DSS was dissolved in DMSO (7.4 mg/100 μ l for 200 mM), and 1:50 dilution was applied to the lysate for a final crosslinker concentration of 4 mM. The solution was incubated for 1 h at 4 °C on a rocker. The crosslinking reaction was stopped by quenching with 100 mM Tris-HCl (1 M, pH 8.0 stock) since it contains a primary amine, and membranes were dissolved by 1 % Triton X-100 (20 % stock). The reaction was incubated for 15 min at 4 °C on a rocker and then centrifuged for 10 min at 12,000 g at 4 °C. The supernatant was carried over to a new tube, and a small amount of approximately 50 μ l was taken as an input control, and immediately 50 μ l of 2x SDS sample buffer with 100 mM DTT was added and heat-treated for 5 min at 95 °C. To 700 μ l supernatant 26.2 μ l 5 M NaCl (+ 175 mM) and 2.2 μ l 5 M imidazole (+ 15 mM) was added for buffer conditions of NaCl \geq 300 mM and imidazole 10 – 20 mM. The supernatant was then incubated with 25 μ l of a 50 % slurry solution of Ni²⁺-NTA agarose beads equilibrated in the same buffer for 1 h at 4 °C on a rocker. After incubation, the mixture was centrifuged for 1 min at 2500 rpm in the cold room, and 50 μ l supernatant was saved for SDS PAGE analysis of unbound protein. The solution was repeatedly washed with 1 ml pre-chilled PBS+ with slow centrifugation of 100 g for 30 s. at room temperature. After three washing steps, the beads were pelleted at full speed for 30 s. and resuspended in 50 μ l buffer and 50 μ l SDS buffer with 100 mM DTT after removing the supernatant. The beads were boiled for 5 min at 95 °C and stored or applied for SDS PAGE analysis.

2.9.3 AEKTA purification

For AEKTA purification 1-liter YPD was inoculated with a 3 ml yeast overnight culture and was incubated at 30 °C and 100 rpm in a Fernbach flask. After cells reached exponential growth ($OD_{600} \leq 1$), the cell culture was harvested at 4000 g in three 350 ml Beckmann tubes for 10 min at 4 °C. After centrifugation, the tubes were weighted to determine the pellet's wet weight. The pellet was then resuspended in 1x PBS pH 7.4 buffer, transferred to a 50 ml Falkontube and pelleted again for 10 min at 4000 g and 4 °C. Centrifuge acceleration was set to 9 and deceleration to 5 to inhibit turbulences inside the tube and get a sharper separation between the pellet and the supernatant. The pellet was mixed with binding buffer 1x PBS pH 7.4 + 1:100 E-Mix in a 1:1 ratio, and about half the volume was filled with acid-washed glass beads. Yeast cells were then lysed in a Fast Prep24 at 4 °C for two times 1 min with 4 m/s speed and a 5 min pause in between shaking to let the suspension cool down. A sample of 50 μ l was taken and mixed with 50 μ l 2x sample buffer with 100 mM DTT for SDS PAGE analysis. The lysate was incubated with 4 mM DSS crosslinker (200 mM = 7.4 mg/100 μ l DMSO, 1:50 dilution) in a

Falkontube for 1 h at 4°C on a rocker. The crosslinking reaction was stopped by quenching with 100 mM Tris-HCl (1 M, pH 8.0) since it contains a primary amine, and membranes were dissolved by 1 % Triton X-100 (20 %). The reaction was incubated for 15 min at 4 °C on a rocker and then centrifuged for 15 min at 15,000 g and 4 °C in a 50 ml Beckmann tube. The supernatant was carried over to a new tube, and 5 M NaCl (+ 175 mM) and 5 M imidazole (+ 15 mM) were added for buffer conditions of NaCl \geq 300 mM and imidazole 10–20 mM. The pH was checked and adjusted to 7.4 if necessary, and afterwards, the solution was filtered through a 0.45 μ m filter. A small amount of approximately 50 μ l was taken as an input control, and immediately 50 μ l of 2x SDS sample buffer with 100 mM DTT was added and heat-treated for 5 min at 95 °C. The sample was then applied to the AEKTA start, and purification of crosslinked proteins was achieved by pumping the solution over a 1 ml HisTrap™ Fast Flow column. The application of lysed cells was monitored by measuring the UV of the flowthrough over time. After applying the lysate, the column was washed with 20 column volumes or more with a mixture of binding and elution buffer that contained 500 mM imidazole. Typically, the elution buffer concentration was set to 10 %, corresponding to an imidazole concentration of 50 mM. Elution of proteins bound to the column was achieved by running a gradient of elution buffer until 100 % buffer that equals 500 mM imidazole was reached, and the eluent was collected in Eppendorf tubes.

2.10 Cycloheximide chase

100 ml YPD were inoculated with a yeast overnight culture and grown overnight at 30 °C and gently shaking at 100 rpm. For the cycloheximide chase, an exponential cell culture of OD₆₀₀ between 0.6 – 0.8 was used. Before the experiment, a new cycloheximide stock solution was prepared by diluting cycloheximide in DMSO to a final concentration of 50 mg/ml. 400 μ l of the new stock solution was pipetted to 100 ml culture for a working concentration of 200 μ g/ml cycloheximide and to initiate the cycloheximide chase. Cells were harvested at 0, 20, 40, 60, 80, and 100 min after cycloheximide treatment. In each cycle, a 5 OD₆₀₀ culture was harvested for 5 min at 4700 rpm, with acceleration and deceleration set to 9, at room temperature. The cells were washed once in 5 ml 10 mM NaN₃ and pelleted again at 3200 rpm for 2 min at room temperature. The pellet was resuspended in 100 μ l lysis buffer (50 mM HEPES pH 7.5, 0.3 M Sorbitol, 10 mM NaN₃, and 1:100 E-Mix) and lysed with glass beads for 5 min at max speed in a vibrax. After lysing the cells, 300 μ l lysis buffer with inhibitor was added to the beads, and

about 300 μl solution was transferred to a new tube. 2x SDS sample buffer with 100 mM DTT was added and boiled for 5 min at 95 °C.

2.11 Fluorescence microscopy

A single yeast colony was diluted in 5 ml dH_2O , and 50 or 100 μl of that solution was inoculated to 5 ml SD_{cas} (1 % casamino acids, 0.67 % yeast nitrogen base w/o amino acids + 50 $\mu\text{g}/\text{ml}$ Tryptophane & + 50 $\mu\text{g}/\text{ml}$ Uracil) medium and incubated overnight at 30 °C and 100 rpm. Glass slides were coated with 15 μl 0.5 mg/ml concanavalin A and allowed to dry for 20 min. For fluorescence microscopy, an exponential cell culture of OD_{600} between 0.6 – 0.8 was used. 1 ml of the cell culture was transferred to a Duran tube and incubated for 1 min with 1 mg/ml 4,6-Diamidino-2-Phenylindol (DAPI). About 15 μl cell solution was pipetted to the concanavalin A covered glass slide, covered with a glass lid, and allowed to settle before observing under the microscope. One drop of immersion oil was applied to the glass cover before fluorescence microscopy.

2.12 SILAC Experiments

For SILAC (stable isotope labeling with amino acids in cell culture) experiments, two cultures were grown in separated flasks containing “heavy” and “light” minimal media. In general, minimal media was prepared by weighing 6.7 g YNB and 50 mg of Ura, Trp, Ade, and His, and 60 mg Lys and 120 mg Leu for a 1 l culture. Cultures using conventional L-lysine and L-arginine powder are referred to as the “light” culture, whereas for the “heavy” culture, the isotope $[\text{}^{13}\text{C}_6/\text{}^{15}\text{N}_2]$ L-lysine hydrochloride and $[\text{}^{13}\text{C}_6/\text{}^{15}\text{N}_2]$ L-arginine hydrochloride was used (MW shift from 182.7 g/mol to 190.7 g/mol for L-lysine and 210.7 g/mol to 220.7 g/mol for L-arginine). For SILAC experiments, 1 l light and heavy medium was inoculated with a 3 ml or 50 ml yeast overnight culture and incubated at 30 °C and 100 rpm in a Fernbach flask. After cells reached exponential growth ($\text{OD}_{600} \leq 1$), the cell culture was harvested in three 350 ml Beckmann tubes for 10 min at 4000 g and 4 °C. After centrifugation, the pellets were then resuspended in 1x PBS pH 7.4 buffer, transferred to a 50 ml Falkontube and pelleted again for 10 min at 4000 g and 4 °C. The pellets were mixed with binding buffer 1x PBS pH 7.4 + 1:100 E-Mix and combined before lysed in a Fast Prep24 with glass beads at 4 °C for two times 1 min with 4 m/s speed and a 5 min pause in between shaking to let the suspension cool down. The mixed cell lysate was either applied for co-immunoprecipitation or IMAC using AEKTA or batch method.

3 RESULTS

3.1 Finding interacting partners of ESCRT-III subunit Mos10

The Class E Vps protein Mos10 is seen as an associated ESCRT-III subunit whose pivotal role in ESCRT-III complex formation, deformation, or overall functionality needs additional insights to be adequately characterized. The idea here was to improve the protein's purpose inside or outside the established standard model by broadening Mos10's interplay spectrum with yet unknown interacting partners. The three distinctive methods used to find these Mos10 linked proteins were IMAC purification of histidine-tagged Mos10 (RKY2889), native Mos10 (RKY1558) purification by purified α -Mos10 antibodies, and immunoprecipitation of superfolder GFP-tagged Mos10 (RKY3210) using α -GFP antibodies. Homologous recombination was used for the tagged variants of Mos10 to add a purification-specific tag to the c-terminal side of the protein. It is worth noticing that these mutants do not necessarily share WT-like behavior visible by a different phenotype observed in succeeding experiments but also become evident by a shift in the WB pattern of the crosslinking partners. Those patterns were seen as protein-specific interacting patterns by fixing WT or tagged Mos10 to connecting proteins by a crosslinker and should not change by the method applied. Crosslinkers like DSP or DSS are chemical agents used to stabilize weak or transient protein to protein interactions in a multimeric complex or pathway, allowing the purification and identification of interacting partners. Once two or more proteins come in close proximity by interacting with each other, the NHS esters located at both sites of a spacer arm of the crosslinker react with primary amines of the involved proteins, thus linking them together and allowing for stable purification. Purified and crosslinked proteins were then separated by SDS PAGE and either visualized by Coomassie or silver staining or transferred to a nitrocellulose membrane and displayed by a target-specific antibody. With the help of mass spectrometry, enriched proteins associated with pull-downed Mos10 were identified. Identifying multiple candidates between the used methods allowed for comparing the quality of the purification process.

To further improve the identification of crosslinked proteins compared to background proteins regularly being purified along with the affinity tagged ones, cells were labeled by SILAC. Stable isotope labeling by amino acids in cell culture labels proteins by non-radioactive isotopes inducing a mass shift, detectable by mass spectrometry. With the SILAC approach, the heavy or non-heavy isotopes being pulled down should directly reflect the abundance of the protein, indicating the detection quality of an actual or artificial crosslink.

3.1.1 IMAC purification of His-tagged Mos10

One of the first experiments performed to visualize Mos10 specific interacting partners was purifying histidine-tagged Mos10 in a batch experiment using Ni²⁺-NTA beads. The principle of IMAC (immobilized metal affinity chromatography) purification is the affinity of histidine to bind the immobilized nickel ions on the beads and allow selective purification of proteins tagged with histidine. If the tagged proteins are being crosslinked with other proteins, this should result in a unique crosslink pattern for the purified protein. To visualize Mos10-6His purification and crosslinking pattern building, Figure 9 provides a step-by-step sample pull-down experiment result by Western Blot analysis by immunoblotting with α -Mos10 antibodies.

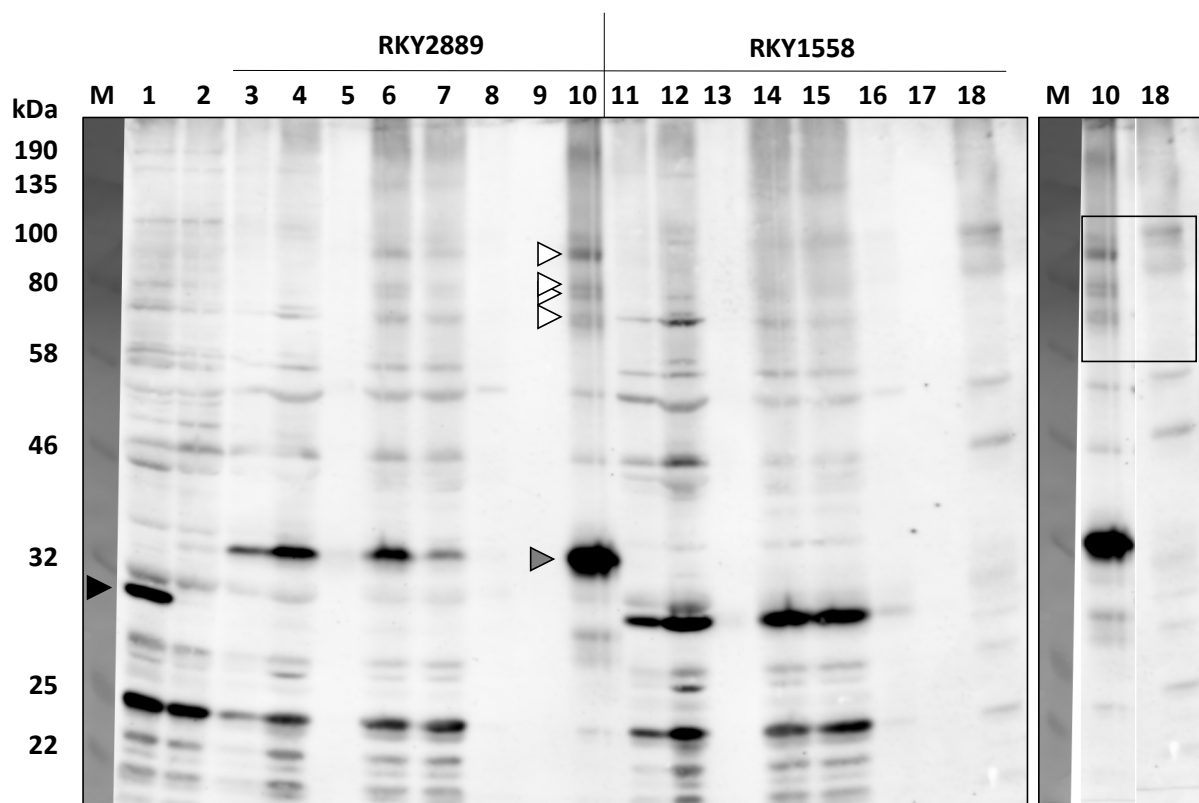


Figure 9: Identification of Mos10 interacting partners by a characteristic WB pattern.

IMAC purification of 6His tagged- (RKY2889) and WT-Mos10 (RKY1558) in a batch experiment utilizing Ni²⁺-NTA His-tag affinity beads. The characteristic crosslinking pattern of Mos10-6His by α -Mos10 antibodies is highlighted and compared to the WT Mos10 pattern in the black rectangle of lanes 10 & 18. **M:** NEB Color Pre-stained Protein Standard (11 - 245 kDa); **Lane 1:** WT extract; **Lane 2:** $\Delta 8$ extract; **Lane 3 & 11:** Lysate debris; **Lane 4 & 12:** Lysate SN; **Lane 5 & 13:** 500 g pellet; **Lane 6 & 14:** 500 g SN; **Lane 7 & 15:** Unbound IMAC SN; **Lane 8 & 16:** 1st washing step; **Lane 9 & 17:** 2nd washing step; **Lane 10 & 17:** IMAC purified protein solution. Arrows: **Black:** WT-Mos10; **Grey:** Mos10-6His; **White:** Crosslinks.

As a control for proper antibody functionality and detection of the protein of interest, Lane 1 and 2 contain a WT (RKY1558) and a $\Delta 8$ (RKY2844) strain sample, which detect WT Mos10

right below the 32 kDa mark by α -Mos10 antibodies, highlighted by a black arrow, that is not present in the deletion strain. The lanes 3 to 10 and 11 to 18 contain samples (OD = 0.2) of the purification process of RKY2889 with Mos10-6His and RKY1558 with WT Mos10. The cell cultures were lysed, the supernatant incubated with Triton X-100 and crosslinker before being quenched to stop the crosslinking process and centrifuged to remove larger cell debris, seen in lanes 3 – 6 and 11 to 14, respectively. The supernatant was subsequently incubated with the IMAC coated beads and twice washed before any protein's affinity attached to the ion beads were cleaved off by boiling (lanes 7 – 10 and 15 – 18).

Within the experiment, enrichment of a band at around 34 kDa becomes visible in the RKY2889 lanes that peak out in lane 10, which contains all proteins affinity bound to the Ni²⁺ beads, including purified Mos10-6His. Between 100 kDa and 70 kDa, additional bands become more abundant along the purification process of Mos10-6His that represent the crosslinks co-purified by being covalently attached to Mos10 by DSS detectable by the α -Mos10 antibody also peaking in lane 10. Compared to the bands visible in lane 10, the WT strain shows no sign of purification of WT Mos10 in lane 18. By comparing the WT Mos10 bands in lanes 14 and 15, the amount of Mos10 incubated with the beads after the centrifugation is equal to the amount found in the fraction of unbound IMAC supernatant. Further, no enrichment of crosslinker being pulled down was observable, as highlighted by comparison in the black rectangle enclosing the 100 to 70 kDa area of lanes 10 and 18. The experiment ensures for target-specific enrichment of Mos10-6His and any crosslinked protein to be purified by the IMAC purification.

3.1.2 AEKTA purification of His-tagged Mos10

Although suitable for purifying minor cell culture sizes up to 50 OD, the batch method relies on the ability of the Ni-NTA beads to come in contact with the histidine-tagged proteins to be attached while being incubated on a rocker. In larger scales with 1000 OD or more, a column filled with Ni-NTA beads was used, and the lysed and processed cell culture was forced through the column either by a peristaltic pump or an AEKTA system. The advantage of an AEKTA purification system is the ability to monitor each step in the purification process of the desired protein to ensure high yield and a better signal-to-noise ratio since the elution of the affinity-captured protein can be tightly timed. An example of an isocratic AEKTA purification of Mos10-6His (RKY2889) can be seen in Figure 10. The diagram serves as a purification protocol in which the UV detector placed behind the column visualizes the amount of protein passing the column. Visible by the blue line's overall peak amplitude between 5 and 35 ml, most of the protein from the cell lysate flows through the Ni-NTA column without binding to the beads.

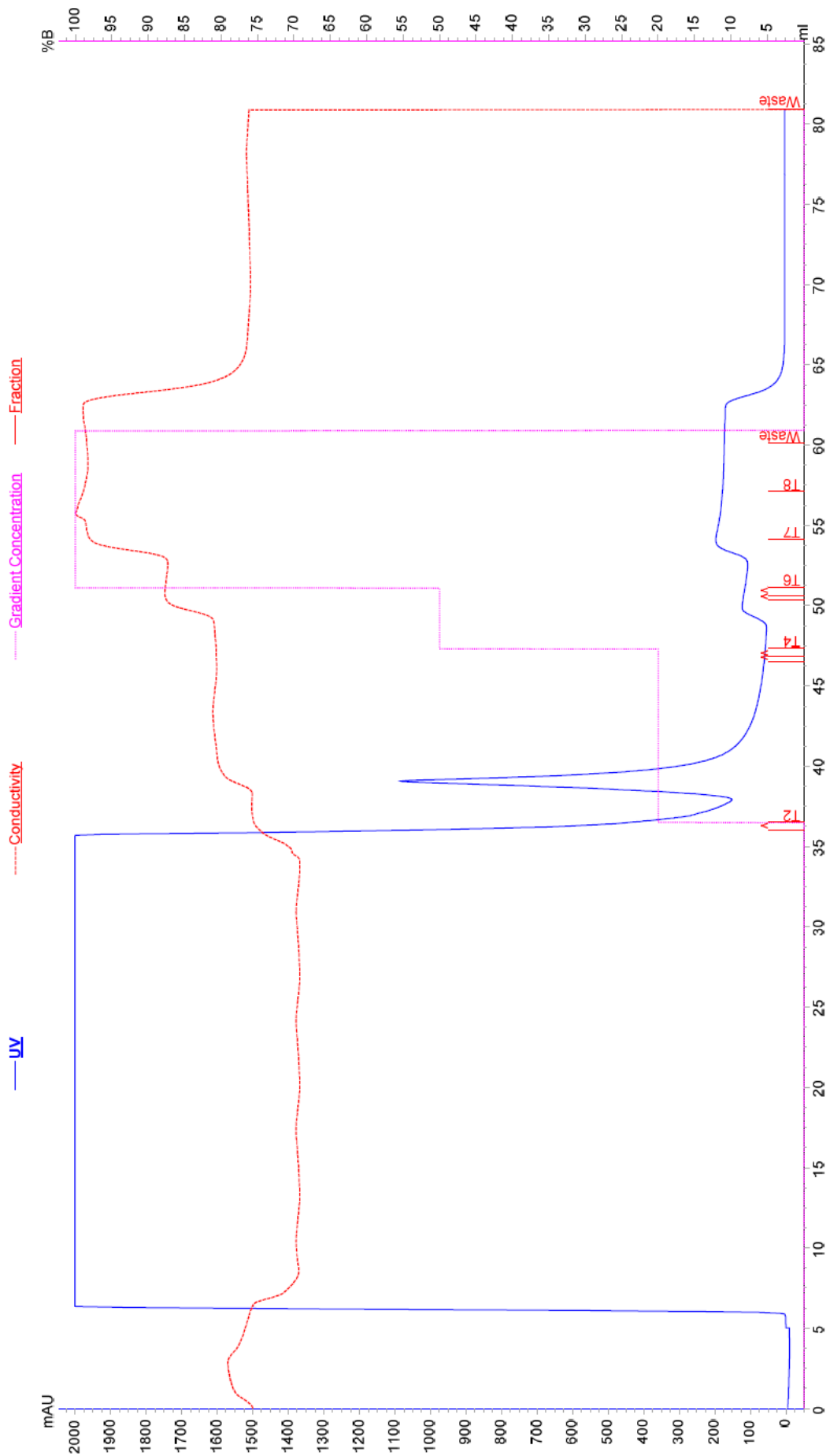


Figure 10: AEKTA purification of Mos10-6His from *S. cerevisiae* culture with Ni-NTA column.

After applying approximately 35 ml cell lysate, the UV intensity in mAU decreases, indicating that the entire sample has passed the system and the column. In the next phase, 20 % buffer B is applied to the system containing 500 mM imidazole for an effective concentration of 100 mM imidazole indicated by the purple line. The imidazole molecules compete with low-affinity impurities on the column and are used to wash the column from background proteins, monitored by an increase in UV intensity, forming a peak at around 39 ml. Afterwards two elution steps are used to elute the affinity attached proteins from the column with an imidazole concentration of 250 mM (50 % buffer B) and 500 mM (100 % buffer B) sufficient to cleave any associated protein from the Ni-NTA beads. At any given point during the purification experiment, samples are collected following the AEKTA fraction nomenclature marked as red lines at the corresponding ml position on the x-axis. Successful affinity purification was verified by WB analysis with α -Mos10 antibodies and Coomassie staining of the SDS PAGE seen in Figure 11.

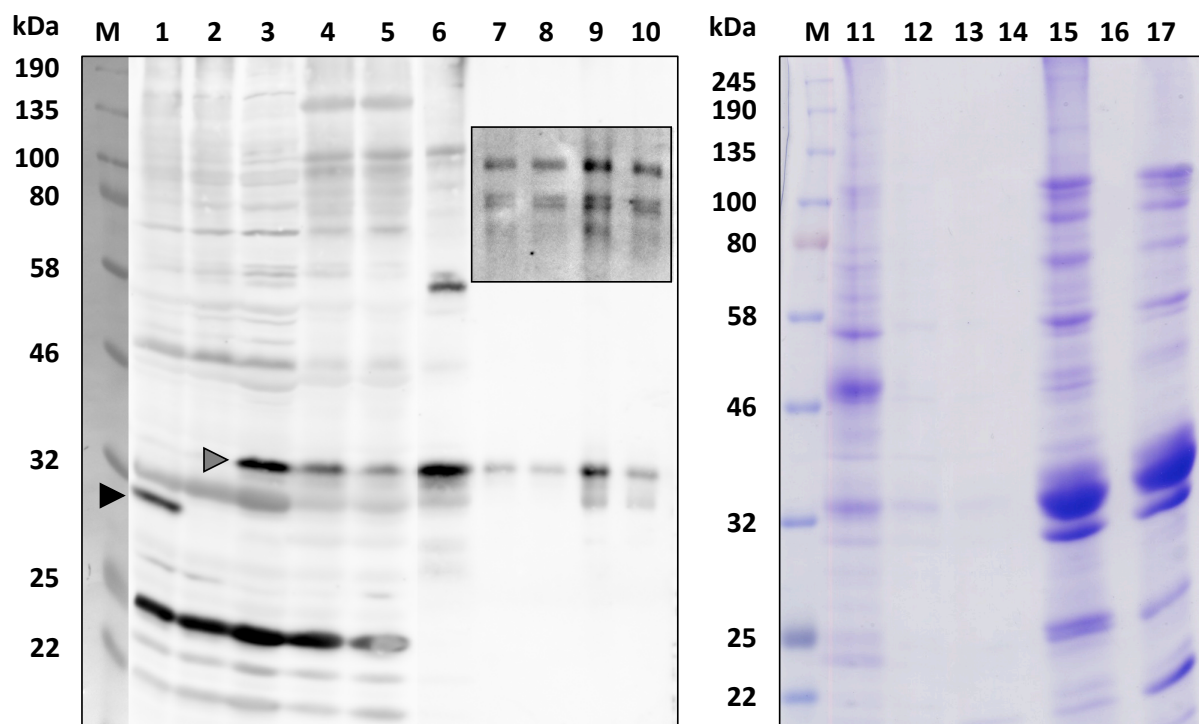


Figure 11: Isocratic AEKTA purification of Mos10-6His using a Ni-NTA column.

IMAC purification of 6His tagged-Mos10 (RKY2889) with the AEKTA system utilizing a Ni²⁺-NTA column. Visualization of the Mos10 characteristic crosslink WB pattern by α -Mos10 antibodies and Coomassie staining of AEKTA specific samples. Samples were concentrated using an AMICON filter with a 10 kDa cut-off. **M**: NEB Color Pre-stained Protein Standard (11 - 245 kDa); **Lane 1**: WT extract; **Lane 2**: Δ^8 extract; **Lane 3**: Lysate debris; **Lane 4**: Sample loaded on AEKTA; **Lane 5**: Flowthrough; **Lane 6**: T2 (wash fraction with 20 % Buffer B); **Lane 7**: T4 fraction (50 % Buffer B); **Lane 8**: T6 fraction (100 % Buffer B); **Lane 9**: concentrated T4 fraction; **Lane 10**: concentrated T6 fraction **Lane 11**: T2; **Lane 12**: T4; **Lane 13**: T6; **Lane 14 & 16**: empty; **Lane 15**: concentrated T4; **Lane 17**: concentrated T6. Arrows: **Black**: WT-Mos10; **Grey**: Mos10-6His.

The results of the WB analysis reveal that most of the Mos10-6His protein detected at the 34 kDa marked with a grey arrow gets lost along the purification process as the band tends to fade from lanes 3 to 5. An estimation of the protein quantity from the signal intensities of the protein bands shows that merely half the amount of Mos10-6His harvested from lysed cell culture is applied to the AEKTA system. 50 % again get lost in the flowthrough and an additional 20 % in the T2 wash fraction with 20 % (100 mM) buffer B. Although purification of Mos10-6His seemed pretty inefficient and needs further adjustment in upcoming experiments, the detection of Mos10-6His crosslinked proteins was successful and followed the same pattern as previously described in the batch experiment. Furthermore, the crosslinking pattern between 100 and 70 kDa becomes prominent in the T4 and T6 fraction with higher imidazole (250 mM and 500 mM) concentrations highlighted with the black rectangle in lanes 7 and 8. Since the experiment initially sought to identify and purify Mos10-6His interacting partners, the method applied seems suitable for purifying Mos10-6His and crosslinks in separate fractions due to the distinct behavior towards imidazole.

AMICON filters with a cut-off of 10 kDa were used to reduce sample volume and concentrate sample proteins, so that higher protein quantities can be loaded onto the gel for subsequent MS analysis. In lanes 9 and 10, samples of the AMICON concentrated T4 and T6 AEKTA fractions were loaded on the WB to verify successful sample concentration compared to lanes 7 and 8. One-fifth of the volume was loaded onto the gel, whereas the total sample volume was reduced from 3 ml after AEKTA elution to 150 µl after AMICON concentration resulting in a theoretical band intensity increase ratio of 4:1. ImageJ calculation reveals a protein band intensity ratio of 2:1 for the concentrated crosslink samples, implying that approximately 50 % of the crosslinks are gone by being stuck onto or precipitated on the filter during the concentration process.

Coomassie staining was used to visualize overall protein abundance and to identify the WB-specific crosslinking pattern of Mos10-6His interacting partners. Most of the proteins are being washed off the column in the T2 washing step seen in lane 11, which leaves almost no visible bands in the T4 and T6 fractions in lanes 12 and 13, considered to contain the crosslinks if compared with the WB. In contrast, lanes 15 and 17 contain the concentrated T4 and T6 fractions, showing vast overall protein abundance. The known crosslinking pattern remains hidden behind background bands and thus is not visible on the Coomassie-stained gel. Due to the loading calculations applied earlier, the band at 34 kDa, although migrating at the proper distance for Mos10-6His, is most definitely a background band since most of the Mos10-6His amount is held back in preceding fractions, leaving Mos10-6His levels below the detection limit.

For MS analysis, a gradient-based elution method was chosen to improve Mos10-6His purification and ensure tighter separation of more abundant proteins from the crosslinked proteins. The experiment follows the same workflow as the isocratic purification attempt except that the imidazole concentration in the T2 washing step was reduced from 20 to 10 % buffer B, corresponding to an imidazole concentration of 50 mM. For the gradient elution, the starting concentration of 50 mM was constantly increased until the final concentration of 500 mM imidazole at 100 % buffer B was reached. During the gradient elution, 30 samples à 500 μ l from fraction T4 to T33 were collected, and each fraction's starting and end imidazole concentration can be seen in Table S 2.

The AEKTA diagram in Figure S 2 protocols the purification process, in which a broad peak of the blue line again indicates the start and endpoint of cell culture application by monitoring the protein content unbound to the Ni-NTA column. In contrast, the blue peak UV signal in the washing step decreased in height compared to the one seen in Figure 10 due to the reduced imidazole concentration of 50 mM instead of 100 mM. Lastly, the purple gradient concentration indicator shows a steep rising path following the continuous increase in buffer B than the step-wise rise within the isocratic purification attempt.

All samples collected during the gradient purification process were applied to WB analysis (Figure 12) and checked by Coomassie staining of the SDS PAGE gel (Figure 13).

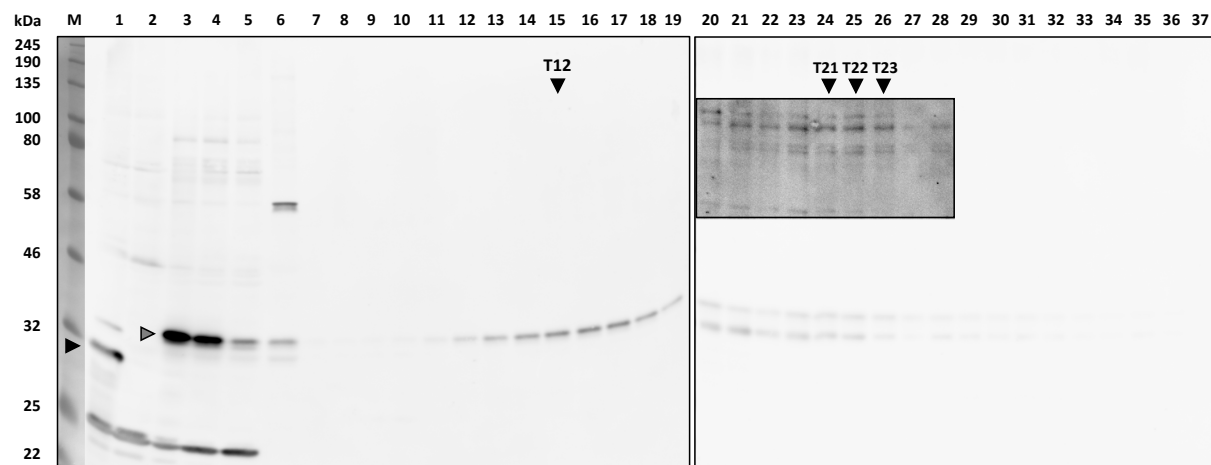


Figure 12: WB results of a gradient AEKTA purification of Mos10-6His using a Ni-NTA column.

IMAC purification of 6His tagged-Mos10 (RKY2889) with the AEKTA system utilizing a Ni²⁺-NTA column. Visualization of the Mos10 characteristic crosslink WB pattern by α -Mos10 antibodies. **M**: NEB Color Pre-stained Protein Standard (11 - 245 kDa); **Lane 1**: WT extract; **Lane 2**: Δ^8 extract; **Lane 3**: Lysate debris; **Lane 4**: Sample loaded on AEKTA; **Lane 5**: Flowthrough; **Lane 6**: T2 (wash fraction with 10 % Buffer B); **Lane 7-36**: AEKTA samples T4-T33 (10 % to 100 % Buffer B gradient). Arrows: **Black**: WT-Mos10; **Grey**: Mos10-6His. Lanes 4 – 6: OD = 0.2 and lanes 7 – 39: OD = 1.

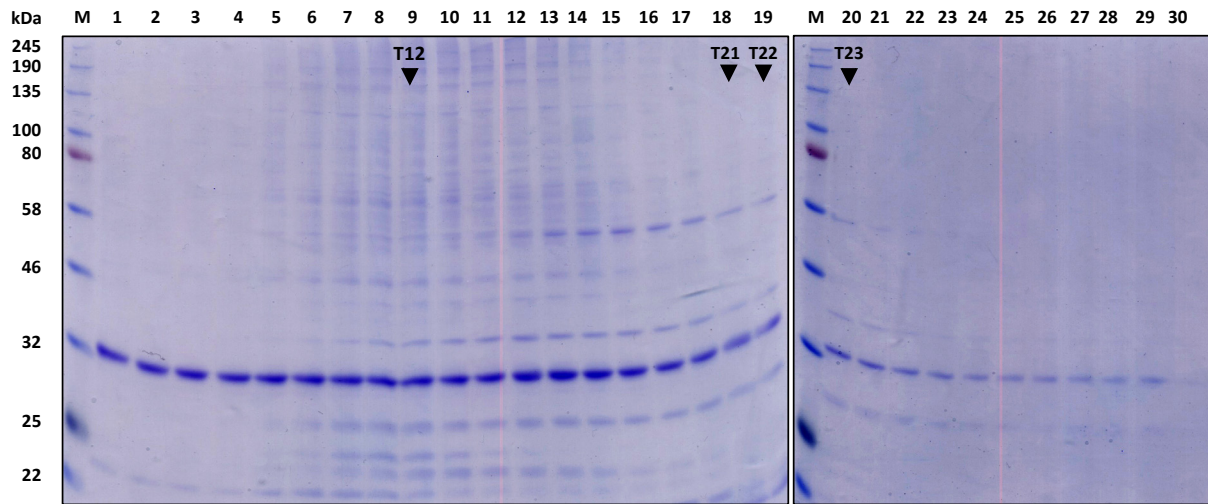


Figure 13: Gradient AEKTA purification of Mos10-6His using a Ni-NTA column Coomassie staining.

IMAC purification of 6His tagged-Mos10 (RKY2889) with the AEKTA system utilizing a Ni²⁺-NTA column. Visualization of the purification process using Coomassie staining of SDS PAGE gel. **M:** NEB Color Pre-stained Protein Standard (11 - 245 kDa); **Lane 1-30:** T4-T33.

After the two known control lanes, the blots reveal a comparable band color intensity at 34 kDa corresponding to Mos10-6His in lanes 3 and 4, indicating that most tagged Mos10 harvested from the cell lysate was applied to the AEKTA system. Due to the reduction in buffer B concentration in the wash fraction, less Mos10-6His was eluted prematurely from the column. Mos10-6His elution starts at lane 11 with an imidazole concentration of 110 to 125 mM and is eluted until lane 19 (230 – 245 mM imidazole), peaking at lane 15 representing fraction T12 (170 – 185 mM imidazole). From lane 20 to 36 on the second blot, two faint bands at the height around 32 kDa can be seen, which could also be Mos10-6His becoming visible due to a longer exposure time of the blot. From lanes 20 to 28 highlighted in the black rectangle, the familiar crosslinking pattern of Mos10-6His becomes visible. The WB results indicate that an imidazole concentration of 100 mM is sufficient to elute Mos10-6His, but imidazole concentrations of 250 mM and higher are necessary to elute crosslinked Mos10-6His. The results are in line with the imidazole concentrations used in the isocratic elution of Mos10-6His, in which crosslinks were present in the 250 mM and 500 mM imidazole fractions.

The SDS PAGE gel staining in Figure 13 implies that Mos10-6His containing fractions elute with most proteins bound to the Nickel column. Since the elution doesn't appear random, a plot against a Gaussian distribution was calculated by summing all band color intensities in each lane and putting the highest intensity sum to 100 %. The graph can be seen in Figure 14, in which the calculated blue curve, according to the Coomassie staining, overly fits a perfect Gaussian standard distribution ($R = 0.9850$), indicating a statistically normal distributed elution.

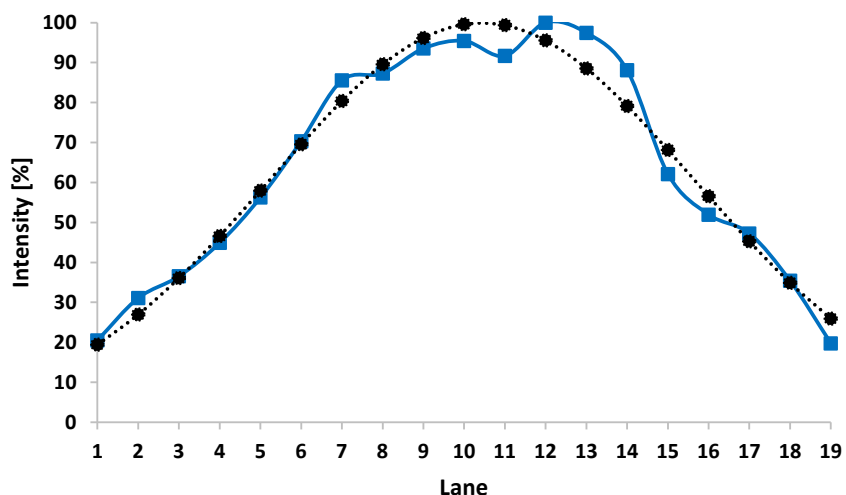


Figure 14: Lane intensity distribution of Coomassie-stained SDS PAGE.

The blue curve highlights the band intensity distribution in each lane from 1 to 19 in Figure 13, and the black line describes a perfect Gaussian standard distribution. The curve's fit is $R = 0.9850$.

To select possible candidates for MS analysis, a fraction with high overall protein abundance and a fraction with solely crosslinks containing fractions were chosen. The WB fraction T12 shows an intense Mos10-6His band compared to the neighboring lanes and includes many other proteins according to the SDS PAGE. For the crosslinking sample, fractions T21 to T23 were chosen for having a comparable strong WB crosslinking pattern and fewer background proteins present, as seen in the Coomassie staining. Lanes with crosslinked proteins were concentrated with an AMICON filter, and all selected lanes were subsequently applied to SDS PAGE.

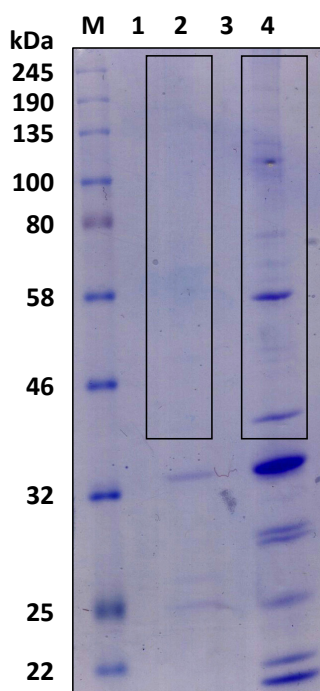


Figure 15: AEKTA purified samples for MS analysis.

Samples initially sent to MS analysis after AMICON filter concentration of AEKTA purified Mos10-6His. Lane 2 represents a sample in which no crosslink pattern was visible, whereas Lane 4 contains the samples which did show a crosslinking pattern on WB. Only the area enclosed in the black rectangles was used for MS analysis. **M:** NEB Color Pre-stained Protein Standard (11 – 245 kDa); **Lane 1:** empty; **Lane 2:** T21 - T23 (sample with crosslinking pattern); **Lane 3:** empty; **Lane 4:** T12 (neg. control).

The SDS PAGE in Figure 15 displays the gel sent to MS analysis to determine the proteins purified by the AEKTA gradient purification. Lane 2 contains the combined fractions T21 to T23 concentrated by AMICON filter, and lane 4 contains the control sample of fraction T12. The area outlined with the black rectangle was cut out and digested with trypsin before being analyzed by MS. According to the WB, the area of approximately 40 kDa and above was chosen since all crosslinks migrate slower in the gel than unlinked Mos10-6His at 34 kDa.

Although a Mos10-6His specific crosslinking pattern could be detected, the experiment proved insufficient in detecting specific interaction partners of Mos10-6His. Large numbers of proteins were identified in both fractions and although several proteins were exclusively present in one or the other fraction, no definite crosslinking partners could be established due to the overcrowded protein population.

Although gradient elution of Mos10-6His was able to separate the Mos10-6His crosslinks from the bulk of Mos10-6His and most other background proteins, it was still not pure enough for MS analysis. Therefore, the SILAC technique was introduced to solve the background problem.

3.1.3 AEKTA purification of His-tagged Mos10 with SILAC

The SILAC technique was introduced to achieve selective detection of crosslinks belonging to Mos10-6His in mass spectrometry. The method requires two cell cultures growing in different growth media containing either standard or stable, heavy amino acid isotopes for protein synthesis. The “heavy” medium was supplemented with arginine and lysine amino acids labeled with carbon-13 instead of carbon-12 atoms, introducing a mass shift in the resulting proteins, detectable by a mass spectrometer.

For the new purification approach, the yeast strain RKY2999 was designed, containing a c-terminal tagged Mos10-6His like the strain RKY 2889 used before but introduces an additional arginine auxotrophy (Δarg) for essential amino acid intake. The growth medium was switched from a complete medium (YPD) to a synthetic, minimal medium (YNB), supplemented with essential amino acids.

In the following experiment, the WT cell culture (RKY1558) was grown in YNB medium supplemented with a standard amino acid cocktail, whereas the Mos10-6His containing strain (RKY2999) grew in supplemented YNB with the isotopic (“heavy”) forms of arginine and lysine. In former Mos10-6His purification experiments, a single yeast cell culture was used, and output fractions were compared with each other. Since two different cultures were needed for the new approach, a novel crosslinking attempt was tested to ensure equal conditions for each culture. Usually, cells are being lysed first and incubated afterwards with the crosslinker,

which would likely result in an uneven outcome for each cell culture treated. The two cultures used for a single SILAC experiment were grown separately but combined after reaching exponential growth and treated equally to ensure homogenous lysing and crosslinking. But, crosslinking with mixed cell extracts may again lead to ambiguous results, since uncomplexed heavy Mos10-6His could again interact with unlabeled proteins and vice versa, leading to a promiscuous crosslinking. To avoid such effects, cultures were incubated with a crosslinker before being lysed and mixed. The standard crosslinking protocol and the new conditions were tested with the yeast strain RKY2999, YNB growth media, and crosslinking, monitored in Figure 16.

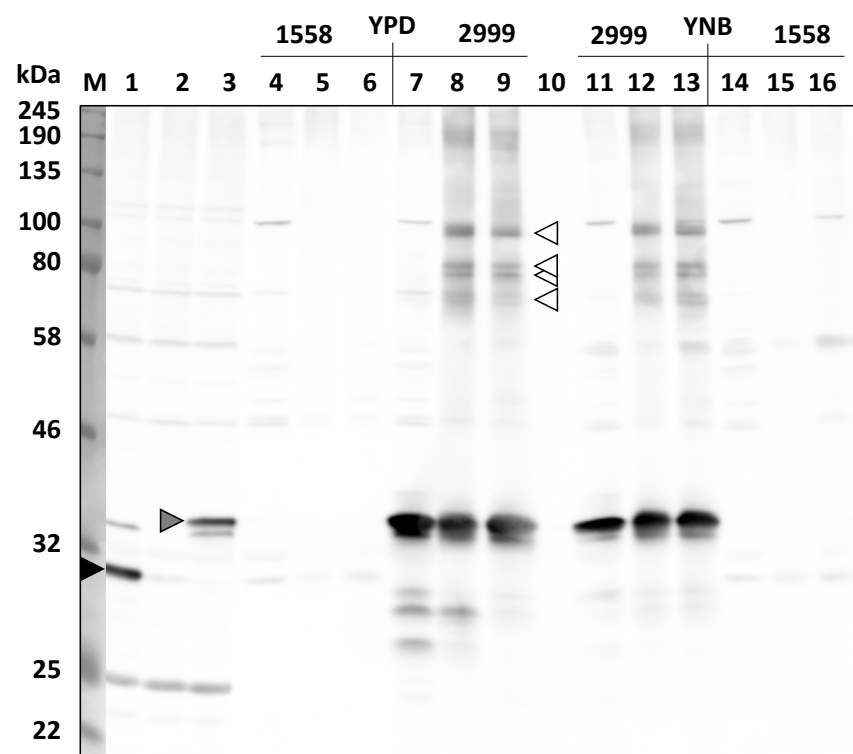


Figure 16: Validating crosslinker induced WB pattern of 6His tagged Mos10 with Arg auxotrophy in YNB.

IMAC purification of 6His tagged- (RKY2999, Δarg) and WT-Mos10 (RKY1558) in a batch experiment utilizing Ni^{2+} -NTA His-tag affinity beads. Cell cultures were grown in either YPD or YNB media. WB results by α -Mos10 antibodies incubation. **M**: NEB Color Pre-stained Protein Standard (11 - 245 kDa); **Lane 1**: WT extract; **Lane 2**: Δ^8 extract; **Lane 3**: RKY2999 extract; **Lane 4, 5 & 6**: RKY1558 in YPD w/o crosslinker, added crosslinker after lysing the cells, and before lysing the cells; **Lane 7, 8 & 9**: RKY2999 in YPD w/o crosslinker, added crosslinker after lysing the cells, and before lysing the cells; **Lane 10**: empty lane; **Lane 11, 12 & 13**: RKY2999 in YNB w/o crosslinker, added crosslinker after lysing the cells, and before lysing the cells; **Lane 14, 15 & 16**: RKY1558 in YPD w/o crosslinker, added crosslinker after lysing the cells, and before lysing the cells. Arrows: **Black**: WT-Mos10; **Grey**: Mos10-6His; **White**: Crosslinks. An OD = 1 was loaded.

The WB results in Figure 16 summarize the new conditions for SILAC purification. Lanes 1 to 3 contain the control samples in which native Mos10 is marked with a black arrow and Mos10-6His from the RKY2999 is marked with a grey arrow, migrating the same distance as seen before by the RKY2889 strain. Batch Ni-NTA purification of Mos10-6His in RKY2999 shows the same crosslinking pattern known from former experiments when incubated in YPD seen in lane 8 and indicated by the white arrows. Comparing lane 8 with lane 9, this crosslinking pattern does not change whether the crosslinker was applied initially to the cell culture before being lysed or after lysing the cells, proving that the hydrophobic crosslinker DSS is capable of passing by the cell membrane and crosslink proteins inside intact cells. It is also worth noticing that the crosslinks gained after lysing the cells seem not artificial but instead follow the same pattern as within viable cells. Comparing lanes 8 and 9 with lanes 12 and 13, the crosslinking pattern does not change, excluding growth media effects on crosslinking. None of the crosslinking patterns is visible in the WT RKY1558 strain regardless of growth medium or chronological order of crosslinker incubation.

AEKTA purification of crosslinked Mos10-6His was performed in YNB media using a SILAC based heavy RKY2999 culture and light RKY1558 cell culture. Cultures were grown until exponential phase, incubated with DSS crosslinker, and applied to AEKTA like mentioned before. The protocol of the gradient elution is monitored in Figure S 3, and for each fraction, a sample was collected for WB analysis incubated with α -Mos10 antibodies seen in Figure 17.

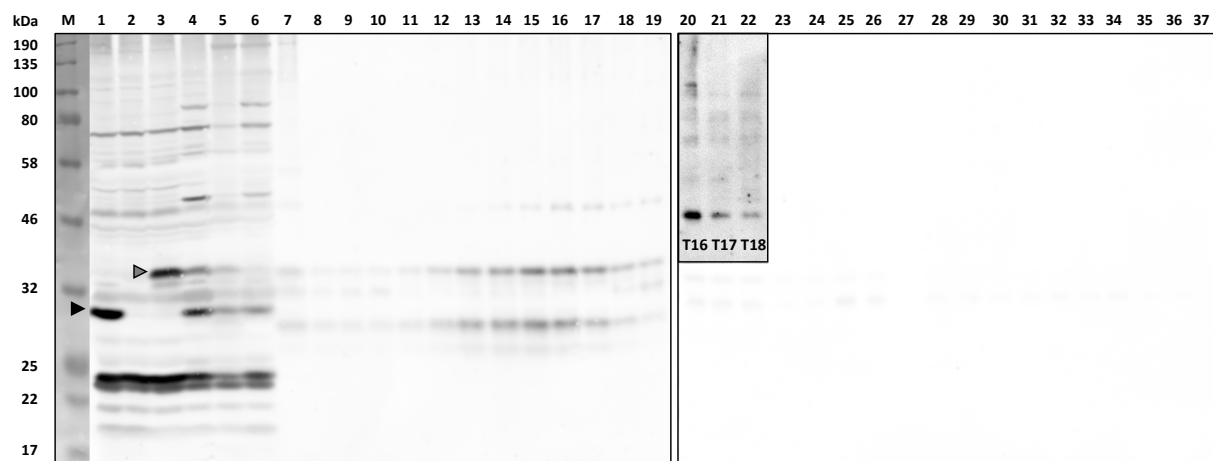


Figure 17: WB results of the Mos10-6His AEKTA purification using a Ni-NTA column with SILAC.

IMAC purification of 6His tagged-Mos10 (RKY2999) with the AEKTA system utilizing a Ni²⁺-NTA column. Visualization of the Mos10 characteristic crosslink WB pattern by α -Mos10 antibodies. **M**: NEB Color Pre-stained Protein Standard (11 - 245 kDa); **Lane 1**: WT extract; **Lane 2**: $\Delta 8$ extract; **Lane 3**: RKY2999 extract; **Lane 4**: Lysate debris **Lane 5**: Sample loaded on AEKTA; **Lane 6**: Flowthrough; **Lane 7**: T2 (wash fraction with 10 % Buffer B); **Lane 8-37**: AEKTA samples T4-T33 (OD = 1). Arrows: **Black**: WT-Mos10; **Grey**: Mos10-6His.

The WB results in Figure 17 illustrate the success of the gradient-based purification of Mos10-6His and associated crosslinks. In lane 5, two bands at around the 32 kDa marker standard are visible, representing native (black arrow) and tagged (grey arrow) Mos10 if compared to the control samples in lanes 1 to 3. In lane 6, the amount of native Mos10 in the flowthrough fraction equals the entire untagged Mos10 loaded onto the AEKTA from lane 5. In contrast, Mos10-6His was completely bound to the Ni-NTA beads and eluted in fractions T8 to T15 (110 – 230 mM imidazole), corresponding to lanes 12 to 19, peaking in fractions T11 and T12. The crosslinks of Mos10-6His eluted at fractions T16 to T18, highlighted by the black rectangle in lanes 21 to 23.

For MS analysis, lanes 21 to 23 were chosen since only these lanes contain crosslinking partner bands and have a relatively low abundance of background bands according to the Coomassie staining of the SDS PAGE seen in Figure S 3. The fractions were combined and concentrated by an AMICON filter before being directly sent to MS.

3.1.4 Improved batch purification by sedimentation and SILAC

Simultaneously with introducing the SILAC technique for gradient purification by the AEKTA system, an enhanced, SILAC based approach of batch purification has proven to be sufficient for detecting Mos10-6His interacting partners. Experience from preceding experiments has shown that recovery of Mos10-6His depends on centrifugation conditions. To make use of these findings, differential centrifugation was used to separate protein fractions based on their sedimentation rate. After cell lysis, the lysate was centrifuged at 500 g to remove cell debris. Then, after incubating the cell lysate with a DSS crosslinker, an additional purification step was added. Differential centrifugation was used to separate the cell content into a P13 fraction, containing the pellet gained after centrifugation at 13.000 g, a P100, and an S100 fraction by harvesting the pellet and supernatant after a 100.000 g spin, respectively. Each pellet fraction was adjusted to the same volume of the supernatant to ensure that equal portions of the total cell extract were loaded on the WB.

To test if the Mos10 crosslinks are membrane associated, the cell extracts were also treated with the detergent Triton X-100, which solubilizes membranes. If the crosslinks are membrane associated, they should be shifted to the soluble fractions by TX-100 treatment.

Pre-testing purification of crosslinked proteins in a batch experiment was done using WT (RKY1558), and the Mos10-6His strain (RKY2999) by differential centrifugation with and without Triton X-100 to gain P13, P100, and S100 fractions seen in Figure 18.

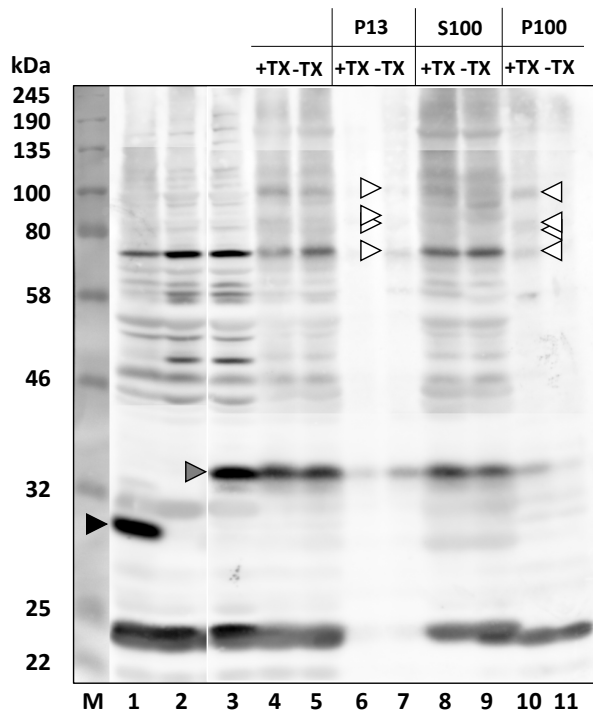


Figure 18: Crosslinking pattern subdivision by differential centrifugation.

Centrifugation experiment to separate the majority of proteins from the putative Mos10 crosslinking partner. **Lane 1:** WT extract; **Lane 2:** $\Delta 8$ extract; **Lane 3:** RKY2999 extract; **Lane 4:** Lysate with Triton X-100; **Lane 5:** Lysate w/o Triton X-100; **Lane 6:** P13 with Triton X-100; **Lane 7:** P13 w/o Triton X-100; **Lane 8:** S100 with Triton X-100; **Lane 9:** S100 w/o Triton X-100; **Lane 10:** P100 with Triton X-100; **Lane 11:** P100 w/o Triton X-100. Arrows: **Black:** Mos10; **Grey:** Mos10-6His; **White:** Crosslinks. Loaded: OD = 0.2.

Figure 18 shows the WB results of Mos10-6His crosslinker purification by differential centrifugation. The control lanes 1 to 3 highlight the migration distances of native and tagged Mos10 marked by a black and a grey arrow. Lanes 4 and 5 represent purification fractions of lysed and crosslinked cell content before being applied to differential centrifugation in which no difference in Triton X-100 treatment is visible. After spinning the samples at 13.000 g and 100.000 g, a different behavior towards sedimentation based on Triton X-100 induced effects became evident. Mos10-6His crosslinks highlighted by white arrows can be seen in lane 7 associated with the P13 fraction that was not treated with Triton X-100. In comparison, adding the detergent pushes the crosslinks into fraction P100. Of note, most proteins accumulate in fraction S100, containing most of Mos10-6His compared to fractions P13 and P100, regardless of Triton X-100 treatment. Whether crosslinked proteins are also present in lanes 8 and 9 cannot be answered, because the characteristic crosslinking pattern is masked by the high protein background in fraction S100. The crosslinking pattern, although clearly visible in P13 without Triton X-100 and in P100 treated with Triton X-100, appeared very faint compared to previous results.

To improve the specificity and yield of IMAC purification, the standard Ni^{2+} -NTA column was replaced by a Co^{2+} -NTA column, since cobalt has a lower affinity towards histidine than nickel. The idea was to reduce background bands and merely bind Mos10-6His to the column by the long and exposed histidine tail. In theory, the exchange of ions coordinated on the NTA beads should lead to a better signal-to-noise ratio regarding purifying and visualizing crosslinks on

the WB blot. Since no Co^{2+} -NTA columns were available for testing, self-packed Ni^{2+} -NTA columns were used and stripped by incubating the beads with a buffer solution containing EDTA that complexes the divalent ions and washes them off the column. The NTA beads were recharged with CoCl_2 and packed to gain a functional Co^{2+} -NTA column, whose purification capability was tested (Figure S 4). Since stripping and recharging of the beads was successful, Mos10-6His was crosslinked and purified over a Ni^{2+} -NTA column and a Co^{2+} -NTA column to compare their purification efficiency.

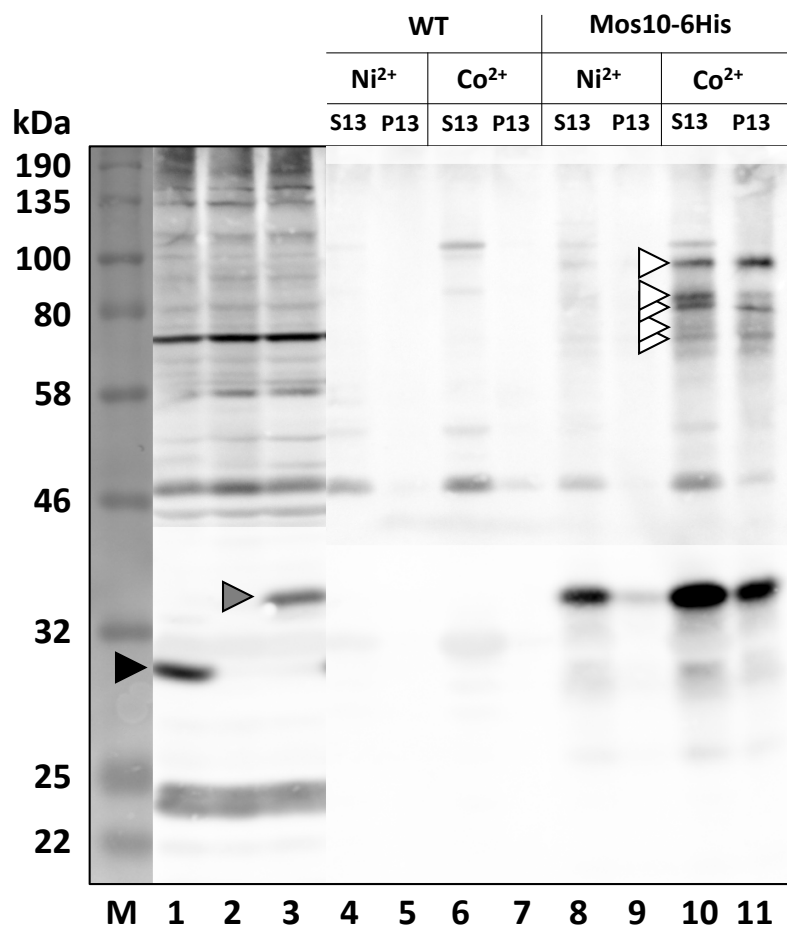


Figure 19: Mos10-6His purification with Ni^{2+} - and Co^{2+} -NTA column with P13 separation.

A differential centrifugation experiment was carried out to separate and highlight crosslinking partners into S13 and P13 fractions and compare a Ni^{2+} -NTA column with a recharged Co^{2+} -NTA column. **Lane 1:** WT extract; **Lane 2:** $\Delta 8$ extract; **Lane 3:** RKY2999 extract; **Lane 4:** WT S13 on Ni^{2+} -NTA; **Lane 5:** WT P13 on Ni^{2+} -NTA; **Lane 6:** WT S13 on Co^{2+} -NTA; **Lane 7:** WT P13 on Co^{2+} -NTA; **Lane 8:** Mos10-6His S13 on Ni^{2+} -NTA; **Lane 9:** Mos10-6His P13 on Ni^{2+} -NTA; **Lane 10:** Mos10-6His S13 on Co^{2+} -NTA; **Lane 11:** Mos10-6His P13 on Co^{2+} -NTA. Arrows: **Black:** Mos10; **Grey:** Mos10-6His; **White:** Crosslinks. Loaded: OD = 0.2.

The WB results in Figure 19 clearly illustrate the advantages of Co^{2+} -NTA over the beforehand used Ni^{2+} -NTA column. Compared to lane 8, where the Mos10-6His specific crosslinking pattern is barely visible, lane 10 shows much clearer western blot signals of the crosslinks and

also more than twice the amount of Mos10-6His was purified (band around 34 kDa). An additional band above 100 kDa complements the established crosslinking pattern, which is also visible in lane 6 and presumably corresponds to a Co^{2+} -NTA specific background band. Overall, the pre-treatment of the cell lysate with Triton X-100 and differential centrifugation seems suitable for Mos10-6His purification and fractionation.

For MS analysis, a SILAC based purification experiment of Mos10-6His (RKY2999) and RKY2998 (WT Δarg) was completed with the conditions worked out and applied on WB for further analysis (Figure S 5). Crosslinking patterns showing fractions were then used for MS analysis by being loaded and visualized on a Coomassie-stained SDS PAGE (Figure 20).

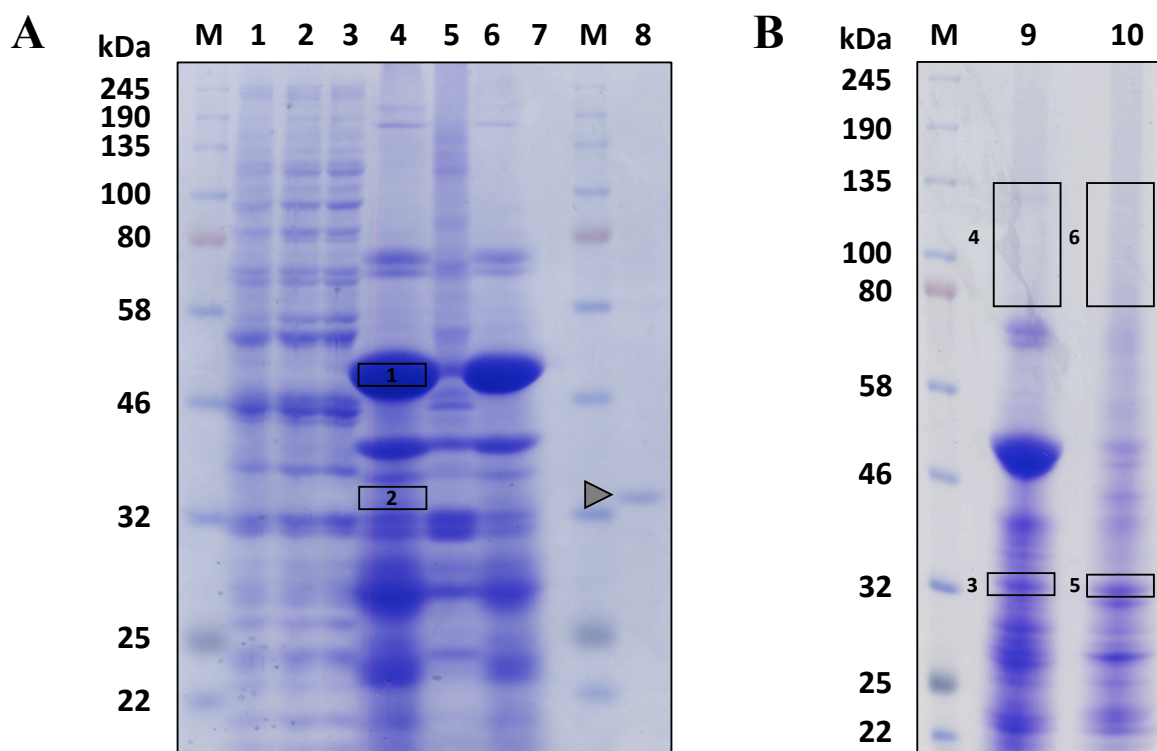


Figure 20: SILAC samples for MS analysis from batch Mos10-6His purification.

Coomassie-stained SDS PAGE gels containing samples sent to MS analysis. Mos10-6His batch purification with differential centrifugation was carried out with arginine auxotroph strains RKY2999 and RKY2998. SILAC technique was applied to both strains to visualize “light” and “heavy” media-induced protein enrichment in MS. Samples analyzed by MS are highlighted by the black rectangles and labeled with numbers for later identification. **(A)** The SDS PAGE gel shows the results of batch purification of proteins from a “light” (L) WT strain (RKY2998) and a “heavy” (H) Mos10-6His strain (RKY299). **(B)** The SDS PAGE gel shows the results of batch purification of proteins from a “heavy” (H) WT strain (RKY2998) and a “light” (L) Mos10-6His strain (RKY299). **M:** NEB Color Pre-stained Protein Standard (11 - 245 kDa); **Lane 1:** RKY2998 extract; **Lane 2:** $\Delta 8$ extract; **Lane 3:** RKY2999 extract; **Lane 4:** S13 of WT(L) and Mos10-6His(H); **Lane 5:** P13 of WT(L) and Mos10-6His(H); **Lane 6:** S13 of WT(L) and WT(H); **Lane 7:** empty; **Lane 8:** Mos10-6His purified from *E. coli*; **Lane 9:** S13 of WT(H) and Mos10-6His(L); **Lane 10:** P13 of WT(H) and Mos10-6His(L). Arrow: **Grey:** Mos10-6His.

Figure 20 shows the two SDS PAGE gels with the samples loaded for MS analysis. In gel A lane 4, the S13 sample eluted from the beads by boiling was loaded containing the WT strain RKY2998 grown in standard amino acid supplemented YNB and the Mos10-6His containing strain RKY2999, grown in YNB supplemented with heavy isotopes. Compared with the pellet fraction P13 in lane 5, an intensively stained band at around 50 kDa becomes visible (area 1). A second intriguing but fuzzy band at approximately 34 kDa seen in lane 4 (area 2) is migrating the same distance as Mos10-6His purified from an *E. coli* culture in lane 8. The two bands are also present in lane 6 containing the WT(H)-WT(L) fraction and should contain background proteins. Nevertheless, both band areas were marked for MS analysis to be further elucidated. Gel B lane 9 shows an overall comparable banding pattern to lane 4, indicating that switching isotopes does not lead to a visible difference on an SDS PAGE gel. The isotope exchange was also analyzed by WB, where no change in the crosslinking pattern was observable. The band at around 34 kDa seemed more prominent in gel B and was again analyzed to clarify if purified Mos10-6His can be seen on the Coomassie gel (areas 3 and 5). Lanes 9 and 10 show no visible bands at around the 70 to 100 kDa, where the crosslink bands are expected. To check the presence and the identity of the crosslinks, areas 4 and 6 were cut out and sent to MS, where area 6 in lane 10 serves as an additional control sample. Candidates from the MS results are summarized in Table S 5.

3.1.5 Purification of untagged Mos10

So far, a 6His tagged variant of Mos10 was used to find potential binding partners. C-terminal tagging of Mos10 compromises its function, thus it cannot be excluded that the crosslinking pattern observed is artificial. For this reason, it was of interest to see, whether the same crosslinking pattern could be obtained with native, untagged Mos10. To this end, Mos10 was immunoprecipitated from cell extracts with polyclonal anti-Mos10 antibodies.

Initially, α -Mos10 antibodies needed to be purified, since previous experiments had shown a large number of crossreacting bands on western blots with the crude antiserum. To produce a significant amount of Mos10 for affinity purification, an *E. coli* strain containing a plasmid for Mos10-6His expression induced by IPTG or galactose was used. Heterologous expression of Mos10-6His in *E. coli* was carried out by an autoinduction medium and samples were checked on an SDS PAGE by Coomassie staining (Figure 21).

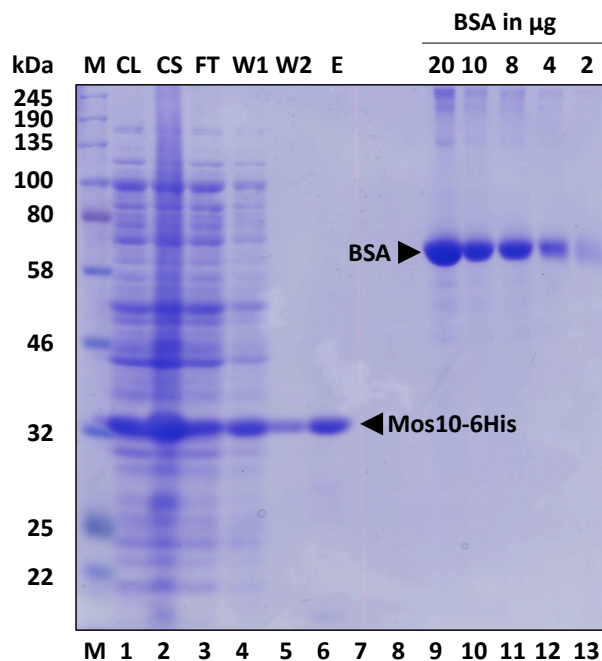


Figure 21: Autoinduction media used for Mos10-6His heterologous expression in *E. coli*.

For each step in the purification process, a sample was taken and applied on SDS PAGE. Band intensities were compared to a BSA standard ranging from 2 µg to 20 µg loaded on the gel. **M:** NEB Color Pre-stained Protein Standard (11 - 245 kDa); Purification fractions: **Lane 1:** CL = cell lysate; **Lane 2:** CS = cell supernatant; **Lane 3:** Ft = Flowthrough; **Lane 4 & 5:** W1/W2 = washing step 1 and 2; **Lane 6:** E = elution; **Lane 7 & 8:** empty; **Lane 9-13:** BSA standard from 20 µg to 2 µg.

E. coli cells were grown in autoinduction media at 25 °C to exclude the formation of inclusion bodies. The bacteria used glucose as the primary carbon source during growth, but switched to lactose after the glucose had vanished. Cleaving lactose molecules to glucose and galactose monomers activates the lac operon and starts gene expression of Mos10-6His inside the cell. After 24 h, the cells were harvested and lysed (CL) before being centrifuged to remove cell debris (CS). The supernatant was applied to a Ni-NTA column to allow the Mos10-6His proteins to bind and background proteins to flow through the column (WT). After washing the column twice with buffer (W1-2), proteins were eluted with 250 mM imidazole (E). According to the BSA standard, the cell culture contained 74 mg of Mos10-6His migrating to 34 kDa marked by a black arrow, of which 6 mg were eluted from the column. Although auto-induced heterologous expression of Mos10-6his seemed successful, only about 8 % of the input protein was purified during standard purification. Having dealt with this complication within previous purifications of Mos10-6His from yeast strains RKY2889 and RKY2999, the situation seems more severe when larger amounts of the protein are applied to the column. Various conditions were tested to improve Mos10-6His binding capacity and elution from the column to address this issue. Standard 1x PBS buffer was supplemented with Tween20 (T20), sodium chloride

(NaCl), glycerol (Gly), and β -mercaptoethanol (BME) to test improvements of Mos10-6His binding. The precise composition of each buffer subset is listed in Table S 3.

Table 20: Testing Buffer conditions according to Affi-Gel 15 manufactures guidelines.

Coupling Buffer	Affi-Gel 10 Coupling Efficiency (%)	Affi-Gel 15 Coupling Efficiency (%)	Coupling Buffer	Affi-Gel 15 Coupling Efficiency (%)
<i>Bovine Serum Albumin, pl 4.9</i>				
0.1 M MOPS, pH 7.5	14	80	0.1 M MOPS, pH7.4	75 %
0.1 M MOPS, pH 7.5 + 80 mM CaCl	90	—	0.1 M MOPS, pH7.4 + 0.3 M NaCl	44 %
0.1 M MOPS, pH 7.5 + 0.3 M NaCl	22	47		
0.1 M MES, pH 4.8	90	38		

The purified Mos10-6His protein was coupled to an Affi-Gel 15 affinity matrix. This matrix was chosen, because it has a higher coupling efficiency with acidic proteins like Mos10, which has an isoelectric point of 4.2. The coupling efficiency was calculated by comparing the protein amounts present before and after coupling. As Table 20 shows, the achieved coupling efficiencies are very close to the efficiencies specified by the manufacturer. Considering 44 % coupling efficiency, a maximal amount of 10 mg Mos10-6His can be bound to 1 ml of Aff-Gel 15 matrix.

The Mos10-6His coupled Affi-Gel 15 was then incubated with 5 ml of crude α -Mos10 antibody serum. After incubation, the bound antibodies were eluted from the beads and dialyzed for further use. The purity of the antibody was tested by immunoprecipitation. The different antibody preparations were added to a yeast cell extract and the immunoprecipitated proteins were then examined by western blotting (Figure 23).

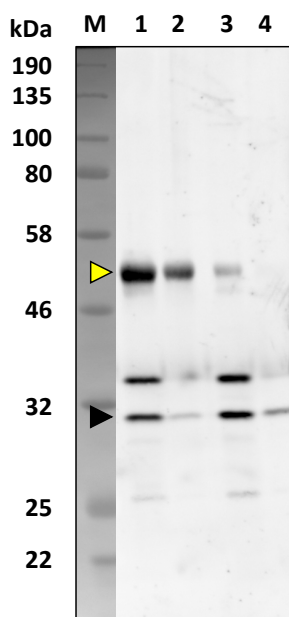


Figure 22: Testing antibody sera against native Mos10 extract.

Various fractions were collected and tested during antibody purification against a WT (RKY1558) extract to compare immunoprecipitation efficiency and purity. Proteins bound to the beads were applied on WB to visualize the antibody purification effect. A complete analysis of antibody purification can be seen in the WB in

. **M:** NEB Color Pre-stained Protein Standard (11 - 245 kDa); Antibody fractions: **Lane 1:** Crude antibody serum; **Lane 2:** Antibody flowthrough (unbound antibodies to Affi-Gel 15; **Lane 3:** Eluted antibodies before dialyzing; **Lane 4:** Dialyzed antibodies. Arrow: **Yellow:** Antibody; **Black:** Mos10.

As seen from the WB result incubated with crude α -Mos10 antibody serum, the process of antibody purification successfully reduced background bands from lanes 1 to 4. Lane 4, containing the dialyzed antibodies, shows only the Mos10 band at 30 kDa and a faint band at 34 kDa. Migrating at around 50 kDa, the antibody band marked by a yellow arrow also faints from lanes 1 to 4, indicating that most of the antibodies in the crude serum were washed off. It is worth noticing that the Mos10 color band intensity is reduced by about 50 % by comparing lane 1 to lane 4 due to a loss of antibodies also detecting the protein.

To test whether the purified α -Mos10 antibody is suitable for specifically detecting Mos10 crosslinks, Mos10 was immunoprecipitated from cell extracts of the wildtype strain RKY1558 and the $\Delta mos10$ strain RKY2892 treated with the non-cleavable crosslinker DSS (Figure 24).

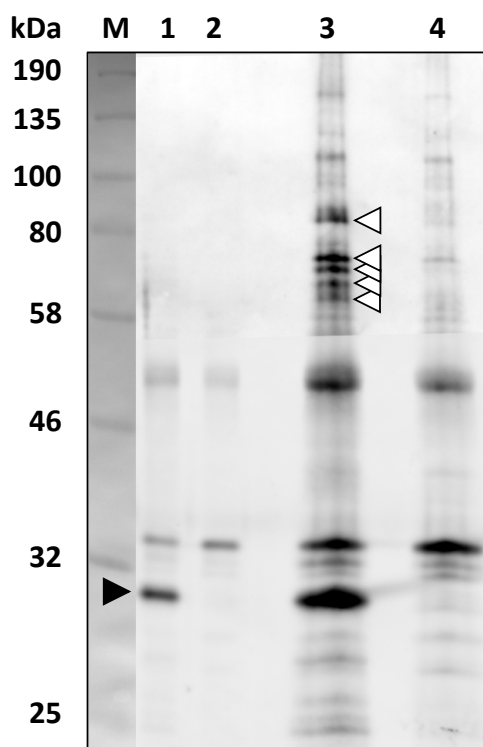


Figure 23: Crosslinking pattern of native Mos10 by α -Mos10 immunoprecipitation.

Yeast strains RKY1558 and RKY2892 were grown until the exponential phase, and an input sample was taken after cell lysing. Regular crosslinking was carried out to visualize the native Mos10 crosslinking pattern with $\Delta mos10$ as a control sample. **M:** NEB Color Pre-stained Protein Standard (11 - 245 kDa); Antibody fractions: **Lane 1:** RKY1558 input; **Lane 2:** RKY2892 input; **Lane 3:** crosslinked RKY1558; **Lane 4:** crosslinked RKY2892. Arrows: **Black:** Mos10; **White:** crosslinks. OD = 0.2 loaded.

The WB result illustrates the detection of Mos10 in lane 1 at approximately 30 kDa marked by a black arrow, since the band is lacking in lane 2 containing the *MOS10* deleted strain. Both lanes have an additional background band at 34 kDa and roughly 50 kDa. Additional bands at 58 kDa and above were detected after immunoprecipitation of proteins from the wildtype strain. With the immunoprecipitate from the *MOS10* deletion strain, a number of faint background bands were observed, but the pronounced bands seen with the wildtype extract in lane 3 were missing. Therefore, it can be concluded that the bands seen in lane 3 correspond to specific Mos10 crosslink bands. The banding pattern with native Mos10 resembles the banding pattern observed with Mos10-6His.

Visualization of the crosslinking pattern on an SDS PAGE gel by Coomassie and silver staining was attempted, seen in Figure S 7. A fuzzy band can be seen in the WT lanes at 30 kDa in both gels, not visible in the Mos10 deletion strain. Due to the small amount of crosslinked proteins present in the samples, no bands were directly associated with one of the crosslink bands. For MS analysis Mos10 was immunoprecipitated from crosslinked cell extracts prepared from a 1-liter culture of the wildtype RKY1558. The gels used and the area cut out can be seen in Figure S 8.

3.1.6 The first set of potential Mos10 interacting partners

In the first set of experiments, Mos10-6His was purified from crosslinked cell extracts with Ni-NTA beads. With the SILAC technique, potential Mos10-6His interaction partners could be distinguished from unspecific background proteins. Various experiments were performed, in which the proteins from the Mos10-6His strain were either labeled with heavy (H) or light (L) isotopes, while the corresponding control strain, expressing only untagged Mos10, was labeled with the opposite isotopes. For each protein detected by MS the ratio of heavy to light isotopes (H/L or L/H, depending on the experiment) was determined. Only those proteins were considered as potential interaction partners that were at least 2-fold enriched for the isotopes used to label Mos10-6His. From these experiments several candidates, whose molecular weight lies in the range of the observed Mos10-6His crosslink bands, were selected (Table 21).

Table 21: Selected crosslinking partners of Mos10.

Gene Symbol	MW
Ald5	56,692
Eft1	93,279
Get3	39,337
Pab1	64,335
Pre6	28,439
Ssc1	63,248
Vps68	20,101

The sizes of the unknown crosslinked proteins were calculated from the migration distance on SDS PAGE gels compared to a molecular weight marker (Figure S 9). The results of the molecular weight determination are summarized in Table S 4.

To verify the interactions, the potential interaction partners were C-terminally tagged with a 13myc affinity tag at their chromosomal loci in the Mos10-His strain RKY2889. Co-

immunoprecipitation (Co-IP) experiments were performed with cell extracts treated with the cleavable crosslinker DSP. The crosslinked proteins can be reversibly detached from the bait protein by DTT treatment to break the disulfide bond present in DSP.

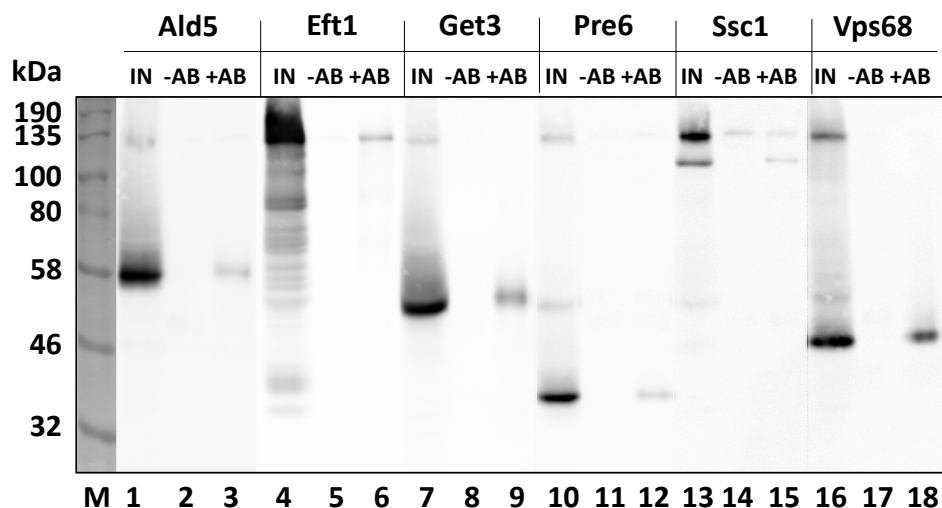


Figure 24: Purification of potential Mos10-6His interacting partners by α -13myc immunoprecipitation.

Results of the α -13myc IP is shown in triplets for each protein investigated: **IN** = input sample; **-AB** = no antibody control, and **+AB** = the antibody purified sample. **M**: NEB Color Pre-stained Protein Standard (11 – 245 kDa). Loaded: IN: OD = 0.2. +/-AB: OD = 1.

The WB results of α -13myc immunoprecipitation of the six candidates Ald5, Eft1, Get3, Pre6, Ssc1, and Vps68 tagged with 13myc are summarized in Figure 24 (Pab1 tagging appears to be lethal, this strain could not be obtained). Although individual protein tagging was confirmed by PCR analysis, validating the implementation of the cassette into the yeast strains genome, the sizes of the detected proteins on the western blots, did not always correspond to the predicted sizes. For each protein MW listed in Table 21, an additional 20 kDa must be added due to the 13myc tag. One reason for the observed discrepancy could be a variable number of myc coding sequences appended to the respective protein coding genes. The variability appears to arise from slippage of the polymerase during PCR amplification of the repetitive myc sequences of the insertion cassette. Ald5, for instance, is 56 kDa large, and the WB reveals a band in lane 1 at the approximately 56 kDa location, indicating that maybe just a single myc-tag is attached to the protein. Pre6 in lane 10, mainly runs at 35 kDa comparable to the native protein of size 28 kDa, and the expected full-size variant is just indicated by a faint band at 50 kDa. In this case, the smaller size of the main band could be the result of proteolysis. It is worth noting that despite the wrong protein size, both proteins were immunoprecipitated with α -myc (lanes 3 and 12) indicated by a band not visible in the fraction lacking antibody. Also, Get3 (lanes 7 and 9)

and Vps68 (lanes 16 and 18) could be successfully immunoprecipitated. In both cases, the most intensively staining band is in the expected range of the tagged protein variant. Eft1 (lane 4) shows a main band around 135 kDa (close to the expected 113 kDa) and many additional degradation bands. Ssc1-myc migrates at 110 kDa, larger than the expected size of 83 kDa. Additionally, all input lanes contain an additional background band at around 130 kDa, which is partially co-purified along with the presumably correct sized band seen in the individual +AB fraction.

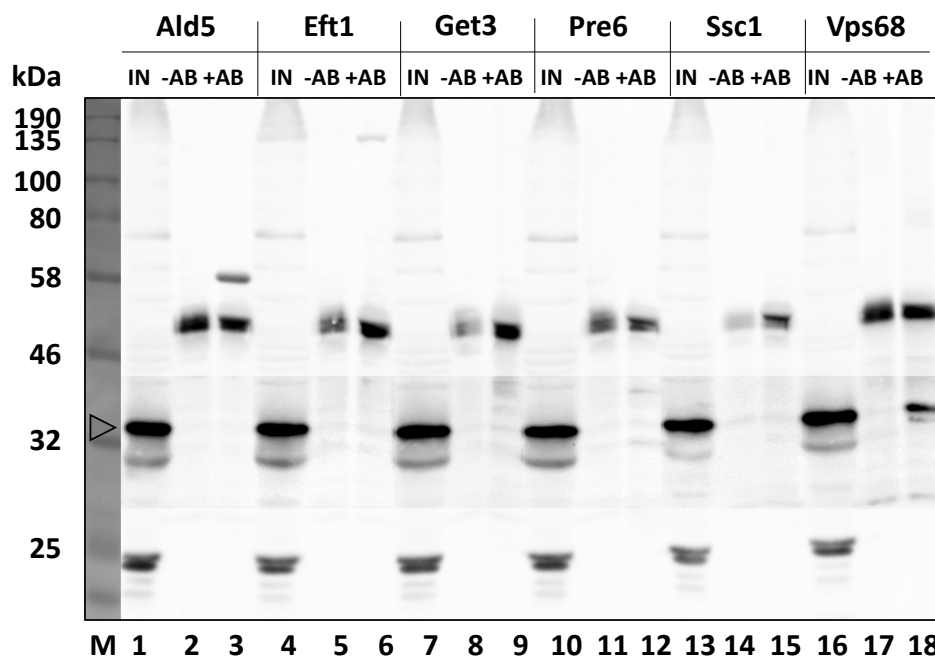


Figure 25: Identification of co-immunoprecipitated Mos10-6His by potential interacting partners.

Results of the α -Mos10 incubated blot showing Mos10-6His Co-IP by the six proteins affinity purified. **IN** = input sample; **-AB** = no antibody control, and **+AB** = the antibody purified sample. **M**: NEB Color Pre-stained Protein Standard (11 - 245 kDa). Arrow: **Grey**: Mos10-6His. Loaded: IN: OD = 0.2. +/-AB: OD = 5.

The immunoprecipitates were now examined for co-immunoprecipitation of Mos10-6His by western blotting with anti-Mos10 antibodies (Figure 25). All input samples show a prominent band at 34 kDa marked by a grey arrow indicating equal amounts of Mos10-6His harvested from cell culture. A successful Co-IP is indicated by a Mos10-6His band in the +AB lane. Only in case of Vps68 (lane 18), co-immunoprecipitation of Mos10-6His could be observed. For the other five proteins no co-IP was detected. From this it can be concluded that Vps68 is a true interaction partner of Mos10.

It should be noted that the established crosslinking pattern of Mos10-6His does not change by introducing a 13myc tag to the six selected proteins, which changes the mobility of the proteins (Figure 26). Thus, none of the examined proteins is part of the observed Mos10-6His

crosslinking pattern. Also, expression of Mos10-6His is not affected by the expression of the myc-tagged proteins variants.

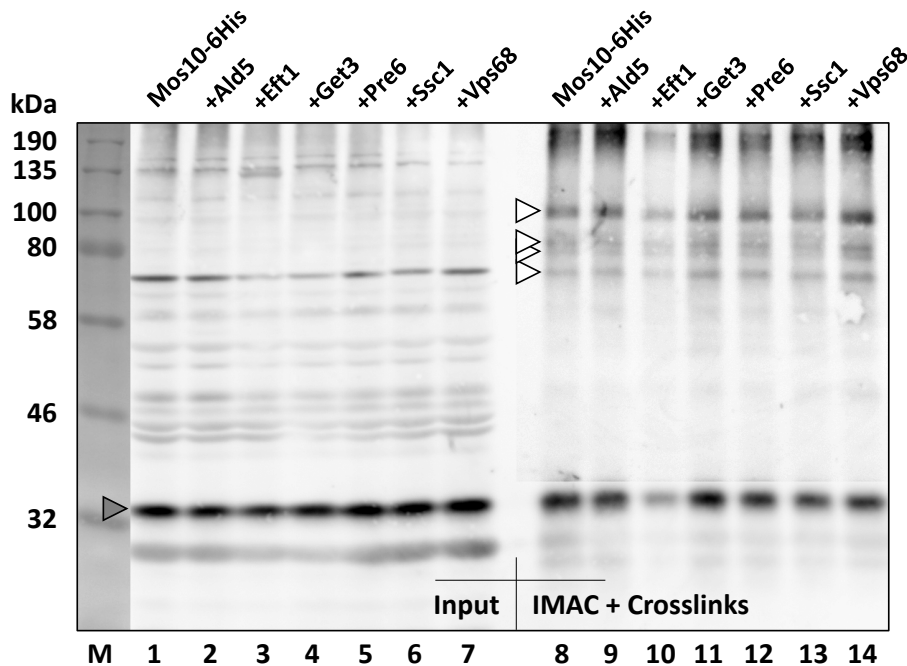


Figure 26: Crosslinking pattern of crosslinked Mos10-6His and 13myc tagged interacting partners.

Mos10-6His and Mos10-6His + 13myc tagged putative interacting partner strains were incubated with crosslinker DSS and IMAC purified to identify changes in the crosslinking pattern of Mos10-6His. WB was incubated with α -Mos10 antibodies. **M:** NEB Color Pre-stained Protein Standard (11 - 245 kDa); **Lanes 1 - 7:** IN samples of Mos10-6His +Ald5, Eft1, Get3, Pre6, Ssc1, or Vps68 (OD = 0.2); **Lanes 8 - 14** IMAC purified samples of Mos10-6His +Ald5, Eft1, Get3, Pre6, Ssc1, or Vps68 (OD = 1). Arrows: **Grey:** Mos10-6His; **White:** Crosslinks.

3.1.7 Tagged Mos10 purification via IP

The next method used for detecting interacting partners of Mos10 was the purification of tagged Mos10 variants via immunoprecipitation. Commercial antibodies were used, targeting a distinct tag attached to the Mos10 C-terminus. In a tag evaluation experiment, Mos10 was C-terminally tagged with -3HA (RKY3209), -sfGFP (RKY3216), -Protein A (RKY1823) and -13myc (RKY1452), respectively and compared to the familiar -6His (RKY2889) tag. Cells were grown to exponential phase, lysed, and crosslinked with DSS before each tagged variant's affinity purification was carried out. For the -3HA, -sfGFP, and -13myc tag, the crosslinked protein was affinity purified by immunoprecipitation using tag-specific antibodies (α -3HA, α -GFP, and α -13myc). For the purification of 6His tagged protein, a Ni-NTA column was used utilizing IMAC. For the purification of protein A tagged Mos10, IgG beads were used to pull out the target protein with crosslinks. All purifications were also applied to a WT control (RKY1558), and the results are summarized in Figure 27.

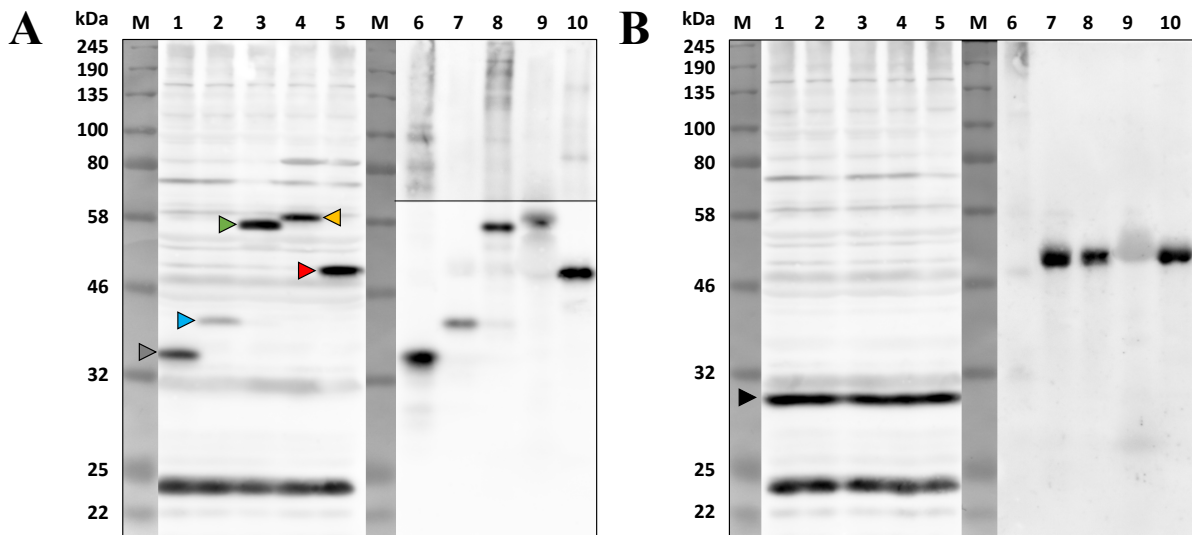


Figure 27: Evaluating Mos10 affinity tags for immunoprecipitation compared to IMAC.

(A) Purification of crosslinked Mos10 by various affinity tags, visualized on a WB with α -Mos10 antibodies. Each Mos10 construct is marked with an arrow in the input lanes 1-5, and the associated crosslinks are blotted in lanes 6-10. **M:** NEB Color Pre-stained Protein Standard (11 - 245 kDa); Antibody fractions: **Lane 1:** IN RKY2889; **Lane 2:** IN RKY3209; **Lane 3:** IN RKY3216; **Lane 4:** IN RKY1823. **Lane 5:** IN RKY1452; **Lane 6:** crosslinked RKY2889; **Lane 7:** crosslinked RKY3209; **Lane 8:** crosslinked RKY3216; **Lane 9:** crosslinked RKY1823; **Lane 10:** crosslinked RKY1452. Arrows: **Grey:** Mos10-6His; **Blue:** Mos10-3HA; **Green:** Mos10-sfGFP; **Orange:** Mos10-Protein A; **Red:** Mos10-13myc. OD = 0.2 loaded. (B) Purification of native Mos10 by various affinity tag-specific techniques for background bands detection visualized on a WB with α -Mos10 antibodies. **Lanes 1-5:** IN RKY1558; **Lanes 6-10:** crosslinked RKY1558. Arrow: **Black:** Mos10.

On the WB **A** in Figure 27, the input samples of each purification technique are blotted, and a colored arrow highlights each Mos10 tag variant. All tagged variants were expressed, Mos10-3HA had the lowest expression level, all other variants were expressed to equal levels. In lanes 6 to 10, the immunoprecipitated proteins are shown. Lane 6 represents the familiar crosslink pattern between 70 and 100 kDa, obtained by purifying Mos10-6His with Ni-NTA. Only the Mos10-sfGFP tagged version had a comparable crosslinking pattern (lane 8) in terms of the proteins sizes and band intensity. For the Mos10-3HA, Mos10-Protein A, and Mos10-13myc, no clear crosslinking pattern could be seen. In a later experiment, in which the effect of cell density on crosslinking efficiency was examined, the Mos10-13myc variant did show a crosslinking pattern (Figure S 10).

In comparison, WB **B** shows the results for the RKY1558 strain when the same purification techniques are applied to native Mos10. Lanes 1 – 5 contain the input samples in which a Mos10 band at 30 kDa and some background bands are visible, not differing between lanes. The immunoprecipitated crosslinked samples in lanes 6 to 10 contain no bands similar to the

crosslinking pattern seen in WB A. In lanes 7, 8, and 10, an intensively stained band at approximately 50 kDa is visible and belongs to the antibody used since only those lanes contained IP purified samples.

For a new IP purification experiment, the Mos10-sfGFP variant was chosen for showing a comparable crosslinking pattern to the one obtained by Mos10-6His. Another advantage of Mos10-sfGFP is the ability to visualize the tagged protein by fluorescence microscopy described later. Mos10-sfGFP IP by α -GFP antibodies was done utilizing the SILAC technique by growing strain RKY2998 in a “light” medium, and RKY3216 in “heavy” YNB supplemented medium. Cell cultures were grown until the exponential phase, harvested, and lysed before being crosslinked with DSS. Due to limitations in the availability of antibody, the cell extracts were incubated with 100 μ l α -GFP, which is less than optimal as judged from the batch experiment, but should still be sufficient for immunoprecipitating tagged Mos10 in detectable amounts for MS analysis. The largest part of the immunoprecipitate was run on an SDS PAGE gel, which was silver stained. A small part was analyzed by western blotting (Figure 28).

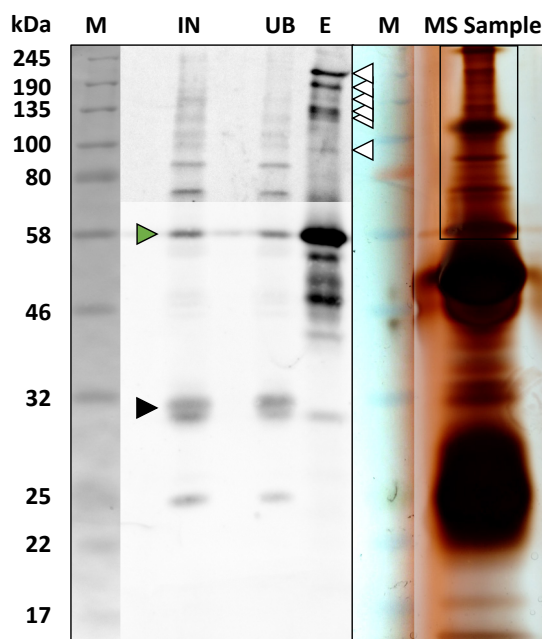


Figure 28: Purification of Mos10-sfGFP by α -GFP antibodies on WB and silver-stained gel for MS.

Summary of the Mos10-sfGFP purification process on WB incubated by α -Mos10 antibodies. The input fraction (**IN**) and the unbound (**UB**) fraction of proteins not bound to the protein A beads are loaded. Fraction **E** contains the proteins boiled of the beads. **M**: NEB Color Pre-stained Protein Standard (11 - 245 kDa). Arrows: **Black**: Mos10; **Green**: Mos10-sfGFP, and **White**: Crosslinks. For MS analysis, the area of 58 kDa and upwards of the silver-stained gel was used, indicated by the black rectangle.

The results of the immunoprecipitation purification of Mos10-sfGFP in Figure 28 reveal that almost equal amounts of native and tagged Mos10 were harvested from the cell cultures indicated by the black and green arrows. The unbound sample loaded shows that most Mos10 was not bound to the column and is therefore absent in the elution fraction. In comparison, Mos10-sfGFP was not fully recovered by the protein A beads and a substantial fraction got lost

in the flowthrough. Nevertheless, a significant amount of Mos10-sfGFP was purified by the α -GFP antibodies indicated by the intense band in the elution lane. The eluted crosslinking pattern of Mos10-sfGFP is highlighted by white arrows in the elution lane and was tried to be identified on the silver-stained SDS PAGE. Although distinct bands can be seen in the silver-stained gel, the indicated pattern on the WB is hard to discern on the silver-stained gel, which is why for MS analysis, the entire area between 245 and 58 kDa was sent for analysis. Mos10 interacting candidates from the MS analysis with a H/L ratio larger than 2 are listed in Table 22. The results from all purifications are summarized in Table S 5.

3.1.8 The second set of potential Mos10 interacting partners

The second set of candidates investigated for being associated with Mos10 contains the proteins listed in Table 22, extended by Ald5, Pre6, and Vps68 from the IP experiment in Table 21 for further testing.

Table 22: Extended set of Mos10 crosslinking partners.

Gene Symbol	MW	CRAPome
Exo84	85,537	1 / 17
Leu1	85,793	1 / 17
Oac1	35,153	/ 17
Tps1	56,147	/ 17
Dnf2	182,62	1 / 17
Ygr130c	92,697	/ 17
Yck2	62,078	1/ 17
Pan1	160,27	1/ 17
Tom71	71,855	/ 17
Cog8	69,828	1/ 17
Mss1	58,351	/ 17
Ptr2	68,043	/ 17
Mnn5	67,204	1/ 17
Ald5	56,692	1/ 17
Pre6	28,439	2/ 17
Vps68	20,101	/ 17

Besides having the criteria of being strongly enriched in one of the SILAC fractions, a CRAPome comparison sorted out more candidates. The Contaminant Repository for Affinity Purification (CRAPome) is an extensive proteomics database describing nonspecifically enriched proteins in various purification experiments supported by the repository of negative

control purifications (Mellacheruvu et al., 2013). The individual protein score is set between 0/17 for proteins not found by MS to be unspecifically co-purified and up to 17/17 for proteins always found by MS regardless of the purification method applied. Putative Mos10 interacting candidates were chosen based on their MW, SILAC enrichment, and low CRAPome score of 0 or 1, besides Pre6 from previous experiments with a CRAPome score of 2/17. Candidates with a high CRAPome score were not considered to be putative crosslink partners, The chosen candidates were 13myc tagged in the WT strain RKY1558 and purified by immunoprecipitation with α -myc antibodies (Figure 29)

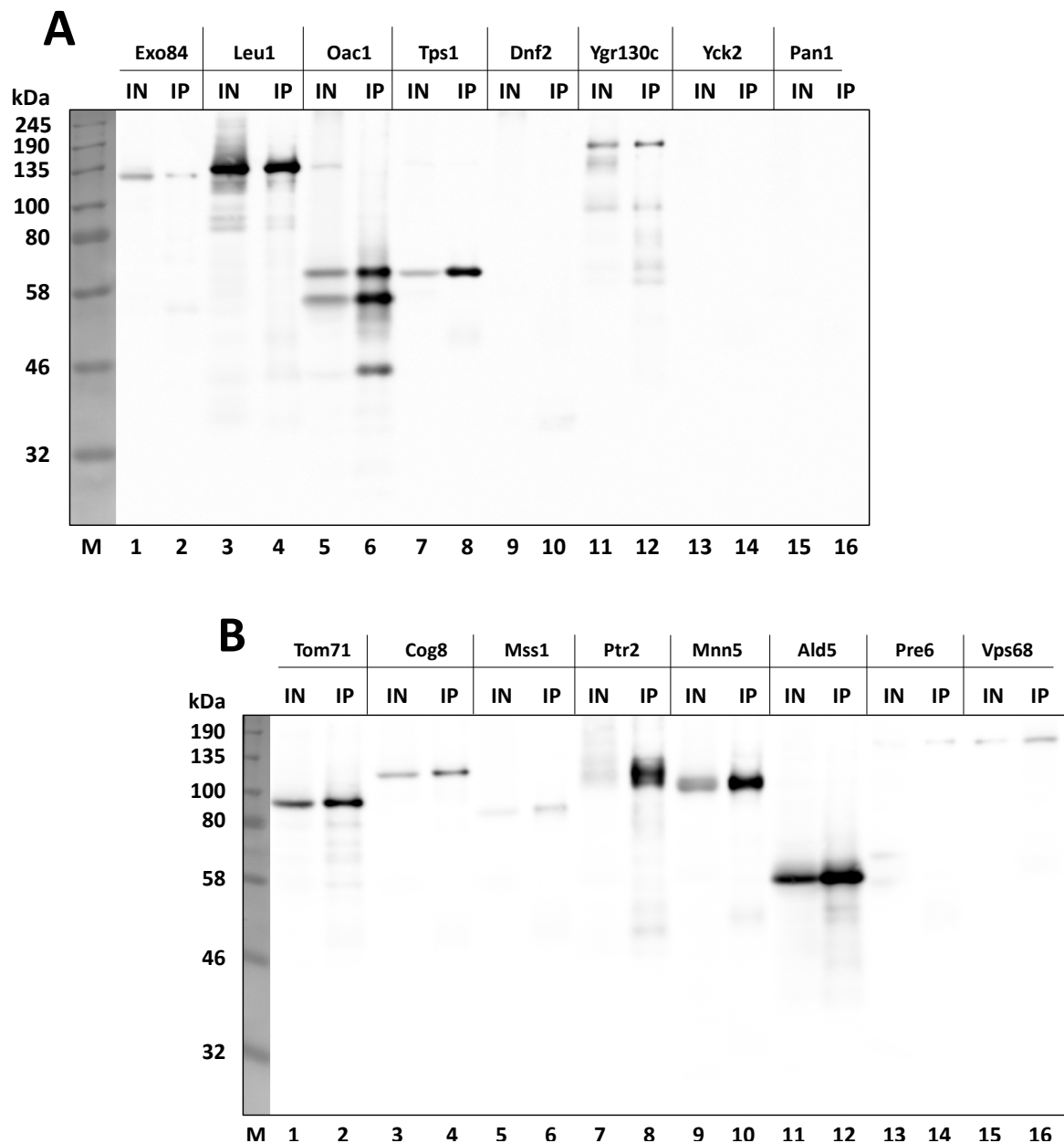


Figure 29: Purification of potential Mos10 interacting partners by α -13myc immunoprecipitation.

Results of the α -13myc blot showing α -13myc IP in doublets for each protein: **IN** = input samples; **IP** = the purified samples. **M**: NEB Color Pre-stained Protein Standard (11 – 245 kDa). Loaded: IN: OD = 0.2; IP: OD = 1.

Although each mutant had a correctly inserted transformation cassette confirmed by PCR, not all 13myc tagged proteins were expressed. A negative result was obtained for Dnf2, Yck2, Pan1, Pre6, and Vps68 (which worked before). Most likely, the integrated tag sequences were not in-frame with the tagged genes. These constructs must be reexamined in further experiments. In contrast, each expressed tagged variant of the other proteins showed a band in the input lanes and was also purified via immunoprecipitation seen in the IP lanes. Immunoprecipitation seemed sufficient to check for crosslinked Mos10 co-purified with the primary IP. But, unfortunately, no Mos10 co-IP could be detected with any to the constructs.

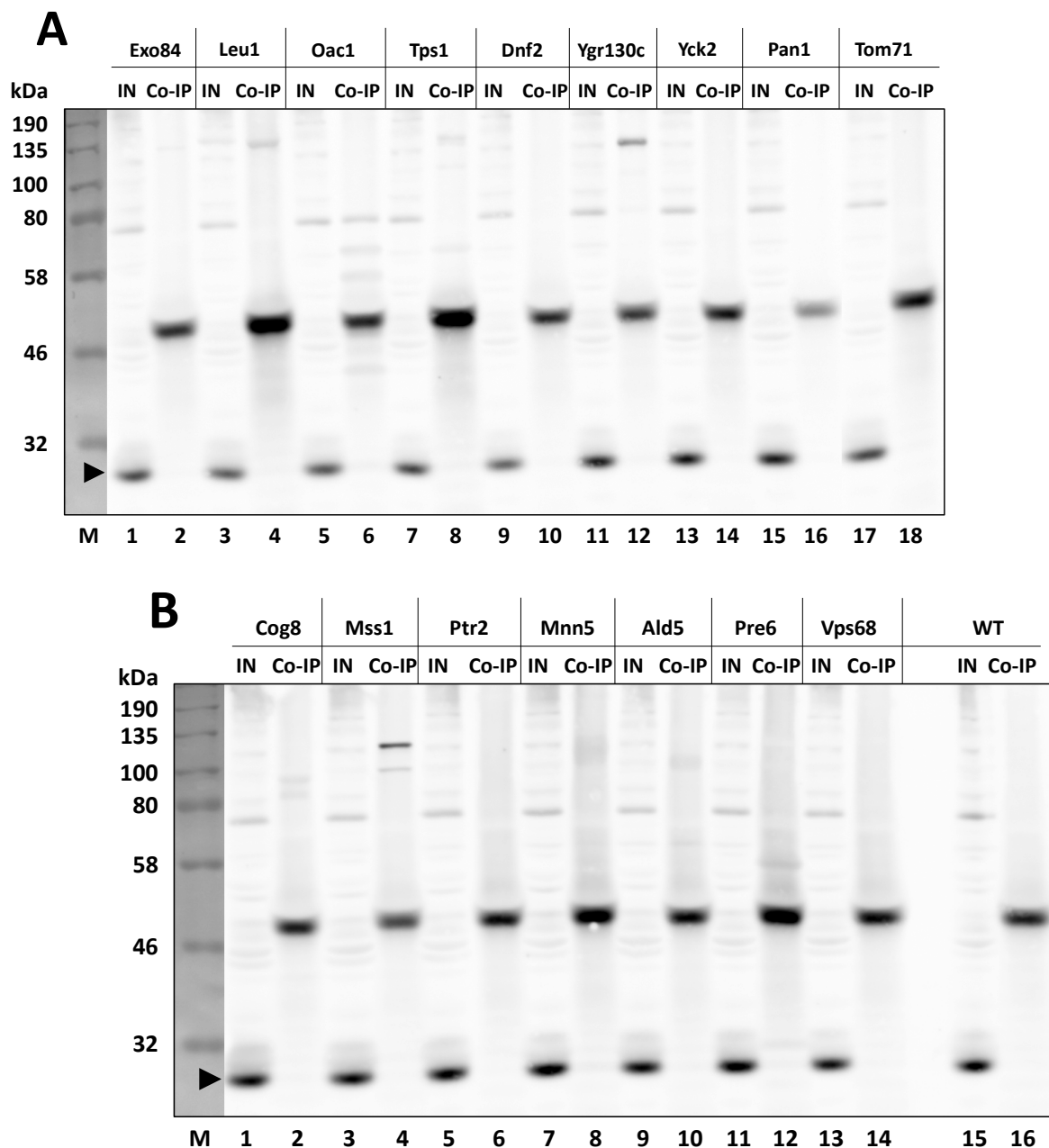


Figure 30: Identification of co-immunoprecipitated Mos10 by potential interacting partners.

Results of the α -Mos10 blot showing α -13myc Co-IP. IN = input sample; Co-IP = purified sample. M: NEB Color Pre-stained Protein Standard (11 - 245 kDa). Arrow: **Black**: Mos10. Loaded: IN: OD = 0.2; Co-IP: OD = 5.

The same experiment was also performed with different tags. The sixteen candidates were tagged with GFP and sfGFP in the WT RKY1558 strain for immunoprecipitation with α -GFP antibody, offering the advantage that the proteins can be additionally investigated by fluorescence microscopy due to the green fluorescence tag. The results with the GFP tag are summarized in Figure S 11 and the results with the sfGFP tag in Figure S 12.

Summarizing the IP and Co-IP experiment results, the most promising candidate for an interacting partner of Mos10 happens to be Vps68. With the Mos10-6His tagged variant, a clear signal could be detected in the Co-IP WB of Vps68-13myc, and at least a very faint signal was detectable in the Co-IP Blot of Vps68-sfGFP for native Mos10.

3.1.9 ESCRT-III interacting partners of Mos10

Besides investigating the new putative interacting partners of Mos10 listed in Table 21 and Table 22, MS analysis revealed a close interaction of Mos10 with the ESCRT-III subunits Did2, Snf7, Vps2, and Vps24. This supports the view that Mos10 is a bona fide member of the ESCRT-III complex. It is tempting to speculate that ESCRT-III subunits could be part of the observed crosslinking pattern of Mos10-6His. Therefore, it was tested whether deletion of individual ESCRT-III proteins alters the crosslinking pattern. For this purpose, the strain RKY2889 with the Mos10-6His affinity tag was mutated by inserting $\Delta chm7$ (RKY3228), $\Delta did2$ (RKY2788), $\Delta ist1$ (RKY2789), $\Delta snf7$ (RKY2790), $\Delta vps2$ (RKY2841), $\Delta vps20$ (RKY2893), and $\Delta vps24$ (RKY2830) gene deletions. Former experiments revealed partial cross interactions of crude ESCRT-III antibody sera, thus identifying more than just the target ESCRT-III protein. For this reason, Mos10-6His purification was carried out by Ni-NTA affinity purification rather than IP, preventing antibody-related cross purification and allowing a better comparison to the experiment shown in Figure 26. For comparison, a WT strain (RKY1558) and the standard IMAC strain RKY2889 with Mos10-6His were used (Figure 31). Each vps single deletion strain, the WT strain RKY1558, and the Mos10-6His strain RKY2889 were incubated with DSS crosslinker and subjected to Ni-NTA affinity purification. Each purification sample was then blotted and incubated with any of the eight ESCRT-III members specific crude antibody sera (Figure S 13 to Figure S 21). To compare the Mos10-6His crosslink patterns in the different deletion strains, the α -Mos10 blots were assembled into one picture and aligned with respect to the Mos10-6His band (Figure 31). In lane 2, the RKY2889 Mos10-6His strain is loaded, showing the familiar crosslinking pattern between 100 kDa and 70 kDa, not present in the control lane with WT Mos10, indicated by a black arrow. It can be seen that the crosslinking pattern is not altered by introducing a $\Delta chm7$, $\Delta did2$, and $\Delta ist1$ deletion, thus none

of the deleted proteins is part of the visible crosslinks. With the deletion of the other four ESCRT-III members, an altered of Mos10-6His pattern was observed. This clearly shows that the Mos10-6His crosslinking pattern is dependent on a functional ESCRT-III complex. Since the common pattern of Mos10-6His crosslinks is lost in this second class of ESCRT-III mutants, the contribution of these proteins to the crosslink pattern cannot be assessed.

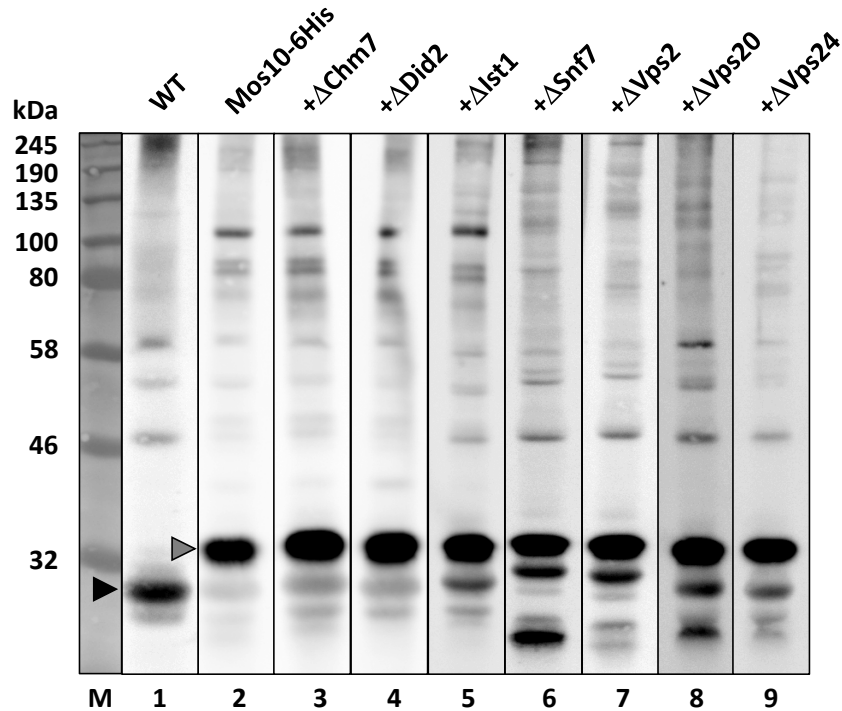


Figure 31: Comparison of Mos10-6His specific IMAC WB patterns of ESCRT-III single deletions.

Summary of the Mos10-6His Ni-NTA purification results of the strains RKY1558 (Woodcock et al.), RKY2889 (Mos10-6His), $\Delta chm7$ (RKY3228), $\Delta did2$ (RKY2788), $\Delta ist1$ (RKY2789), $\Delta snf7$ (RKY2790), $\Delta vps2$ (RKY2841), $\Delta vps20$ (RKY2893), and $\Delta vps24$ (RKY2830). The Mos10 lanes of Figure S 13 - Figure S 21 incubated with α -Mos10 are shown and height adjusted to the Mos10-6His migrated band. **M**: NEB Color Pre-stained Protein Standard (11 - 245 kDa). Arrows: **Black**: Mos10; **Grey**: Mos10-6His. Loaded: OD = 1.

3.2 Influence of *VPS68* deletion on ESCRT-III

The identification of Vps68 as a Mos10 interacting protein led to the assumption that Vps68 could have a direct effect on ESCRT-III complex formation or function. To address this idea, a series of experiments attempted to elucidate changes in ESCRT-III complex composition and cellular distribution upon *VPS68* deletion.

3.2.1 IP and Co-IP in WT

Biochemical analysis of ESCRT-III composition under native conditions was previously carried out, revealing overall consistent findings with the current model of ESCRT-III (Heinzle

et al., 2019). Here, immunoprecipitation analysis using antibodies against seven ESCRT-III subunits (excluding Chm7 due to poor IP) as individual baits were used to pull out the associated ESCRT-III proteins to reveal ESCRT-III complex composition. IP and Co-IP experiments were done in duplicates using DSP as a cleavable crosslinker and the WT strain RKY1558 as the unperturbed control.

The intensities of the input and co-IP signals (Figure S 22) were quantified with ImageJ. The co-IP intensities were normalized to the primary IP intensities achieved with the bait antibody (e.g. if anti-Did2 antibodies precipitate 20 % of the total Did2 protein, then the co-IP efficiencies were multiplied by a factor of five). Then the intensities were converted into molecules per cell, according to the molecule numbers determined in a previous study (Heinzle et al, 2019, Table S 8). Thus, we know how many molecules of ESCRT-III subunits in a cell are engaged in ESCRT-III complex formation (Table S 6, Figure S 23). Because, the absolute numbers of ESCRT-III proteins precipitated varies between the different antibodies (e.g. due to different accessibility of the epitopes), the molar fraction of each ESCRT-III protein engaged in complex formation was calculated (e.g. molecules of Did2 in the complex divided by the total number of ESCRT-III molecules in a complex). This normalization leads to very consistent results among the different bait antibodies (Figure 32).

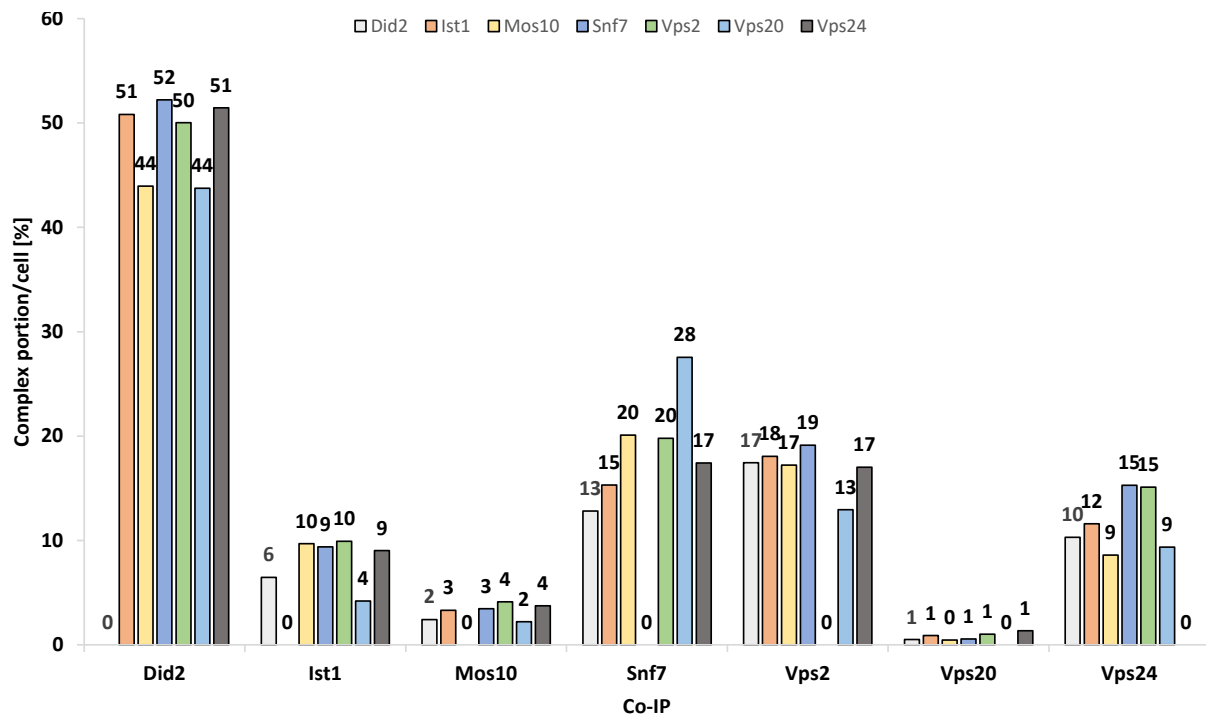


Figure 32: Molar fraction of ESCRT-III proteins in ESCRT-III complexes in the WT strain RKY1558.

Graphical representation of the co-immunoprecipitation of each ESCRT-III subunit by the seven ESCRT-III IPs. The percentage value of each Co-IP protein represents the fraction the protein has in ratio to the entire complex.

Did2 turned out to be the most abundant protein in the complex. Roughly half of ESCRT-III consists of Did2, Snf7, Vps2 and Vps24 are present in about equimolar amounts (with slightly less Vps24) and make up most of the rest of the complex. The other proteins, like Vps20, Ist1 and Mos10 are present in minor amounts. A simplified version of the diagram is presented in Figure 33. Here the average of all co-IP efficiencies (expressed as molar fraction of protein in a complex) over all bait antibodies is shown.

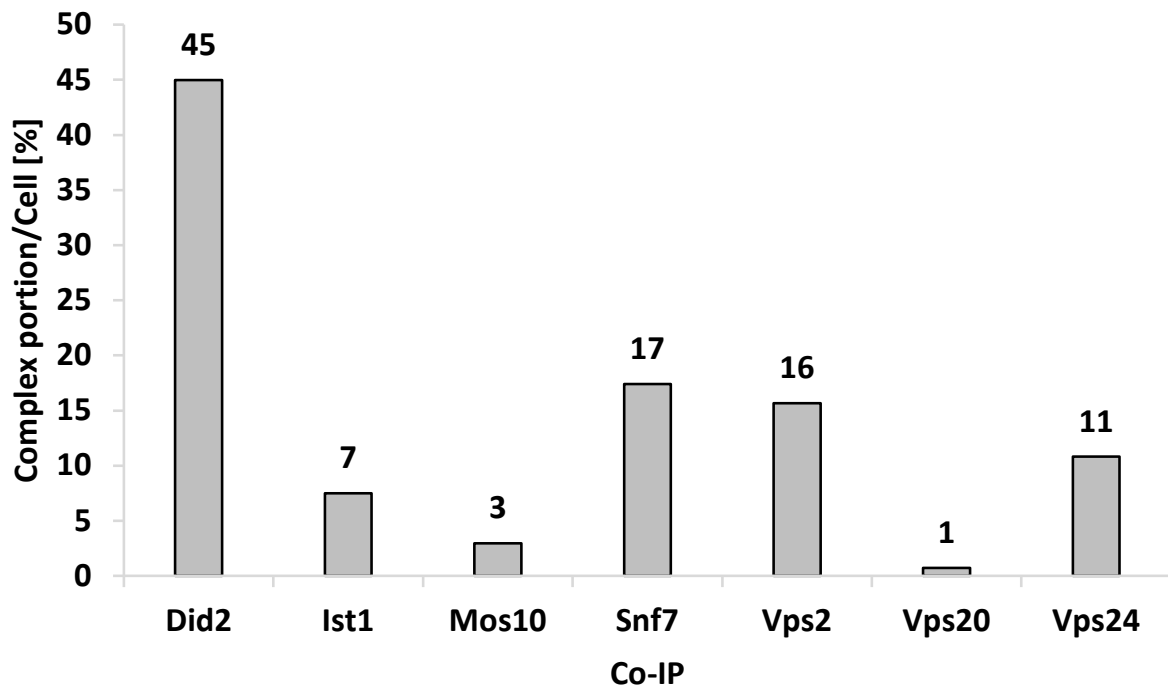


Figure 33: Simplified ESCRT-III complex composition based on the co-IP in WT strain RKY1558.

Co-immunoprecipitated proteins in reference to the ESCRT-III complex portion in percentage.

3.2.2 IP and Co-IP in the $\Delta vps68$ strain RKY3222

To investigate the influence of Vps68 on ESCRT-III composition, the WT strain RKY1558 was modified to carry a Vps68 deletion mutation ($\Delta vps68$ in RKY3222). IP and co-IP experiments were performed like with RKY1558 by measuring the intensities of the WB signals (Figure S 24), conversion into molecule numbers (Table S 7) and summarizing the results in Figure S 25. Again, the molar fraction of a given ESCRT-III protein in the complex was calculated as described for Figure 32. Changes of the molar fraction of a given ESCRT-III protein compared to wildtype are represented in Figure 34. The simplified version with the average over all bait antibodies is presented in Figure 35.

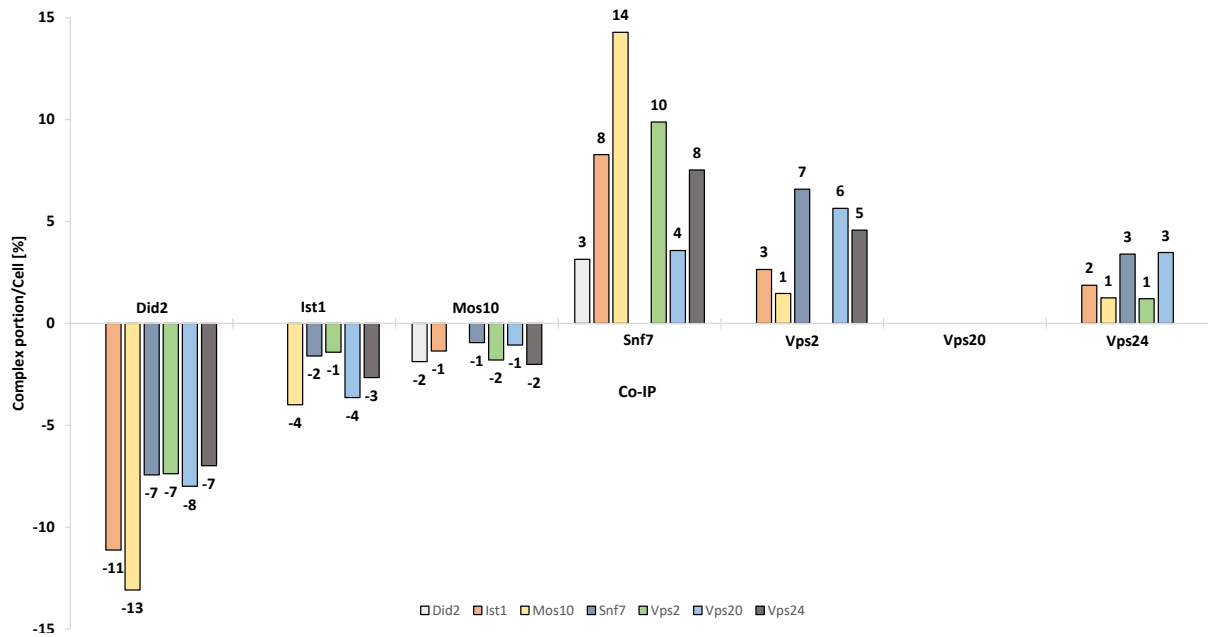


Figure 34: Difference between the co-immunoprecipitated values of strains RKY1558 and RKY3222.

Each value of complex portion in percentage gained by the IP from WT strain RKY1558 was set regarding the values acquired by the IP experiments of RKY3222 strain carrying the Vps68 deletion. Results are gathered and grouped according to the ESCRT-III protein being co-immunoprecipitated. Values are percentage points.

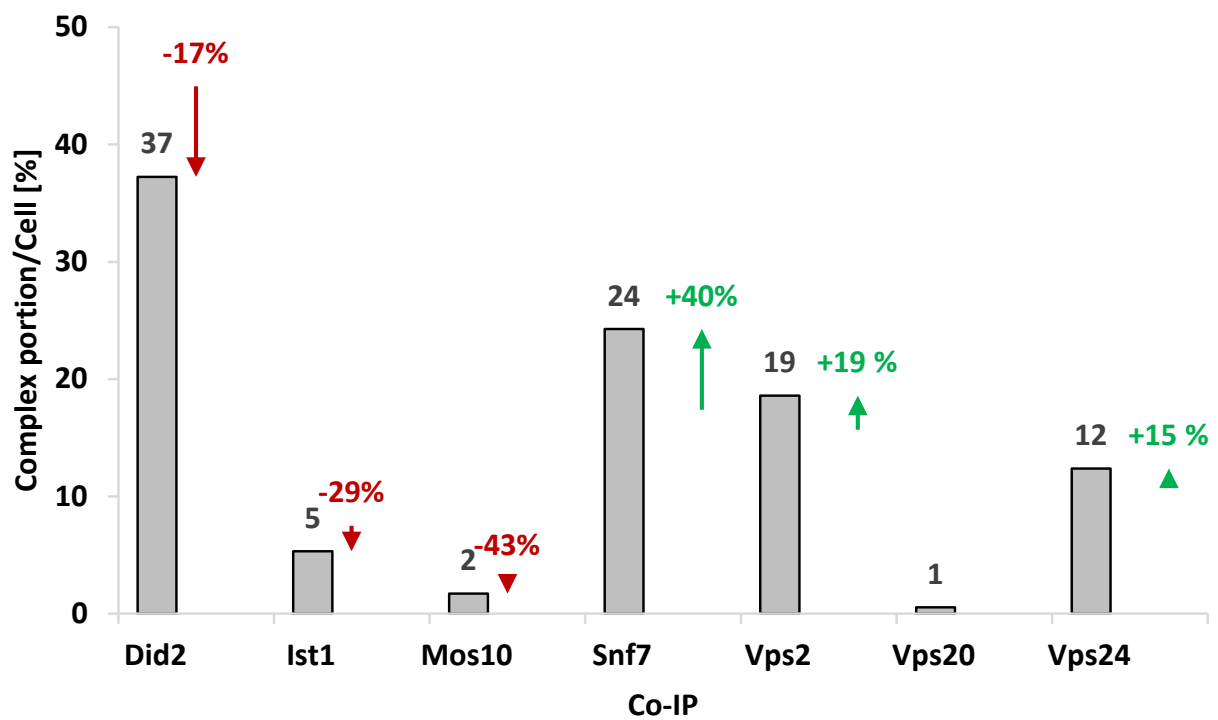


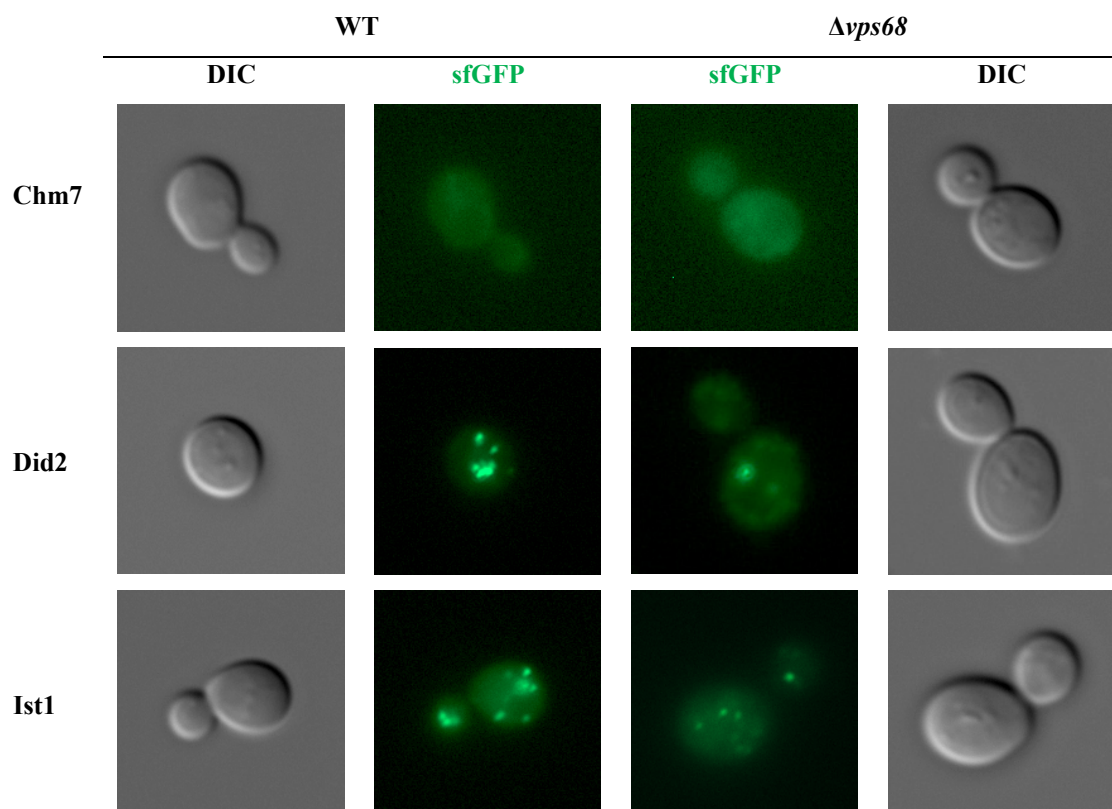
Figure 35: Co-IP values of strain Δ vps68 RKY3222 in comparison to the WT strain RKY1558.

As seen in Figure 33, values of each individual (co-)IP experiment were averaged and adjusted to 100 % before being plotted. For each co-immunoprecipitated ESCRT-III subunit, the difference between the complex portion in the deletion strain and the WT strain was highlighted by arrows. Red arrows indicate a decrease in complex portions compared to the WT strain, whereas green arrows indicate increased protein precipitation.

As seen in Figure 34 and Figure 35, there is an effect on ESCRT-III complex composition due to the introduction of a Vps68 deletion. Basically, what we see is that the number of core ESCRT-III proteins Snf7, Vps2 and Vps24 is increased in the *VPS68* deletion strain compared to wildtype, while the number of ESCRT-III associated proteins Did2, Ist1 and Mos10 (implicated in disassembly of ESCRT-III) is decreased. Snf7 polymer assembly is being increased by 40 % with increased values for Snf7 associated proteins Vps2 and Vps24 of 19 % and 15 %, respectively. Mos10 seems most influenced by the deletion of Vps68 for being reduced by 43 %, followed by Ist1 with 29 % and Did2 with 17 % less precipitated due to a lack of Vps68. This result is in line with the notion that the transition from an active ESCRT-III complex to a disassembly complex is delayed in the *VPS68* deletion strain.

3.2.3 Effect of *VPS68* deletion on the intracellular ESCRT-III protein distribution

Fluorescence microscopy was used to observe proteins under a microscope to detect changes in the intracellular distribution of ESCRT-III subunits upon Vps68 deletion. Therefore, every ESCRT-III protein was C-terminally tagged with sfGFP in the WT and $\Delta vps68$ background. Each of the eight WT and eight $\Delta vps68$ strains was examined by fluorescence microscopy. For each strain, a representative cell is depicted in Figure 36.



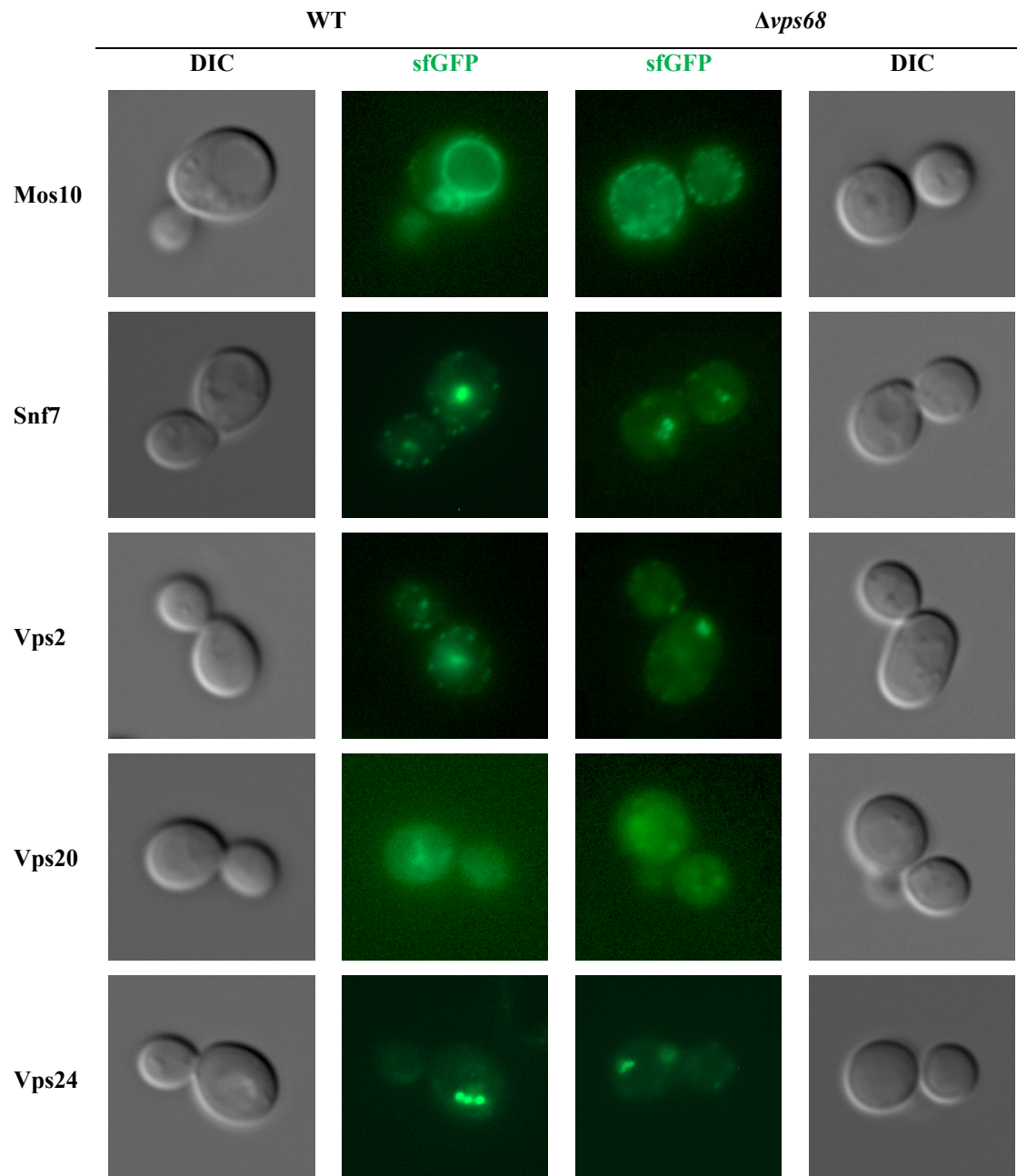


Figure 36: Intracellular distribution of ESCRT-III proteins by fluorescence microscopy.

Every ESCRT-III subunit was C-terminally tagged with sfGFP in the WT RKY 1558 background and the $\Delta vps68$ RKY3222 background. A representative cell was chosen to visualize the typical distribution of each protein.

The fluorescence staining directly reflects the protein distribution inside the cell. A uniformly distributed signal indicates a cytosolic distribution of the protein, like seen with Chm7 and Vps20. Did2, Ist1, and Vps24 were present in distinct dot-like structures, which presumably correspond to endosomes. Another phenotype seen with Vps2 and Snf7 is the assembly into small cortical dots, which could be associated with the plasma membrane, with one or more additional, presumably endosomal dots inside the cell. The intracellular distribution of these proteins was not significantly affected by the *VPS68* deletion. A clear difference, however, was

noted for the Mos10 protein. In the wildtype strain, Mos10 shows a classical "class E" distribution with staining around the vacuole and a patchy structure at the vacuolar membrane. However, the fluorescence signal drastically changed when Vps68 was lacking, leading to dotlike staining distributed inside the cell and primarily located close to the cell's plasma membrane. Besides minor changes within the different strains, the phenotypical alteration of Mos10 staining seems most severe. Since the fluorescence signal directly reflects protein distribution, Mos10 localization shifts from the class E compartment to the PM.

Vps68 interacts biochemically with Mos10. To see, whether this result can be reproduced by fluorescence microscopy, double mutant strains were created carrying sfGFP and mCherry tagged variants for the simultaneous detection of both proteins. A typical cell showing the overall staining of the mutant strains RKY3221 (Mos10-sfGFP) and RKY3226 (RKY3221 + Vps68-mCherry) can be seen in Figure 37.

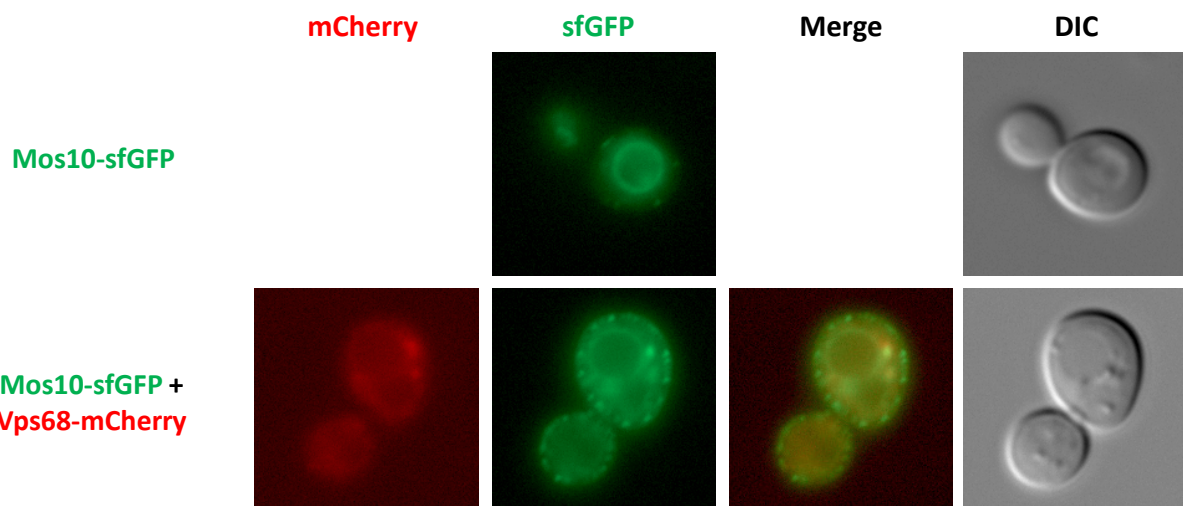


Figure 37: Vps68-mCherry induced localization shift of Mos10-sfGFP.

Images of fluorescence microscopy with sfGFP tagged Mos10 strain RKY3221 (top panels) and Mos10-sfGFP & Vps68-mCherry strain RKY3226 (bottom panels) carrying two different fluorescent tags.

As presented above (Figure 37), the sfGFP tagged variant of Mos10 led to a typical class E staining (upper row of Figure 37). Introduction of Vps68-mCherry into this strain changed the localization of Mos10-sfGFP to a distribution reminiscent to the *VPS68* deletion. From this, it can be concluded that Vps68-mCherry is largely non-functional. Some of the structures, especially those close to the vacuole, stained for both proteins. Thus, Vps68-mCherry and Mos10-sfGFP colocalize in these structures. The cortical Mos10-sfGFP dots, however, do not seem to be stained for Vps68-mCherry. To exclude a tag-induced phenotype and to get a better fluorescence signal for Vps68, three new strains were constructed, which express Vps68-sfGFP

(RKY3183), Mos10-mCherry (RKY3262) and both proteins with the respective tags (RKY3264). As seen in Figure 38, switching the tags did not change the localization of the two tagged proteins. What can be seen in this figure is that the localization of both tagged proteins is altered by tagging of the respective partner protein. Vps68-sfGFP alone displays a class E staining pattern. This staining is dispersed when Mos10 is simultaneously tagged with mCherry.

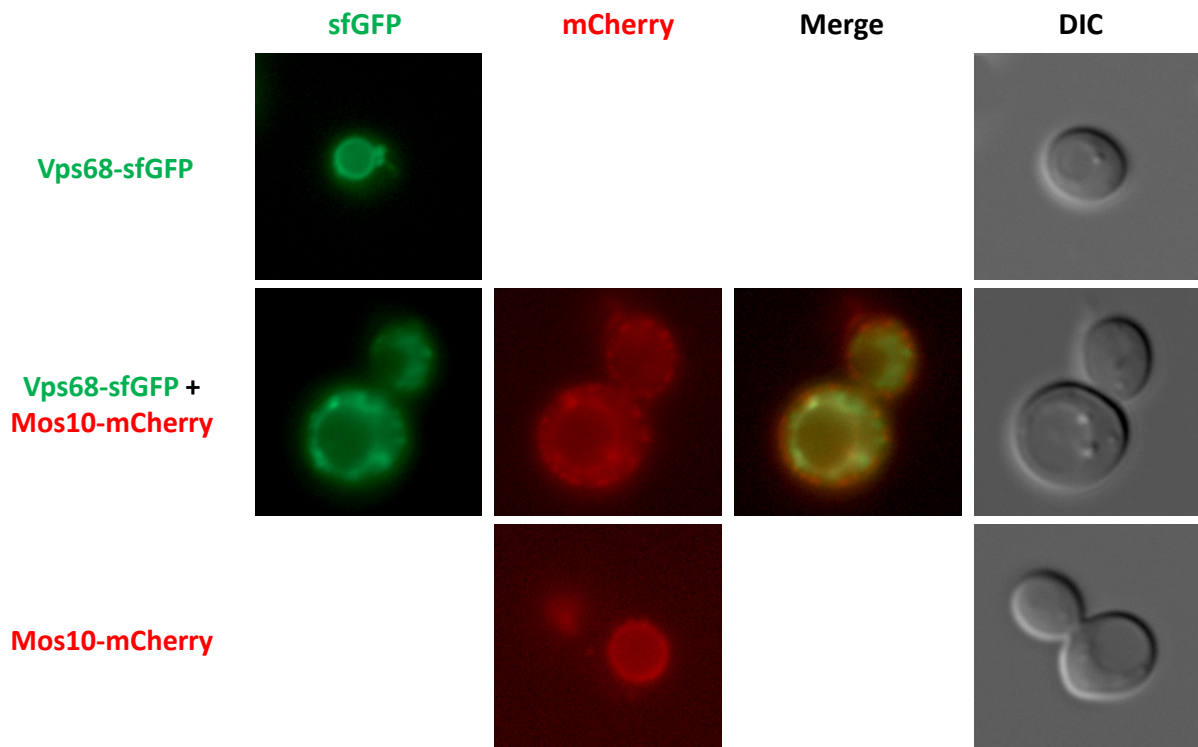


Figure 38: Reverse Vps68 and Mos10 tagging to visualize protein distribution.

Images of fluorescence microscopy with sfGFP tagged Vps68, Mos10-mCherry, and the Vps68-sfGFP & Mos10mCherry double staining.

3.3 Cell-fractionation

To complement the fluorescence experiments, the influence of Vps68 on the intracellular localization of ESCRT-III proteins was examined by cell-fractionation, with a focus on Mos10. The advantage of this approach is that it can be performed with native, untagged proteins.

3.3.1 Differential centrifugation experiments

Cellular components in a cell extract can be separated by their sedimentation velocity during centrifugation. To this end, cell extracts were first centrifuged at 500 g to remove cell debris, followed by a 13.000 g spin to sediment larger or heavier particles (P13). The S13 supernatant is then subjected to a centrifugation at 100.000 g to obtain a P100 pellet, containing smaller

particles and a S100 supernatant, containing soluble proteins. In a parallel experiment, the detergent Triton X-100 is added to the cell extract to solubilize the membranes.

For this purpose, cell cultures were lysed after reaching exponential growth and before being centrifuged treated with Triton X-100 for the Triton X-100 + fraction. For each ESCRT-III member, the total amount of protein recovered by each centrifugation step was summed up, and the fraction values were calculated for the P13, P100 and S100 fractions (Figure 39).

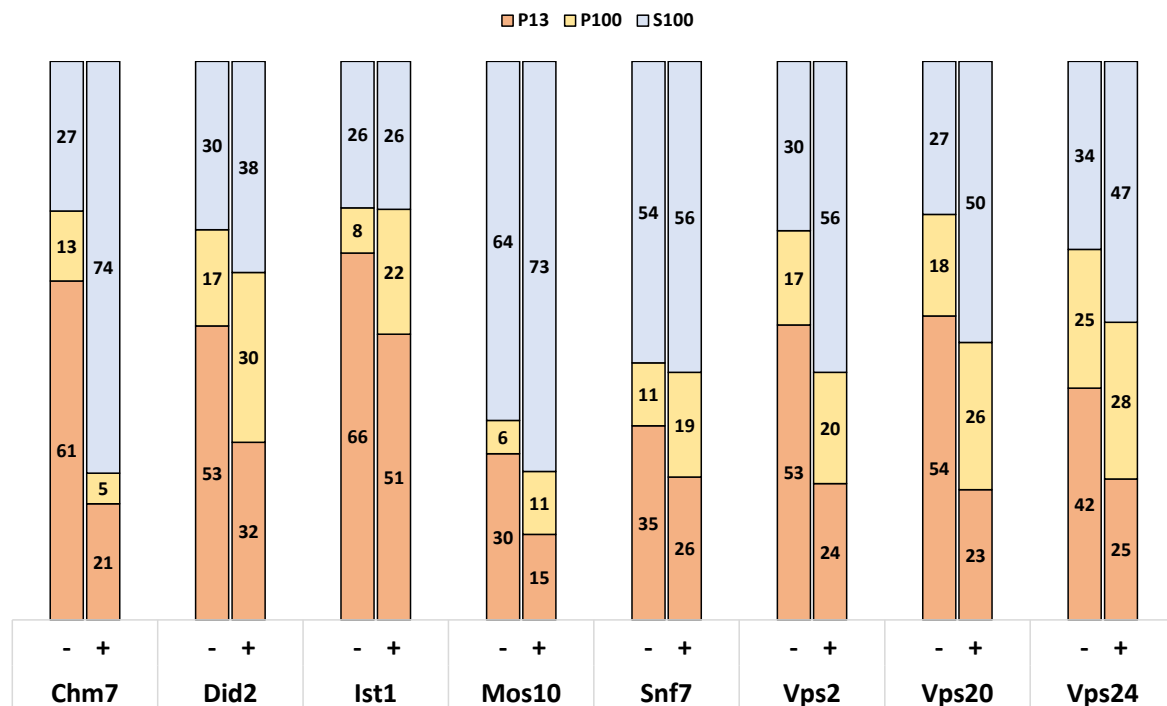


Figure 39: ESCRT-III distribution in the WT strain RKY 1558 with and without Triton X-100 treatment.

Fractionated ESCRT-III proteins by centrifugal sedimentation are analyzed by WB analysis (Figure S 28), done in triplicates. The fraction values for P13, P100, and S100 for the cultures treated with and without are summarized and adjusted to 100 % (Figure S 26&Figure S 27). For tighter comparison, the results are combined in the diagram.

As seen in Figure 39, without being treated with detergent, the most prominent fraction for most ESCRT-III proteins containing about half the amount of protein is the P13 fraction. Only for Snf7 and Mos10 the S100 fraction was the dominant fraction, indicating that less protein is associated with membranes than in the case of the other ESCRT-III proteins. The detergent-induced membrane solubilization, which in most cases shifts proteins from the P13 into the P100 and S100 fractions, had only a moderate effect on Snf7. After Triton X100 treatment, most ESCRT-III proteins tend to be shifted to the P100 pellet rather than to the soluble S100 fraction. The reason could be that ESCRT-III proteins may form larger protein assemblies that can be sedimented at 100.000 g. The P100 fraction of Mos10 almost doubles from roughly 6 to 11 %, as seen with most ESCRT-III associated proteins like Did2 and Ist1, also doubling and

nearly tripling in P100 fraction sedimentation. After Triton X-100 treatment, all ESCRT-III core proteins show an almost identical distribution of 25 % P13, 25 % P100, and 50 % S100. To elucidate Vps68 induced alterations in the distribution of all ESCRT-III subunits, the experiment was also conducted in the Vps68 deletion strain RKY3222 (Figure 40).

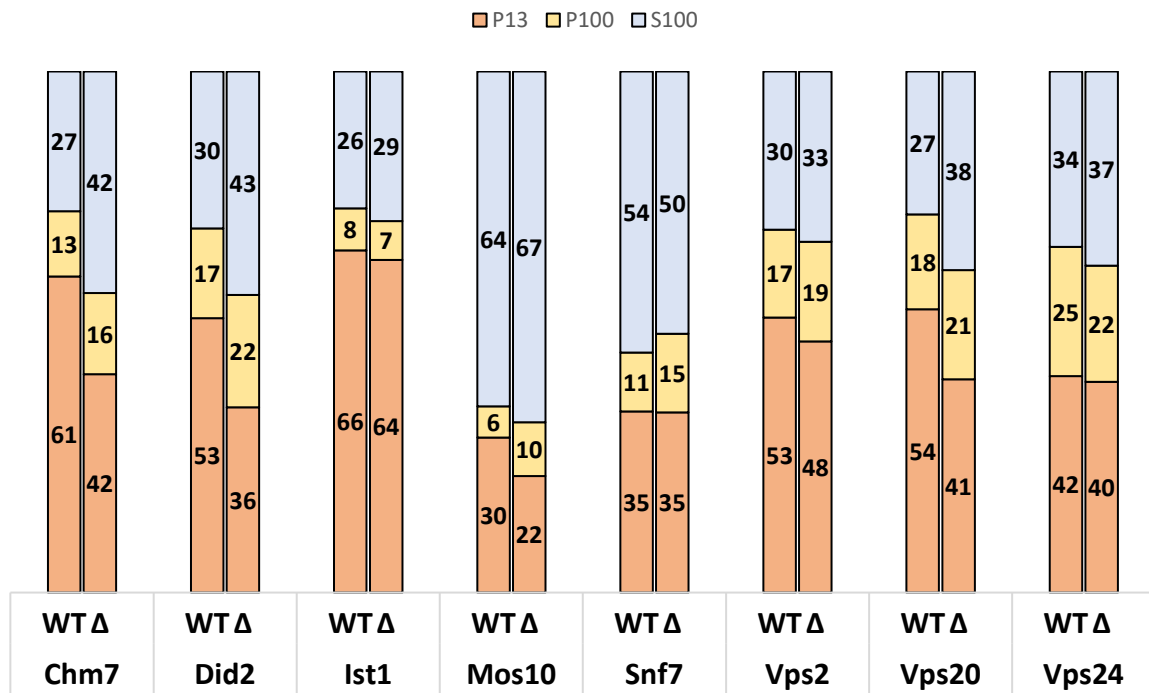


Figure 40: Sedimentation comparison between WT strain RKY1558 and Vps68 deletion strain RKY3222.

Comparison of the WB results gained from the differential centrifugation experiment results seen in Figure S 28 & Figure S 33. The fraction values for P13, P100, and S100 for the cell extracts without Triton X-100 treatment are summarized and adjusted to 100 % (Figure S 26 & Figure S 30). For better comparison, the results are combined in one diagram.

Similar to the co-immunoprecipitation experiment, two classes of ESCRT-III proteins can be distinguished. The core ESCRT-III proteins Snf7, Vps2 and Vps24 showed basically the same distribution in the *VPS68* deletion strain as in the wildtype. No significant changes were observed. In the case of the ESCRT-III associated proteins Chm7, Did2 and Mos10 a reduction in the P13 fraction could be seen in the *VPS68* deletion strain compared to wildtype. Only Ist1 showed a different behavior here by not being altered in $\Delta vps68$. A comparison of the Triton X-100 treated samples showed no significant differences between $\Delta vps68$ and wildtype (Figure S 32).

3.3.2 Flotation

An alternative fractionation experiment was chosen since the fractionation of proteins based on their sedimentation cannot differentiate between membrane associated protein and protein in larger aggregates. A series of flotation experiments was performed to directly determine the membrane associated fraction, since in the flotation experiment membranes float to the top of the gradient, where they are collected.

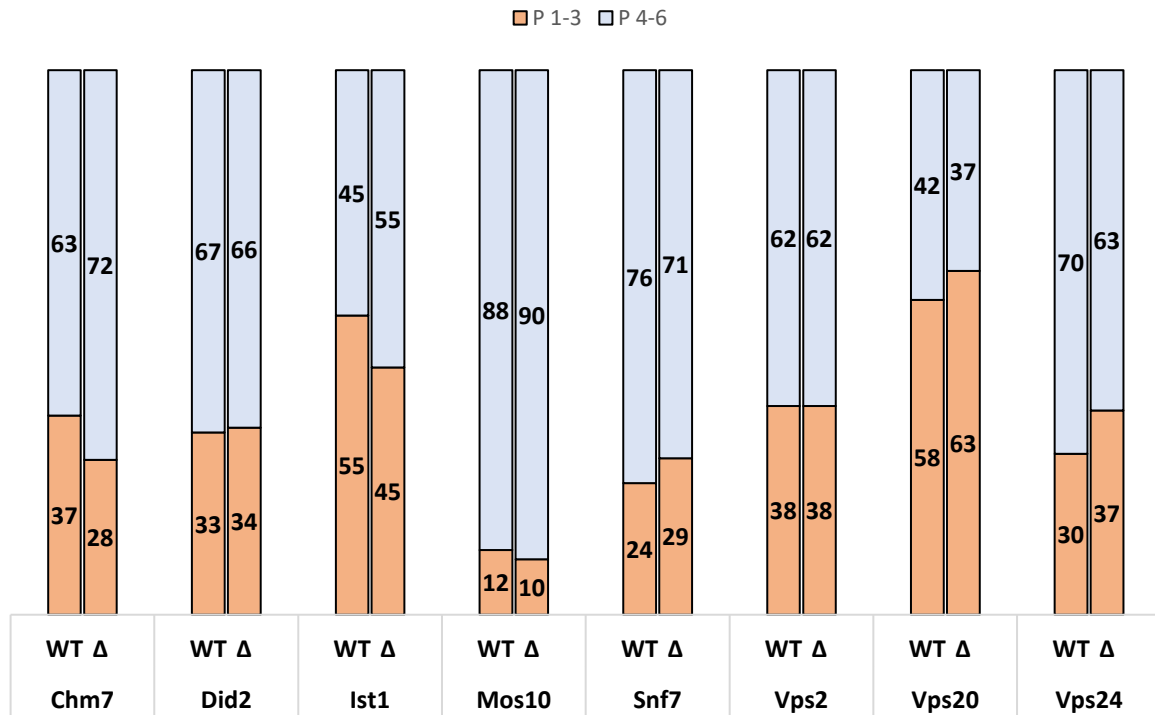


Figure 41: Flotation comparison between WT strain RKY1558 and Vps68 deletion strain RKY3222.

A flotation experiment was carried out with both strains collecting six fractions from the gradient. After evaluating each fraction by WB analysis and ImageJ, quantification values were summed up and grouped into fractions 1-3 and 4-6 containing either the first three (membrane) fractions or the last three (cytosolic) fractions.

For a better overview, the topmost three fractions containing the membrane-associated proteins and the last three fractions at the bottom of the tube containing cytosolic proteins were combined (the percentage of the total protein is given). Figure 41 sums up the flotation results from Figure S 34 & Figure S 35 obtained from the WB results in Figure S 38 & Figure S 40. For most ESCRT-III proteins, 30-50 % of the protein proved to be membrane associated, only for Mos10 hardly any protein could be detected in the membrane fraction. The determined values for the float fraction roughly correspond to the P13 fraction seen in the differential centrifugation experiment. Deletion of *VPS68* had no significant effect on membrane association of the proteins.

Snf7 has a crucial role in the formation of the ESCRT-III complex. Loss of Snf7 should be reflected in a reduced membrane association of the other ESCRT-III components. To test this prediction a flotation experiment was performed with a *SNF7* deletion strain (RKY2790). As summarized in Figure 42, membrane association of all ESCRT-III proteins, except Mos10, was reduced in $\Delta snf7$ compared to wildtype. Interestingly, a basal level of membrane association was maintained in the deletion strain. This could point to a Snf7-independent function of the other ESCRT-III proteins, or it could be an indication of unspecific membrane binding. At this point, it cannot be distinguished between these two possibilities. The lack of effect on Mos10 membrane association could indicate that the observed membrane binding of 11-12 % is unspecific.

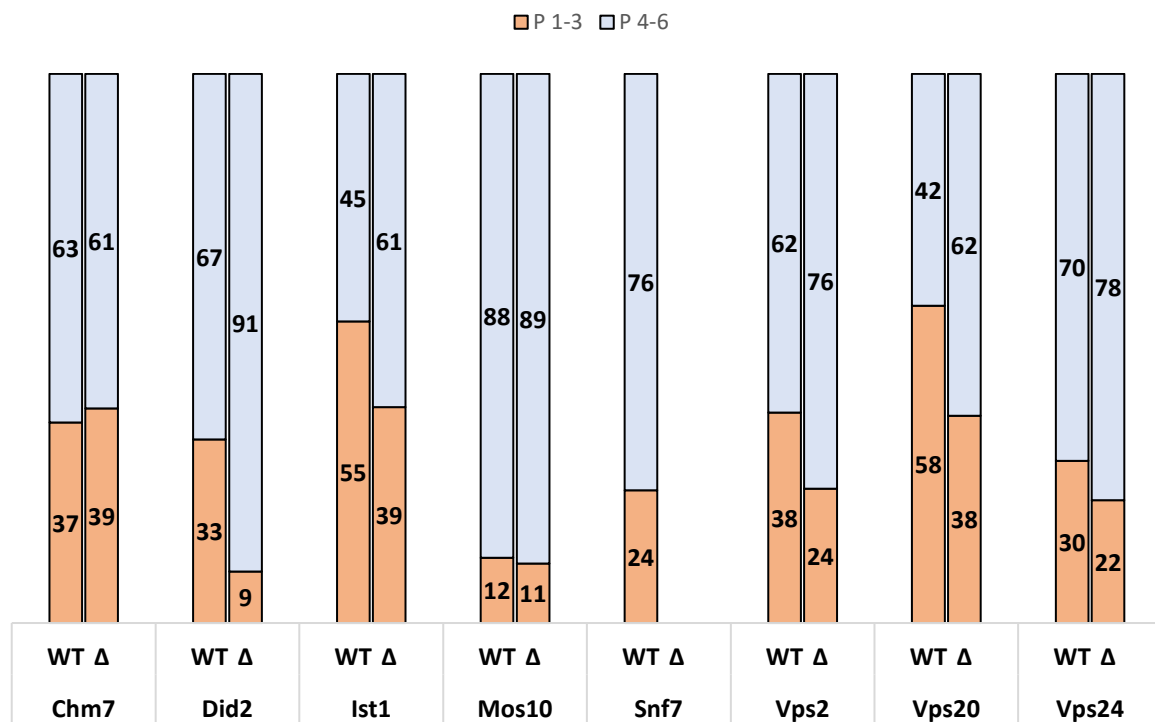


Figure 42: Flotation comparison between the WT strain RKY1558 and the $\Delta snf7$ strain RKY2790.

The diagram sums up the flotation results from Figure S 34 & Figure S 36 obtained from the WB results in Figure S 38 & Figure S 39.

3.3.3 Sucrose Gradients

For a more detailed overview of ESCRT-III distribution, yeast strains were fractionated by a sucrose density gradient giving 18 fractions going from cytosolic through different membrane-bound states. The fractionation of the WT strain RKY1558 is depicted in Figure 43.

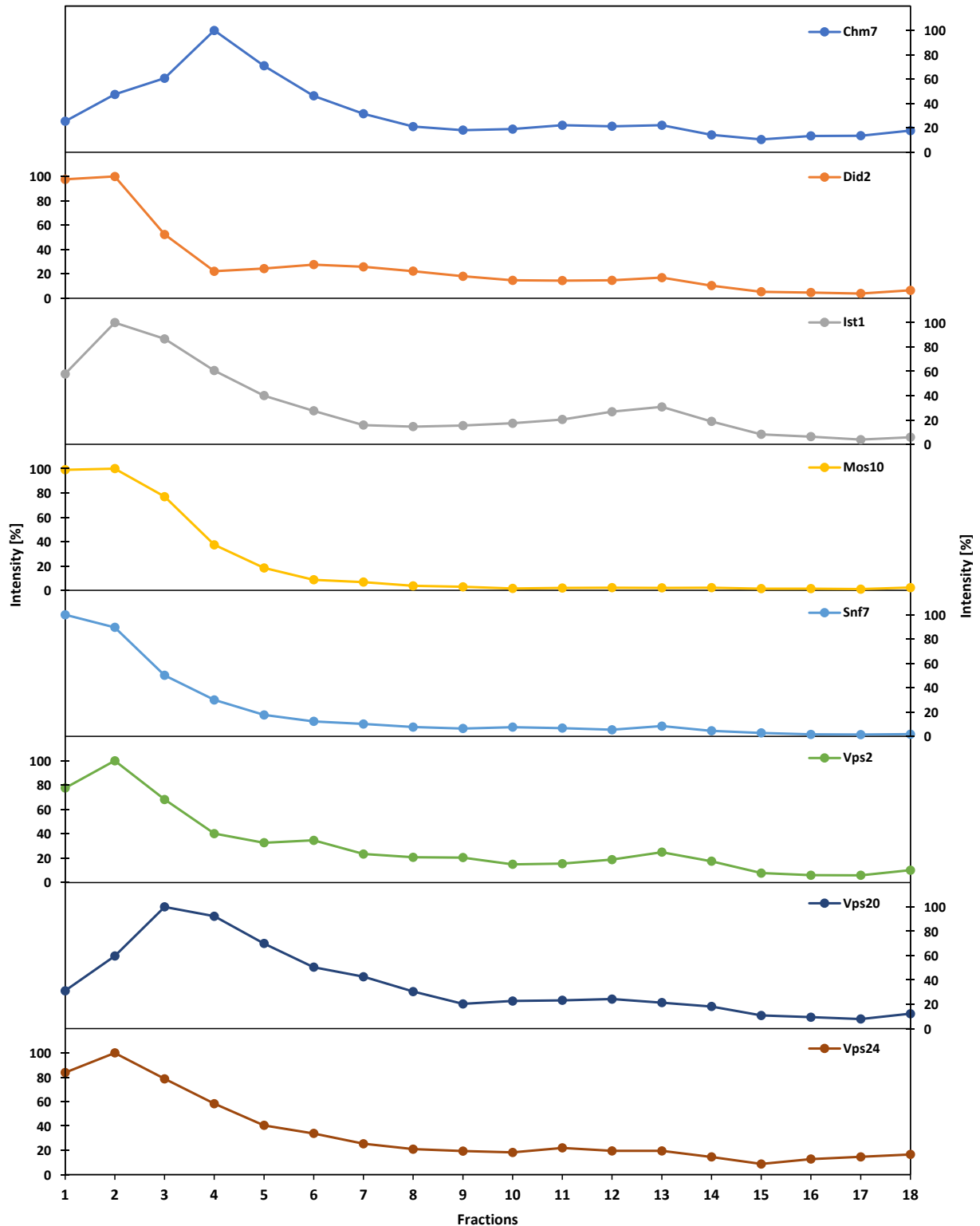


Figure 43: ESCRT-III distribution fractionation by sucrose density gradient separation.

Sucrose density fractionation into 18 fractions based on the sedimentation rate of all ESCRT-III proteins.

Each ESCRT-III protein is presented on an intensity scale depending on the abundance in each fraction calculated by the band intensities of the WB in Figure S 44. The highest value was set to 100 %. All proteins have their maximum in the fractions 1-4, representing the cytosolic

fractions. ESCRT-III proteins Did2, Mos10, and Snf7 start with 100 % in fraction 1 before continuously decreasing in succeeding fractions. Ist1, Vps2, and Vp24 reach their maximum fraction abundance in fraction 2 before continually dropping in later fractions. Slight shifts are only detectable with Vps20 peaking in fraction 3 and Chm7 getting the highest value in fraction 4. It is further worth noticing that most proteins after reaching a small plateau phase have a slight local maximum at fraction 13. The fraction 13 contribution is most visible with Did2, Ist1, Vps2, and Vps20. Lastly, an increase in intensity can be measured in the last fraction (18) since the fraction showed the highest variance in sample size and density collects everything sedimented throughout the entire tube.

To compare the WT results with the $\Delta vps68$ strain, the sucrose gradient was also performed in the altered strain background seen in Figure S 42. Like in previous experiments, the differences between each strain are minor, resulting in the highest sedimentation in the first four sucrose gradient fractions. The gradients of Vps2 and Vps20 seem shifted to slightly denser fractions, by which it should be highlighted that the overall presence of these proteins often led to variations in analyzing the WB (Figure S 46). What remains evident is the local peak observed in fraction 13, which is still present in the Vps68 lacking strain and seems slightly increased for proteins like Did2, Ist1, and Vps2. The only difference regarding Mos10 (and Snf7) localization is the maximum peak shift from fraction 1 to fraction 2, not hinting at any altered distribution or association inside the cell's organization.

Although the different experiments are designed to visualize native protein distribution, the effect observed by fluorescence microscopy of an altered localization of Mos10 was done with the sfGFP tagged variant. To address the impact of the tag, the sucrose density gradient was repeated using the tagged Mos10 variant in the WT and the Vps68 depleted strain. Different marker proteins were additionally applied to assign protein distribution to specific cell organelles. The marker protein alkaline phosphatase (Alp1) was chosen for the vacuolar compartment targeting the vacuole like the established ESCRT-III localization (Klionsky and Emr, 1989). Further, the ER marker dolichol phosphate mannosyl synthase (Dpm1), the acetolactate synthase Ilv2 for mitochondria, and the protein Pep12 for marking the late endosome were applied to sucrose gradient fractionation (Bassham et al., 1995, Falco et al., 1985, Orlean, 1990).

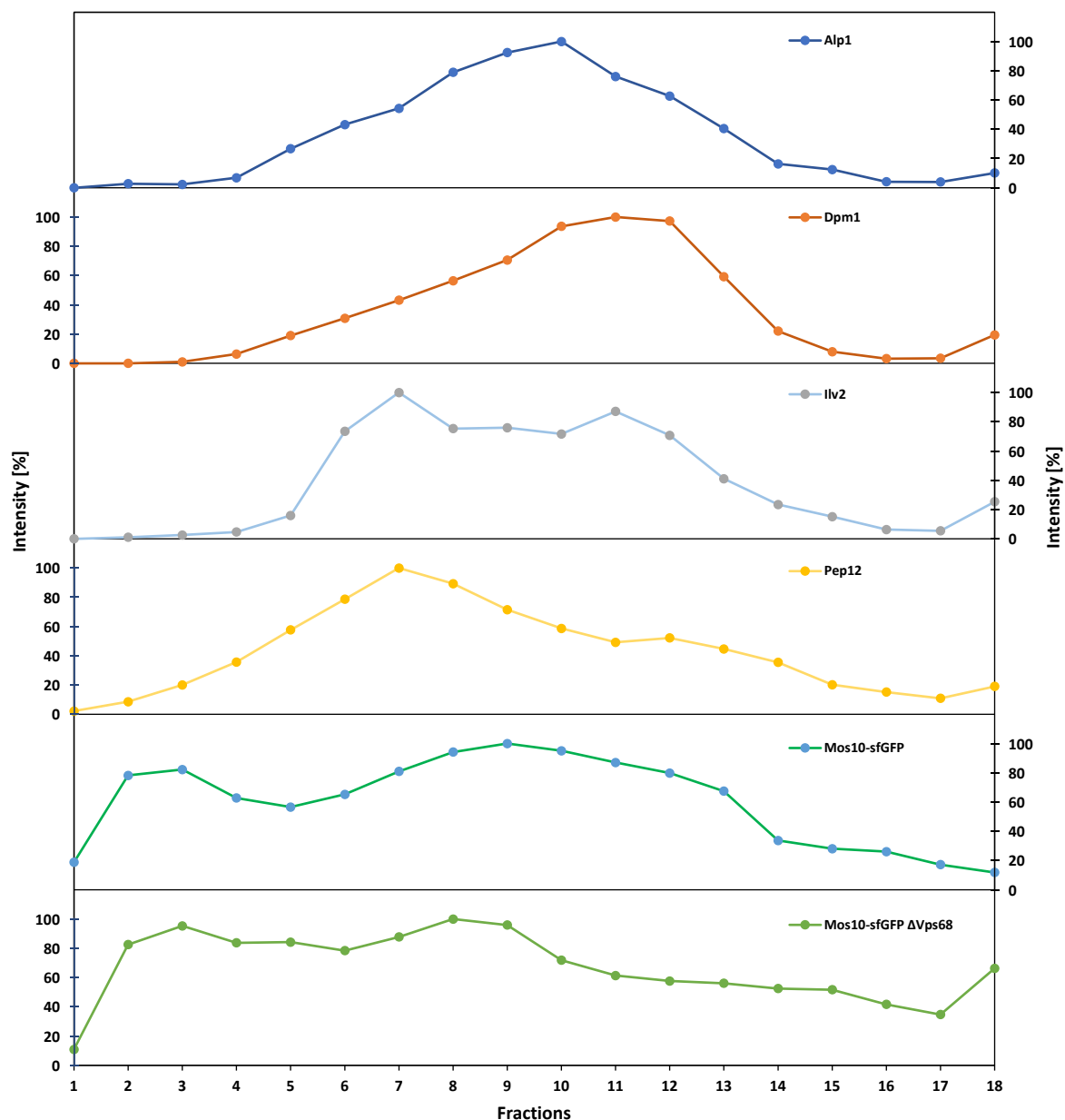


Figure 44: Gradient of tagged Mos10 in WT and $\Delta vps68$ background in comparison with marker proteins.

Gradient separation of protein and marker fractions based on the sedimentation rate. Marker proteins Alp1, Dpm1, Ilv2, and Pep12, were chosen to mark subcellular organelles and compare those compartment distributions with the tagged variant of Mos10 in WT and Vps68 depletion strain.

As seen in Figure 44, each of the marker proteins shows a unique distribution on the sucrose gradient. The peak for Alp1 was collected in fraction 10, whereas Dpm1 peaks in fractions 11 and 12. Pep12 has a peak in fraction 7, and Ilv2 shows two peaks in fraction 7 and 11.

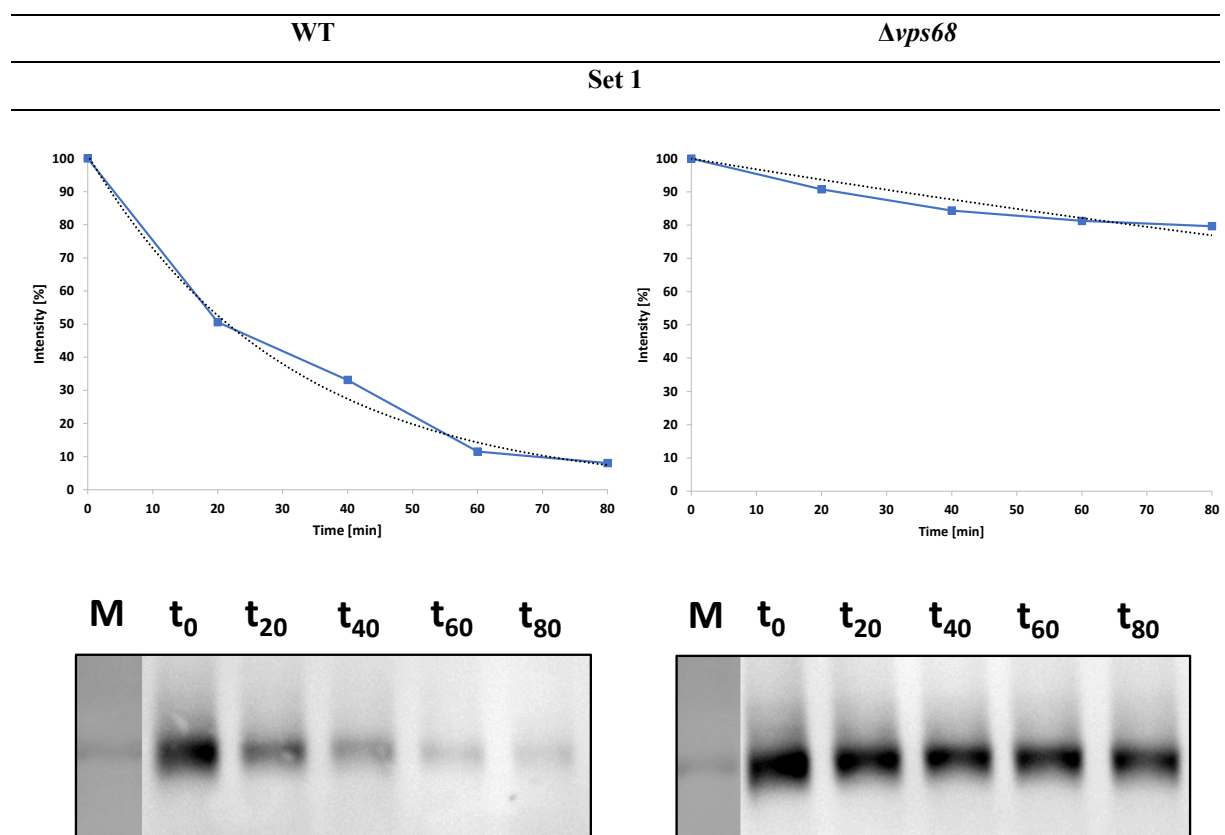
The distribution of Mos10-sfGFP was clearly different from the distribution of the native protein. While native Mos10 was exclusively found in the soluble fraction (Figure 43), Mos10-

sfGFP now formed a broad peak in the middle of the gradient centered around fraction 9. The distribution of Mos10-sfGFP in the $\Delta vps68$ background looked somehow similar.

The profile of Mos10-sfGFP appears quite different compared to the marker proteins, and the peak values also do not fit to any other protein. The closest match is with the Alp1 profile marking the vacuole in line the class E localization of Mos10-sfGFP in the fluorescence images. In the $\Delta vps68$ background the Mos10-sfGFP profile is shifted more towards the left with a peak in fraction 8 and thus resembles more the Pep12 profile.

3.4 Perturbations in endocytic cargo degradation and transport

As a vacuolar *protein sorting (vps)* function, Vps68 has been implicated in protein transport to the vacuole. To confirm this role of Vps68 in the transport of endocytic cargo proteins to the vacuole, the turnover of the ABC transporter Ste6 was examined by a cycloheximide chase experiment. Ste6 is transported to the vacuole for degradation and has short half-life (Kölling and Hollenberg, 1994). Cycloheximide (CHX) blocks protein synthesis, so the fate of pre-existing Ste6 protein can be followed over time after CHX addition. After applying CHX, a sample was taken every 20 min for 80 mins, and the degradation was monitored by WB analysis.



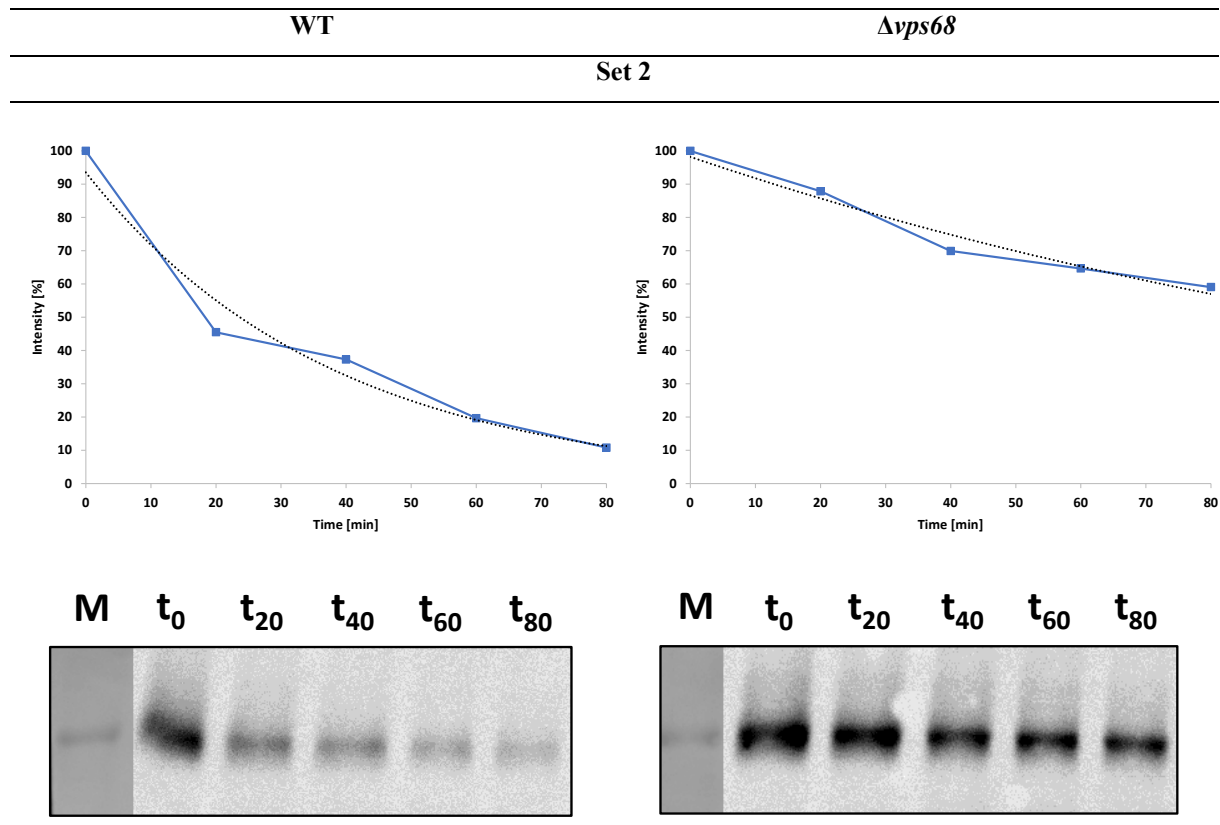


Figure 45: Cycloheximide chases of Ste6 in WT strain RKY1558 and $\Delta vps68$ strain RKY3222.

Degradation of native Ste6 was monitored by WB analysis from 0 min, thus portraying the absolute amount of protein present in the cell, up to 80 min after cycloheximide treatment and inhibition of protein biosynthesis. The experiment was done twice to highlight variation in the experimental outcome.

Two sets of experiments were performed with the wildtype and the $\Delta vps68$ strain, summarized in Figure 45, which includes the WB pictures directly visualizing degradation of Ste6. In the wildtype Ste6 is quickly degraded with a half-life of about 24 min (Table 23). In the $\Delta vps68$ strain Ste6 is clearly stabilized with a half-life of about 165 min. This shows that Vps68 is involved in transport of Ste6 to the vacuole.

Table 23: Half-life of CPS in WT and Vps68 depleted strain.

Experiment	WT [min]	R^2	$\Delta vps68$ [min]	R^2
1	21	0.9793	231	0.9311
2	27	0.969	99	0.970
Average	24		165	

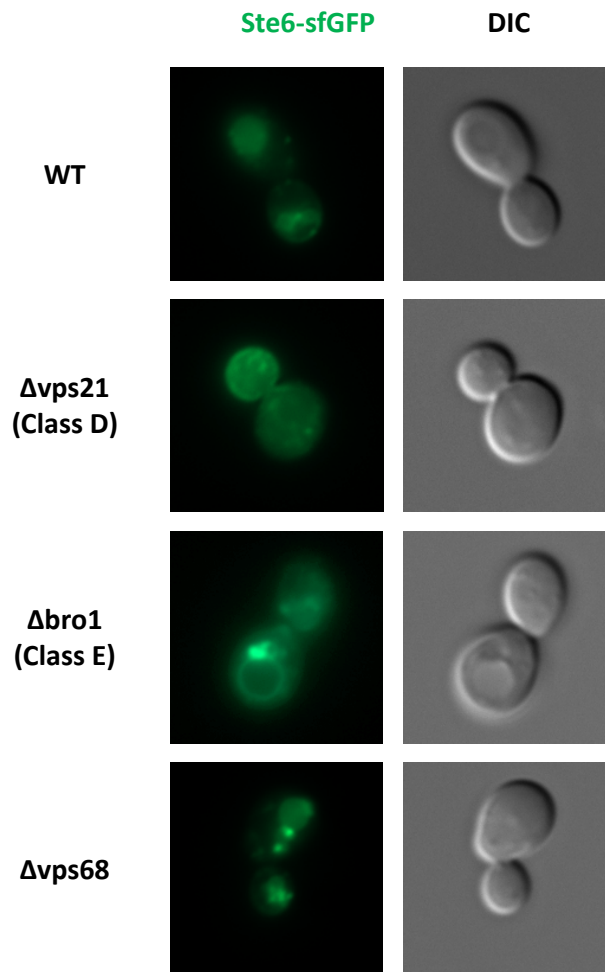


Figure 46: Classifying Vps68 deletion by established Class D & E protein null mutations.

The strain was compared to known class D and class E phenotypes of the single deletion strains of Vps21 (RKY1920) and Bro1 (RKY1922) to classify $\Delta vps68$ Ste6-sfGFP phenotype. Classical class E is depicted as a ring around the vacuole with a dot on one side and class D as an accumulation of fluorescence signal on the tip of the daughter cell.

To see at which step in the endocytic pathway Vps68 acts, the localization of Ste6-sfGFP (pRK1785) was examined by fluorescence microscopy. The phenotype of the $\Delta vps68$ mutant was compared with other *vps*-mutants with an established sorting phenotype (Figure 46). In the WT strain, a uniformly stained vacuole indicates that Ste6-GFP is transported into the lumen of the vacuole.

The Rab GTPase Vps21 is a class D protein that is required for fusion of endocytic vesicles with the endosome. Previously, it was shown that Ste6-GFP exhibits enhanced recycling to the cell surface in a $\Delta vps21$ mutant (Krsmanovic et al., 2005). As can be seen in Figure 46, Ste6-GFP stains the bud surface and localizes to small vesicles concentrated in the bud. The class E phenotype is exemplified by the $\Delta bro1$ mutation, where Ste6-GFP stains the vacuolar membrane and a patchy structure at the vacuole. The $\Delta vps68$ mutant showed neither a class D

nor a class E phenotype. The Ste6-GFP staining resembled wildtype with a somewhat enhanced staining of endosomal dots. This indicates that the ESCRT-III function is not blocked in a $\Delta vps68$ mutant (otherwise a class E compartment should have been formed).

As seen in Figure 47, sorting CPS-sfGFP (pRK1405) into the vacuole interior in the WT strain leads to a uniform staining of the vacuole's internal space. When Vps68 becomes absent, the transport inside the cell seems disturbed, highlighted by the fluorescence signal appearing to be a class E phenotype-like ring with two dots attached to it like seen with Mos10- & Vps68-sfGFP tagging. Multi copy CPS expression seems to cause this phenotype which needs to be further addressed by chromosomal integration of the CPS-sfGFP cassette.

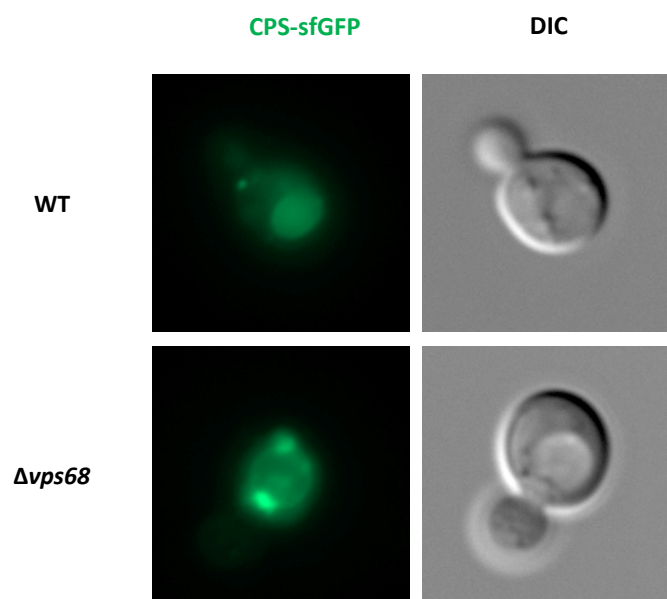


Figure 47: Perturbation of CPS cargo sorting by Vps68 deletion.

Fluorescence microscopy was used to monitor CPS cargo distribution in a WT and $\Delta vps68$ strain by attaching sfGFP to the cargo, thus visualizing Vps68 deletion-induced perturbations in proper cargo degradation. A distinct vacuolar and class E staining becomes visible.

3.5 Synchronized ESCRT-III assembly

When a cell extract is prepared for biochemical analysis, it contains a mixture of different functional states of ESCRT-III. To dissect the changes of ESCRT-III during a functional cycle, it would be useful, if the ESCRT-III cycles in the cell culture could be synchronized. It was explored, whether this goal could be reached by making use of a temperature sensitive *vps27* mutant. Vps27 is part of ESCRT-0, which is involved in cargo recruitment and represents the entry point of the ESCRT cascade. A shift to non-permissive temperature (37°C) should block

the ESCRT cascade at this early step. After release to permissive temperature (23°C), the ESCRT cascade should resume, hopefully in a synchronized way. A yeast strain was constructed that contains the *vps27-ts* mutation in the genome. When this strain is incubated at higher temperatures, the protein's function is inhibited, leading to a disturbed ESCRT machinery resulting in a class E phenotype for the Ste6-GFP cargo protein as observed by fluorescence microscopy. Figure 48 shows how the Ste6-GFP signal changes over time after the shift to non-permissive temperature (37°C).

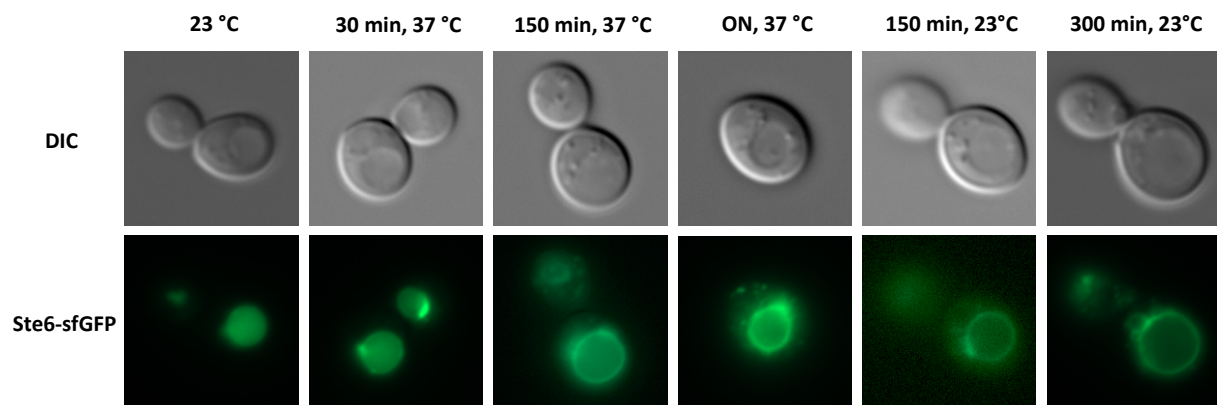


Figure 48: Heat-induced alteration of ESCRT-III assembly and disassembly by a Vps27 variant.

Timewise visualization of class E phenotype development induced by heating the samples to 37 °C before cooling back to 23 °C. Class E phenotype formation is pictured by fluorescence Ste6-GFP distribution.

Initially, the *Vps27^{ts}* strain RKY3208 was incubated at 23 °C to ensure WT-like growth and behavior as visible by a typical vacuole lumen staining of Ste6-GFP. The cells were then shifted to 37°C and examined after 30 min for changes in the fluorescence signal. As can be seen in the second column, the vacuole is still uniformly stained, but a dot becomes attached to the vacuoles. The class E phenotype with staining of the vacuolar membrane became clearer after incubating for 150 min. After ON incubation, all cells in the culture showed a typical class E phenotype resulting from the ESCRT machinery disruption by *Vps27* inhibition. Then the culture was incubated again at 23 °C to ensure *Vps27* functionality and reverse the repression of the ESCRT function. As seen in the fifth column, after incubating the culture for 150 min at 23 °C, the class E phenotype remains visible, and even after incubating for about six hours, the class E phenotype persisted. Thus, the class E structures appear to be dead-end structures that will not resolve after release of the *vps27-ts* block. For this reason, this system does not seem to be suitable to observe the changes in ESCRT-III composition during the ESCRT-III functional cycle.

3.6 Linking ESCRT-III to non-endosomal functions

The initial idea was to link the ESCRT-III subunit Mos10 (and later also Did2) to non-endosomal functions, since in the classical ESCRT-III complex assembly the protein function still needed to be elucidated. Experiments were carried out based on literature research and unpublished data from our lab to search for the protein's purpose outside the established complex.

3.6.1 Potential association of ESCRT-III with nucleic acids

Upon sucrose density gradient fractionation of ESCRT-III proteins, a massive accumulation of certain ESCRT-III proteins (Did2, Ist1, Vps2 and Vps24) in the middle of the gradients was observed (Heinzle et al., 2019). Since no Snf7 was detected within these fractions, it appeared unlikely that these structures represent normal endosomal ESCRT-III complexes engaged in ILV formation at MVBs. A number of findings point to a nuclear role of ESCRT-III proteins. For instance, for yeast and mammalian cells, it has been shown that ESCRT-III complexes can assemble at the inner nuclear membrane in a Chm7/CHMP7 dependent manner. Further association of ESCRT-III protection against genomic instability by micronuclei formation and additional work on the LEMD2 and ESCRT-III connection to suppress nuclear deformation and DNA damage led to the idea of an ESCRT-III-DNA connection (Vietri et al., 2020, von Appen et al., 2020, Willan et al., 2019).

To test whether an ESCRT-III-DNA/RNA association is responsible for the formation of the observed peaks on our sucrose gradients, cell extracts were treated with DNaseI or RNaseA before sucrose density gradient fractionation. Mg^{2+} was added to the buffer, because nucleases in general require Mg^{2+} as a cofactor. The cell extracts were incubated with the enzymes for 30 min at 37°C before centrifugation. Unfortunately, a direct effect of the enzyme treatment on ESCRT-III complex formation or location could not be verified, since the enzyme treatment caused precipitation of proteins. An example blot developed with anti-Did2 antibodies can be seen in Figure S 41. When the blots were stained with the dye Ponceau S, barely any protein bands were visible. Instead, a strong band in the range of 17 kDa was observed, which probably corresponds to the added RNaseA enzyme.

Although the initial idea was abandoned, a remarkable effect was noted. The incubation of the cell extracts at 37°C before centrifugation led to a massive accumulation of Did2 in the heavy fractions of the gradient. The effect was even detectable without addition of enzymes or other additives (Figure 49).

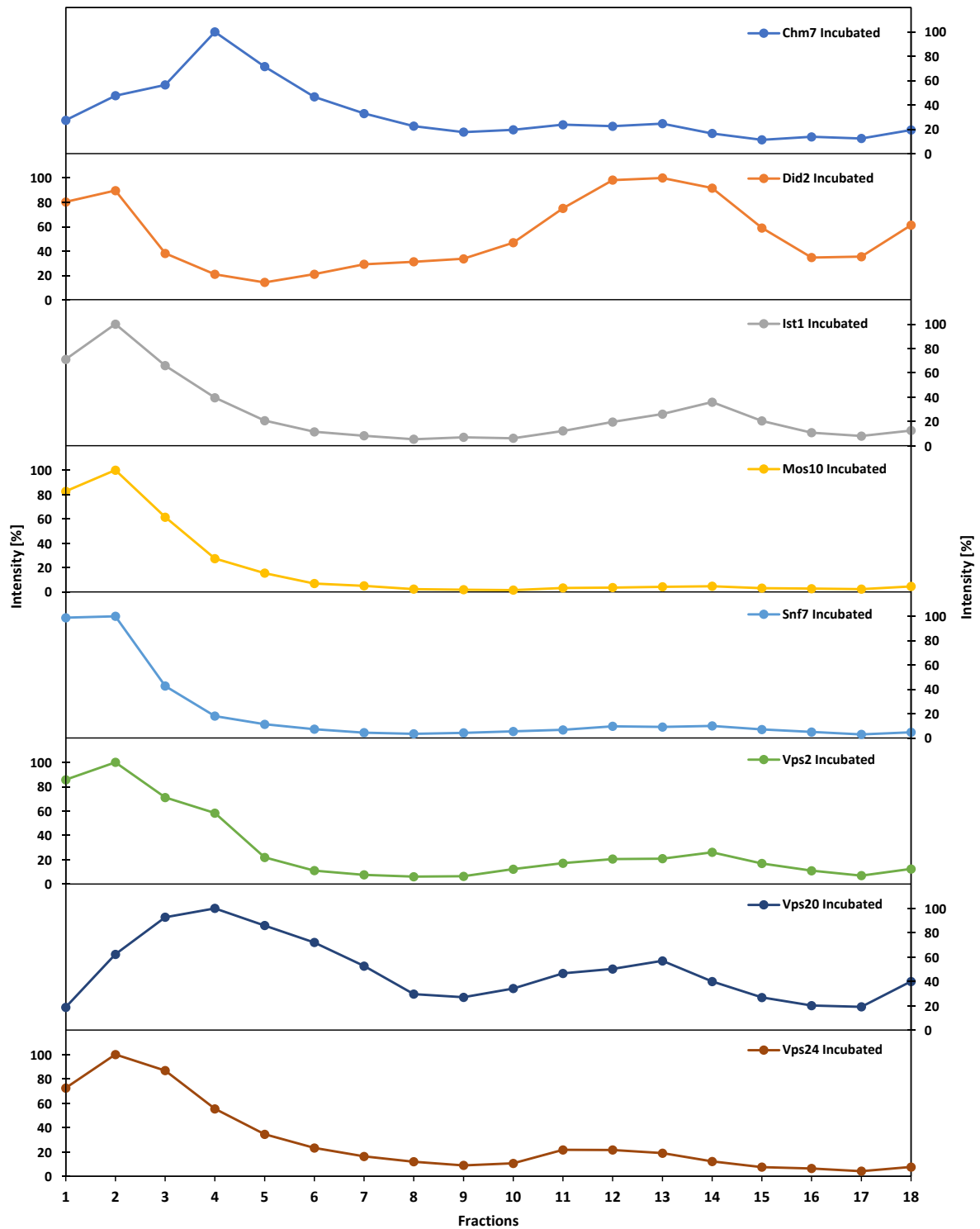


Figure 49: ESCRT-III distribution on sucrose density gradients after pre-incubation.

Sucrose density fractionation into 18 fractions based on the sedimentation rate of all ESCRT-III proteins after incubation for 30 min at 37 °C in SPBS10 buffer.

The profiles in Figure 49 can be directly compared to the profiles in Figure 44, where no pre-incubation of cell extracts was performed. Did2 showed a pronounced peak around fraction 13 after pre-incubation. Similar, but smaller effects could also be observed for Ist1, Vps20 and

Vps24. This effect does not depend on Vps68, since the profiles were unchanged in the *VPS68* deletion strain RKY3222 (Figure S 43). A flotation experiment was carried out and compared with the sucrose gradient data to exclude an experimental artifact (Figure 50).

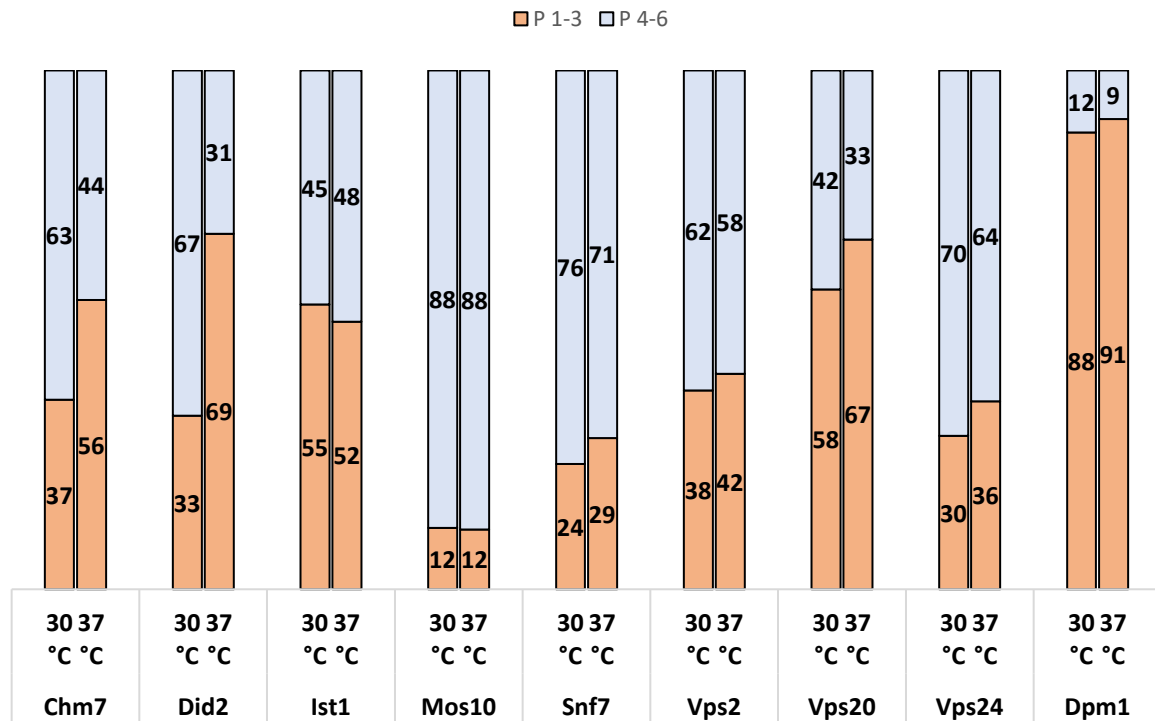


Figure 50: Flotation experiment with WT strain RKY1558 with and without incubation.

Comparison of the flotation experiments by analyzing the WB results with ImageJ and calculating the protein distribution into the P1-3 or 4-6 fraction groups.

Comparing the results of the untreated cell extracts with the heat-treated cell extracts revealed changes in the distribution of the ESCRT-III members Chm7 and Did2. These proteins showed a marked increase of the floating membrane fraction (P1-3), which at least for Did2 correlates nicely with the results gained by the sucrose gradients. For Did2, the membrane associated fraction increased by a factor of two (33 % to 69 %). On the other hand, proteins that do not seem to be affected by the heat treatment on the sucrose gradients also do not show an altered distribution in the flotation experiment as seen for Mos10, which remains the least membrane-associated protein of the entire ESCRT-III family. The Dpm1 marker protein was also examined in the flotation experiment to control for a general effect of heat treatment on the membrane proteins. Dpm1 was only slightly increased in the membrane fraction (+ 3 %) upon pre-incubation at 37°C. The strong effect on Did2 therefore seems to be specific.

Further, it was tested how GFP tagging affects the distribution of Did2 on sucrose gradients. Therefore, the distribution of native Did2, with and without pre-incubation, and the distribution

of N- or C-terminally tagged Did2 was analyzed. For comparison, the distribution of the marker proteins Alp1, Dpm1, Ilv2 and Pep12 was determined (Figure 51).

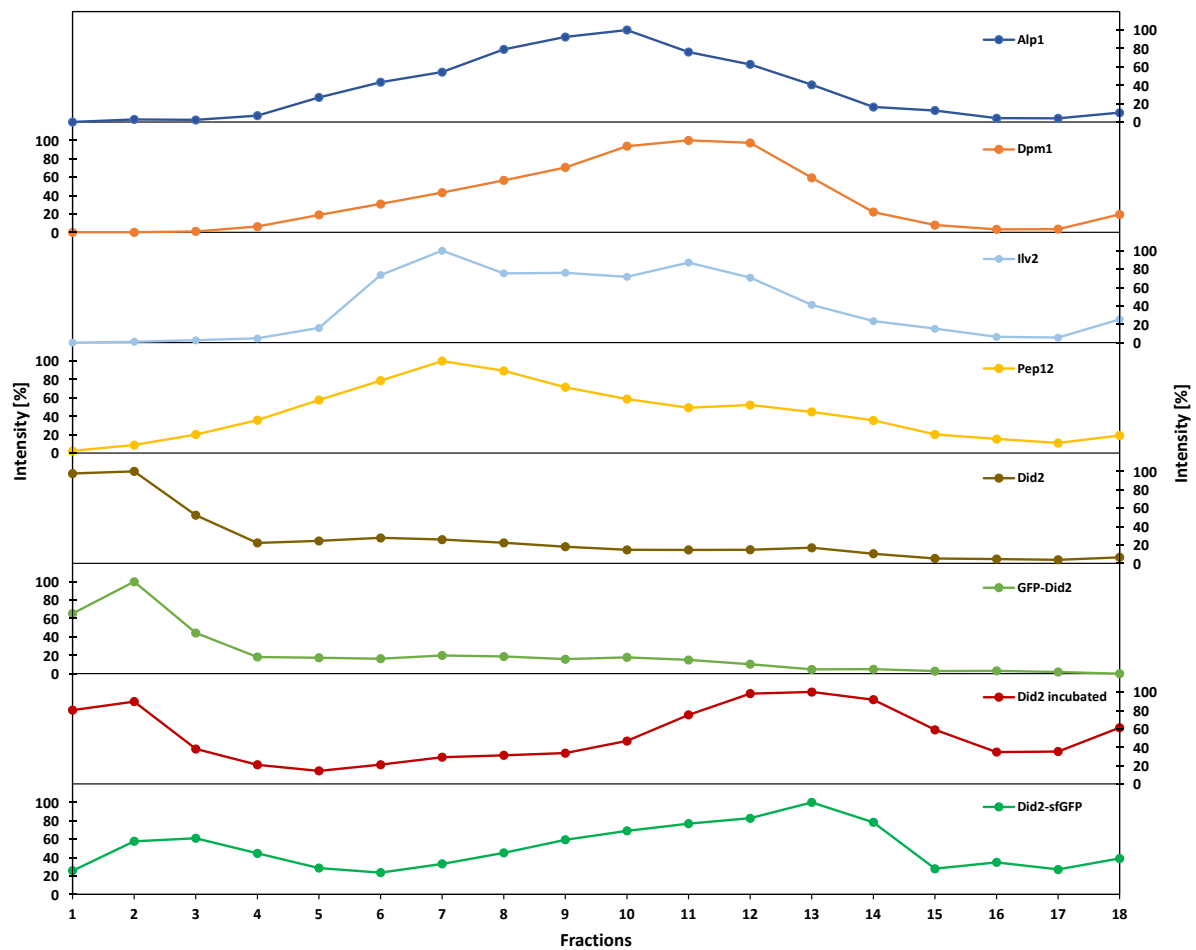


Figure 51: Sucrose gradients of N- & C-terminally tagged Did2 in comparison with marker proteins.

Gradient separation of protein and marker fractions based on the sedimentation rate. Marker proteins Alp1, Dpm1, Ilv2, and Pep12, were chosen to mark subcellular organelles and compare those compartment distributions with the distribution of Did2, incubated Did2, GFP-Did2, and Did2-sfGFP.

The results show that C-terminally tagged Did2-sfGFP had an altered distribution compared to native Did2, with a pronounced peak around fraction 13. Apparently, Did2 function or behavior is compromised by C-terminal tagging. Interestingly, the profile for Did2-sfGFP looked very similar to the profile for native Did2 after pre-incubation at 37°C. Thus, pre-incubation seems to exert the same effect on the protein as C-terminal tagging. One explanation could be that both treatments convert Did2 from a closed into an open conformation, thus leading to an activation of the protein. Activation could result into filament formation and enhanced membrane association of the protein. N-terminal tagging of Did2 did not have this effect. Apparently, sfGFP-Did2 is more wildtype-like. The Did2 peak around fraction 13 does not coincide with any of the markers tested.

The tag position also affected Did2 staining pattern under fluorescence microscope (Figure 52). In both cases dot-like structures, presumably endosomes, were observed, but in case of the C-terminally tagged protein the dots were more numerous and brighter than in the case of the N-terminally tagged protein. This is in line with the sucrose gradient results, which show that more C-terminally tagged protein is at the membrane compared to the N-terminally tagged protein.

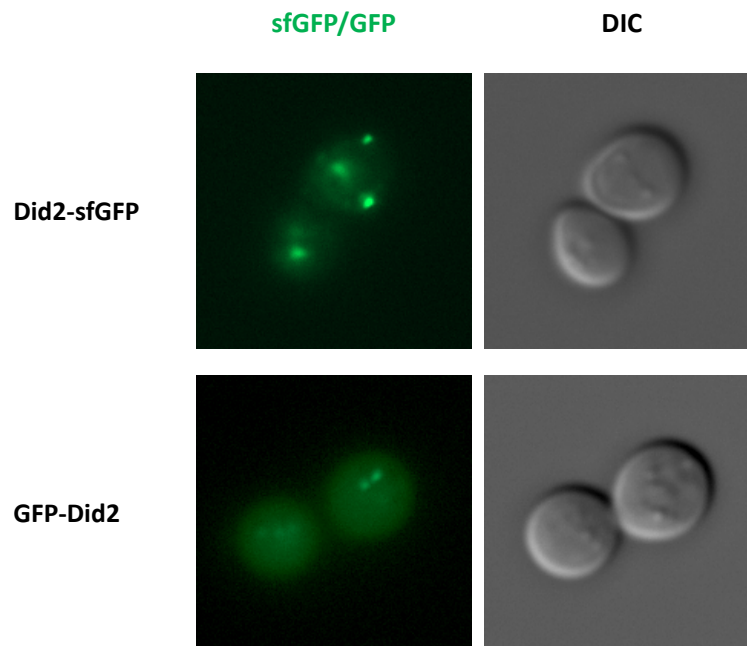


Figure 52: C- & N-terminal tagging of Did2 by GFP/sfGFP.

Monitoring protein distribution by n-terminal tagged GFP-Did2 and c-terminal tagged Did2-sfGFP under a fluorescence microscope with equal set exposure times.

3.6.2 P-bodies and stress markers

Due to experiments done in our lab, 2-hybrid interactions between Mos10 and the ER/Golgi associated proteins Ltc2 and Emp47 were detected. This could point to a function of Mos10 at the ER. Functions for ESCRT-III proteins at the ER have been described. For instance, it could be shown that RNA viruses, heterologously expressed in yeast, mature in ER invaginations and that the maturation is ESCRT-III dependent. Such viruses normally do not exist in yeast, thus there must be a natural process that is hijacked by the viruses. A potential process could be P-body formation, which has been shown to occur at the ER membrane.

Therefore, it was examined whether different P-body and stress markers are associated with Mos10 or the ESCRT-III machinery (Kilchert et al., 2010). P-body markers were tagged with sfGFP and their distribution was visualized by fluorescence microscopy in the WT (RKY1558), $\Delta mos10$ (RKY2892), and $\Delta 8$ (RKY2844) strains under native conditions and after incubating at 37 °C for 30 min or treatment with 0.5 % (w/v) NaN₃, which are P-body inducing conditions.

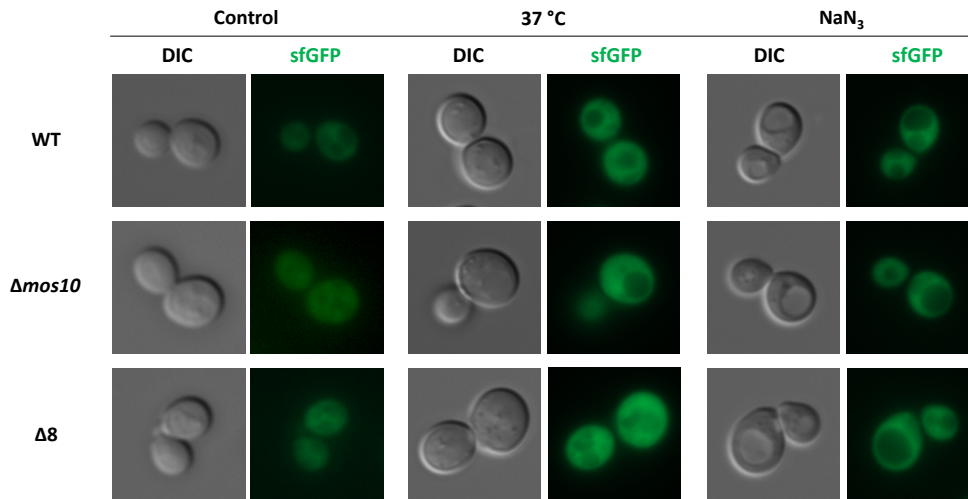


Figure 53: Heat and sodium azide-induced stress granule formation visualized by Pub1-sfGFP.

WT (RKY1558), *Δmos10* (RKY2892), and *Δ8* (RKY2844) strains were grown in YPD media as the control sample. Additionally, cell cultures were either incubated at 37 °C for 30 min or treated with the addition of 0.5 % (w/v) NaN₃ to induce a stress response and thus the formation of compartments identified by Pub1-sfGFP.

For Pub1-sfGFP, the fluorescence signal appears uniformly distributed inside the cell regardless of the strain background or condition used (Figure 53). The only difference noted was an increase in signal intensity upon incubation at 37°C. In all cases, the vacuolar space can be identified due to a lack of fluorescence signal. In contrast to reports in the literature, no P-bodies were formed under these conditions. Lack of P-body formation could be a property of our strain background used. Thus, conclusion about the contribution of Mos10 or ESCRT-III to P-body formation cannot be made by this experiment.

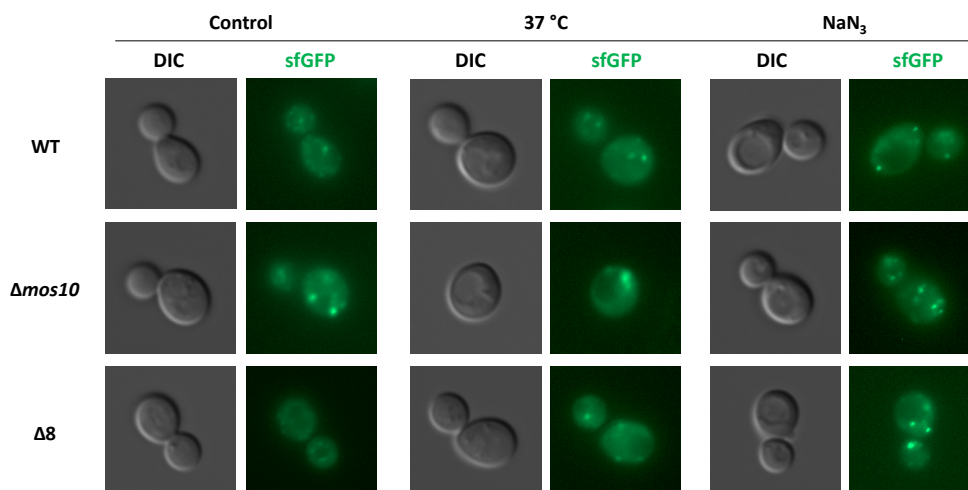


Figure 54: Heat and sodium azide-induced replication stress visualized by Dcp2-sfGFP.

WT (RKY1558), *Δmos10* (RKY2892), and *Δ8* (RKY2844) strains were grown in YPD media as the control sample. Additionally, cell cultures were either incubated at 37 °C for 30 min or treated with the addition of 0.5 % (w/v) NaN₃ to induce a stress response and thus the formation of compartments identified by Dcp2-sfGFP.

With the second marker Dcp2-sfGFP, which forms stress-related dots in the cell, distinct dots became visible under native conditions in the WT and the $\Delta mos10$ strain, but not in the $\Delta 8$ strain, which shows more uniformly distributed staining inside the cell. When stressing the cells with heat or azide, all strains show dots distributed in the cell, which do not appear to be associated with a specific compartment. Also, the $\Delta 8$ strain now shows dots with no distinguishable difference to the other strains. Since WT and $\Delta mos10$ strain are similar, a specific Mos10 related function in replication stress response by Dcp2 was excluded.

The last marker tested was Nmd2 involved in the nonsense-mediated mRNA stress response (Figure 55). The cells show similar fluorescence signals under native and heat-treated conditions with a uniformly distributed staining of the cell. When introducing NaN_3 to the cell, dots are formed, which seem primarily associated with the PM. Unfortunately, again all strains behaved the same, thus no specific effect of *MOS10* or ESCRT-III deletion could be demonstrated. In conclusion, none of the marker proteins tested showed an ESCRT-III dependence on P-body or stress granule formation.

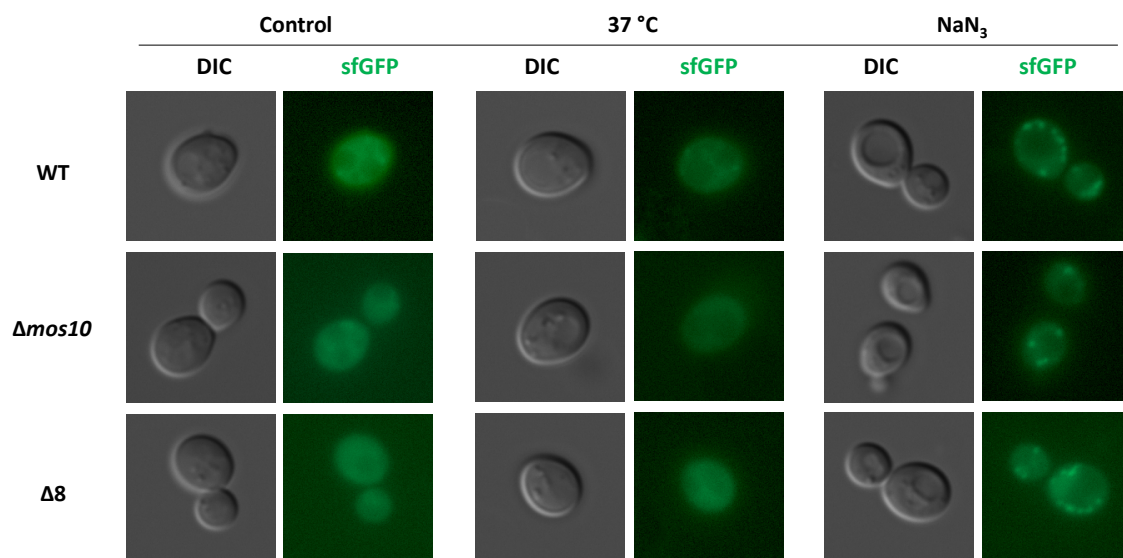


Figure 55: Heat and sodium azide-induced mRNA stress visualized by Nmd2-sfGFP.

WT (RKY1558), $\Delta mos10$ (RKY2892), and $\Delta 8$ (RKY2844) strains were grown in YPD media as the control sample. Additionally, cell cultures were either incubated at 37 °C for 30 min or treated with the addition of 0.5 % (w/v) NaN_3 to induce a stress response and thus the formation of compartments identified by Nmd2-sfGFP.

4 DISCUSSION

4.1 The Mos10 crosslinking pattern

The most consistent result through all different purification experiments done in this thesis is the crosslinking pattern identified by WB analysis of α -Mos10 antibody incubated blots. Since the first batch crosslinking experiment with Mos10-6His, the crosslinking pattern was consistent throughout all experiments showing five bands between 100 kDa and 80 kDa, the lowest two mostly appearing as one fuzzy band but distinguishable by ImageJ analysis. IMAC purification using a peristaltic pump or an AEKTA system, an exchange from Nickel to Cobalt ions, or the introduction of a stepwise or gradient elution compared to the batch experiment did not change the pattern.

An interesting side effect introduced by the gradient elution of crosslinked Mos10-6His coordinated on IMAC columns was the delayed elution of the crosslinked proteins with respect to the non-crosslinked protein. In the classical batch experiment, the entire protein content associated with the Ni-NTA beads is released by heating with SDS, and the resulting supernatant is observed by WB analysis. The elution procedure within the AEKTA system is based on the competing interaction of the poly his tag with the imidazole molecules, which release proteins at higher imidazole concentrations. The effect of imidazole-induced release was reproducible for Mos10-6His with concentrations of 100 mM and more within the standard elution of most content present in the column as shown in Figure 12 and Figure 13, thus following a standard distributed elution profile (Figure 14). However, unlike non-crosslinked Mos10-6His, the proteins from the crosslinking pattern eluted much later at imidazole concentrations of 250 mM and above. There is no magical or unifying imidazole concentration for which all his-tagged proteins tend to elute, since the elution also depends on the accessibility of the his-tag and the oligomeric state of the protein. The accessibility of one Mos10-6His could be altered within a complex formed by crosslinking the protein to many interacting partners. The scenario would most likely lead to a reduced association of the complex to the column due to a weakened binding of the tag, but this was not observed. In contrast, many Mos10-6His tagged proteins could be gathered in a heteromeric protein complex, creating an aggregated protein cluster with multiple Ni-NTA interactions that is harder to release from the column. Instead of being bound to the column by one poly-his tag from a single his tagged protein, the tag of many proteins could lead to a cooperative, tighter binding, thus arresting the complex inside the column. It is worth noting that due to the fact that all crosslinked proteins elute

together, it can be assumed that all crosslinks visible on the WB blot are organized in a single complex.

However, the nature of the crosslinking induced agglomerate or complex remains to be elucidated, since none of the proteins in the crosslinking pattern could be identified in this thesis. The idea was to enrich Mos10-6His and the specific crosslinks in considerable amounts until they become visible on an SDS PAGE gel by either Coomassie or silver staining. In theory, harvesting 1000 OD cells would result in roughly 4 μg Mos10-6His, assuming an average of 3000 molecules per cell (Heinzle et al., 2019). According to the results gained by overexpressing Mos10-6His in *E. coli*, an estimated binding of 25 % would reduce the, in theory, optimal Mos10 harvest to 1 μg . Even if distributed over multiple fractions, a Mos10-6His band and a crosslinking pattern should be detectable on a stained SDS PAGE gel. A visible crosslinking pattern on a Coomassie stained SDS PAGE gel, similar to the one seen on α -Mos10 incubated blots would allow cutting out the exact bands to be analyzed by MS. Due to the high abundance of background proteins still associated with the Ni-NTA column after washing, no distinct band could be linked to the pattern from the WB. Despite the reduction of the total number of proteins co-eluted, even the gradient elution led to no visible banding pattern on a stained SDS PAGE gel, as seen, for example, in Figure 13. The appearance of distinct bands was only achievable by the precipitation experiment using sfGFP tagged Mos10 to pull down interacting partners. In the silver-stained gel in Figure 28, distinct bands became visible, which could be related to the proteins seen on WB. The benefit of silver staining is the increased sensitivity up to 100-fold compared to the Coomassie staining detection limit of roughly 100 ng, allowing the identification of proteins in low nanogram quantities (Mitra et al., 1994, Switzer et al., 1979). However, the multitude of protein bands in the area of interest made it impossible to pinpoint the right crosslink bands.

After identification of the first set of potential interacting partners of Mos10, the candidates were tagged with 13myc to check, if one of the bands of the crosslinking pattern had a reduced mobility on the SDS gel. As described earlier and illustrated in Figure 26, the bands in the Mos10-6His crosslinking pattern were not altered by tagging of any of the candidate proteins. Also the second set of potential interaction partners led to the same result, in part due to the lack of expression of some of the tagged proteins, an effect that needs to be explored further, before dismissing these proteins as Mos10 crosslinking partners.

The most obvious candidates for the crosslinking pattern would be other ESCRT-III subunits, since ESCRT-III proteins were consistently purified as Mos10 interactors. This was tested with deletion strains, where single ESCRT-III genes were deleted in the Mos10-6His background.

Deletion of *CHM7*, *DID2* and *ISTI* had no effect on the crosslinking pattern, thus these proteins can be excluded as crosslinking partners. Loss of the core ESCRT-III units Snf7, Vps2, Vps20, and Vps24 completely wiped out the pattern, thus a contribution of individual ESCRT-III proteins cannot be assessed. At least this result shows that the Mos10 crosslinking pattern is ESCRT-III dependent, i.e. it does not form when ESCRT-III is not formed.

4.2 Choosing a proper tag

This thesis sought to evaluate new Mos10 interacting partners outside the established ESCRT-III complex. As mentioned before, the primary function of Mos10 remains to be elucidated (Remec Pavlin and Hurley, 2020). Different tags were evaluated for their suitability for the purification of Mos10 and its associated proteins. The initially used Mos10 fusion tag was a poly his tag with six consecutive histidine residues attached to the C-terminus of the protein. Due to its small size and lack of charge within the pH range needed for purification, the poly his tag presumably preserves the integrity of the protein's morphology and function (Carson et al., 2007, Waugh, 2005). A drawback of the 6His tag is high background upon purification of yeast proteins. Yeasts naturally code for many proteins with poly-his sequences (>15) and many other yeast proteins stick to the Ni-NTA column. Trying to find a suitable candidate out of thousands of proteins recognized by MS analysis seems like the search for the needle in the haystack.

The introduction of the SILAC technique improved the situation substantially. With this technique, the ESCRT-III proteins Vps2, Did2, Vps24 and Snf7 were consistently identified as Mos10 interaction partners. The most highly enriched protein (with the highest H/L ratio) was Vps2. The other ESCRT-III proteins Did2, Vps24 and Snf7 had a lower enrichment factor. This indicates that Vps2 could be a direct binding partner of Mos10, while the other ESCRT-III proteins are maybe indirectly bound to Mos10 via Vps2. Of note, other Mos10 binding proteins reported in the literature, like Vta1 and Vps4, could not be identified in this thesis. In addition to the ESCRT-III proteins a number of other potential Mos10 interacting proteins were identified, which need to be explored further.

The sfGFP tag appeared to be a good alternative to the 6His tag. The results of the MS analysis showed the highest specificity and yield compared to the other methods like IMAC purification. Although exchanging the tag was suitable for detecting additional potential candidates associated with Mos10, there was a noticeable change in the crosslinking pattern of Mos10 when introducing the sfGFP tag. The chosen tag should not only allow for the efficient purification of interacting proteins, but it should also preserve the function of the tagged

proteins. The comparison of the crosslinking patterns of native Mos10 and Mos10-6His shows that the patterns are largely identical. This indicates that Mos10-6His behaves more or less like wildtype. The reason for the slightly altered pattern with Mos10-sfGFP could be that by putting the relatively large sfGFP tag at the C-terminus of Mos10, Mos10 could be converted from a closed to an open conformation, which leads to an activation of the protein. This is supported by the sucrose density gradient fractionation of wildtype and tagged Mos10. While there was hardly any Mos10 detectable in the membrane fractions, a large peak was obtained for Mos10-sfGFP in the middle of the gradient.

4.3 Choosing suitable Mos10 interaction candidates

As mentioned before, the limited number of candidates tested by co-IP experiments were based on the pre-selection of identified proteins by MS analysis. Candidates were chosen by either their protein size fitting the crosslink pattern, the number of unique peptides detected by MS, or a low CRAPome score. The latter implies that a high score in the CRAPome database results from a protein usually co-purified with other candidates by the applied purification method. However, it should be mentioned that due to the application of the SILAC technique, it is difficult to explain why these potential background proteins are being enriched in only one of the isotopic fractions (heavy or light). A possible explanation could be statistical fluctuations in the detection of peptides during mass spectrometry (significance of detection) and the assignment of the peptides to the corresponding proteins (significance of protein identification). Statistical test would be necessary to resolve these issues. At least three independent replicates of the experiments would be necessary for a statistical analysis. This was, however, not feasible within the scope of this thesis. Thus, it is likely that a certain fraction of the obtained candidates is not real.

Out of the over 80 already pre-selected candidates in Table S 5, many possible candidates were not considered due to the additional criteria mentioned. Sorting out these proteins was necessary to reduce the number of candidates tested in this thesis, but should be considered for further putative Mos10 association when more information becomes available. Since the field of ESCRT involving processes is constantly expanding, mitochondrial proteins like COX4, TIM10, or OAC1 identified by MS, but not connected to ESCRT-III function yet, may be interesting candidates for further study.

Taken together, the only candidate so far, for which an interaction with Mos10 is firmly established is Vps68. An interaction between Mos10 and Vps68 seems highly likely due to the two sets of different co-precipitation experiments applied, resulting in a bi-directional pull-

down of the proteins from either side regardless of the tag. Also, repeatedly peptides of Vps68 could be identified in one of the isotopic fractions by MS analysis, hardening the anticipated Mos10 to Vps68 interaction.

4.4 Influence of *VPS68* deletion

Focusing on the newly found association of Mos10 to Vps68, a set of experiments was performed to examine the influence of Vps68 on ESCRT-III complex formation and function. *VPS68* was initially identified in a genome-wide screen with single deletion strains looking for a CPY sorting phenotype (Bonangelino et al., 2002). Further, genome-wide screening of GFP-tagged proteins led to the localization of Vps68-GFP to the vacuole membrane, further linking Vps68 to endocytic trafficking (Huh et al., 2003). In another study, a global identification screening of endosomal transport factors identified an uncharacterized protein complex of Vps55 and Vps68 believed to act with or downstream of ESCRT in endosomal traffic (Schluter et al., 2008). However, in all screens performed so far, no direct interaction between Vps68 and a particular ESCRT-III subunit was reported. This offers a good starting point to study the protein redistribution and cargo sorting defects by Vps68 depletion.

The sorting of the endocytic cargo protein Ste6 was examined. Under normal conditions, this protein is constitutively endocytosed from the plasma membrane and transported to the vacuole for degradation. Decreased cargo degradation was quantified by a cycloheximide chase with native Ste6 revealing a seven-fold increased half-life of the protein in the *VPS68* deletion compared to WT (Figure 45 & Table 23). Further, the intracellular distribution was studied by fluorescence microscopy. In a wildtype strain, Ste6-GFP staining is seen in the vacuolar lumen and occasionally in some endosomal dots. The Ste6-GFP localization was examined in a *VPS68* deletion strain and compared with mutants of the endocytic pathway, whose defects had been characterized. It turned out that $\Delta vps68$ neither showed a class D phenotype, as in $\Delta vps21$, nor a class E phenotype, as in $\Delta snf7$. The staining resembles the wildtype staining with a more pronounced staining of endosomal dots. Since the *VPS68* deletion does not show the same phenotype as an ESCRT-III deletion, it is unlikely that Vps68 is directly required for the function of ESCRT-III. It rather seems that it acts after ILV formation by ESCRT-III. The results are in line with Ste3-GFP fluorescence images revealing a similar phenotype (Schluter et al., 2008). Both cargoes (Ste3 & Ste6) demonstrate a decreased but still present occupation inside the vacuolar lumen in a $\Delta vps68$ strain underlying the assumption of functional MVB sorting, but inhibited cargo delivery from the late endosome to the vacuole.

Assuming a perturbation downstream of the ESCRT-III complex by a functional MVB sorting but disturbed cargo delivery from the late endosome, changes of the ESCRT-III composition were investigated. After all, the initial identification of Vps68 was made by associating the protein to the ESCRT-III subunit Mos10, assuming a functional connection between the proteins. A divergent behavior towards Vps68 depletion was observed between the ESCRT-III core subunits compared to the so-called ESCRT-III associated members. In cells lacking Vps68, the concentration of the core components Snf7, Vps2 and Vps24 was higher in the ESCRT-III complex compared to wildtype, while the concentration of ESCRT-III associated proteins Did2, Ist1 and Mos10 was lower. Following the current model of a step-wise assembly of the ESCRT-III complex, the data suggest that in the $\Delta vps68$ mutant ESCRT-III is arrested at a certain state of the ESCRT-III functional cycle with an increased number of the core subunits and lower number of associated subunits. The results are in line with previous findings that cells lacking Mos10 and Vta1 accumulate ESCRT-III at the endosome (Nickerson et al., 2010), which is assumed to be the result of reduced disassembly of ESCRT-III by Vps4. However, in this thesis, a Vps68 induced alteration in Vps4 function on ESCRT-III disassembly could not be examined.

The Mos10-sfGFP staining changes dramatically when Vps68 is missing. It is no longer associated with the vacuole, but is dispersed into smaller vesicles, which tend to be enriched at the cell cortex. Tagged variants of Vps68, like Vps68-sfGFP or Vps68-mCherry, cause a partial relocation of Mos10 not as severe as the *VPS68* knockout. This indicates that the tagged variants are only partially functional. Mos10-sfGFP is not a functional protein, but it appears to preserve part of its functions, like the ability to bind to ESCRT-III complexes. Previous work has suggested that Mos10 is not required for ILV formation, but acts at a later stage, probably at the disassembly step. Thus, it is reasonable to assume that ESCRT-III disassembly is blocked in the Mos10-sfGFP strain. This could explain why we see Mos10-sfGFP at the vacuolar membrane, because in this scenario disassembly resistant ESCRT-III complexes would pile up at the vacuolar membrane. At the same time, we would have to assume that disassembly of ESCRT-III is a prerequisite for fusion of MVBs with the vacuolar membrane, i.e. the presence of ESCRT-III complexes blocks fusion. Now in the *VPS68* deletion, Mos10-sfGFP does not accumulate at the vacuolar membrane. This could mean that Vps68 is required for the transition of a post-ILV ESCRT-III complex to a disassembly-competent complex or that it is required for tethering MVBs to the vacuolar membrane.

Besides the redistribution seen by fluorescence microscopy, an altered fractionation of Mos10 or, in general, ESCRT-III subunits by *VPS68* deletion could not be observed. Slight changes in

the cytosolic and membrane-associated fractions are likely caused by variations during the experiment rather than by the loss of Vps68. Amongst all ESCRT-III members, Mos10 remained mostly cytosolic, as shown by flotation and sucrose gradient fractionation. The reason for this could be that Mos10 associates only transiently with ESCRT-III followed by rapid disassembly of the complex. The situation is different though for Mos10-sfGFP, which seems to be blocked in disassembly. This variant accumulates to substantial levels at membranes as exemplified by the sucrose gradients.

The Mos10 localization to cortical structures in $\Delta vps68$ strain background was further investigated. For instance, by dual tagging with a number of cortical marker proteins, like the ER-PM contact site markers Ist2 and Tcb1, no co-localization with Mos10 with these structures could be detected (Figure S 49). Further, in preliminary experiments the contribution of Vps55 to Vps68 function was explored. Vps55 is supposed to form a complex with Vps68. The double mutant $\Delta vps68 \Delta vps55$ showed the same Mos10-sfGFP staining as the single $\Delta vps68$ mutant (Figure S 50) supporting the view that both proteins are in one complex.

4.5 Non-endosomal functions

In addition to the multitude of different processes already established to be influenced by ESCRT-III, new non-endosomal functions were tried to be discovered. As mentioned in 4.3, putative interacting partners of Mos10 were identified by MS analysis after crosslinking and purification of the tagged proteins, leading to the assumption of still unknown functions to be uncovered. For instance, the trafficking of fatty acids from lipid droplets to mitochondria was recently found to be influenced by ESCRT-III (Wang et al., 2021).

The involvement of ESCRT-III in the response of yeast to stress conditions was explored further. For instance, the stress-induced formation of stress granules or P-bodies was investigated, but no connection to ESCRT-III could be established. By considering more stress conditions, an effect may well be visible. After all, the lab conditions do not reflect the environmental circumstances yeast strains have to withstand outside the established standard habitat, facing oxidative stress, exposure to xenobiotics, arsenates, heavy metal ions, besides tolerating ethanol concentrations up to 20 % (v/v) (Casey and Ingledew, 1986, Aung-Htut et al., 2012, Thorsen et al., 2009).

The behavior of Did2 upon sucrose density fractionation also points to a non-endosomal function of at least this ESCRT-III protein. Did2 accumulates markedly at membranes upon incubation of the cell extracts at 37°C before sucrose gradient fractionation. The relocation was further confirmed by the flotation experiment reducing the cytosolic fraction of Did2 by 50 %

towards the membrane-bound fraction. The reason for this effect is unclear, but it could be related to osmotic stress. It has been reported that ESCRT-III associates with the plasma membrane and also with endosomes under hyperosmotic conditions, i.e. when membrane tension is reduced. Since high sucrose concentrations are employed in sucrose density gradient fractionation, this may well lead to loss of water from endosomes, which would reduce membrane tension in these organelles. This is an exciting topic that should be explored further.

5 LITERATURE

- Adell MA, Vogel GF, Pakdel M, Muller M, Lindner H, Hess MW, Teis D (2014) Coordinated binding of Vps4 to ESCRT-III drives membrane neck constriction during MVB vesicle formation. *J Cell Biol* 205: 33-49 doi: 10.1083/jcb.201310114
- Alam SL, Sun J, Payne M, Welch BD, Blake BK, Davis DR, Meyer HH, Emr SD, Sundquist WI (2004) Ubiquitin interactions of NZF zinc fingers. *EMBO J* 23: 1411-1421 doi: 10.1038/sj.emboj.7600114
- Allison R, Lumb JH, Fassier C, Connell JW, Ten Martin D, Seaman MN, Hazan J, Reid E (2013) An ESCRT-spastin interaction promotes fission of recycling tubules from the endosome. *J Cell Biol* 202: 527-543 doi: 10.1083/jcb.201211045
- Ambrose CT (2006) The Osler slide, a demonstration of phagocytosis from 1876 Reports of phagocytosis before Metchnikoff's 1880 paper. *Cell Immunol* 240: 1-4 doi: 10.1016/j.cellimm.2006.05.008
- Aung-Htut MT, Ayer A, Breitenbach M, Dawes IW (2012) Oxidative stresses and ageing. *Subcell Biochem* 57: 13-54 doi: 10.1007/978-94-007-2561-4_2
- Azmi IF, Davies BA, Xiao J, Babst M, Xu Z, Katzmann DJ (2008) ESCRT-III family members stimulate Vps4 ATPase activity directly or via Vta1. *Dev Cell* 14: 50-61 doi: 10.1016/j.devcel.2007.10.021
- Babst M, Katzmann DJ, Estepa-Sabal EJ, Meerloo T, Emr SD (2002a) Escrt-III: an endosome-associated heterooligomeric protein complex required for mvb sorting. *Dev Cell* 3: 271-282 doi: 10.1016/s1534-5807(02)00220-4
- Babst M, Katzmann DJ, Snyder WB, Wendland B, Emr SD (2002b) Endosome-associated complex, ESCRT-II, recruits transport machinery for protein sorting at the multivesicular body. *Dev Cell* 3: 283-289 doi: 10.1016/s1534-5807(02)00219-8
- Babst M, Wendland B, Estepa EJ, Emr SD (1998) The Vps4p AAA ATPase regulates membrane association of a Vps protein complex required for normal endosome function. *EMBO J* 17: 2982-2993 doi: 10.1093/emboj/17.11.2982
- Baietti MF, Zhang Z, Mortier E, Melchior A, Degeest G, Geeraerts A, Ivarsson Y, Depoortere F, Coomans C, Vermeiren E, Zimmermann P, David G (2012) Syndecan-syntenin-ALIX regulates the biogenesis of exosomes. *Nat Cell Biol* 14: 677-685 doi: 10.1038/ncb2502

- Bajorek M, Schubert HL, McCullough J, Langelier C, Eckert DM, Stubblefield WM, Uter NT, Myszka DG, Hill CP, Sundquist WI (2009) Structural basis for ESCRT-III protein autoinhibition. *Nat Struct Mol Biol* 16: 754-762 doi: 10.1038/nsmb.1621
- Bassham DC, Gal S, da Silva Conceicao A, Raikhel NV (1995) An Arabidopsis syntaxin homologue isolated by functional complementation of a yeast pep12 mutant. *Proc Natl Acad Sci U S A* 92: 7262-7266 doi: 10.1073/pnas.92.16.7262
- Bauer I, Brune T, Preiss R, Kolling R (2015) Evidence for a Nonendosomal Function of the *Saccharomyces cerevisiae* ESCRT-III-Like Protein Chm7. *Genetics* 201: 1439-1452 doi: 10.1534/genetics.115.178939
- Baum DA, Baum B (2014) An inside-out origin for the eukaryotic cell. *BMC Biol* 12: 76 doi: 10.1186/s12915-014-0076-2
- Baumgartel V, Ivanchenko S, Dupont A, Sergeev M, Wiseman PW, Krausslich HG, Brauchle C, Muller B, Lamb DC (2011) Live-cell visualization of dynamics of HIV budding site interactions with an ESCRT component. *Nat Cell Biol* 13: 469-474 doi: 10.1038/ncb2215
- Bertin A, de Franceschi N, de la Mora E, Maity S, Alqabandi M, Miguet N, di Cicco A, Roos WH, Mangenot S, Weissenhorn W, Bassereau P (2020) Human ESCRT-III polymers assemble on positively curved membranes and induce helical membrane tube formation. *Nat Commun* 11: 2663 doi: 10.1038/s41467-020-16368-5
- Bonangelino CJ, Chavez EM, Bonifacino JS (2002) Genomic screen for vacuolar protein sorting genes in *Saccharomyces cerevisiae*. *Mol Biol Cell* 13: 2486-2501 doi: 10.1091/mbc.02-01-0005
- Brune T, Kunze-Schumacher H, Kolling R (2019) Interactions in the ESCRT-III network of the yeast *Saccharomyces cerevisiae*. *Curr Genet* 65: 607-619 doi: 10.1007/s00294-018-0915-8
- Bryant NJ, Stevens TH (1998) Vacuole biogenesis in *Saccharomyces cerevisiae*: protein transport pathways to the yeast vacuole. *Microbiol Mol Biol Rev* 62: 230-247 doi: 10.1093/mbr/62.2.230
- Buchkovich NJ, Henne WM, Tang S, Emr SD (2013) Essential N-terminal insertion motif anchors the ESCRT-III filament during MVB vesicle formation. *Dev Cell* 27: 201-214 doi: 10.1016/j.devcel.2013.09.009
- Bullock W (1987) XL1-Blue: a high efficiency plasmid transforming recA *Escherichia coli* strain with beta-galactosidase selection. *Bio Techniques* 5: 376-379 doi: 10.1016/0731-5722(87)90011-1

- Cai H, Reinisch K, Ferro-Novick S (2007) Coats, tethers, Rab, and SNAREs work together to mediate the intracellular destination of a transport vesicle. *Dev Cell* 12: 671-682 doi: 10.1016/j.devcel.2007.04.005
- Carlson LA, Hurley JH (2012) In vitro reconstitution of the ordered assembly of the endosomal sorting complex required for transport at membrane-bound HIV-1 Gag clusters. *Proc Natl Acad Sci U S A* 109: 16928-16933 doi: 10.1073/pnas.1211759109
- Carlton JG, Martin-Serrano J (2007) Parallels between cytokinesis and retroviral budding: a role for the ESCRT machinery. *Science* 316: 1908-1912 doi: 10.1126/science.1143422
- Carson M, Johnson DH, McDonald H, Brouillette C, Delucas LJ (2007) His-tag impact on structure. *Acta Crystallogr D Biol Crystallogr* 63: 295-301 doi: 10.1107/S0907444906052024
- Casey GP, Ingledew WM (1986) Ethanol tolerance in yeasts. *Crit Rev Microbiol* 13: 219-280 doi: 10.3109/10408418609108739
- Chiaruttini N, Redondo-Morata L, Colom A, Humbert F, Lenz M, Scheuring S, Roux A (2015) Relaxation of Loaded ESCRT-III Spiral Springs Drives Membrane Deformation. *Cell* 163: 866-879 doi: 10.1016/j.cell.2015.10.017
- Chu T, Sun J, Saksena S, Emr SD (2006) New component of ESCRT-I regulates endosomal sorting complex assembly. *J Cell Biol* 175: 815-823 doi: 10.1083/jcb.200608053
- Conibear E (2010) Converging views of endocytosis in yeast and mammals. *Curr Opin Cell Biol* 22: 513-518 doi: 10.1016/j.ceb.2010.05.009
- Curtiss M, Jones C, Babst M (2007) Efficient cargo sorting by ESCRT-I and the subsequent release of ESCRT-I from multivesicular bodies requires the subunit Mvb12. *Mol Biol Cell* 18: 636-645 doi: 10.1091/mbc.e06-07-0588
- Day KJ, Casler JC, Glick BS (2018) Budding Yeast Has a Minimal Endomembrane System. *Dev Cell* 44: 56-72 e54 doi: 10.1016/j.devcel.2017.12.014
- De Duve C (1963) The lysosome. *Sci Am* 208: 64-72 doi: 10.1038/scientificamerican0563-64
- Delic M, Valli M, Graf AB, Pfeffer M, Mattanovich D, Gasser B (2013) The secretory pathway: exploring yeast diversity. *FEMS Microbiol Rev* 37: 872-914 doi: 10.1111/1574-6976.12020
- Doherty GJ, McMahon HT (2009) Mechanisms of endocytosis. *Annu Rev Biochem* 78: 857-902 doi: 10.1146/annurev.biochem.78.081307.110540
- Falco SC, Dumas KS, Livak KJ (1985) Nucleotide sequence of the yeast ILV2 gene which encodes acetolactate synthase. *Nucleic Acids Res* 13: 4011-4027 doi: 10.1093/nar/13.11.4011

- Felder S, Miller K, Moehren G, Ullrich A, Schlessinger J, Hopkins CR (1990) Kinase activity controls the sorting of the epidermal growth factor receptor within the multivesicular body. *Cell* 61: 623-634 doi: 10.1016/0092-8674(90)90474-s
- Finlay BJ, Clarke KJ (1999) Ubiquitous dispersal of microbial species. *Nature* 400: 828-828 doi: 10.1038/23616
- Garrus JE, von Schwedler UK, Pornillos OW, Morham SG, Zavitz KH, Wang HE, Wettstein DA, Stray KM, Cote M, Rich RL, Myszka DG, Sundquist WI (2001) Tsg101 and the vacuolar protein sorting pathway are essential for HIV-1 budding. *Cell* 107: 55-65 doi: 10.1016/s0092-8674(01)00506-2
- Gietz RD, Schiestl RH (2007) High-efficiency yeast transformation using the LiAc/SS carrier DNA/PEG method. *Nat Protoc* 2: 31-34 doi: 10.1038/nprot.2007.13
- Gietz RD, Sugino A (1988) New yeast-*Escherichia coli* shuttle vectors constructed with in vitro mutagenized yeast genes lacking six-base pair restriction sites. *Gene* 74: 527-534 doi: 10.1016/0378-1119(88)90185-0
- Gill DJ, Teo H, Sun J, Perisic O, Veprintsev DB, Vallis Y, Emr SD, Williams RL (2007) Structural studies of phosphoinositide 3-kinase-dependent traffic to multivesicular bodies. *Biochem Soc Symp*: 47-57 doi: 10.1042/BSS0740047
- Goldstein JL, Anderson RG, Brown MS (1979) Coated pits, coated vesicles, and receptor-mediated endocytosis. *Nature* 279: 679-685 doi: 10.1038/279679a0
- Goliand I, Nachmias D, Gershony O, Elia N (2014) Inhibition of ESCRT-II-CHMP6 interactions impedes cytokinetic abscission and leads to cell death. *Mol Biol Cell* 25: 3740-3748 doi: 10.1091/mbc.E14-08-1317
- Grissom JH, Segarra VA, Chi RJ (2020) New Perspectives on SNARE Function in the Yeast Minimal Endomembrane System. *Genes (Basel)* 1110.3390/genes11080899
- Gu M, LaJoie D, Chen OS, von Appen A, Ladinsky MS, Redd MJ, Nikolova L, Bjorkman PJ, Sundquist WI, Ullman KS, Frost A (2017) LEM2 recruits CHMP7 for ESCRT-mediated nuclear envelope closure in fission yeast and human cells. *Proc Natl Acad Sci U S A* 114: E2166-E2175 doi: 10.1073/pnas.1613916114
- Guizetti J, Schermelleh L, Mantler J, Maar S, Poser I, Leonhardt H, Muller-Reichert T, Gerlich DW (2011) Cortical constriction during abscission involves helices of ESCRT-III-dependent filaments. *Science* 331: 1616-1620 doi: 10.1126/science.1201847
- Hadders MA, Agromayor M, Obita T, Perisic O, Caballe A, Kloc M, Lamers MH, Williams RL, Martin-Serrano J (2012) ESCRT-III binding protein MITD1 is involved in

- cytokinesis and has an unanticipated PLD fold that binds membranes. *Proc Natl Acad Sci U S A* 109: 17424-17429 doi: 10.1073/pnas.1206839109
- Haglund K, Dikic I (2012) The role of ubiquitylation in receptor endocytosis and endosomal sorting. *J Cell Sci* 125: 265-275 doi: 10.1242/jcs.091280
- Han H, Monroe N, Sundquist WI, Shen PS, Hill CP (2017) The AAA ATPase Vps4 binds ESCRT-III substrates through a repeating array of dipeptide-binding pockets. *Elife* 610.7554/eLife.31324
- Hanson PI, Roth R, Lin Y, Heuser JE (2008) Plasma membrane deformation by circular arrays of ESCRT-III protein filaments. *J Cell Biol* 180: 389-402 doi: 10.1083/jcb.200707031
- Harker-Kirschneck L, Baum B, Saric AE (2019) Changes in ESCRT-III filament geometry drive membrane remodelling and fission in silico. *BMC Biol* 17: 82 doi: 10.1186/s12915-019-0700-2
- Heinzle C, Mucke L, Brune T, Kolling R (2019) Comprehensive analysis of yeast ESCRT-III composition in single ESCRT-III deletion mutants. *Biochem J* 476: 2031-2046 doi: 10.1042/BCJ20190141
- Henne WM, Buchkovich NJ, Zhao Y, Emr SD (2012) The endosomal sorting complex ESCRT-II mediates the assembly and architecture of ESCRT-III helices. *Cell* 151: 356-371 doi: 10.1016/j.cell.2012.08.039
- Hesketh GG, Wartosch L, Davis LJ, Bright NA, Luzio JP (2018) The Lysosome and Intracellular Signalling. *Prog Mol Subcell Biol* 57: 151-180 doi: 10.1007/978-3-319-96704-2_6
- Hierro A, Sun J, Rusnak AS, Kim J, Prag G, Emr SD, Hurley JH (2004) Structure of the ESCRT-II endosomal trafficking complex. *Nature* 431: 221-225 doi: 10.1038/nature02914
- Hoeller D, Volarevic S, Dikic I (2005) Compartmentalization of growth factor receptor signalling. *Curr Opin Cell Biol* 17: 107-111 doi: 10.1016/j.ceb.2005.01.001
- Horii M, Shibata H, Kobayashi R, Katoh K, Yorikawa C, Yasuda J, Maki M (2006) CHMP7, a novel ESCRT-III-related protein, associates with CHMP4b and functions in the endosomal sorting pathway. *Biochem J* 400: 23-32 doi: 10.1042/BJ20060897
- Huh WK, Falvo JV, Gerke LC, Carroll AS, Howson RW, Weissman JS, O'Shea EK (2003) Global analysis of protein localization in budding yeast. *Nature* 425: 686-691 doi: 10.1038/nature02026
- Huotari J, Helenius A (2011) Endosome maturation. *EMBO J* 30: 3481-3500 doi: 10.1038/emboj.2011.286

- Hurley JH (2010) The ESCRT complexes. *Crit Rev Biochem Mol Biol* 45: 463-487 doi: 10.3109/10409238.2010.502516
- Hurley JH (2015) ESCRTs are everywhere. *EMBO J* 34: 2398-2407 doi: 10.15252/emboj.201592484
- Hurley JH, Hanson PI (2010) Membrane budding and scission by the ESCRT machinery: it's all in the neck. *Nat Rev Mol Cell Biol* 11: 556-566 doi: 10.1038/nrm2937
- Im YJ, Hurley JH (2008) Integrated structural model and membrane targeting mechanism of the human ESCRT-II complex. *Dev Cell* 14: 902-913 doi: 10.1016/j.devcel.2008.04.004
- Im YJ, Wollert T, Boura E, Hurley JH (2009) Structure and function of the ESCRT-II-III interface in multivesicular body biogenesis. *Dev Cell* 17: 234-243 doi: 10.1016/j.devcel.2009.07.008
- Janke C, Magiera MM, Rathfelder N, Taxis C, Reber S, Maekawa H, Moreno-Borchart A, Doenges G, Schwob E, Schiebel E, Knop M (2004) A versatile toolbox for PCR-based tagging of yeast genes: new fluorescent proteins, more markers and promoter substitution cassettes. *Yeast* 21: 947-962 doi: 10.1002/yea.1142
- Jimenez AJ, Maiuri P, Lafaurie-Janvire J, Divoux S, Piel M, Perez F (2014) ESCRT machinery is required for plasma membrane repair. *Science* 343: 1247136 doi: 10.1126/science.1247136
- Jung E, Choi TI, Lee JE, Kim CH, Kim J (2020) ESCRT subunit CHMP4B localizes to primary cilia and is required for the structural integrity of the ciliary membrane. *FASEB J* 34: 1331-1344 doi: 10.1096/fj.201901778R
- Kato M, Miyazawa K, Kitamura N (2000) A deubiquitinating enzyme UBPY interacts with the Src homology 3 domain of Hrs-binding protein via a novel binding motif PX(V/I)(D/N)RXXKP. *J Biol Chem* 275: 37481-37487 doi: 10.1074/jbc.M007251200
- Katzmann DJ, Babst M, Emr SD (2001) Ubiquitin-dependent sorting into the multivesicular body pathway requires the function of a conserved endosomal protein sorting complex, ESCRT-I. *Cell* 106: 145-155 doi: 10.1016/s0092-8674(01)00434-2
- Katzmann DJ, Odorizzi G, Emr SD (2002) Receptor downregulation and multivesicular-body sorting. *Nat Rev Mol Cell Biol* 3: 893-905 doi: 10.1038/nrm973
- Katzmann DJ, Stefan CJ, Babst M, Emr SD (2003) Vps27 recruits ESCRT machinery to endosomes during MVB sorting. *J Cell Biol* 162: 413-423 doi: 10.1083/jcb.200302136
- Kieffer C, Skalicky JJ, Morita E, De Domenico I, Ward DM, Kaplan J, Sundquist WI (2008) Two distinct modes of ESCRT-III recognition are required for VPS4 functions in

- lysosomal protein targeting and HIV-1 budding. *Dev Cell* 15: 62-73 doi: 10.1016/j.devcel.2008.05.014
- Kilchert C, Weidner J, Prescianotto-Baschong C, Spang A (2010) Defects in the secretory pathway and high Ca²⁺ induce multiple P-bodies. *Mol Biol Cell* 21: 2624-2638 doi: 10.1091/mbc.E10-02-0099
- Kirchhausen T, Owen D, Harrison SC (2014) Molecular structure, function, and dynamics of clathrin-mediated membrane traffic. *Cold Spring Harb Perspect Biol* 6: a016725 doi: 10.1101/cshperspect.a016725
- Klionsky DJ, Emr SD (1989) Membrane protein sorting: biosynthesis, transport and processing of yeast vacuolar alkaline phosphatase. *EMBO J* 8: 2241-2250 doi:
- Kolling R, Hollenberg CP (1994) The ABC-transporter Ste6 accumulates in the plasma membrane in a ubiquitinated form in endocytosis mutants. *EMBO J* 13: 3261-3271 doi:
- Kostelansky MS, Schluter C, Tam YY, Lee S, Ghirlando R, Beach B, Conibear E, Hurley JH (2007) Molecular architecture and functional model of the complete yeast ESCRT-I heterotetramer. *Cell* 129: 485-498 doi: 10.1016/j.cell.2007.03.016
- Kranz A, Kinner A, Kolling R (2001) A family of small coiled-coil-forming proteins functioning at the late endosome in yeast. *Mol Biol Cell* 12: 711-723 doi: 10.1091/mbc.12.3.711
- Krsmanovic T, Pawelec A, Sydor T, Kolling R (2005) Control of Ste6 recycling by ubiquitination in the early endocytic pathway in yeast. *Mol Biol Cell* 16: 2809-2821 doi: 10.1091/mbc.e04-10-0941
- Kumar B, Roy A, Veettil MV, Chandran B (2018) Insight into the Roles of E3 Ubiquitin Ligase c-Cbl, ESCRT Machinery, and Host Cell Signaling in Kaposi's Sarcoma-Associated Herpesvirus Entry and Trafficking. *J Virol* 92:10.1128/JVI.01376-17
- Lata S, Schoehn G, Solomons J, Pires R, Gottlinger HG, Weissenhorn W (2009) Structure and function of ESCRT-III. *Biochem Soc Trans* 37: 156-160 doi: 10.1042/BST0370156
- Lee HH, Elia N, Ghirlando R, Lippincott-Schwartz J, Hurley JH (2008) Midbody targeting of the ESCRT machinery by a noncanonical coiled coil in CEP55. *Science* 322: 576-580 doi: 10.1126/science.1162042
- Lee S, Chang J, Renvoise B, Tipirneni A, Yang S, Blackstone C (2012) MITD1 is recruited to midbodies by ESCRT-III and participates in cytokinesis. *Mol Biol Cell* 23: 4347-4361 doi: 10.1091/mbc.E12-04-0292
- Lemmon SK, Traub LM (2000) Sorting in the endosomal system in yeast and animal cells. *Curr Opin Cell Biol* 12: 457-466 doi: 10.1016/s0955-0674(00)00117-4

- Lens SMA, Medema RH (2019) Cytokinesis defects and cancer. *Nat Rev Cancer* 19: 32-45 doi: 10.1038/s41568-018-0084-6
- Leung KF, Dacks JB, Field MC (2008) Evolution of the multivesicular body ESCRT machinery; retention across the eukaryotic lineage. *Traffic* 9: 1698-1716 doi: 10.1111/j.1600-0854.2008.00797.x
- Li L, Francke U, Cohen SN (1998) Retraction. The TSG101 tumor susceptibility gene is located in chromosome 11 band p15 and is mutated in human breast cancer. *Cell* 93: following 660 doi: 10.1016/s0092-8674(00)89342-3
- Lindas AC, Karlsson EA, Lindgren MT, Ettema TJ, Bernander R (2008) A unique cell division machinery in the Archaea. *Proc Natl Acad Sci U S A* 105: 18942-18946 doi: 10.1073/pnas.0809467105
- Lipinski KA, Kaniak-Golik A, Golik P (2010) Maintenance and expression of the *S. cerevisiae* mitochondrial genome--from genetics to evolution and systems biology. *Biochim Biophys Acta* 1797: 1086-1098 doi: 10.1016/j.bbabi.2009.12.019
- Loncle N, Agromayor M, Martin-Serrano J, Williams DW (2015) An ESCRT module is required for neuron pruning. *Sci Rep* 5: 8461 doi: 10.1038/srep08461
- Longtine MS, McKenzie A, 3rd, Demarini DJ, Shah NG, Wach A, Brachat A, Philippsen P, Pringle JR (1998) Additional modules for versatile and economical PCR-based gene deletion and modification in *Saccharomyces cerevisiae*. *Yeast* 14: 953-961 doi: 10.1002/(SICI)1097-0061(199807)14:10<953::AID-YEA293>3.0.CO;2-U
- Losko S, Kopp F, Kranz A, Kolling R (2001) Uptake of the ATP-binding cassette (ABC) transporter Ste6 into the yeast vacuole is blocked in the *doa4* Mutant. *Mol Biol Cell* 12: 1047-1059 doi: 10.1091/mbc.12.4.1047
- Lozach PY, Huotari J, Helenius A (2011) Late-penetrating viruses. *Curr Opin Virol* 1: 35-43 doi: 10.1016/j.coviro.2011.05.004
- Lu R, Drubin DG, Sun Y (2016) Clathrin-mediated endocytosis in budding yeast at a glance. *J Cell Sci* 129: 1531-1536 doi: 10.1242/jcs.182303
- Luo Z, Gallwitz D (2003) Biochemical and genetic evidence for the involvement of yeast Ypt6-GTPase in protein retrieval to different Golgi compartments. *J Biol Chem* 278: 791-799 doi: 10.1074/jbc.M209120200
- Luzio JP, Pryor PR, Bright NA (2007) Lysosomes: fusion and function. *Nat Rev Mol Cell Biol* 8: 622-632 doi: 10.1038/nrm2217

- Mast FD, Herricks T, Strehler KM, Miller LR, Saleem RA, Rachubinski RA, Aitchison JD (2018) ESCRT-III is required for scissioning new peroxisomes from the endoplasmic reticulum. *J Cell Biol* 217: 2087-2102 doi: 10.1083/jcb.201706044
- Matusek T, Wendler F, Poles S, Pizette S, D'Angelo G, Furthauer M, Therond PP (2014) The ESCRT machinery regulates the secretion and long-range activity of Hedgehog. *Nature* 516: 99-103 doi: 10.1038/nature13847
- Maxfield FR, McGraw TE (2004) Endocytic recycling. *Nat Rev Mol Cell Biol* 5: 121-132 doi: 10.1038/nrm1315
- McCullough J, Clippinger AK, Talledge N, Skowyra ML, Saunders MG, Naismith TV, Colf LA, Afonine P, Arthur C, Sundquist WI, Hanson PI, Frost A (2015) Structure and membrane remodeling activity of ESCRT-III helical polymers. *Science* 350: 1548-1551 doi: 10.1126/science.aad8305
- McCullough J, Frost A, Sundquist WI (2018) Structures, Functions, and Dynamics of ESCRT-III/Vps4 Membrane Remodeling and Fission Complexes. *Annu Rev Cell Dev Biol* 34: 85-109 doi: 10.1146/annurev-cellbio-100616-060600
- McCullough J, Sundquist WI (2020) Membrane Remodeling: ESCRT-III Filaments as Molecular Garrotes. *Curr Biol* 30: R1425-R1428 doi: 10.1016/j.cub.2020.09.086
- McMillan BJ, Tibbe C, Jeon H, Drabek AA, Klein T, Blacklow SC (2016) Electrostatic Interactions between Elongated Monomers Drive Filamentation of Drosophila Shrub, a Metazoan ESCRT-III Protein. *Cell Rep* 16: 1211-1217 doi: 10.1016/j.celrep.2016.06.093
- Mechnikov I (1908) On the present state of the question of immunity in infectious diseases. *The Nobel Prize in Physiology or Medicine: 1901-1921* doi:
- Meister M, Banfer S, Gartner U, Koskimies J, Amaddii M, Jacob R, Tikkanen R (2017) Regulation of cargo transfer between ESCRT-0 and ESCRT-I complexes by flotillin-1 during endosomal sorting of ubiquitinated cargo. *Oncogenesis* 6: e344 doi: 10.1038/oncsis.2017.47
- Mellacheruvu D, Wright Z, Couzens AL, Lambert JP, St-Denis NA, Li T, Miteva YV, Hauri S, Sardi ME, Low TY, Halim VA, Bagshaw RD, Hubner NC, Al-Hakim A, Bouchard A, Faubert D, Fermin D, Dunham WH, Goudreault M, Lin ZY, Badillo BG, Pawson T, Durocher D, Coulombe B, Aebersold R, Superti-Furga G, Colinge J, Heck AJ, Choi H, Gstaiger M, Mohammed S, Cristea IM, Bennett KL, Washburn MP, Raught B, Ewing RM, Gingras AC, Nesvizhskii AI (2013) The CRAPome: a contaminant repository for

- affinity purification-mass spectrometry data. *Nat Methods* 10: 730-736 doi: 10.1038/nmeth.2557
- Mierzwa BE, Chiaruttini N, Redondo-Morata L, von Filseck JM, Konig J, Larios J, Poser I, Muller-Reichert T, Scheuring S, Roux A, Gerlich DW (2017) Dynamic subunit turnover in ESCRT-III assemblies is regulated by Vps4 to mediate membrane remodelling during cytokinesis. *Nat Cell Biol* 19: 787-798 doi: 10.1038/ncb3559
- Miller S, Krijnse-Locker J (2008) Modification of intracellular membrane structures for virus replication. *Nat Rev Microbiol* 6: 363-374 doi: 10.1038/nrmicro1890
- Mitra P, Pal AK, Basu D, Hati RN (1994) A staining procedure using Coomassie brilliant blue G-250 in phosphoric acid for detection of protein bands with high resolution in polyacrylamide gel and nitrocellulose membrane. *Anal Biochem* 223: 327-329 doi: 10.1006/abio.1994.1594
- Monroe N, Han H, Shen PS, Sundquist WI, Hill CP (2017) Structural basis of protein translocation by the Vps4-Vta1 AAA ATPase. *Elife* 6:10.7554/eLife.24487
- Monroe N, Hill CP (2016) Meiotic Clade AAA ATPases: Protein Polymer Disassembly Machines. *J Mol Biol* 428: 1897-1911 doi: 10.1016/j.jmb.2015.11.004
- Morita E, Sandrin V, McCullough J, Katsuyama A, Baci Hamilton I, Sundquist WI (2011) ESCRT-III protein requirements for HIV-1 budding. *Cell Host Microbe* 9: 235-242 doi: 10.1016/j.chom.2011.02.004
- Moser von Filseck J, Barberi L, Talledge N, Johnson IE, Frost A, Lenz M, Roux A (2020) Anisotropic ESCRT-III architecture governs helical membrane tube formation. *Nat Commun* 11: 1516 doi: 10.1038/s41467-020-15327-4
- Mosesso N, Nagel MK, Isono E (2019) Ubiquitin recognition in endocytic trafficking - with or without ESCRT-0. *J Cell Sci* 132:10.1242/jcs.232868
- Muller M, Schmidt O, Angelova M, Faserl K, Weys S, Kremser L, Pfaffenwimmer T, Dalik T, Kraft C, Trajanoski Z, Lindner H, Teis D (2015) The coordinated action of the MVB pathway and autophagy ensures cell survival during starvation. *Elife* 4: e07736 doi: 10.7554/eLife.07736
- Murphy RF (1991) Maturation models for endosome and lysosome biogenesis. *Trends Cell Biol* 1: 77-82 doi: 10.1016/0962-8924(91)90022-2
- Nabhan JF, Hu R, Oh RS, Cohen SN, Lu Q (2012) Formation and release of arrestin domain-containing protein 1-mediated microvesicles (ARMs) at plasma membrane by recruitment of TSG101 protein. *Proc Natl Acad Sci U S A* 109: 4146-4151 doi: 10.1073/pnas.1200448109

- Nakatogawa H, Suzuki K, Kamada Y, Ohsumi Y (2009) Dynamics and diversity in autophagy mechanisms: lessons from yeast. *Nat Rev Mol Cell Biol* 10: 458-467 doi: 10.1038/nrm2708
- Nguyen HC, Talledge N, McCullough J, Sharma A, Moss FR, 3rd, Iwasa JH, Vershinin MD, Sundquist WI, Frost A (2020) Membrane constriction and thinning by sequential ESCRT-III polymerization. *Nat Struct Mol Biol* 27: 392-399 doi: 10.1038/s41594-020-0404-x
- Nickerson DP, West M, Henry R, Odorizzi G (2010) Regulators of Vps4 ATPase activity at endosomes differentially influence the size and rate of formation of intraluminal vesicles. *Mol Biol Cell* 21: 1023-1032 doi: 10.1091/mbc.E09-09-0776
- Obita T, Saksena S, Ghazi-Tabatabai S, Gill DJ, Perisic O, Emr SD, Williams RL (2007) Structural basis for selective recognition of ESCRT-III by the AAA ATPase Vps4. *Nature* 449: 735-739 doi: 10.1038/nature06171
- Oestreich AJ, Davies BA, Payne JA, Katzmann DJ (2007) Mvb12 is a novel member of ESCRT-I involved in cargo selection by the multivesicular body pathway. *Mol Biol Cell* 18: 646-657 doi: 10.1091/mbc.e06-07-0601
- Olmos Y, Hodgson L, Mantell J, Verkade P, Carlton JG (2015) ESCRT-III controls nuclear envelope reformation. *Nature* 522: 236-239 doi: 10.1038/nature14503
- Olmos Y, Perdrix-Rosell A, Carlton JG (2016) Membrane Binding by CHMP7 Coordinates ESCRT-III-Dependent Nuclear Envelope Reformation. *Curr Biol* 26: 2635-2641 doi: 10.1016/j.cub.2016.07.039
- Orlean P (1990) Dolichol phosphate mannose synthase is required in vivo for glycosyl phosphatidylinositol membrane anchoring, O mannosylation, and N glycosylation of protein in *Saccharomyces cerevisiae*. *Mol Cell Biol* 10: 5796-5805 doi: 10.1128/mcb.10.11.5796-5805.1990
- Palade GE (1955) A small particulate component of the cytoplasm. *J Biophys Biochem Cytol* 1: 59-68 doi: 10.1083/jcb.1.1.59
- Papadopoulos C, Meyer H (2017) Detection and Clearance of Damaged Lysosomes by the Endo-Lysosomal Damage Response and Lysophagy. *Curr Biol* 27: R1330-R1341 doi: 10.1016/j.cub.2017.11.012
- Pfifzner AK, Mercier V, Jiang X, Moser von Filseck J, Baum B, Saric A, Roux A (2020) An ESCRT-III Polymerization Sequence Drives Membrane Deformation and Fission. *Cell* 182: 1140-1155 e1118 doi: 10.1016/j.cell.2020.07.021

- Piper RC, Cooper AA, Yang H, Stevens TH (1995) VPS27 controls vacuolar and endocytic traffic through a prevacuolar compartment in *Saccharomyces cerevisiae*. *J Cell Biol* 131: 603-617 doi: 10.1083/jcb.131.3.603
- Piper RC, Katzmann DJ (2007) Biogenesis and function of multivesicular bodies. *Annu Rev Cell Dev Biol* 23: 519-547 doi: 10.1146/annurev.cellbio.23.090506.123319
- Piper RC, Lehner PJ (2011) Endosomal transport via ubiquitination. *Trends Cell Biol* 21: 647-655 doi: 10.1016/j.tcb.2011.08.007
- Prag G, Watson H, Kim YC, Beach BM, Ghirlando R, Hummer G, Bonifacino JS, Hurley JH (2007) The Vps27/Hse1 complex is a GAT domain-based scaffold for ubiquitin-dependent sorting. *Dev Cell* 12: 973-986 doi: 10.1016/j.devcel.2007.04.013
- Radulovic M, Schink KO, Wenzel EM, Nahse V, Bongiovanni A, Lafont F, Stenmark H (2018) ESCRT-mediated lysosome repair precedes lysophagy and promotes cell survival. *EMBO J* 37: 10.15252/embj.201899753
- Raiborg C, Bache KG, Mehlum A, Stenmark H (2001) Function of Hrs in endocytic trafficking and signalling. *Biochem Soc Trans* 29: 472-475 doi: 10.1042/bst0290472
- Raiborg C, Stenmark H (2009) The ESCRT machinery in endosomal sorting of ubiquitylated membrane proteins. *Nature* 458: 445-452 doi: 10.1038/nature07961
- Raiborg C, Wesche J, Malerod L, Stenmark H (2006) Flat clathrin coats on endosomes mediate degradative protein sorting by scaffolding Hrs in dynamic microdomains. *J Cell Sci* 119: 2414-2424 doi: 10.1242/jcs.02978
- Raymond CK, Howald-Stevenson I, Vater CA, Stevens TH (1992) Morphological classification of the yeast vacuolar protein sorting mutants: evidence for a prevacuolar compartment in class E vps mutants. *Mol Biol Cell* 3: 1389-1402 doi: 10.1091/mbc.3.12.1389
- Remec Pavlin M, Hurley JH (2020) The ESCRTs - converging on mechanism. *J Cell Sci* 133: 10.1242/jcs.240333
- Ren J, Kee Y, Huibregtse JM, Piper RC (2007) Hse1, a component of the yeast Hrs-STAM ubiquitin-sorting complex, associates with ubiquitin peptidases and a ligase to control sorting efficiency into multivesicular bodies. *Mol Biol Cell* 18: 324-335 doi: 10.1091/mbc.e06-06-0557
- Ren X, Hurley JH (2010) VHS domains of ESCRT-0 cooperate in high-avidity binding to polyubiquitinated cargo. *EMBO J* 29: 1045-1054 doi: 10.1038/emboj.2010.6

- Ren X, Kloer DP, Kim YC, Ghirlando R, Saidi LF, Hummer G, Hurley JH (2009) Hybrid structural model of the complete human ESCRT-0 complex. *Structure* 17: 406-416 doi: 10.1016/j.str.2009.01.012
- Richter C, West M, Odorizzi G (2007) Dual mechanisms specify Doa4-mediated deubiquitination at multivesicular bodies. *EMBO J* 26: 2454-2464 doi: 10.1038/sj.emboj.7601692
- Rink J, Ghigo E, Kalaidzidis Y, Zerial M (2005) Rab conversion as a mechanism of progression from early to late endosomes. *Cell* 122: 735-749 doi: 10.1016/j.cell.2005.06.043
- Robijns J, Houthaeve G, Braeckmans K, De Vos WH (2018) Loss of Nuclear Envelope Integrity in Aging and Disease. *Int Rev Cell Mol Biol* 336: 205-222 doi: 10.1016/bs.ircmb.2017.07.013
- Robinson JS, Klionsky DJ, Banta LM, Emr SD (1988) Protein sorting in *Saccharomyces cerevisiae*: isolation of mutants defective in the delivery and processing of multiple vacuolar hydrolases. *Mol Cell Biol* 8: 4936-4948 doi: 10.1128/mcb.8.11.4936
- Roth TF, Porter KR (1964) Yolk Protein Uptake in the Oocyte of the Mosquito *Aedes Aegypti*. *J Cell Biol* 20: 313-332 doi: 10.1083/jcb.20.2.313
- Rothman JH, Howald I, Stevens TH (1989) Characterization of genes required for protein sorting and vacuolar function in the yeast *Saccharomyces cerevisiae*. *EMBO J* 8: 2057-2065 doi:
- Sahu R, Kaushik S, Clement CC, Cannizzo ES, Scharf B, Follenzi A, Poticchio I, Nieves E, Cuervo AM, Santambrogio L (2011) Microautophagy of cytosolic proteins by late endosomes. *Dev Cell* 20: 131-139 doi: 10.1016/j.devcel.2010.12.003
- Saksena S, Sun J, Chu T, Emr SD (2007) ESCRTing proteins in the endocytic pathway. *Trends Biochem Sci* 32: 561-573 doi: 10.1016/j.tibs.2007.09.010
- Saksena S, Wahlman J, Teis D, Johnson AE, Emr SD (2009) Functional reconstitution of ESCRT-III assembly and disassembly. *Cell* 136: 97-109 doi: 10.1016/j.cell.2008.11.013
- Samson RY, Obita T, Freund SM, Williams RL, Bell SD (2008) A role for the ESCRT system in cell division in archaea. *Science* 322: 1710-1713 doi: 10.1126/science.1165322
- Scheffer LL, Sreetama SC, Sharma N, Medikayala S, Brown KJ, Defour A, Jaiswal JK (2014) Mechanism of Ca²⁺(+)-triggered ESCRT assembly and regulation of cell membrane repair. *Nat Commun* 5: 5646 doi: 10.1038/ncomms6646

- Schluter C, Lam KK, Brumm J, Wu BW, Saunders M, Stevens TH, Bryan J, Conibear E (2008) Global analysis of yeast endosomal transport identifies the vps55/68 sorting complex. *Mol Biol Cell* 19: 1282-1294 doi: 10.1091/mbc.E07-07-0659
- Schoneberg J, Lee IH, Iwasa JH, Hurley JH (2017) Reverse-topology membrane scission by the ESCRT proteins. *Nat Rev Mol Cell Biol* 18: 5-17 doi: 10.1038/nrm.2016.121
- Schoneberg J, Pavlin MR, Yan S, Righini M, Lee IH, Carlson LA, Bahrami AH, Goldman DH, Ren X, Hummer G, Bustamante C, Hurley JH (2018) ATP-dependent force generation and membrane scission by ESCRT-III and Vps4. *Science* 362: 1423-1428 doi: 10.1126/science.aat1839
- Schopf JW, Kitajima K, Spicuzza MJ, Kudryavtsev AB, Valley JW (2018) SIMS analyses of the oldest known assemblage of microfossils document their taxon-correlated carbon isotope compositions. *Proc Natl Acad Sci U S A* 115: 53-58 doi: 10.1073/pnas.1718063115
- Scott A, Gaspar J, Stuchell-Brereton MD, Alam SL, Skalicky JJ, Sundquist WI (2005) Structure and ESCRT-III protein interactions of the MIT domain of human VPS4A. *Proc Natl Acad Sci U S A* 102: 13813-13818 doi: 10.1073/pnas.0502165102
- Scott CC, Vacca F, Gruenberg J (2014) Endosome maturation, transport and functions. *Semin Cell Dev Biol* 31: 2-10 doi: 10.1016/j.semcdb.2014.03.034
- Scourfield EJ, Martin-Serrano J (2017) Growing functions of the ESCRT machinery in cell biology and viral replication. *Biochem Soc Trans* 45: 613-634 doi: 10.1042/BST20160479
- Shestakova A, Hanono A, Drosner S, Curtiss M, Davies BA, Katzmann DJ, Babst M (2010) Assembly of the AAA ATPase Vps4 on ESCRT-III. *Mol Biol Cell* 21: 1059-1071 doi: 10.1091/mbc.E09-07-0572
- Shiflett SL, Ward DM, Huynh D, Vaughn MB, Simmons JC, Kaplan J (2004) Characterization of Vta1p, a class E Vps protein in *Saccharomyces cerevisiae*. *J Biol Chem* 279: 10982-10990 doi: 10.1074/jbc.M312669200
- Shim S, Kimpler LA, Hanson PI (2007) Structure/function analysis of four core ESCRT-III proteins reveals common regulatory role for extreme C-terminal domain. *Traffic* 8: 1068-1079 doi: 10.1111/j.1600-0854.2007.00584.x
- Skibinski G, Parkinson NJ, Brown JM, Chakrabarti L, Lloyd SL, Hummerich H, Nielsen JE, Hodges JR, Spillantini MG, Thusgaard T, Brandner S, Brun A, Rossor MN, Gade A, Johannsen P, Sorensen SA, Gydesen S, Fisher EM, Collinge J (2005) Mutations in the

- endosomal ESCRTIII-complex subunit CHMP2B in frontotemporal dementia. *Nat Genet* 37: 806-808 doi: 10.1038/ng1609
- Skjeldal FM, Haugen LH, Mateus D, Frei DM, Rodseth AV, Hu X, Bakke O (2021) De novo formation of early endosomes during Rab5 to Rab7 transition. *J Cell Sci* 10.1242/jcs.254185
- Skowrya ML, Schlesinger PH, Naismith TV, Hanson PI (2018) Triggered recruitment of ESCRT machinery promotes endolysosomal repair. *Science* 36010.1126/science.aar5078
- Slagsvold T, Aasland R, Hirano S, Bache KG, Raiborg C, Trambaiolo D, Wakatsuki S, Stenmark H (2005) Eap45 in mammalian ESCRT-II binds ubiquitin via a phosphoinositide-interacting GLUE domain. *J Biol Chem* 280: 19600-19606 doi: 10.1074/jbc.M501510200
- Sollner T, Bennett MK, Whiteheart SW, Scheller RH, Rothman JE (1993) A protein assembly-disassembly pathway in vitro that may correspond to sequential steps of synaptic vesicle docking, activation, and fusion. *Cell* 75: 409-418 doi: 10.1016/0092-8674(93)90376-2
- Spang A, Saw JH, Jorgensen SL, Zaremba-Niedzwiedzka K, Martijn J, Lind AE, van Eijk R, Schleper C, Guy L, Ettema TJG (2015) Complex archaea that bridge the gap between prokaryotes and eukaryotes. *Nature* 521: 173-179 doi: 10.1038/nature14447
- Stahelin RV, Long F, Diraviyam K, Bruzik KS, Murray D, Cho W (2002) Phosphatidylinositol 3-phosphate induces the membrane penetration of the FYVE domains of Vps27p and Hrs. *J Biol Chem* 277: 26379-26388 doi: 10.1074/jbc.M201106200
- Stevens TH, Rothman JH, Payne GS, Schekman R (1986) Gene dosage-dependent secretion of yeast vacuolar carboxypeptidase Y. *J Cell Biol* 102: 1551-1557 doi: 10.1083/jcb.102.5.1551
- Strack B, Calistri A, Craig S, Popova E, Gottlinger HG (2003) AIP1/ALIX is a binding partner for HIV-1 p6 and EIAV p9 functioning in virus budding. *Cell* 114: 689-699 doi: 10.1016/s0092-8674(03)00653-6
- Stringer DK, Piper RC (2011) Terminating protein ubiquitination: Hasta la vista, ubiquitin. *Cell Cycle* 10: 3067-3071 doi: 10.4161/cc.10.18.17191
- Stuchell-Brereton MD, Skalicky JJ, Kieffer C, Karren MA, Ghaffarian S, Sundquist WI (2007) ESCRT-III recognition by VPS4 ATPases. *Nature* 449: 740-744 doi: 10.1038/nature06172
- Studier FW (2014) Stable expression clones and auto-induction for protein production in *E. coli*. *Methods Mol Biol* 1091: 17-32 doi: 10.1007/978-1-62703-691-7_2

- Su M, Guo EZ, Ding X, Li Y, Tarrasch JT, Brooks CL, 3rd, Xu Z, Skiniotis G (2017) Mechanism of Vps4 hexamer function revealed by cryo-EM. *Sci Adv* 3: e1700325 doi: 10.1126/sciadv.1700325
- Sun S, Zhou X, Corvera J, Gallick GE, Lin SH, Kuang J (2015) ALG-2 activates the MVB sorting function of ALIX through relieving its intramolecular interaction. *Cell Discov* 1: 15018 doi: 10.1038/celldisc.2015.18
- Sundborger AC, Fang S, Heymann JA, Ray P, Chappie JS, Hinshaw JE (2014) A dynamin mutant defines a superconstricted pre-fission state. *Cell Rep* 8: 734-742 doi: 10.1016/j.celrep.2014.06.054
- Swanson KA, Kang RS, Stamenova SD, Hicke L, Radhakrishnan I (2003) Solution structure of Vps27 UIM-ubiquitin complex important for endosomal sorting and receptor downregulation. *EMBO J* 22: 4597-4606 doi: 10.1093/emboj/cdg471
- Switzer RC, 3rd, Merrill CR, Shifrin S (1979) A highly sensitive silver stain for detecting proteins and peptides in polyacrylamide gels. *Anal Biochem* 98: 231-237 doi: 10.1016/0003-2697(79)90732-2
- Tabata K, Arimoto M, Arakawa M, Nara A, Saito K, Omori H, Arai A, Ishikawa T, Konishi E, Suzuki R, Matsuura Y, Morita E (2016) Unique Requirement for ESCRT Factors in Flavivirus Particle Formation on the Endoplasmic Reticulum. *Cell Rep* 16: 2339-2347 doi: 10.1016/j.celrep.2016.07.068
- Takahashi Y, He H, Tang Z, Hattori T, Liu Y, Young MM, Serfass JM, Chen L, Gebru M, Chen C, Wills CA, Atkinson JM, Chen H, Abraham T, Wang HG (2018) An autophagy assay reveals the ESCRT-III component CHMP2A as a regulator of phagophore closure. *Nat Commun* 9: 2855 doi: 10.1038/s41467-018-05254-w
- Tang S, Buchkovich NJ, Henne WM, Banjade S, Kim YJ, Emr SD (2016) ESCRT-III activation by parallel action of ESCRT-I/II and ESCRT-0/Bro1 during MVB biogenesis. *Elife* 510.7554/eLife.15507
- Teis D, Saksena S, Emr SD (2008) Ordered assembly of the ESCRT-III complex on endosomes is required to sequester cargo during MVB formation. *Dev Cell* 15: 578-589 doi: 10.1016/j.devcel.2008.08.013
- Teis D, Saksena S, Emr SD (2009) SnapShot: the ESCRT machinery. *Cell* 137: 182-182 e181 doi: 10.1016/j.cell.2009.03.027
- Teis D, Saksena S, Judson BL, Emr SD (2010) ESCRT-II coordinates the assembly of ESCRT-III filaments for cargo sorting and multivesicular body vesicle formation. *EMBO J* 29: 871-883 doi: 10.1038/emboj.2009.408

- Teo H, Perisic O, Gonzalez B, Williams RL (2004) ESCRT-II, an endosome-associated complex required for protein sorting: crystal structure and interactions with ESCRT-III and membranes. *Dev Cell* 7: 559-569 doi: 10.1016/j.devcel.2004.09.003
- They C (2011) Exosomes: secreted vesicles and intercellular communications. *F1000 Biol Rep* 3: 15 doi: 10.3410/B3-15
- Thorsen M, Perrone GG, Kristiansson E, Traini M, Ye T, Dawes IW, Nerman O, Tamas MJ (2009) Genetic basis of arsenite and cadmium tolerance in *Saccharomyces cerevisiae*. *BMC Genomics* 10: 105 doi: 10.1186/1471-2164-10-105
- Toshima JY, Toshima J, Kaksonen M, Martin AC, King DS, Drubin DG (2006) Spatial dynamics of receptor-mediated endocytic trafficking in budding yeast revealed by using fluorescent alpha-factor derivatives. *Proc Natl Acad Sci U S A* 103: 5793-5798 doi: 10.1073/pnas.0601042103
- Tuthill TJ, Bubeck D, Rowlands DJ, Hogle JM (2006) Characterization of early steps in the poliovirus infection process: receptor-decorated liposomes induce conversion of the virus to membrane-anchored entry-intermediate particles. *J Virol* 80: 172-180 doi: 10.1128/JVI.80.1.172-180.2006
- Ventimiglia LN, Cuesta-Geijo MA, Martinelli N, Caballe A, Macheboeuf P, Miguet N, Parnham IM, Olmos Y, Carlton JG, Weissenhorn W, Martin-Serrano J (2018) CC2D1B Coordinates ESCRT-III Activity during the Mitotic Reformation of the Nuclear Envelope. *Dev Cell* 47: 547-563 e546 doi: 10.1016/j.devcel.2018.11.012
- Vietri M, Schink KO, Campsteijn C, Wegner CS, Schultz SW, Christ L, Thoresen SB, Brech A, Raiborg C, Stenmark H (2015) Spastin and ESCRT-III coordinate mitotic spindle disassembly and nuclear envelope sealing. *Nature* 522: 231-235 doi: 10.1038/nature14408
- Vietri M, Schultz SW, Bellanger A, Jones CM, Petersen LI, Raiborg C, Skarpen E, Pedurupillay CRJ, Kjos I, Kip E, Timmer R, Jain A, Collas P, Knorr RL, Grellscheid SN, Kusumaatmaja H, Brech A, Micci F, Stenmark H, Campsteijn C (2020) Unrestrained ESCRT-III drives micronuclear catastrophe and chromosome fragmentation. *Nat Cell Biol* 22: 856-867 doi: 10.1038/s41556-020-0537-5
- von Appen A, LaJoie D, Johnson IE, Trnka MJ, Pick SM, Burlingame AL, Ullman KS, Frost A (2020) LEM2 phase separation promotes ESCRT-mediated nuclear envelope reformation. *Nature* 582: 115-118 doi: 10.1038/s41586-020-2232-x
- Votteler J, Sundquist WI (2013) Virus budding and the ESCRT pathway. *Cell Host Microbe* 14: 232-241 doi: 10.1016/j.chom.2013.08.012

- Walther TC, Brickner JH, Aguilar PS, Bernales S, Pantoja C, Walter P (2006) Eisosomes mark static sites of endocytosis. *Nature* 439: 998-1003 doi: 10.1038/nature04472
- Wang J, Fang N, Xiong J, Du Y, Cao Y, Ji WK (2021) An ESCRT-dependent step in fatty acid transfer from lipid droplets to mitochondria through VPS13D-TSG101 interactions. *Nat Commun* 12: 1252 doi: 10.1038/s41467-021-21525-5
- Wang T, Hong W (2006) RILP interacts with VPS22 and VPS36 of ESCRT-II and regulates their membrane recruitment. *Biochem Biophys Res Commun* 350: 413-423 doi: 10.1016/j.bbrc.2006.09.064
- Wang T, Li L, Hong W (2017) SNARE proteins in membrane trafficking. *Traffic* 18: 767-775 doi: 10.1111/tra.12524
- Waugh DS (2005) Making the most of affinity tags. *Trends Biotechnol* 23: 316-320 doi: 10.1016/j.tibtech.2005.03.012
- Webster BM, Thaller DJ, Jager J, Ochmann SE, Borah S, Lusk CP (2016) Chm7 and Heh1 collaborate to link nuclear pore complex quality control with nuclear envelope sealing. *EMBO J* 35: 2447-2467 doi: 10.15252/embj.201694574
- Weinberg J, Drubin DG (2012) Clathrin-mediated endocytosis in budding yeast. *Trends Cell Biol* 22: 1-13 doi: 10.1016/j.tcb.2011.09.001
- Wemmer M, Azmi I, West M, Davies B, Katzmann D, Odorizzi G (2011) Bro1 binding to Snf7 regulates ESCRT-III membrane scission activity in yeast. *J Cell Biol* 192: 295-306 doi: 10.1083/jcb.201007018
- Wideman JG, Leung KF, Field MC, Dacks JB (2014) The cell biology of the endocytic system from an evolutionary perspective. *Cold Spring Harb Perspect Biol* 6: a016998 doi: 10.1101/cshperspect.a016998
- Willan J, Cleasby AJ, Flores-Rodriguez N, Stefani F, Rinaldo C, Pisciottoni A, Grant E, Woodman P, Bryant HE, Ciani B (2019) ESCRT-III is necessary for the integrity of the nuclear envelope in micronuclei but is aberrant at ruptured micronuclear envelopes generating damage. *Oncogenesis* 8: 29 doi: 10.1038/s41389-019-0136-0
- Wood WB (1966) Host specificity of DNA produced by *Escherichia coli*: bacterial mutations affecting the restriction and modification of DNA. *J Mol Biol* 16: 118-133 doi: 10.1016/s0022-2836(66)80267-x
- Woodcock DM, Crowther PJ, Doherty J, Jefferson S, DeCruz E, Noyer-Weidner M, Smith SS, Michael MZ, Graham MW (1989) Quantitative evaluation of *Escherichia coli* host strains for tolerance to cytosine methylation in plasmid and phage recombinants. *Nucleic Acids Res* 17: 3469-3478 doi: 10.1093/nar/17.9.3469

- Xiao J, Xia H, Zhou J, Azmi IF, Davies BA, Katzmann DJ, Xu Z (2008) Structural basis of Vta1 function in the multivesicular body sorting pathway. *Dev Cell* 14: 37-49 doi: 10.1016/j.devcel.2007.10.013
- Yang B, Stjepanovic G, Shen Q, Martin A, Hurley JH (2015) Vps4 disassembles an ESCRT-III filament by global unfolding and processive translocation. *Nat Struct Mol Biol* 22: 492-498 doi: 10.1038/nsmb.3015
- Yang D, Rismanchi N, Renvoise B, Lippincott-Schwartz J, Blackstone C, Hurley JH (2008) Structural basis for midbody targeting of spastin by the ESCRT-III protein CHMP1B. *Nat Struct Mol Biol* 15: 1278-1286 doi: 10.1038/nsmb.1512
- Yang Z, Vild C, Ju J, Zhang X, Liu J, Shen J, Zhao B, Lan W, Gong F, Liu M, Cao C, Xu Z (2012) Structural basis of molecular recognition between ESCRT-III-like protein Vps60 and AAA-ATPase regulator Vta1 in the multivesicular body pathway. *J Biol Chem* 287: 43899-43908 doi: 10.1074/jbc.M112.390724
- Yanguas F, Moscoso-Romero E, Valdivieso MH (2019) Ent3 and GGA adaptors facilitate diverse anterograde and retrograde trafficking events to and from the prevacuolar endosome. *Sci Rep* 9: 10747 doi: 10.1038/s41598-019-47035-5
- Yeo SC, Xu L, Ren J, Boulton VJ, Wagle MD, Liu C, Ren G, Wong P, Zahn R, Sasajala P, Yang H, Piper RC, Munn AL (2003) Vps20p and Vta1p interact with Vps4p and function in multivesicular body sorting and endosomal transport in *Saccharomyces cerevisiae*. *J Cell Sci* 116: 3957-3970 doi: 10.1242/jcs.00751
- Yorikawa C, Shibata H, Waguri S, Hatta K, Horii M, Katoh K, Kobayashi T, Uchiyama Y, Maki M (2005) Human CHMP6, a myristoylated ESCRT-III protein, interacts directly with an ESCRT-II component EAP20 and regulates endosomal cargo sorting. *Biochem J* 387: 17-26 doi: 10.1042/BJ20041227
- Zhang H, Wang Y, Wong JJ, Lim KL, Liou YC, Wang H, Yu F (2014) Endocytic pathways downregulate the L1-type cell adhesion molecule neuroglian to promote dendrite pruning in *Drosophila*. *Dev Cell* 30: 463-478 doi: 10.1016/j.devcel.2014.06.014
- Zhen Y, Spangenberg H, Munson MJ, Brech A, Schink KO, Tan KW, Sorensen V, Wenzel EM, Radulovic M, Engedal N, Simonsen A, Raiborg C, Stenmark H (2020) ESCRT-mediated phagophore sealing during mitophagy. *Autophagy* 16: 826-841 doi: 10.1080/15548627.2019.1639301
- Zhou F, Wu Z, Zhao M, Segev N, Liang Y (2019) Autophagosome closure by ESCRT: Vps21/RAB5-regulated ESCRT recruitment via an Atg17-Snf7 interaction. *Autophagy* 15: 1653-1654 doi: 10.1080/15548627.2019.1628547

6 SUPPLEMENTARY MATERIAL

Table S 1: CSM Single Drop-out media (-Trp left; -His right).

Compound	mg/l	Compound	mg/l
Adenine	10	Adenine	10
L-Arginine	50	L-Arginine	50
L-Aspartic acid	80	L-Aspartic acid	80
L-Histidine HCl	20	L-Isoleucine	50
L-Isoleucine	50	L-Leucine	100
L-Leucine	100	L-Lysine HCl	50
L-Lysine HCl	50	L-Methionine	20
L-Methionine	20	L-Phenylalanine	50
L-Phenylalanine	50	L-Threonine	100
L-Threonine	100	L-Tryptophan	50
L-Tyrosine	50	L-Tyrosine	50
Uracil	20	Uracil	20
Valine	140	Valine	140
Total	740	Total	770

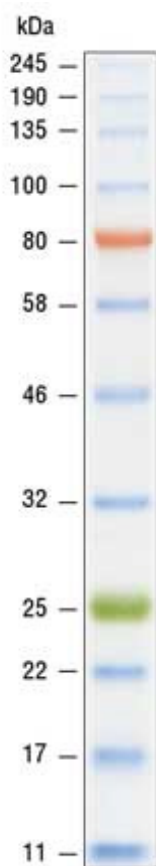


Figure S 1: Color Pre-stained Protein Standard, Broad Range (11–245 kDa).

Table S 2: Corresponding sample concentrations of the gradient purification.

Lane	Sample	Start [%]	End [%]	Start conc. [mM]	End conc. [mM]
7	T4	10	13	50	65
8	T5	13	16	65	80
9	T6	16	19	80	95
10	T7	19	22	95	110
11	T8	22	25	110	125
12	T9	25	28	125	140
13	T10	28	31	140	155
14	T11	31	34	155	170
15	T12	34	37	170	185
16	T13	37	40	185	200
17	T14	40	43	200	215
18	T15	43	46	215	230
19	T16	46	49	230	245
20	T17	49	52	245	260
21	T18	52	55	260	275
22	T19	55	58	275	290
23	T20	58	61	290	305
24	T21	61	64	305	320
25	T22	64	67	320	335
26	T23	67	70	335	350
27	T24	70	73	350	365
28	T25	73	76	365	380
29	T26	76	79	380	395
30	T27	79	82	395	410
31	T28	82	85	410	425
32	T29	85	88	425	440
33	T30	88	91	440	455
34	T31	91	94	455	470
35	T32	94	97	470	485
36	T33	97	100	485	500

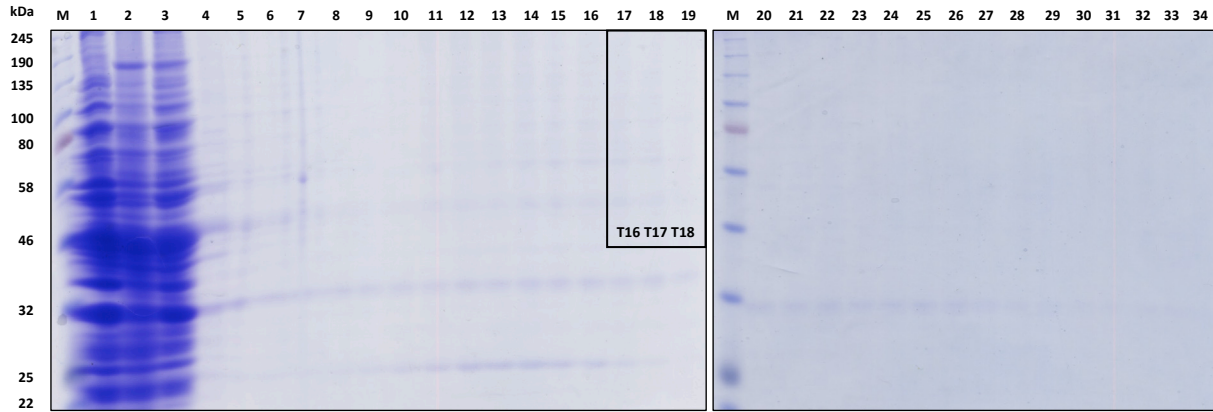


Figure S 3: SDS PAGE of gradient Mos10-6His AEKTA purification using a Ni-NTA column and SILAC. IMAC purification of 6His tagged-Mos10 (RKY2999) with the AEKTA system utilizing a Ni²⁺-NTA column. Visualization of the purification process using Coomassie staining of the SDS PAGE gels. Area in the black rectangle used for MS analysis. **M:** NEB Color Pre-stained Protein Standard (11 - 245 kDa); **Lane 1:** Lysis debris; **Lane 2:** Sample loaded on AEKTA; **Lane 3:** Flowthrough; **Lane 4:** T2; **Lane 5-34:** T4-T33.

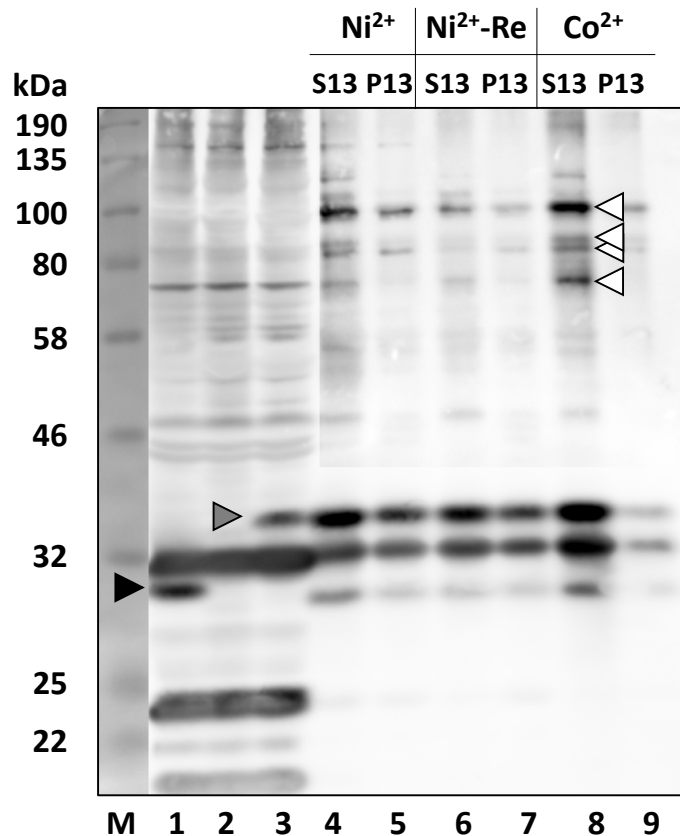


Figure S 4: Ni²⁺- vs. Co²⁺-NTA column assay for purifying crosslinked Mos10-6His.

A differential centrifugation experiment was done to separate and highlight crosslinking partners into S13 and P13 fractions. Beads were stripped with EDTA and recharged with Ni²⁺ (Ni²⁺-Re) or loaded with Co²⁺ ions. **Lane 1:** WT extract; **Lane 2:** Δ8 extract; **Lane 3:** RKY2999 extract; **Lane 4:** S13 on Ni²⁺-NTA; **Lane 5:** P13 on Ni²⁺-NTA; **Lane 6:** S13 on recharged Ni²⁺-NTA; **Lane 7:** P13 on recharged Ni²⁺-NTA; **Lane 8:** S13 on Co²⁺-NTA; **Lane 9:** P13 on Co²⁺-NTA; Arrows: **Black:** Mos10; **Grey:** Mos10-6His; **White:** Crosslinks. Loaded: OD = 0.2.

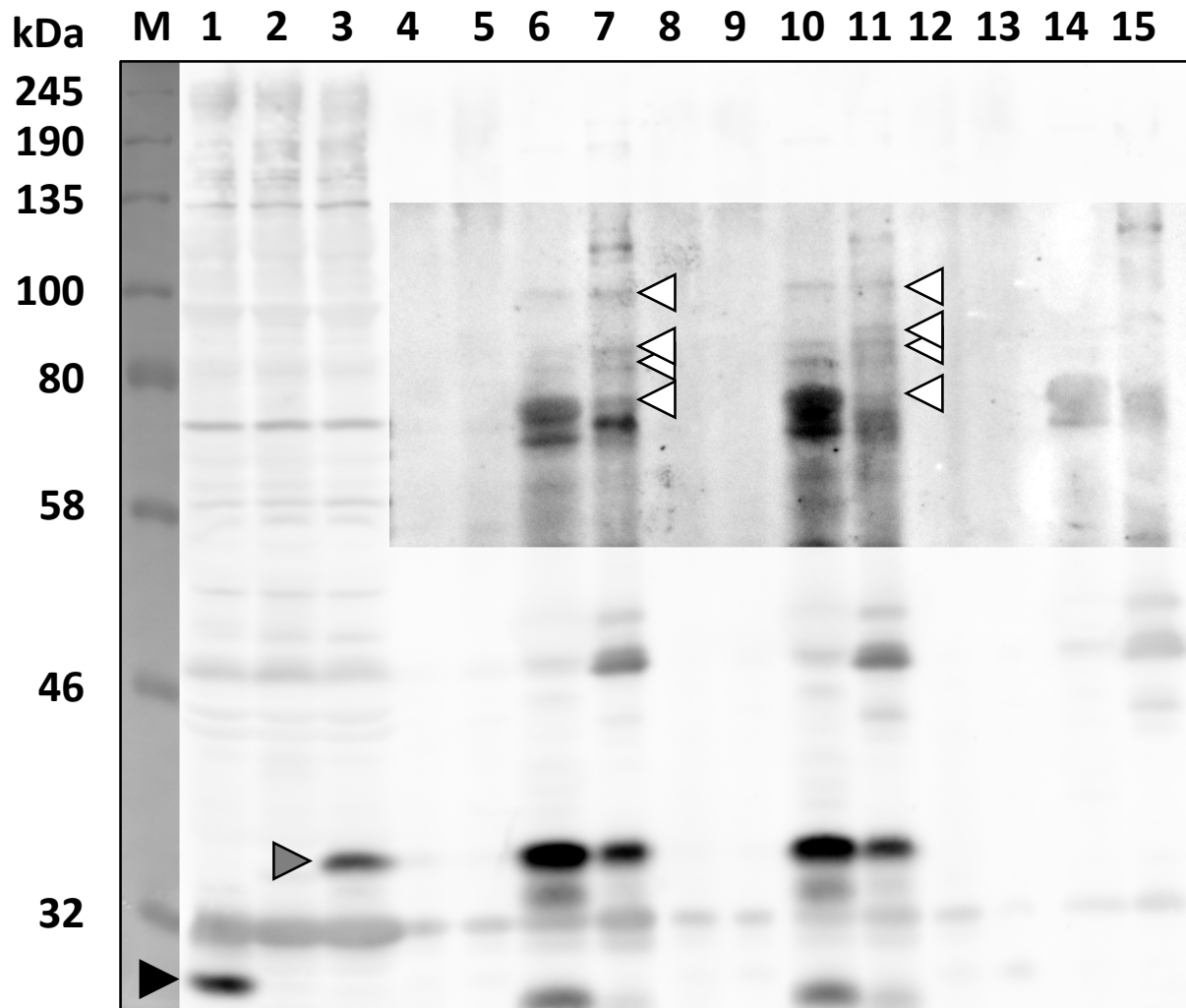


Figure S 5: SILAC Experiment with mixed “light” and “heavy” RKY2998 and RKY2999 purification.

Mos10-6His batch purification with differential centrifugation was carried out with arginine auxotroph strains RKY2999 and RKY2998. SILAC technique was applied to both strains to visualize “light” (L) and “heavy” (H) media-induced protein enrichment differences. Additionally, a differential centrifugation experiment was carried out to separate and highlight crosslinking partners into S13 and P13 fractions with a recharged Co^{2+} -NTA column. Additionally, the beads supernatant’s unbound (UB) content collected was applied to WB analysis to visualize the bead’s binding capacity. An empty unbound fraction implies sufficient Co^{2+} -NTA column volume to affinity coordinate and purify the entire Mos10-6His content in the cell culture. **M:** NEB Color Pre-stained Protein Standard (11 - 245 kDa); **Lane 1:** RKY2998 extract; **Lane 2:** $\Delta 8$ extract; **Lane 3:** RKY2999 extract; **Lane 4:** UB S13 of RKY2998(L) and RKY2999(H); **Lane 5:** UB P13 of RKY2998(L) and RKY2999(H); **Lane 6:** beads S13 of RKY2998(L) and RKY2999(H); **Lane 7:** beads P13 of RKY2998(L) and RKY2999(H); **Lane 8:** UB S13 of RKY2998(H) and RKY2999(L); **Lane 9:** UB P13 of RKY2998(H) and RKY2999(L); **Lane 10:** beads S13 of RKY2998(H) and RKY2999(L); **Lane 11:** beads P13 of RKY2998(H) and RKY2999(L); **Lane 12:** UB S13 of RKY2998(L) and RKY2998(H); **Lane 13:** UB P13 of RKY2998(L) and RKY2998(H); **Lane 14:** beads S13 of RKY2998(L) and RKY2998(H); **Lane 15:** beads P13 of RKY2998(L) and RKY2998(H). Arrows: **Black:** Mos10; **Grey:** Mos10-6His; **White:** Crosslinks. Loaded: OD = 0.2.

Table S 3: Mos-6His to Ni-NTA binding condition test.

NaCl [mM]	Tween20 [%]	Glycerol [%]	Beta [mM]
300	0	0	0
300	0	0	5
300	0	10	0
300	0	10	5
300	0.1	0	0
300	0.1	0	5
300	0.1	10	0
300	0.1	10	5
1000	0	0	0
1000	0	0	5
1000	0	10	0
1000	0	10	5
1000	0.1	0	0
1000	0.1	0	5
1000	0.1	10	0
1000	0.1	10	5

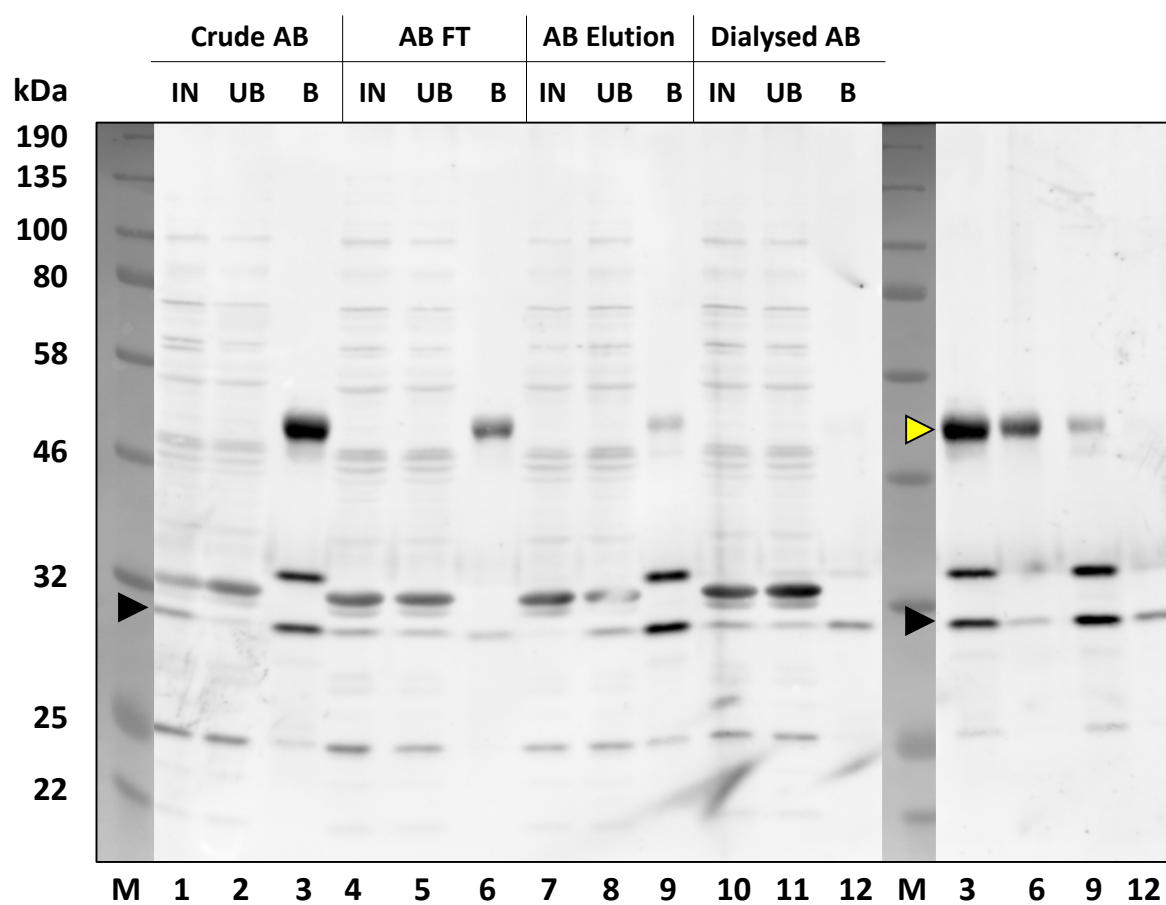


Figure S 6: Analyzing antibody sera efficiency against native Mos10 extract.

Various fractions were collected and tested during antibody purification against a WT (RKY1558) extract to compare immunoprecipitation efficiency and purity. The sera tested are the crude antibody extract, antibodies not purified by Affi-Gel 15 crosslinked Mos10-6His (AB FT), the eluted antibodies, and the dialyzed antibodies. For each input (IN), 20 OD of an exponential WT (RKY1558) culture were harvested, lysed, and incubated with 5 μ l AB sera before being harvested by Protein A Sepharose beads (supernatant = UB for unbound), washed and boiled (B for beads fraction). **M:** NEB Color Pre-stained Protein Standard (11 - 245 kDa); **Lane 1:** Crude AB IN; **Lane 2:** Crude AB UB; **Lane 3:** Crude AB B; **Lane 4:** FT AB IN; **Lane 5:** FT AB UB; **Lane 6:** FT AB B; **Lane 7:** Eluted AB IN; **Lane 8:** Eluted AB UB; **Lane 9:** Eluted AB B; **Lane 10:** dialyzed AB IN **Lane 11:** dialyzed AB UB; **Lane 12:** dialyzed AB B. Arrows: **Black:** Mos10; **Yellow:** Antibody. Loaded: OD = 0.2.

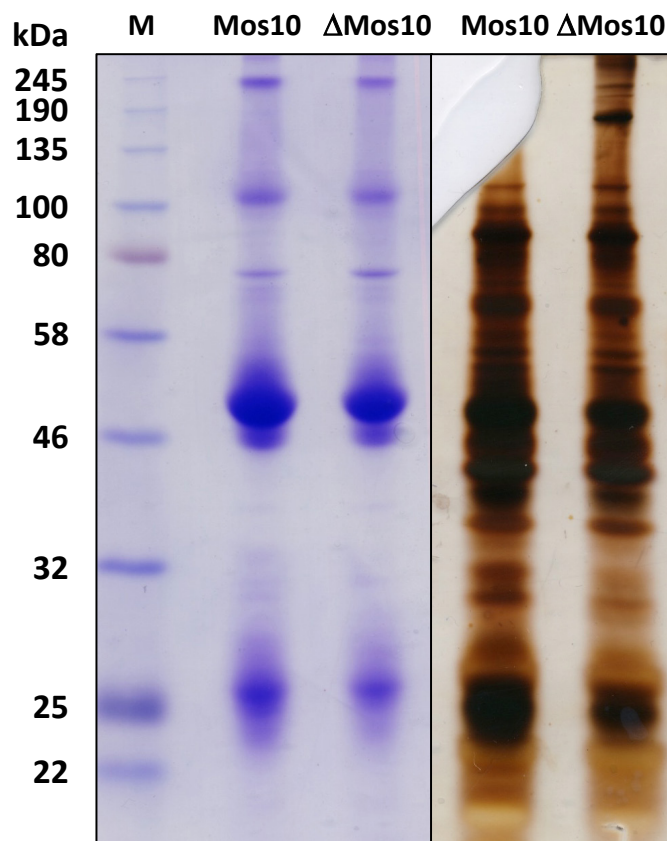


Figure S 7: Comparison of WT and Δ Mos10 purification on SDS PAGE with Coomassie and silver staining.

Crosslinked protein samples of Mos10 (RKY1558) and Δ Mos10 (RKY2892) strains were applied to SDS PAGE and stained by Coomassie and silver staining. Additional content at 30 kDa can be seen in the Mos10 samples indicating Mos10 protein bands. In the region of detected crosslinks from the WB at around 58 to 90 kDa, no difference in band intensities can be seen on the Coomassie-stained gel. The silver staining appears over-stained due to the higher sensitivity of the stain, which makes detecting single bands belonging to the crosslinks absurd. **M:** NEB Color Pre-stained Protein Standard (11 - 245 kDa); Mos10 = RKY1558; Δ Mos10 = RKY2892.

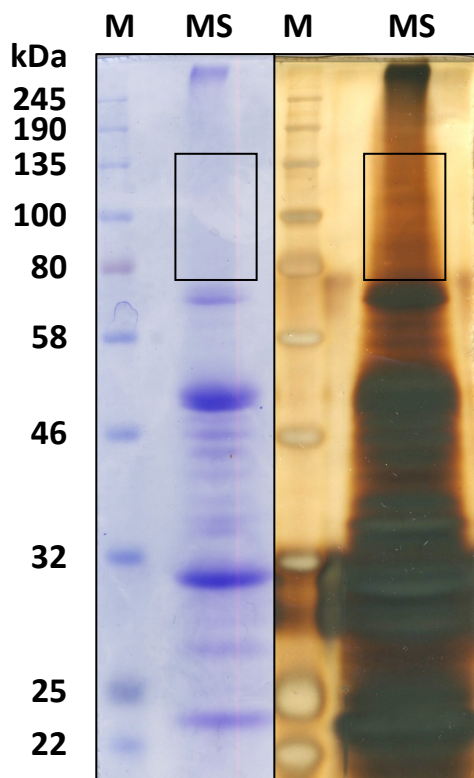


Figure S 8: Samples for MS once stained with Coomassie and once with silver staining.

RKY1558 yeast culture was grown until the exponential phase before being crosslinked according to standard protocol and immunoprecipitated with purified α -Mos10 antibodies. Samples were applied on SDS PAGE to be stained by either Coomassie or silver staining. The black rectangles highlight the areas to be analyzed by MS. **M:** NEB Color Pre-stained Protein Standard (11 - 245 kDa); **MS:** samples for mass spectrometry.

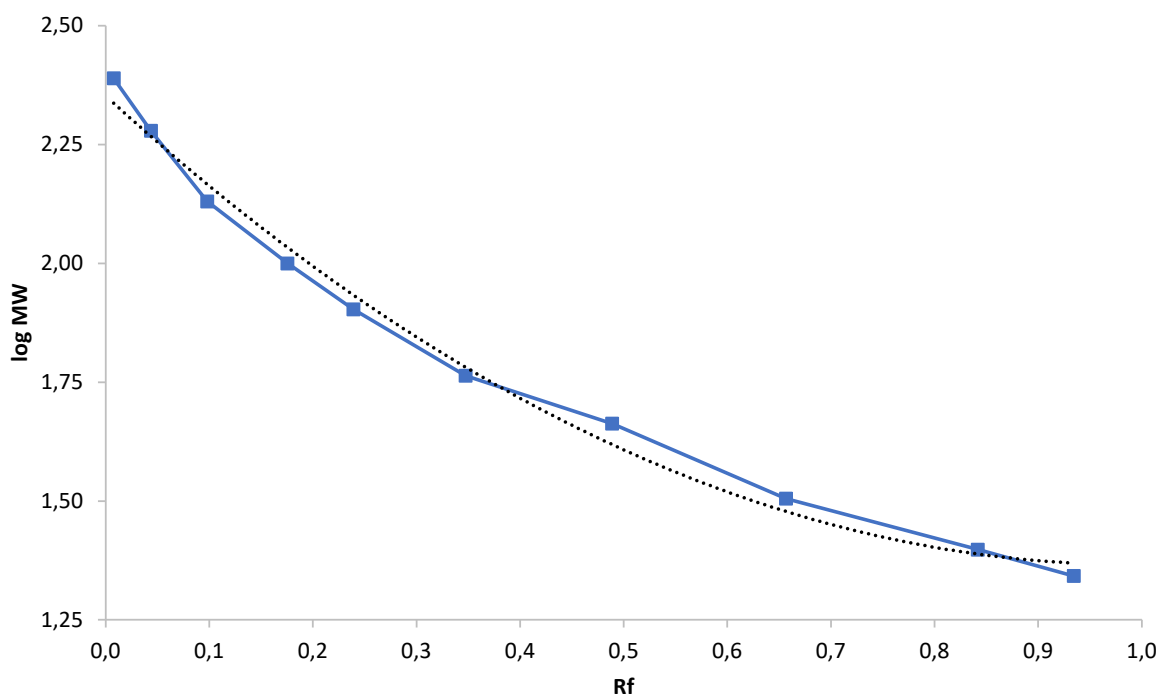


Figure S 9: Graphing electrophoresis results of WB bands.

The blue curve indicates the relative migration distance of marker bands in reference to the standard protein's logarithmic scaled molecular weight. The black dotted line represents a polynomial fit of the blue curve to calculate unknown protein band weights by their migration distance. The polynomial equation was used to calculate the log MW of the unknown protein bands: $\log MW = 1.0065 \cdot Rf^2 - 1.992 \cdot Rf + 2.3521$, whereas Rf is calculated by the band migration distance X divided by the front distance. The curve's fit is $R = 0.9916$.

Table S 4: Calculation of the unknown protein bands sized of the established crosslinking pattern partner.

Label	X	MW Standard (kDa)	Rf	logMW	MW CL (kDa)	MW CL w/o Mos10-6His (kDa)
Standard 1	8,0	245	0,01	2,39		
Standard 2	44,8	190	0,04	2,28		
Standard 3	100,2	135	0,10	2,13		
Standard 4	179,5	100	0,18	2,00		
Standard 5	244,8	80	0,24	1,90		
Standard 6	355,5	58	0,35	1,76		
Standard 7	500,2	46	0,49	1,66		
Standard 8	671,8	32	0,66	1,51		
Standard 9	861,2	25	0,84	1,40		
Standard 10	955,8	22	0,93	1,34		
Unknown 1	50,2		0,05	2,26	183	149
Unknown 2	192,2		0,19	2,01	93	59
Unknown 3	243,5		0,24	1,93	79	45
Unknown 4	256,8		0,25	1,92	76	42
Unknown 5	286,8		0,28	1,87	71	36
Unknown 6	298,2		0,29	1,86	69	34
Mos10-6His	638,2		0,62	1,50	34	
Front	1023					

WB protein bands were used from Figure 16, and migration distances were calculated by ImageJ.

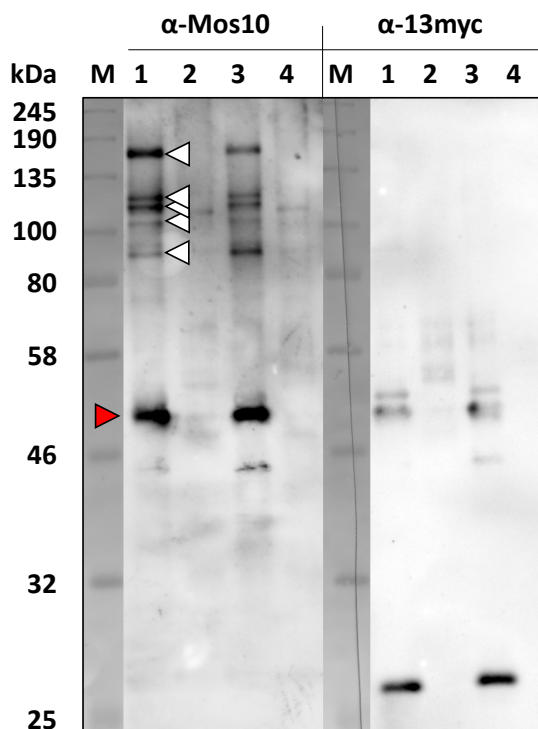


Figure S 10: Crosslink pattern of Mos10-13myc OD 1 and OD 4 cultures.

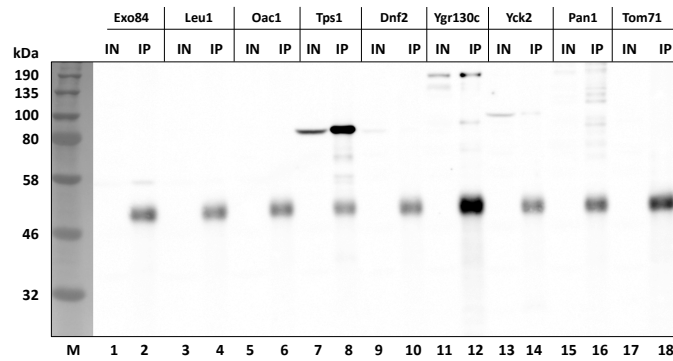
Two RKY1452 cultures with an OD = 1 and OD = 4 were grown in YPD and crosslinked according to standard protocol. Samples were immunoprecipitated with α -13myc antibodies and bound to protein A beads before being boiled. Blots are either incubated with α -Mos10 or α -13myc antibodies. **M:** NEB Color Pre-stained Protein Standard (11 – 245 kDa); **Lane 1:** bead fraction of OD = 1 culture; **Lane 2:** supernatant fraction of OD = 1 culture; **Lane 3:** bead fraction of OD = 4 culture; **Lane 4:** supernatant fraction of OD = 4 culture; **Arrow: Red:** Mos10-13myc; **White:** Crosslinks.

Table S 5: MS Results overview (ESCRT-III in bold).

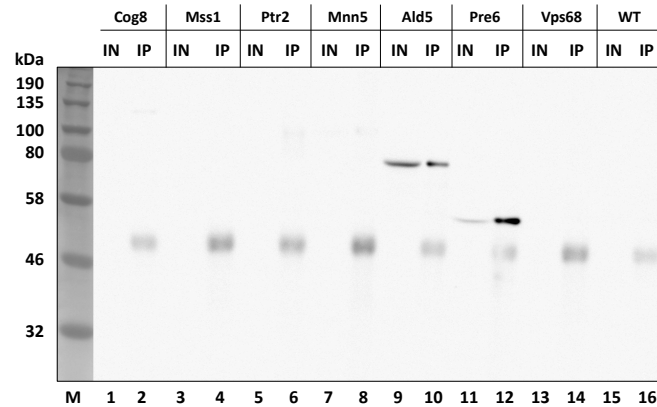
Gene Symbol	CRAPome	MW
ACS2	3 / 17	75,483
ACT1	14 / 17	41,679
ALD4	1 / 17	56,721
ALD5	1 / 17	56,692
ARP3	1 / 17	49,541
BAG7	/ 17	46,216
CBK1	4 / 17	86,945
CDC28	/ 17	34,061
COG8	1 / 17	69,828
COX4	/ 17	17,142
DID2	/ 17	23,091
DID4 (Vps2)	/ 17	26,290
DNF2	1 / 17	182,620
EFT1	16 / 17	93,279
ERV29	/ 17	35,028
EXO84	1 / 17	85,537
FAS1	9 / 17	228,654
FKS1	7 / 17	214,85
FRT2	/ 17	58,749
GET3	1 / 17	39,337
GPH1	1 / 17	103,252
HBT1	/ 17	113,610
HEF3	7 / 17	115,870
HHT1	12 / 17	15,356
HSP26	1 / 17	23,874
HSP78	/ 17	91,340
HXK1;HXK2	1 / 17; 6 / 17	53,738
HXT1	/ 17	63,261
ILV5	7 / 17	44,368
LEU1	1 / 17	85,793
MHP1	2 / 17	155,204
MNN5	1 / 17	67,204
MSS1	/ 17	58,351
NCR1	/ 17	132,616
NEW1	11 / 17	134,33
OAC1	/ 17	35,153
PAB1	17 / 17	64,335
PAN1	1 / 17	160,270

Gene Symbol	CRAPome	MW
PDC1	15 / 17	61,486
PMA1;PMA2	17 / 17	99,618
PRE6	2 / 17	28,439
PTR2	/ 17	68,043
RPL11B;RPL11A	17 / 17	19,762
RPL9B;RPL9A	17 / 17	21,657
RPS3	17 / 17	26,502
RTN2	/ 17	44,358
RTS1	/ 17	85,334
SAH1	5 / 17	49,115
SER33;SER3	/ 17	51,181
SNF7	/ 17	26,987
SSB1	17 / 17	66,601
SSC1	9 / 17	63,248
SSE2	5 / 17	77,620
STB6	/ 17	88,835
TAF7	/ 17	67,555
TDH1	12 / 17	35,750
TGS1	2 / 17	36,547
TIF35	6 / 17	30,500
TIM10	1 / 17	10,305
TOF1	/ 17	141,104
TOM71	/ 17	71,855
TPS1	/ 17	56,147
TY1B-BL;TY1B-MR1	11 / 17	198,979
TY1B-MR1;TY1B-BL	11 / 17	198,900
VMA5	4 / 17	44,188
VPS24	/ 17	26,242
VPS60 (Mos10)	/ 17	25,861
VPS68	/ 17	20,101
YAT2	/ 17	103,330
YCK1	/ 17	61,726
YCK2	1 / 17	62,078
YGR130C	/ 17	92,697
YJR154W	/ 17	38,964
YKR075C	/ 17	36,113
YSP2	/ 17	160,577
YTA12	1 / 17	93,275
ZPS1	1 / 17	27,567

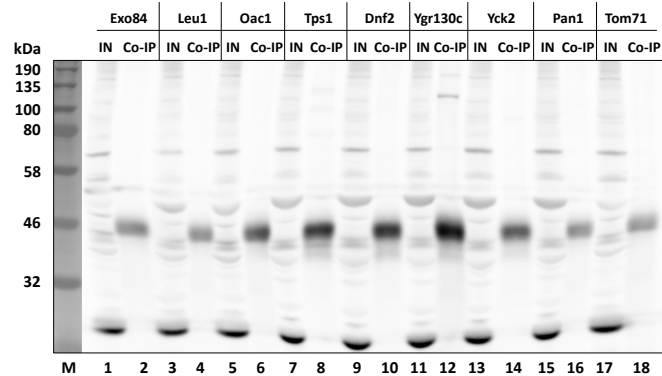
IP A



IP B



Co-IP A



Co-IP B

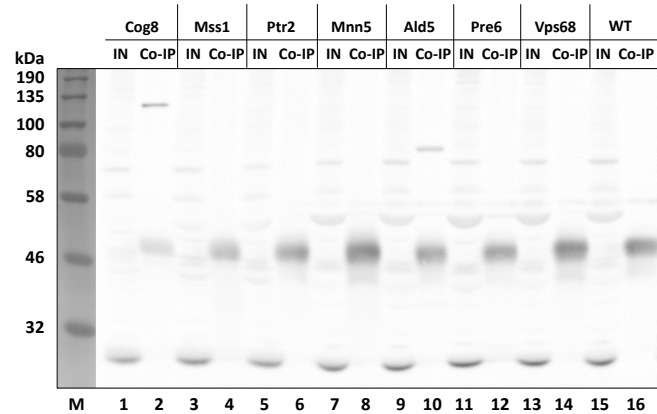
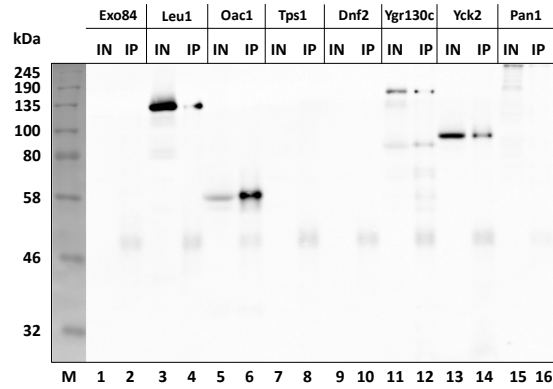


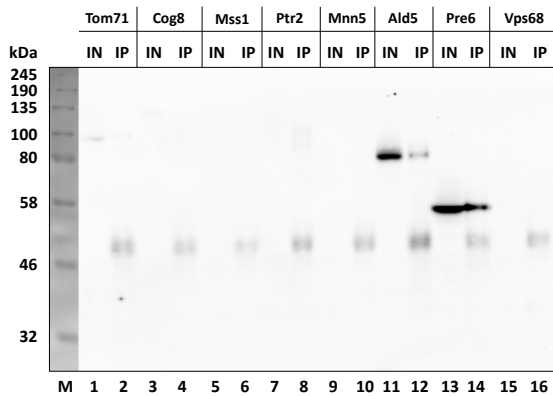
Figure S 11: IP of potential Mos10 interacting partners with a GFP-tag and Co-IP of Mos10.

Results of the α -GFP (Co-)IP. IN = input samples; (Co-)IP = the (co-)immunoprecipitated samples. M: NEB Color Pre-stained Protein Standard (11 – 245 kDa). Loaded: IN: OD = 0.2; IP: OD = 1; Co-IP: OD = 5.

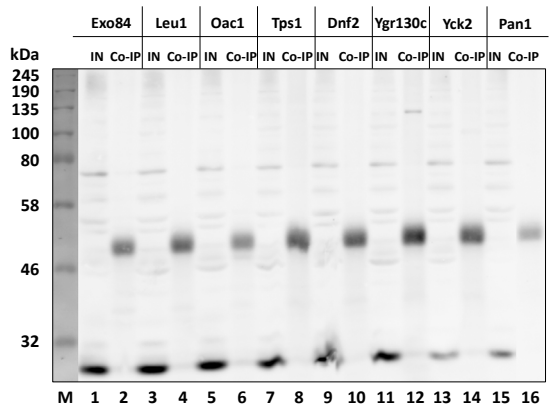
IP A



IP B



Co-IP A



Co-IP B

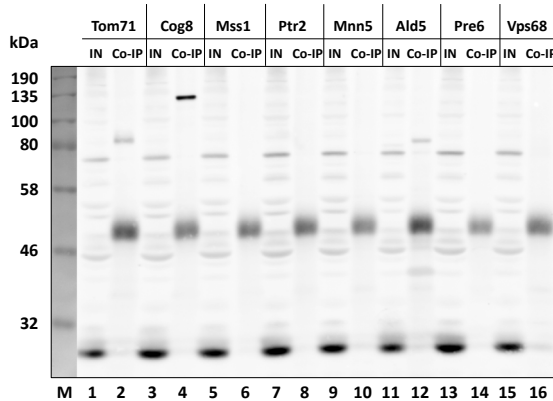


Figure S 12: IP of potential Mos10 interacting partners with a sfGFP-tag and Co-IP of Mos10.

Results of the α -sfGFP (Co-)IP. **IN** = input samples; **(Co-)IP** = the (co-)immunoprecipitated samples. **M**: NEB Color Pre-stained Protein Standard (11 – 245 kDa). Loaded: IN: OD = 0.2; IP: OD = 1; Co-IP: OD = 5.

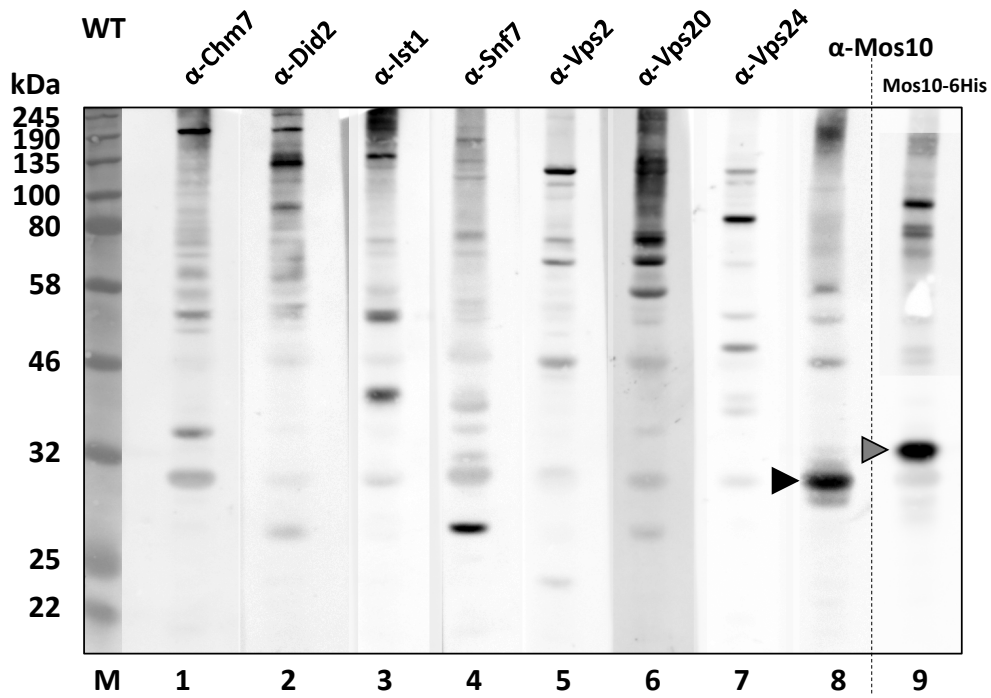


Figure S 13: IMAC purification of WT (RKY1558) strain with RKY2889 (Mos10-6His) control sample.

Ni-NTA purified samples of DSS crosslinked RKY1558 and RKY2889, incubated with any ESCRT-III antibody.

M: NEB Color Pre-stained Protein Standard (11 – 245 kDa). Arrows: **Black**: Mos10; **Grey**: Mos10-6His. Loaded: OD = 1

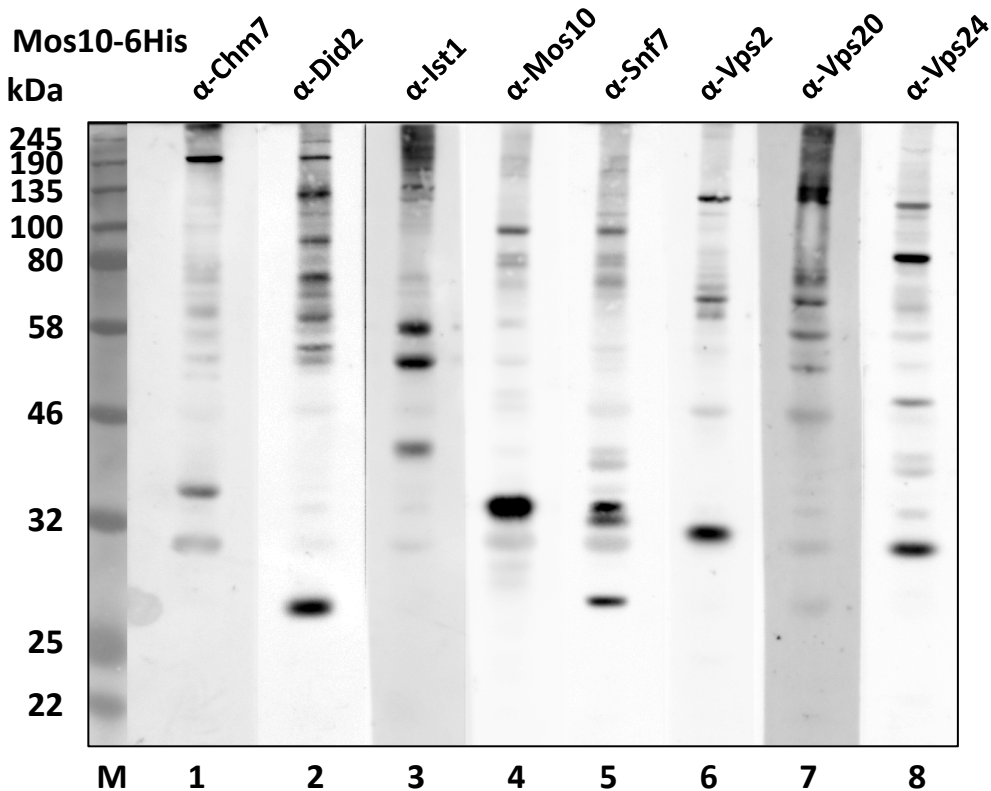


Figure S 14: IMAC purification of RKY2889 (Mos10-6His).

Ni-NTA purified samples of DSS crosslinked RKY2889, incubated with any ESCRT-III antibody. **M**: NEB Color Pre-stained Protein Standard (11 – 245 kDa). Loaded: OD = 1.

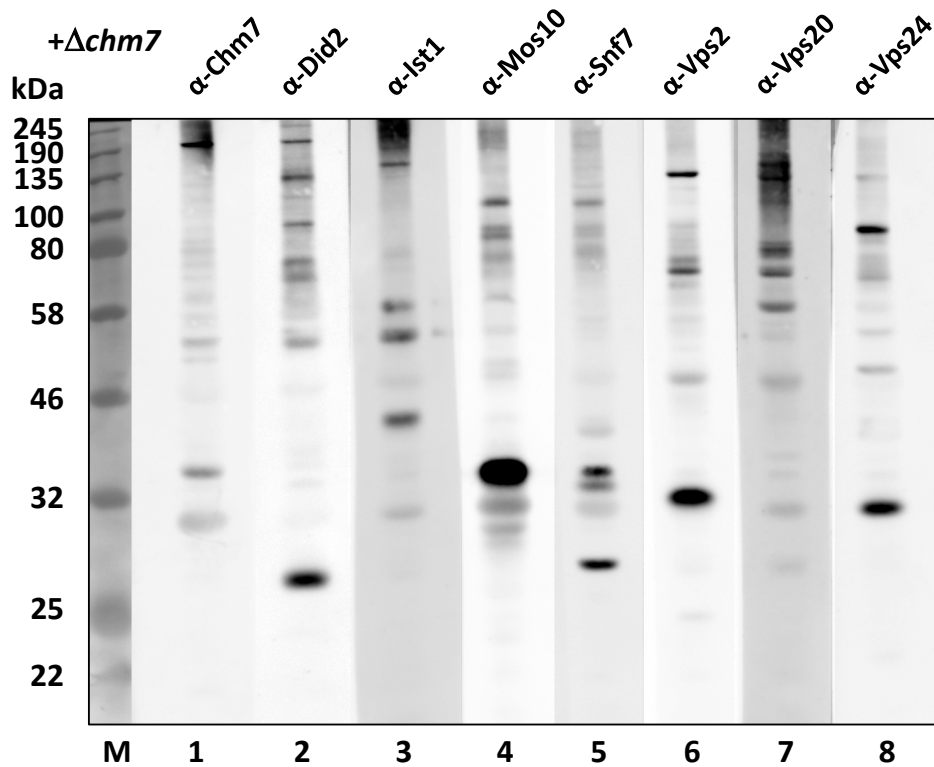


Figure S 15: IMAC purification of RKY3228 (Mos10-6His + Δ chm7).

Ni-NTA purified samples of DSS crosslinked RKY3228, incubated with any ESCRT-III antibody. **M:** NEB Color Pre-stained Protein Standard (11 – 245 kDa). Loaded: OD = 1.

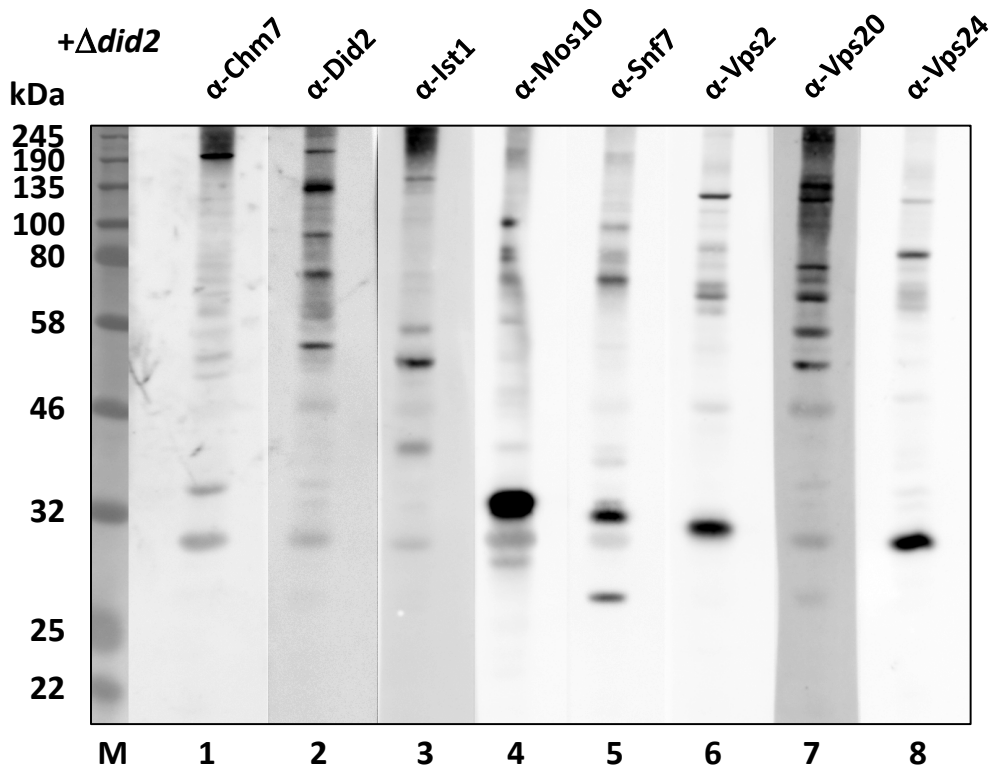


Figure S 16: IMAC purification of RKY2788 (Mos10-6His + Δ did2).

Ni-NTA purified samples of DSS crosslinked RKY2788, incubated with any ESCRT-III antibody. **M:** NEB Color Pre-stained Protein Standard (11 – 245 kDa). Loaded: OD = 1.

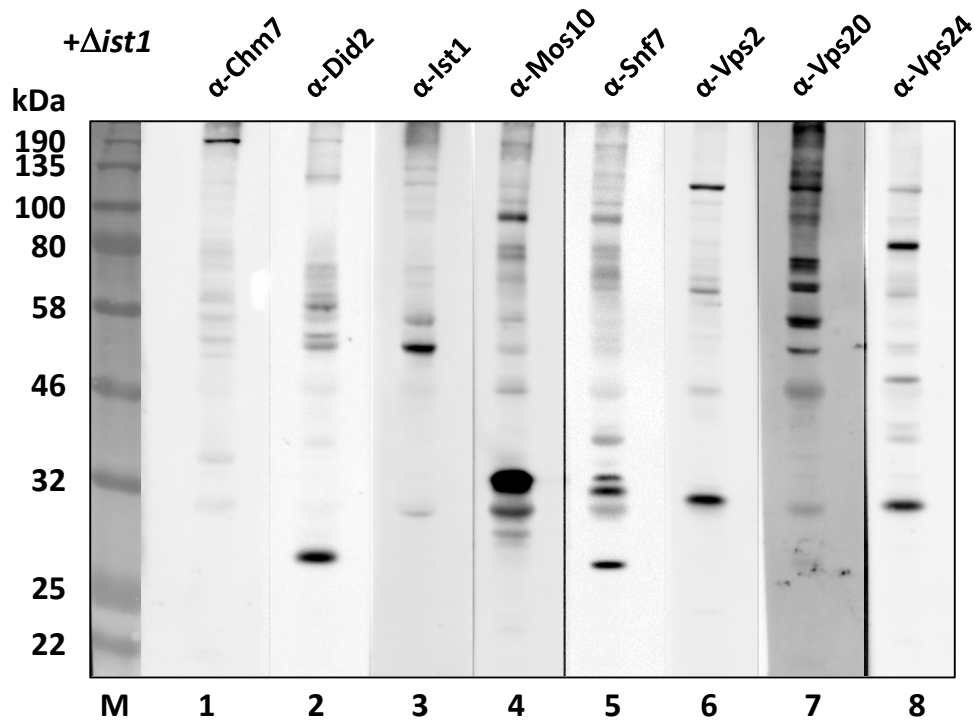


Figure S 17: IMAC purification of RKY2789 (Mos10-6His + Δ ist1).

Ni-NTA purified samples of DSS crosslinked RKY2789, incubated with any ESCRT-III antibody. **M:** NEB Color Pre-stained Protein Standard (11 – 245 kDa). Loaded: OD = 1.

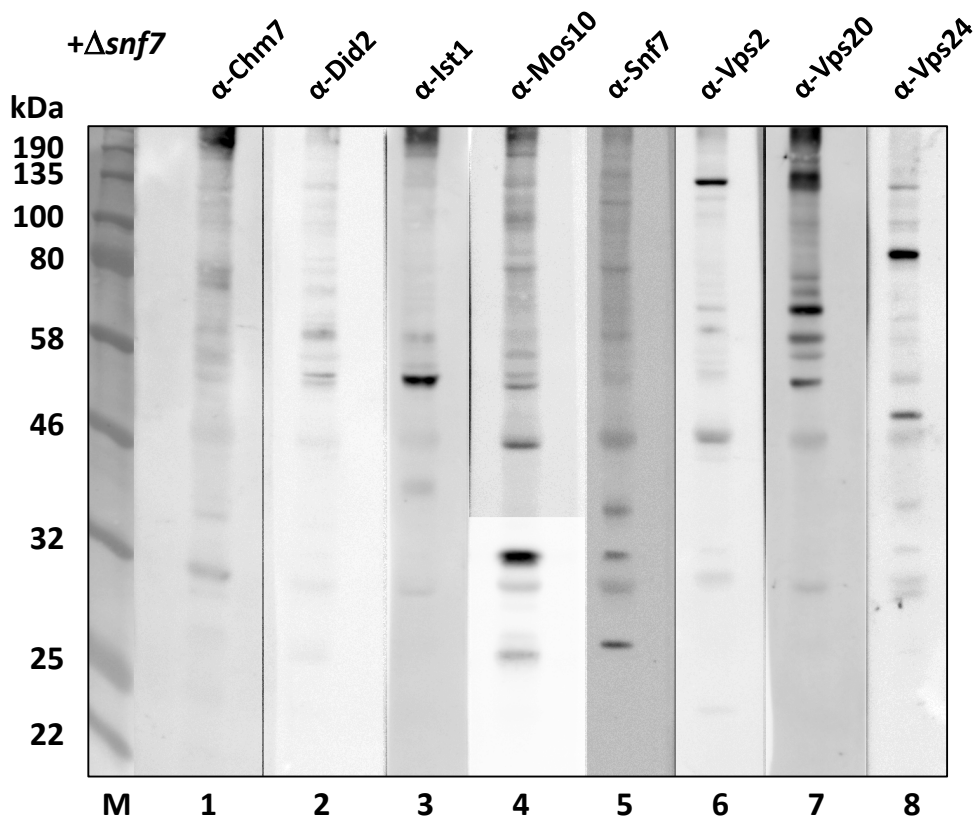


Figure S 18: IMAC purification of RKY2790 (Mos10-6His + Δ snf7).

Ni-NTA purified samples of DSS crosslinked RKY2790, incubated with any ESCRT-III antibody. **M:** NEB Color Pre-stained Protein Standard (11 – 245 kDa). Loaded: OD = 1.

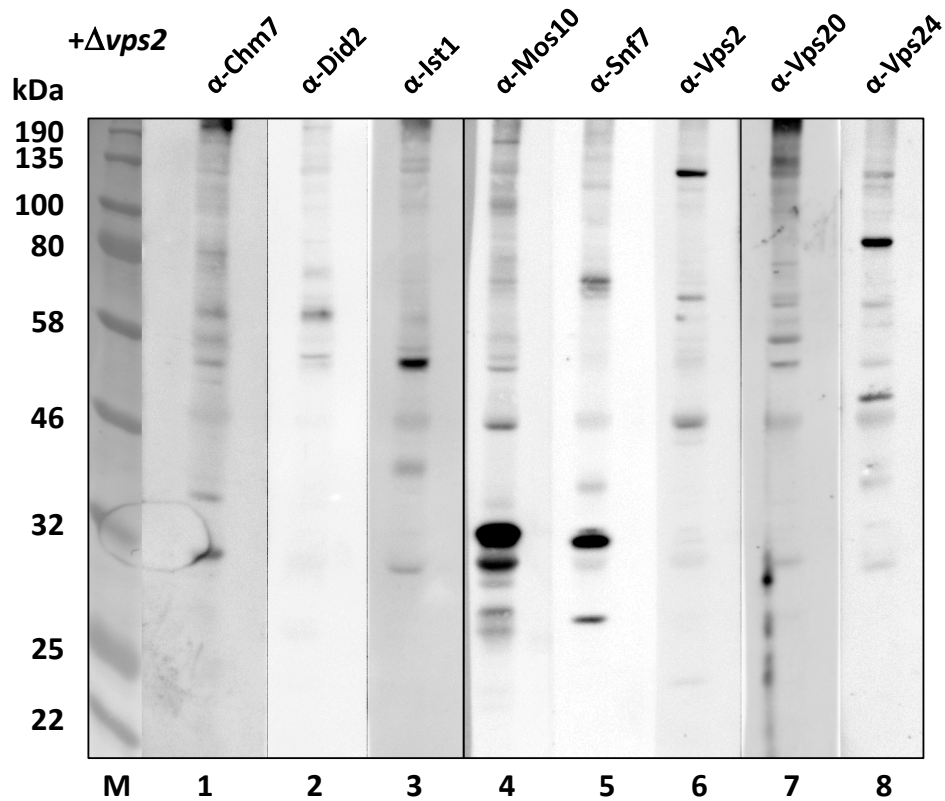


Figure S 19: IMAC purification of RKY2841 (Mos10-6His + $\Delta vps2$).

Ni-NTA purified samples of DSS crosslinked RKY2841, incubated with any ESCRT-III antibody. **M:** NEB Color Pre-stained Protein Standard (11 – 245 kDa). Loaded: OD = 1.

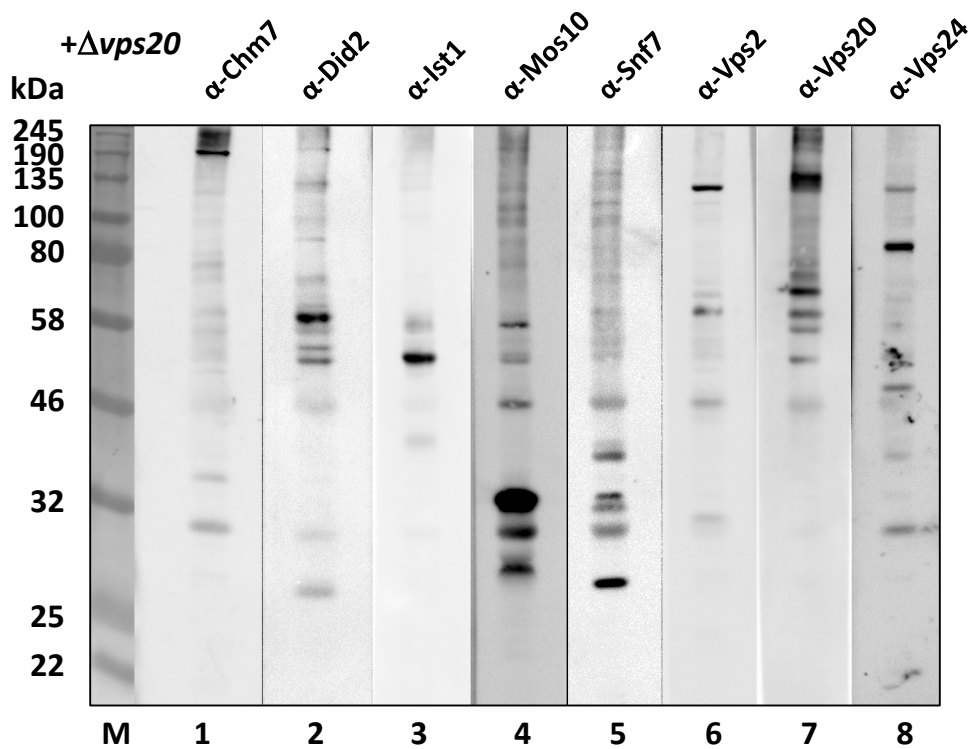


Figure S 20: IMAC purification of RKY2893 (Mos10-6His + $\Delta vps20$).

Ni-NTA purified samples of DSS crosslinked RKY2893, incubated with any ESCRT-III antibody. **M:** NEB Color Pre-stained Protein Standard (11 – 245 kDa). Loaded: OD = 1.

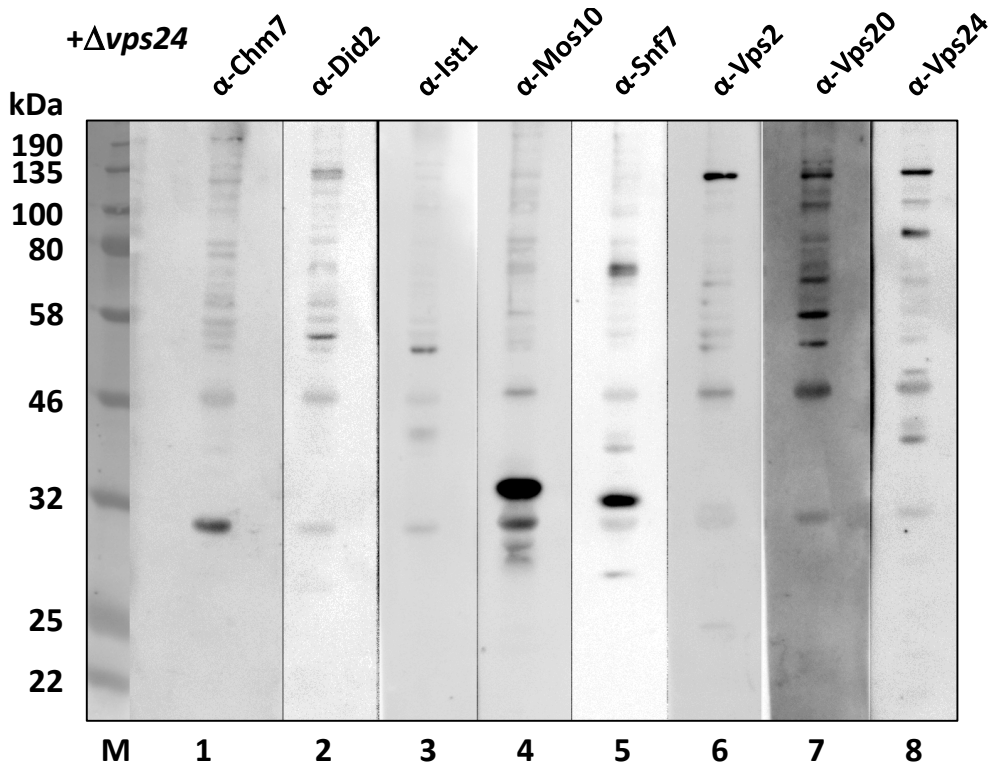


Figure S 21: IMAC purification of RKY2830 (Mos10-6His + Δ vps24).

Ni-NTA purified samples of DSS crosslinked RKY2830, incubated with any ESCRT-III antibody. **M:** NEB Color Pre-stained Protein Standard (11 – 245 kDa). Loaded: OD = 1.

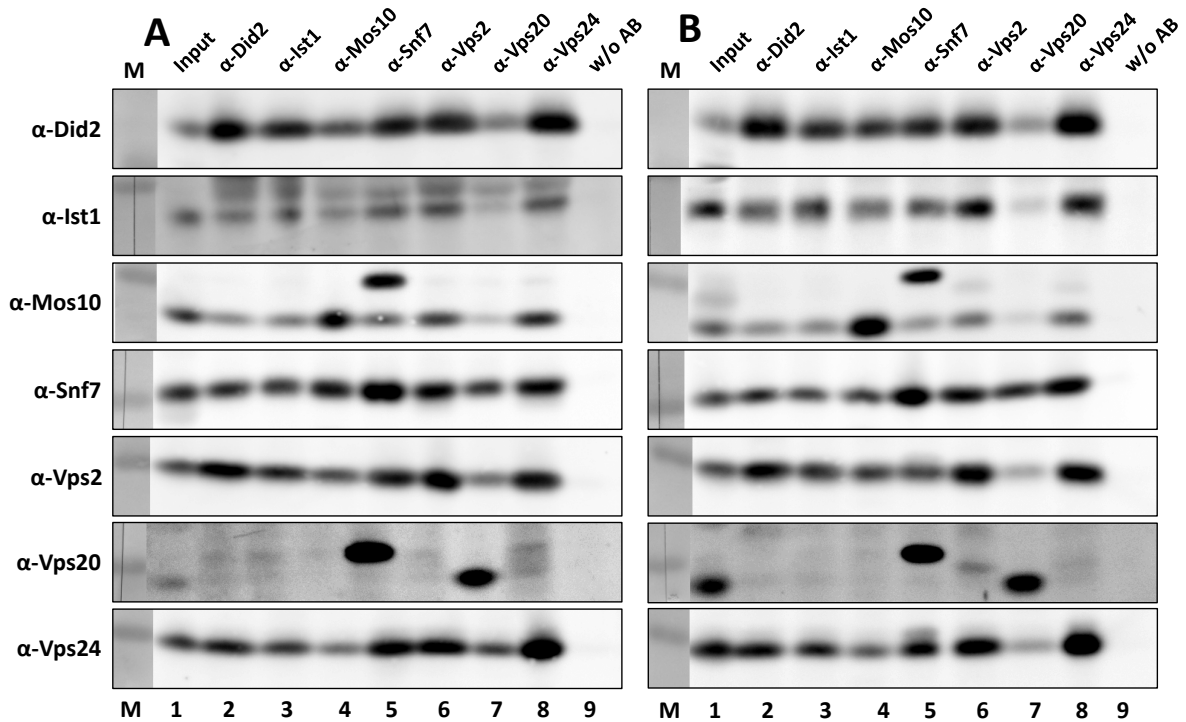
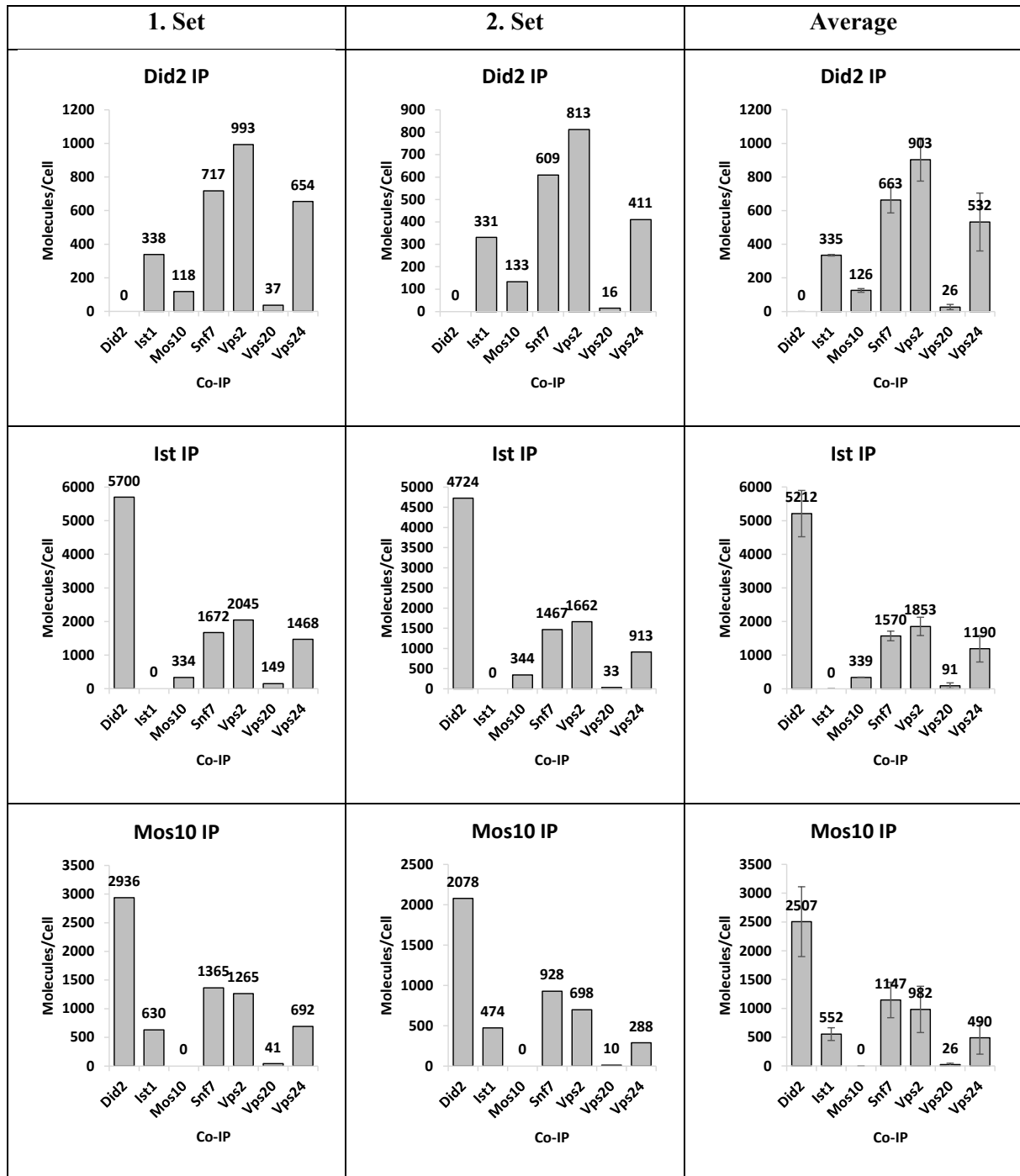


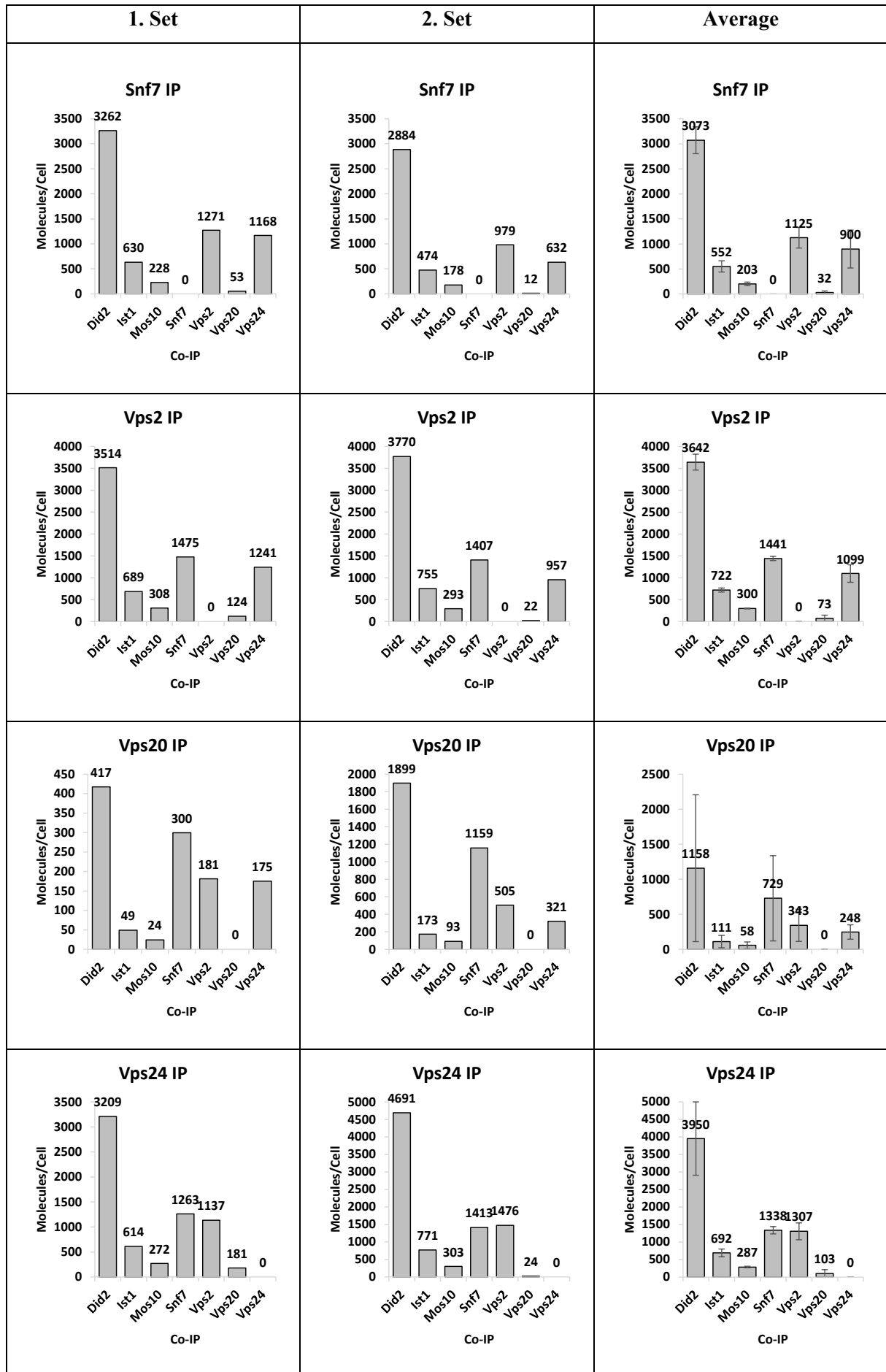
Figure S 22: IP and Co-IP of all ESCRTs in WT strain. RKY1558.

Shown are both sets (**A** and **B**), with the antibody used for incubating the blot is on the y-axis and the co-immunoprecipitated proteins on the column's header.

Table S 6: Co-IP Overview in WT strain.

The amount of each individual ESCRT-III subunit co-immunoprecipitated by the IP is measured in molecules per cell according to the numbers by Heinzle *et al.*





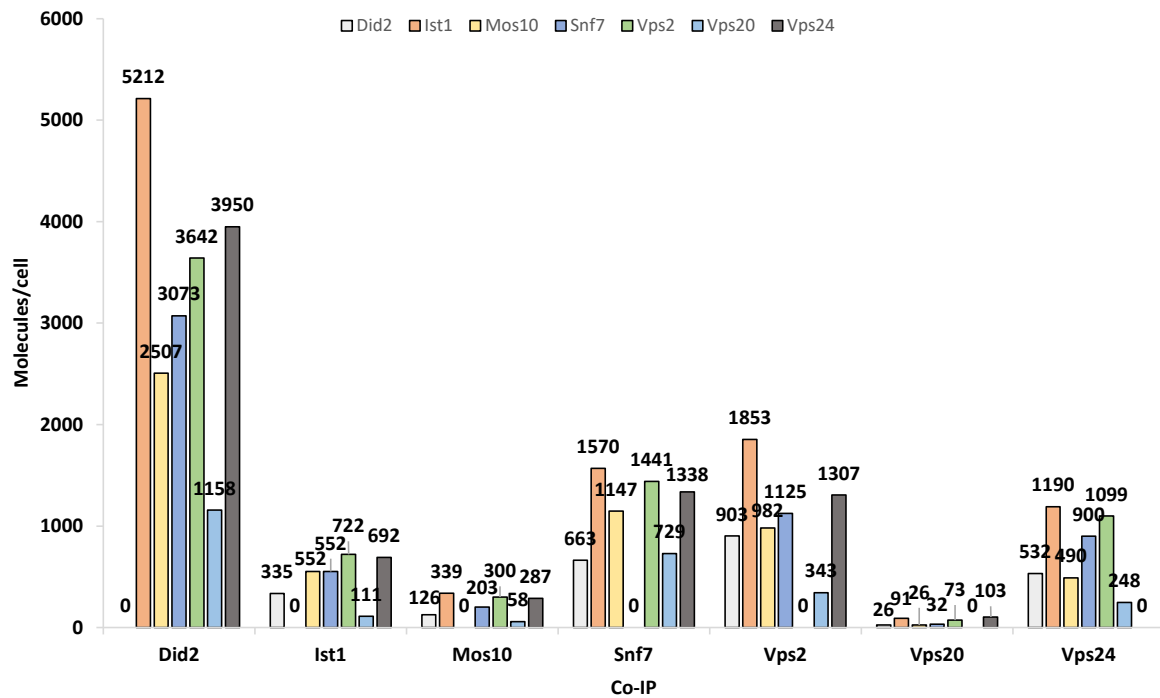


Figure S 23: Total amount of protein co-immunoprecipitated by ESCRT-III IP in WT strain RKY1558. IP of seven ESCRT-III members and their associated ECRT-III co-IP values assembled to the co-IP protein and graphed against the total molecules per cell.

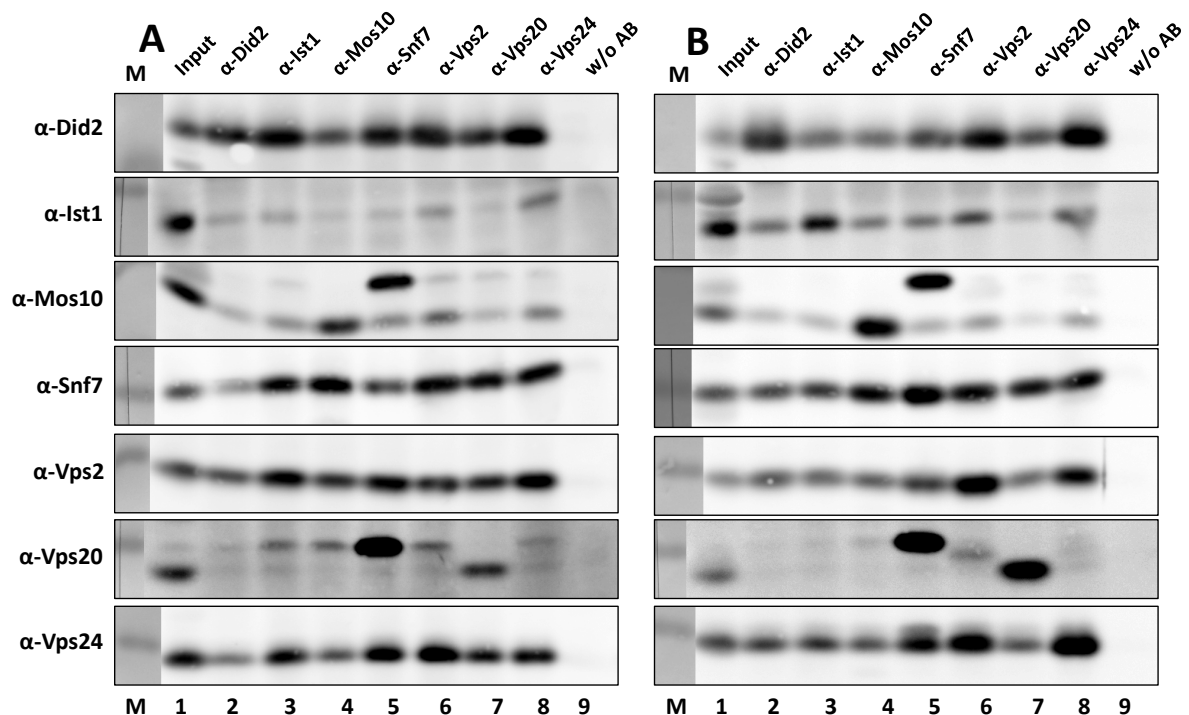
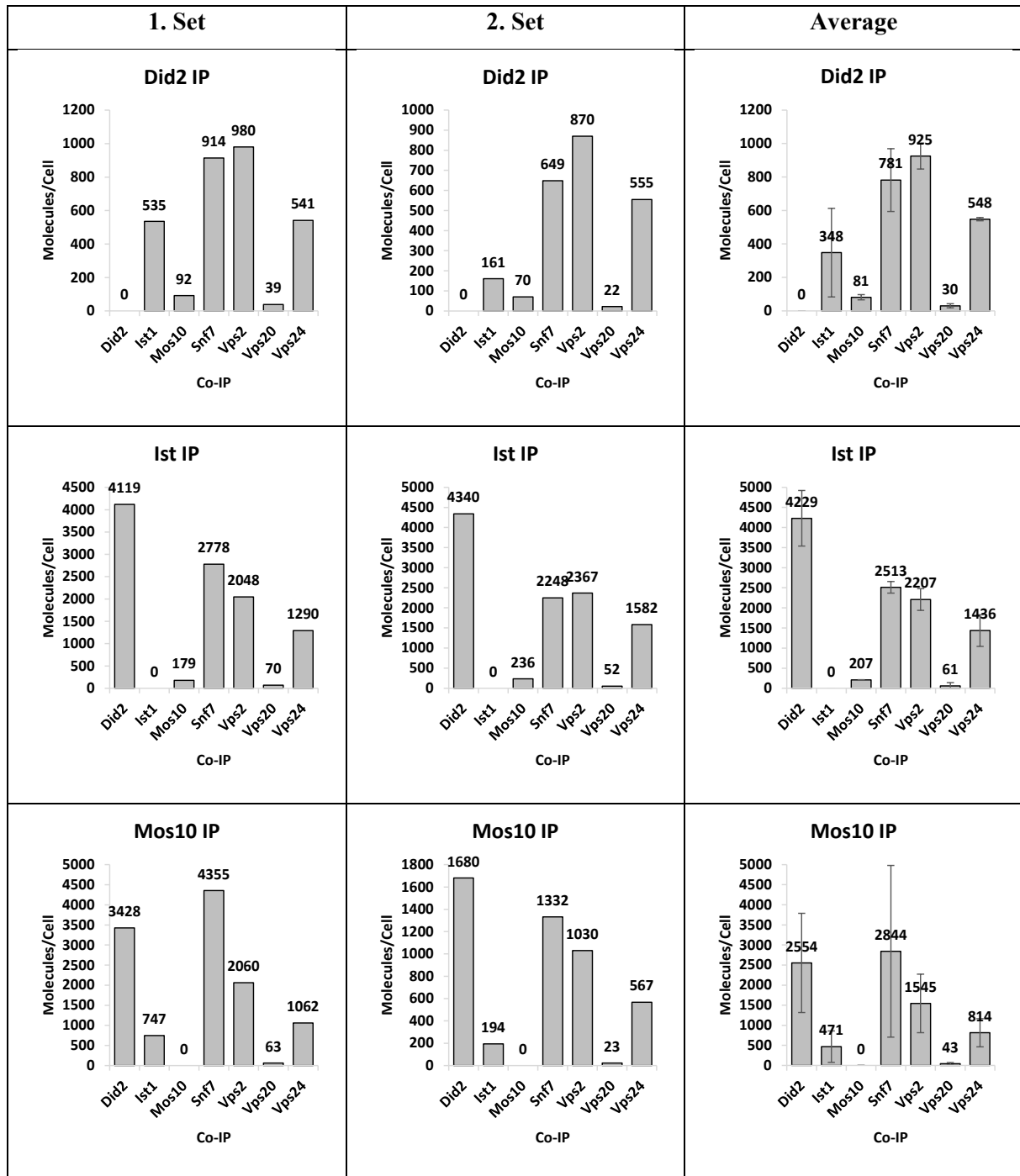


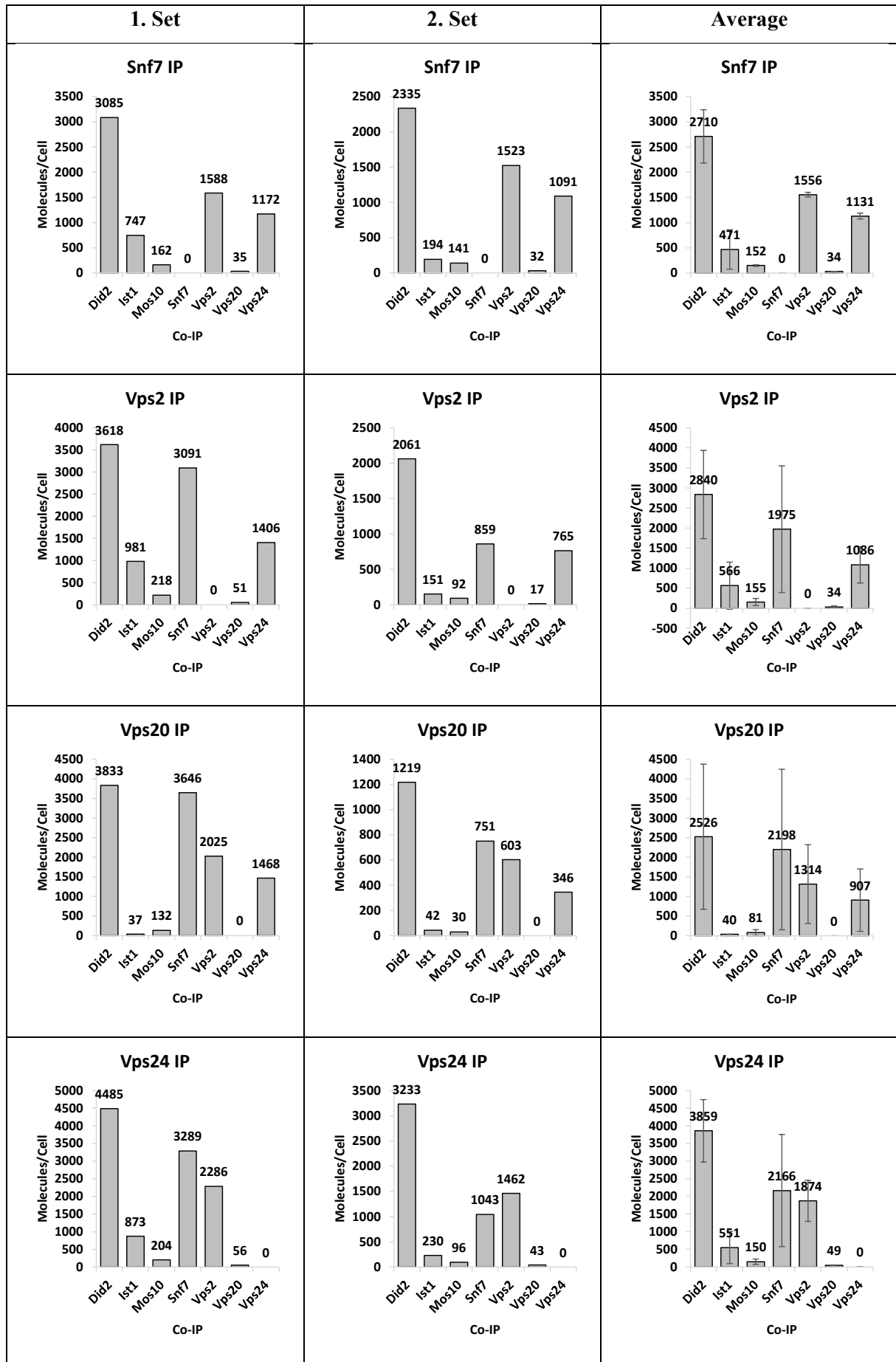
Figure S 24: IP and Co-IP of all ESCRTs in VPS68 deletion strain RKY3222.

Shown are both sets (A and B), with the antibody used for incubating the blot is on the y-axis and the co-immunoprecipitated proteins on the column's header.

Table S 7: Co-IP Overview in $\Delta vps68$ strain RKY3222.

The amount of each individual ESCRT-III subunit co-immunoprecipitated by the IP is measured in molecules per cell according to the numbers by Heinzle *et al.*





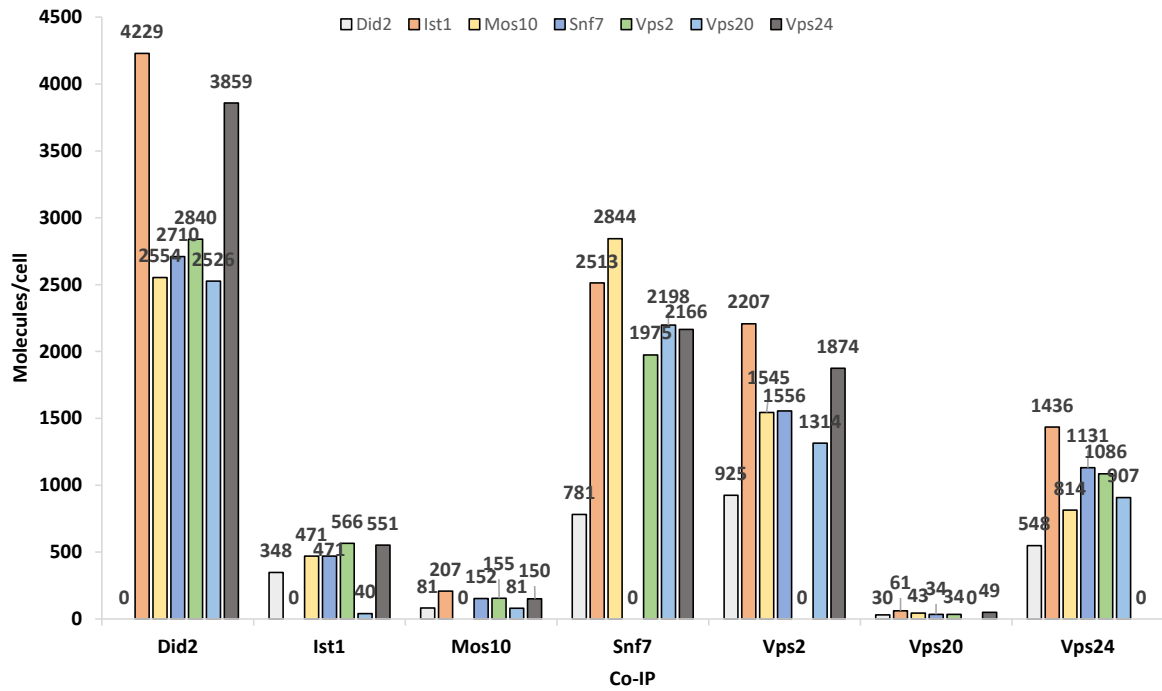


Figure S 25: Total amount of protein co-immunoprecipitated by ESCRT-III IP in Δvps68 strain RKY3222. IP of seven ESCRT-III members and their associated ECRT-III co-IP values assembled to the co-IP protein and graphed against the total molecules per cell.

Table S 8: ESCRT-III molecules per cell.

Protein	Molecules/cell ¹	SD
Chm7	10300	±2900
Did2	12700	±3300
Ist1	5000	±1600
Mos10	3000	±1000
Snf7	8800	±3700
Vps2	7700	±2700
Vps20	1900	±300
Vps24	6800	±2400

¹Average of four independent determinations, SD = standard deviation

*Values taken from Heinze et al., 2019

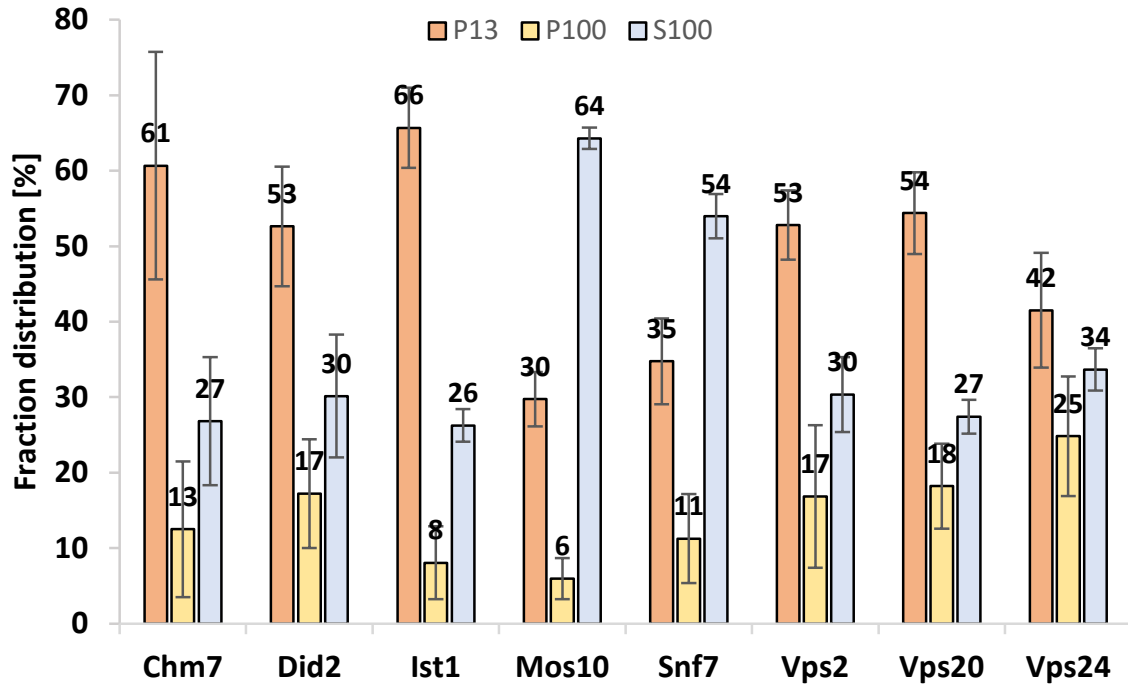


Figure S 26: Differential centrifugation experiment without Triton X-100 in the WT strain RKY 1558.

Sedimentation experiments without Triton X-100 treatment done in triplets and averaged to 100 % over the P13, P100, and S100 fractions for each ESCRT-III protein with error bars.

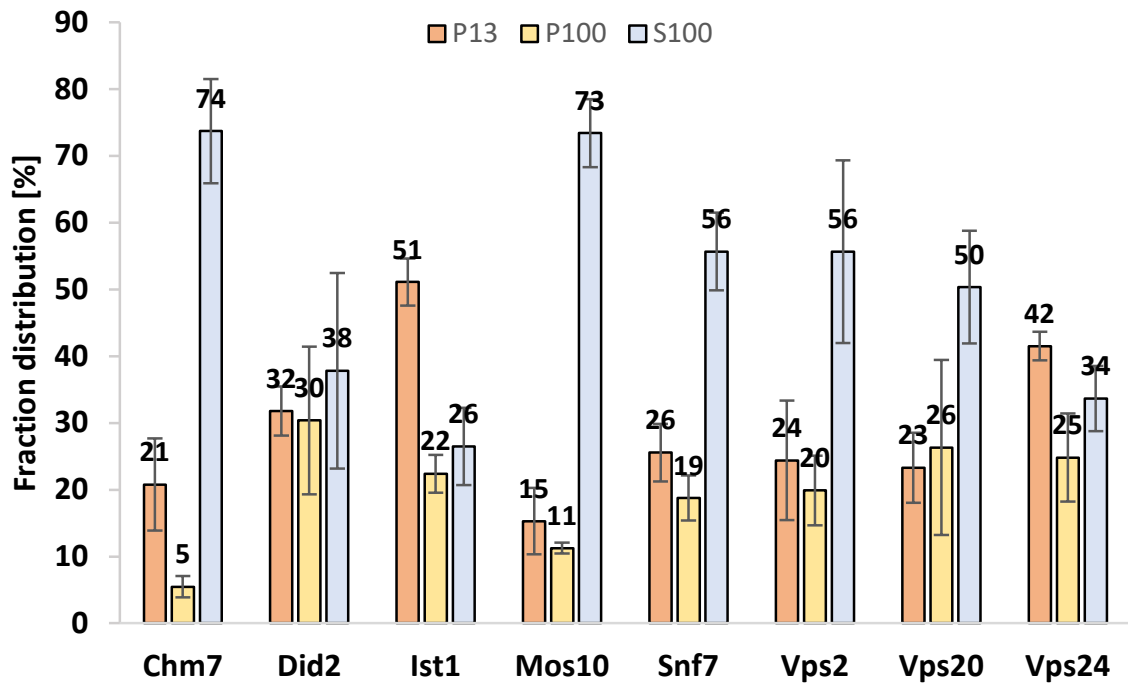


Figure S 27: Differential centrifugation experiment with Triton X-100 in the WT strain RKY 1558.

Sedimentation experiments with Triton X-100 treatment done in triplets and averaged to 100 % over the P13, P100, and S100 fractions for each ESCRT-III protein with error bars.

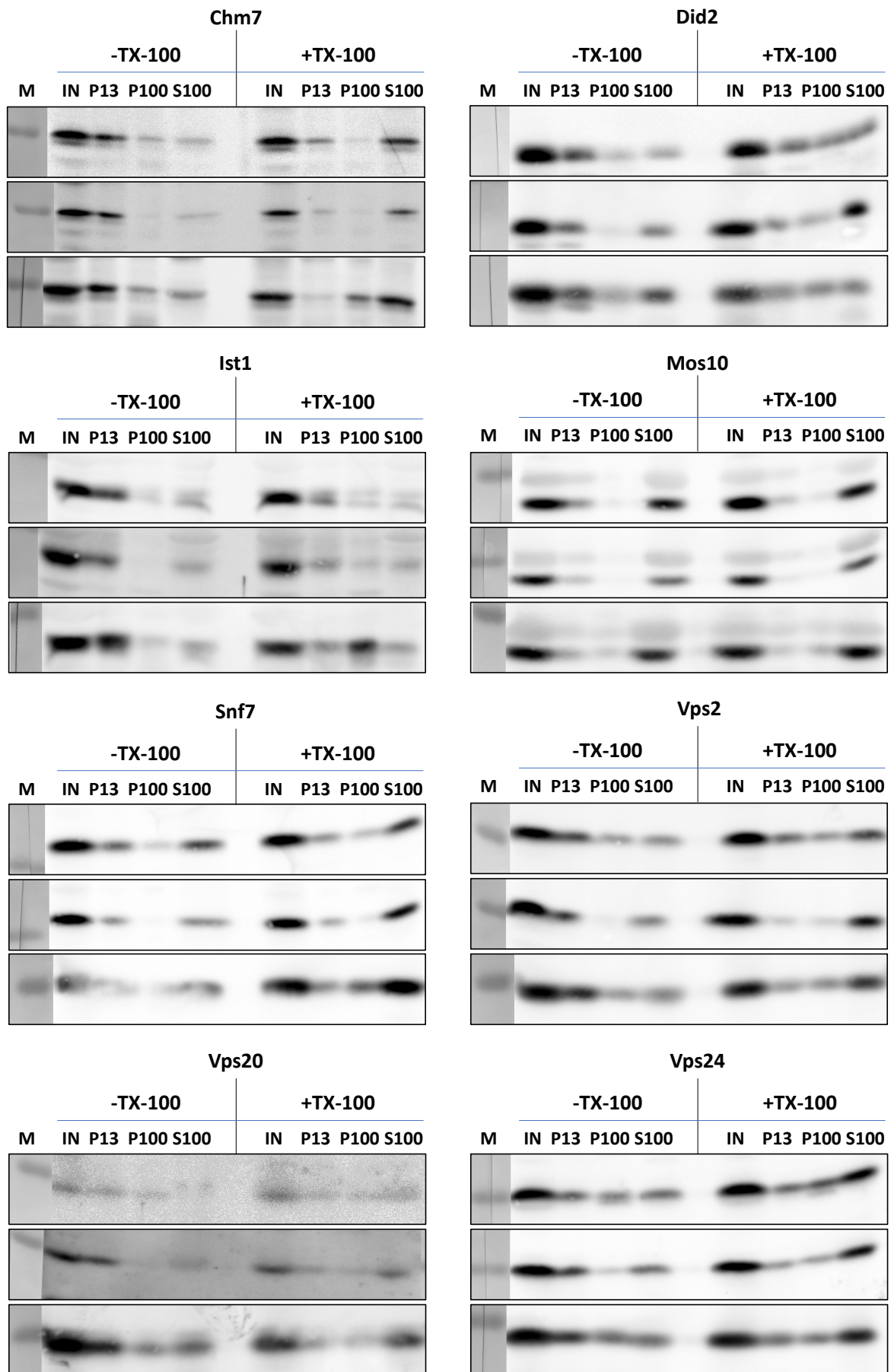


Figure S 28: Western Blots of differential centrifugation of WT strain RKY1558 in triplets.

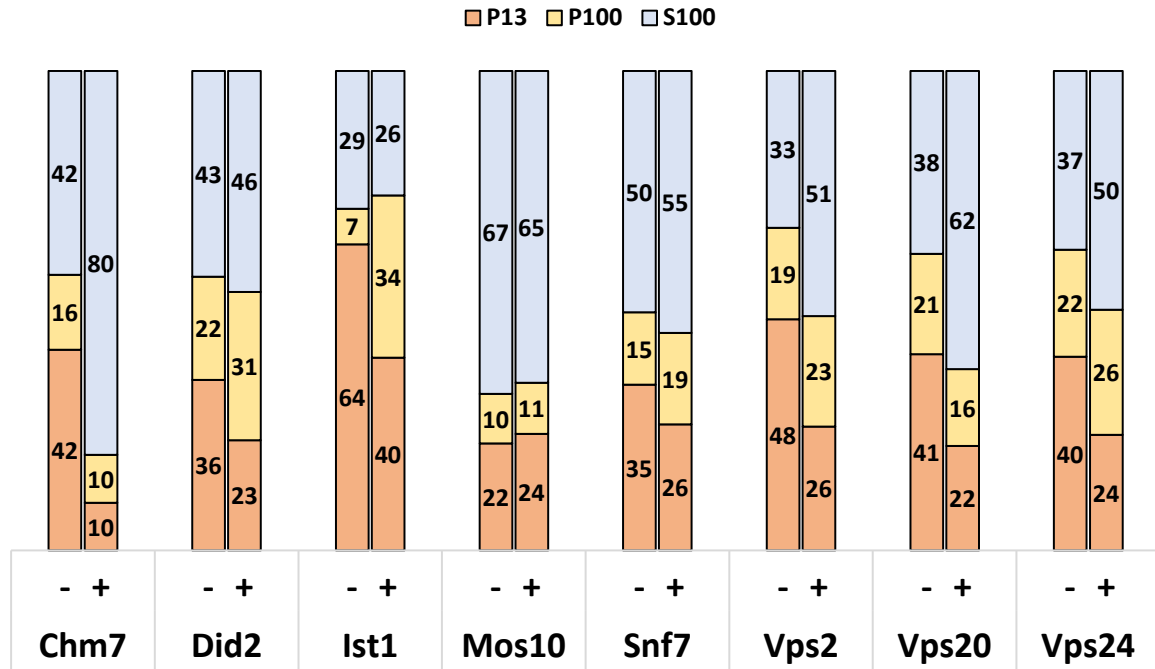


Figure S 29: Protein distribution in the $\Delta vps68$ strain RKY 3221 with and without Triton X-100 treatment. ESCRT-III protein distribution based on the sedimentation fractions P13, P100, and S100 summed to 100 % in the $\Delta vps68$ strain RKY 3221 with (+) and without (-) Triton X-100 treatment.

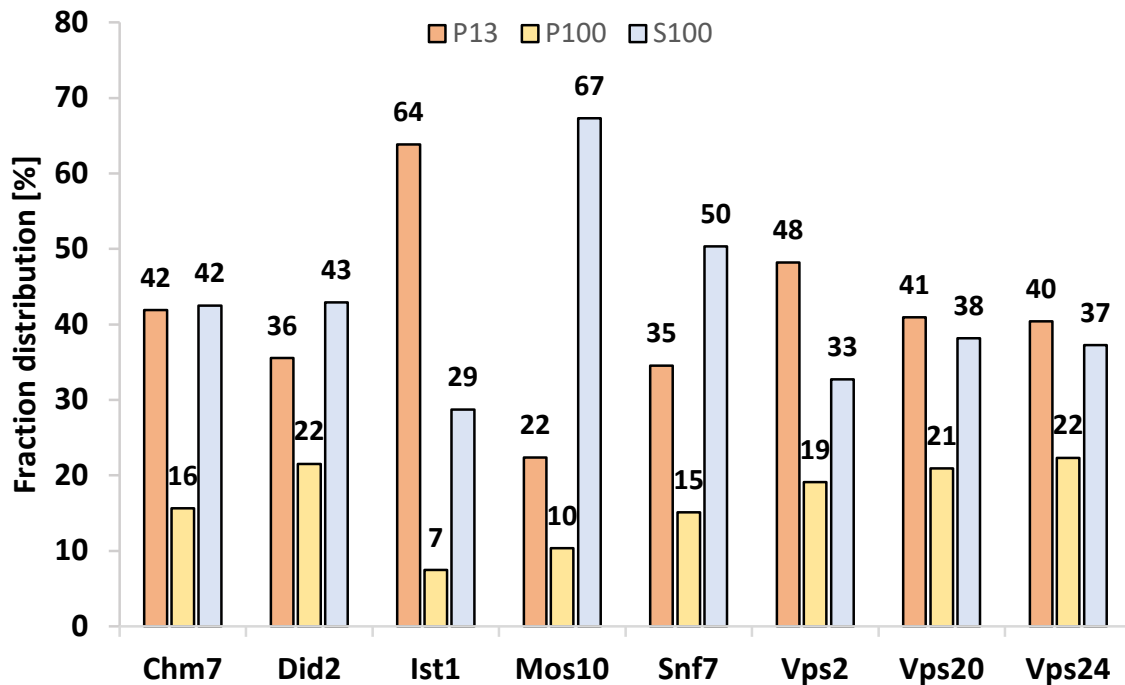


Figure S 30: Differential centrifugation experiment without TX-100 in the $\Delta vps68$ strain RKY 3221. Sedimentation experiments without Triton X-100 treatment averaged to 100 % over the P13, P100, and S100 fractions for each ESCRT-III protein.

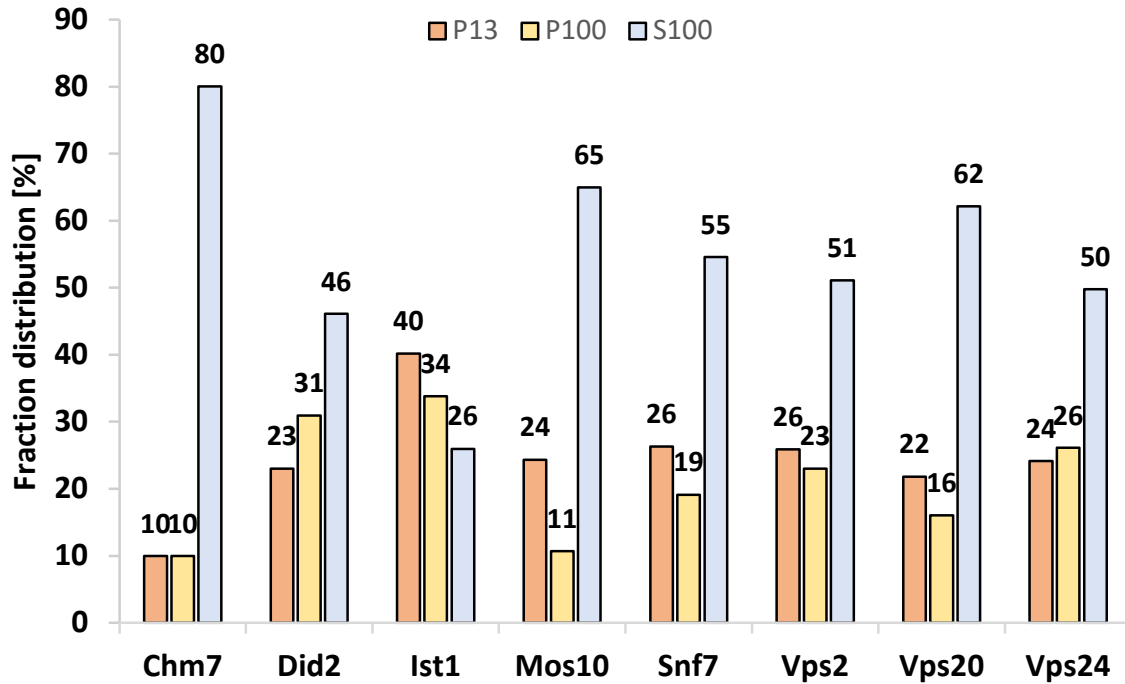


Figure S 31: Differential centrifugation experiment with TX-100 in the $\Delta vps68$ strain RKY 3221.

Sedimentation experiments with Triton X-100 treatment averaged to 100 % over the P13, P100, and S100 fractions for each ESCRT-III protein.

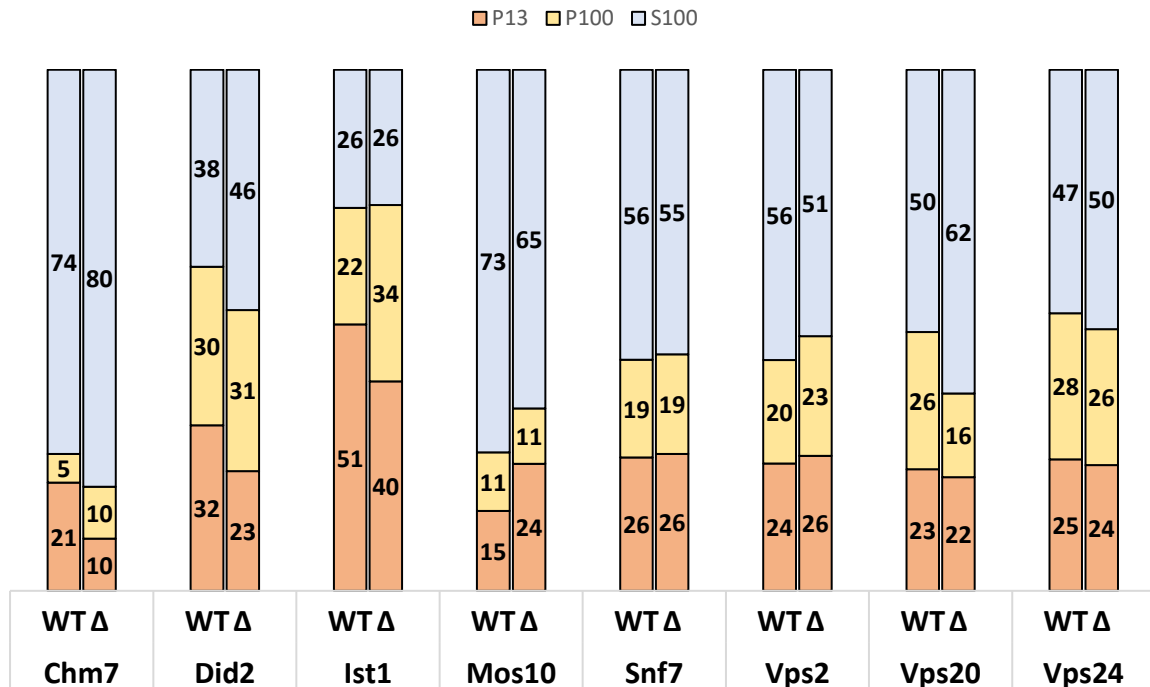


Figure S 32: Sedimentation comparison between RKY1558 and RKY3222 with Triton X-100 treatment.

Comparison of the WB results gained from the differential centrifugation experiment results seen in Figure S 28 & Figure S 33. The fraction values for P13, P100, and S100 for the cultures treated with Triton X-100 are summarized and adjusted to 100 % (Figure S 27 & Figure S 31). For tighter comparison, the results are combined in the diagram.

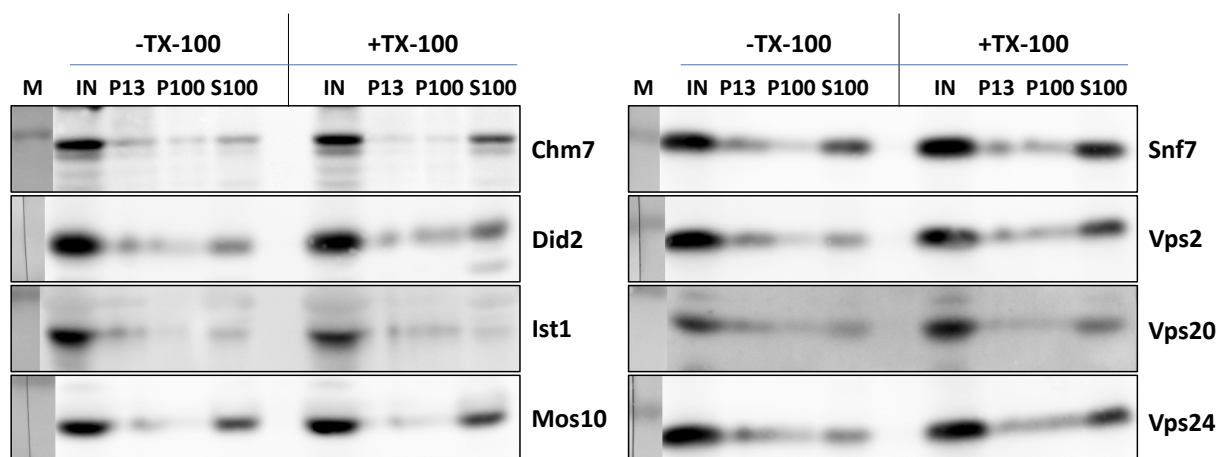


Figure S 33: Western Blots of differential centrifugation results from the $\Delta vps68$ strain RKY 3221.

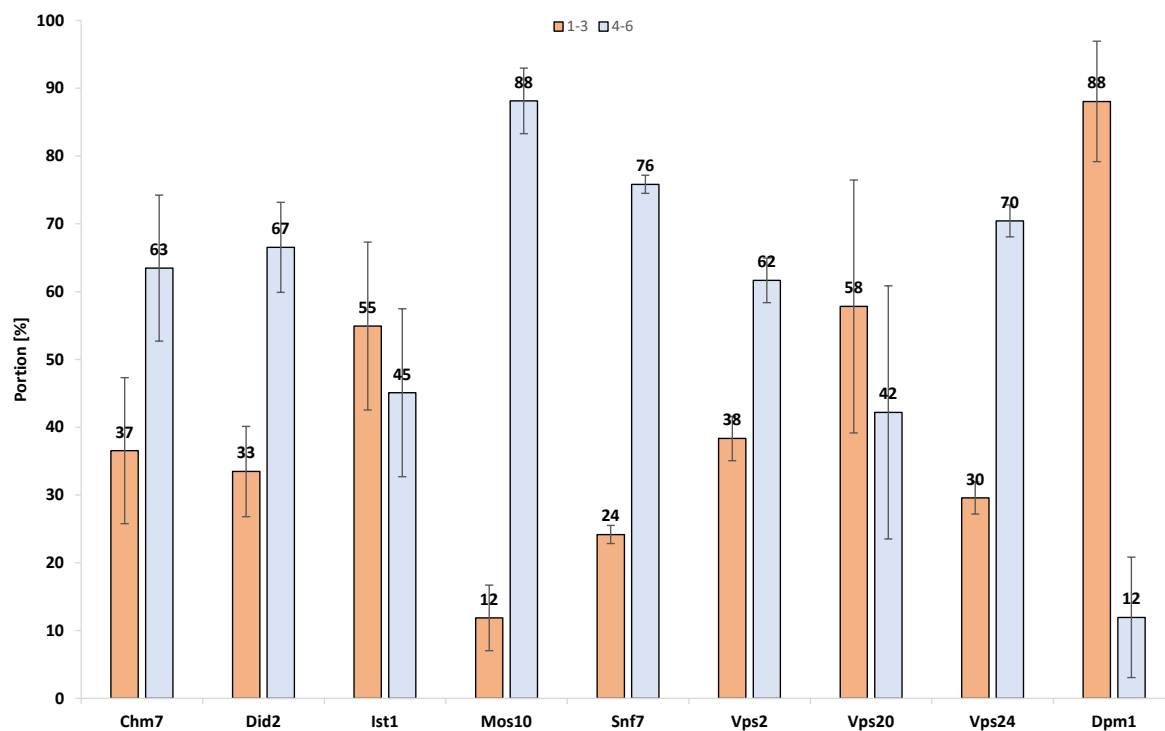


Figure S 34: Summary of the flotation results from the WT strain RKY1558.

Flotation experiments done in triplets collecting six fractions and combining the first three fractions (1-3) and the last three fractions (4-6) to distinguish between the membrane and cytosolic associated proteins. Dpm1 was chosen as a marker for the membrane fractions. All fractions are summed up to 100 %.

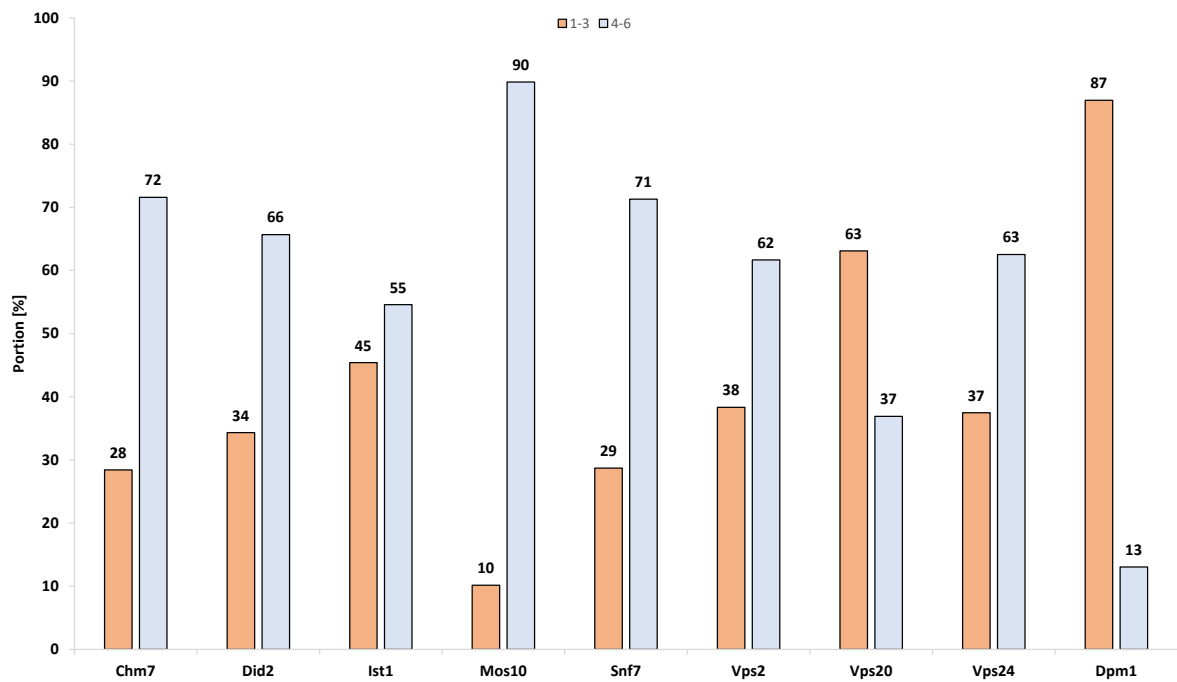


Figure S 35: Summary of the flotation results from the $\Delta vps68$ strain RKY3222.

Flotation experiment collecting six fractions and combining the first three fractions (1-3) and the last three fractions (4-6) to distinguish between the membrane and cytosolic associated proteins. Dpm1 was chosen as a marker for the membrane fractions. All fractions are summed up to 100 %.

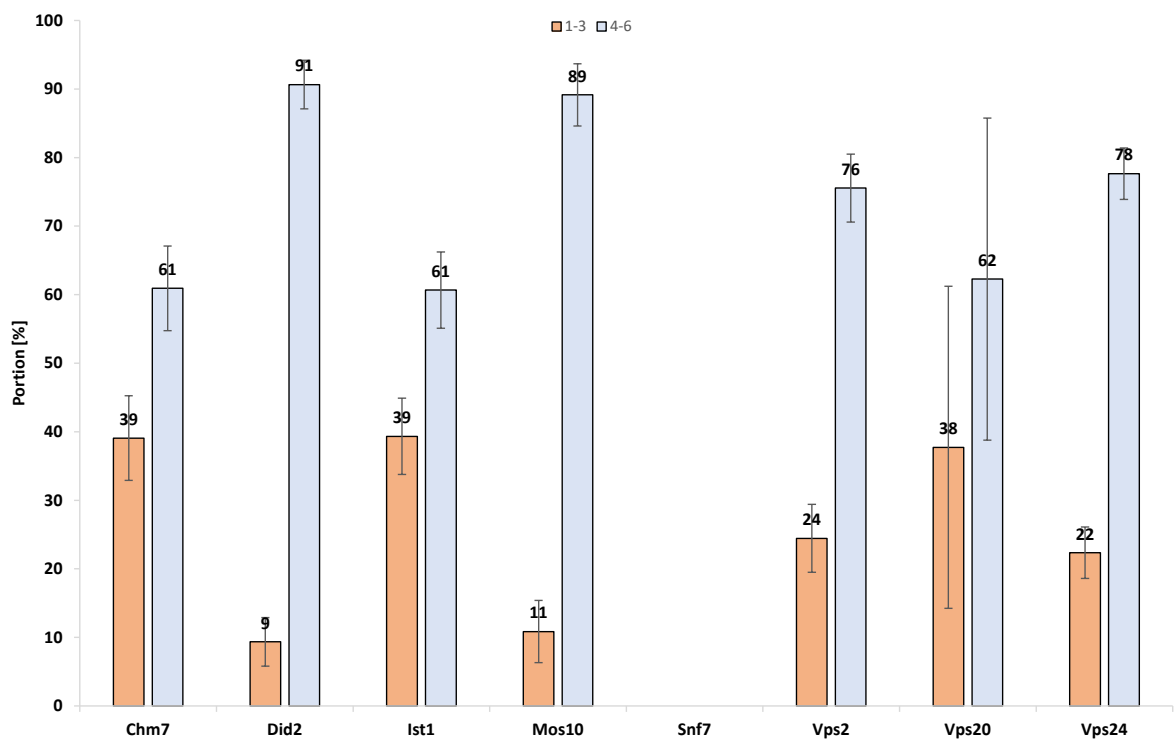


Figure S 36: Summary of the flotation results from the $\Delta snf7$ strain RKY2790.

Flotation experiments done in triplets collecting six fractions and combining the first three fractions (1-3) and the last three fractions (4-6) to distinguish between the membrane and cytosolic associated proteins. Dpm1 was chosen as a marker for the membrane fractions. All fractions are summed up to 100 %.

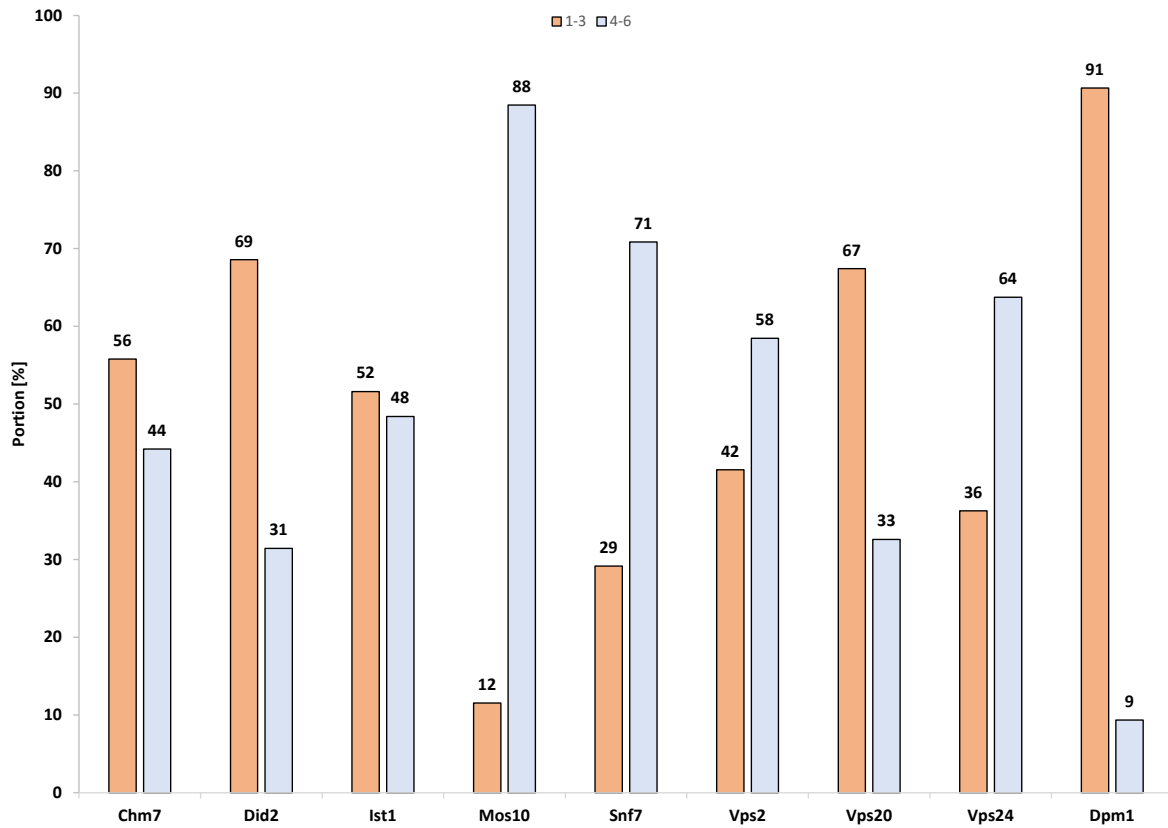


Figure S 37: Summary of the flotation results from the WT strain RKY1558 after incubation.

Flotation experiment collecting six fractions and combining the first three fractions (1-3) and the last three fractions (4-6) to distinguish between the membrane and cytosolic associated proteins. Dpm1 was chosen as a marker for the membrane fractions. All fractions are summed up to 100 %.

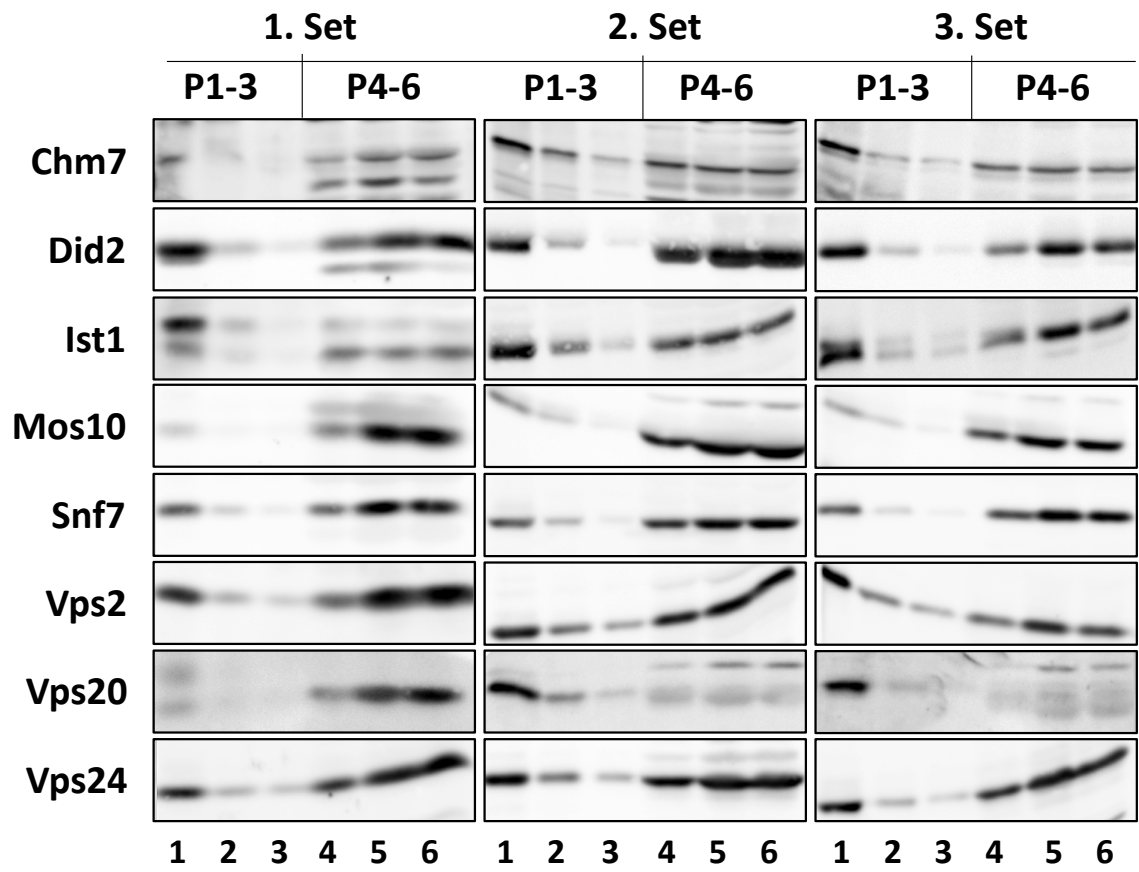


Figure S 38: WB results of the flotation experiments of WT strain RKY1558.

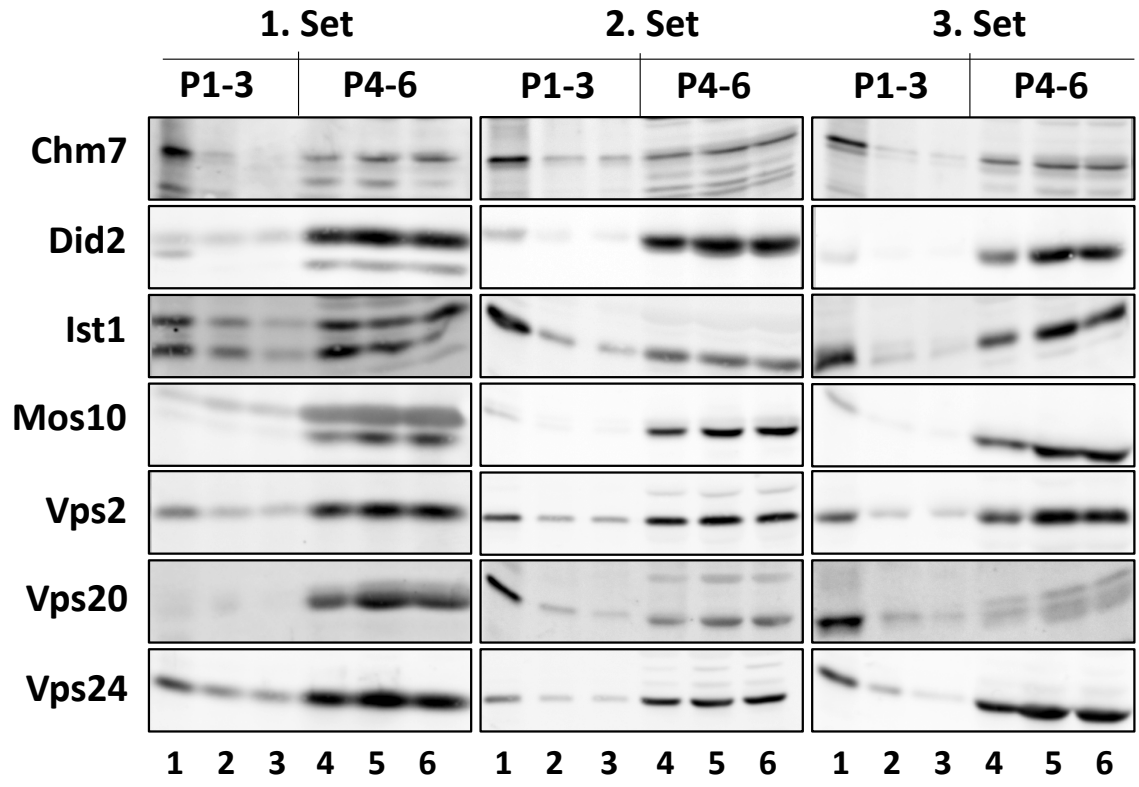


Figure S 39: WB results of the flotation experiments of $\Delta snf7$ strain RKY2790.

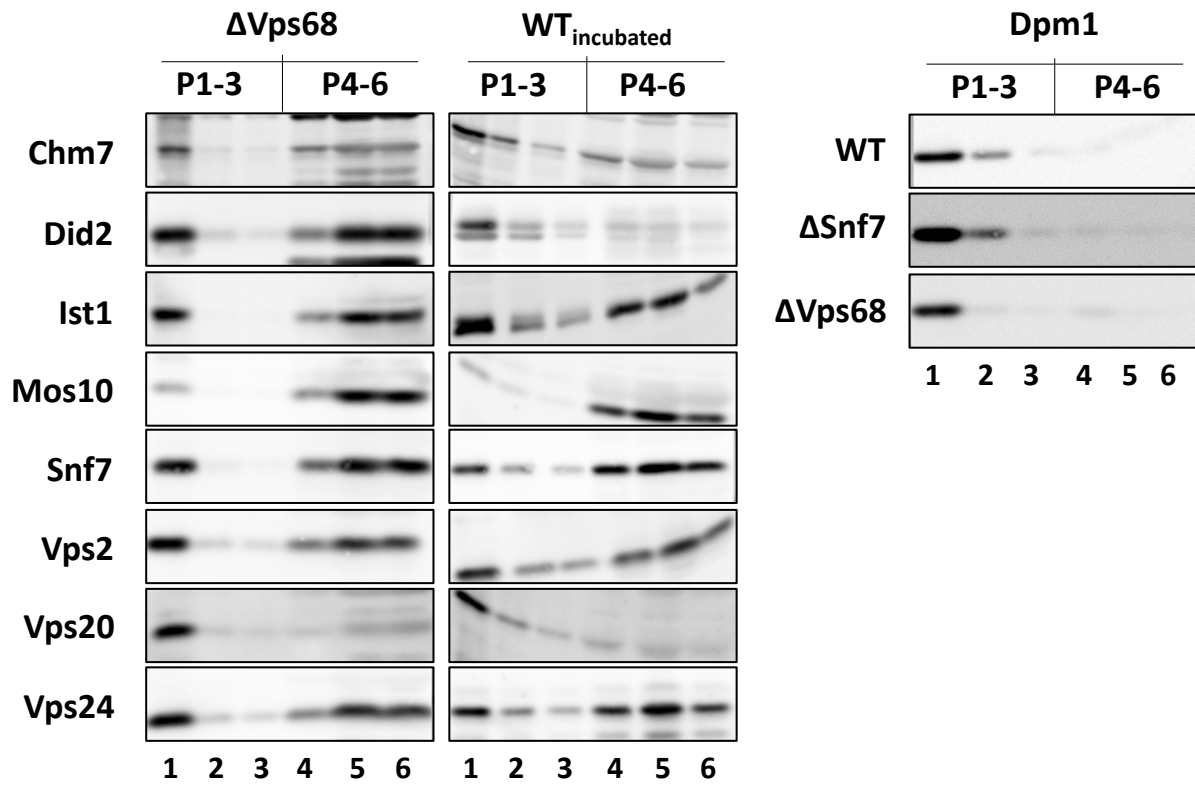


Figure S 40: Flotation results regarding WT incubation, Dpm1 marker protein, and Vps68 deletion.

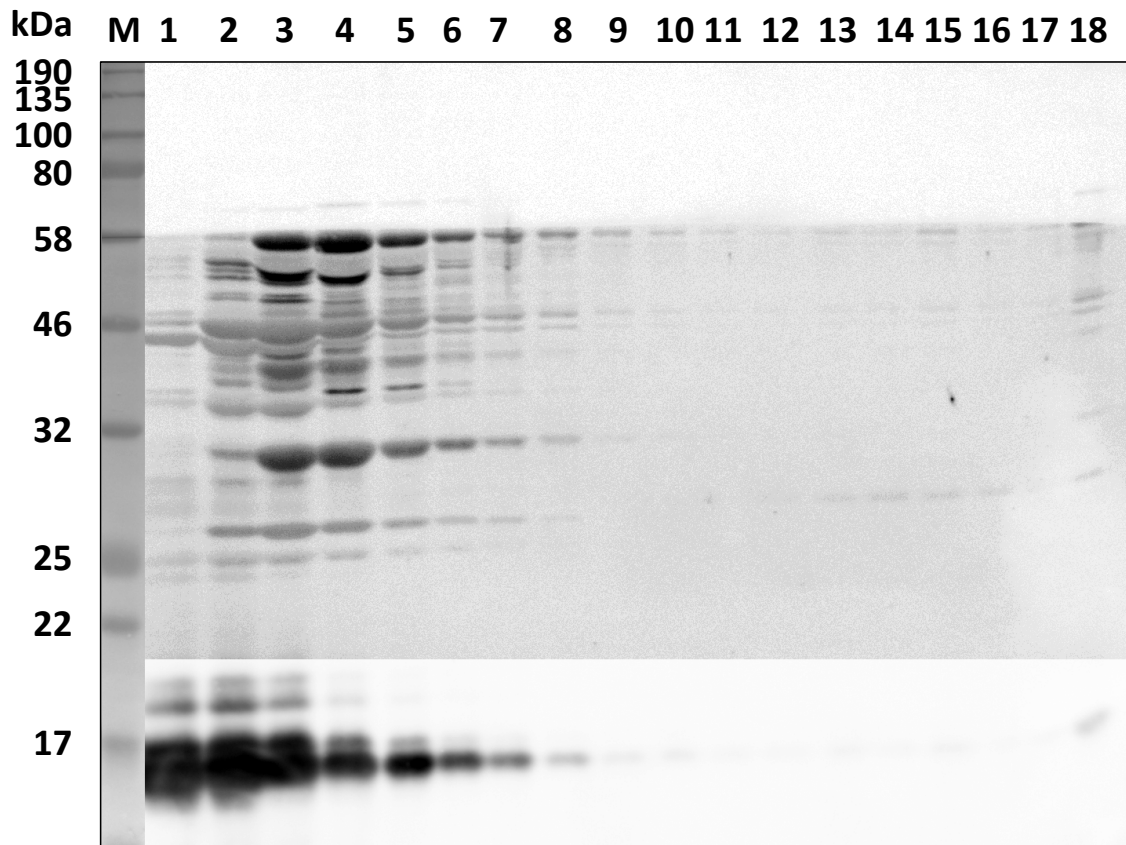


Figure S 41: Sucrose gradient incubated Did2 WB results of RNaseA treated cells.

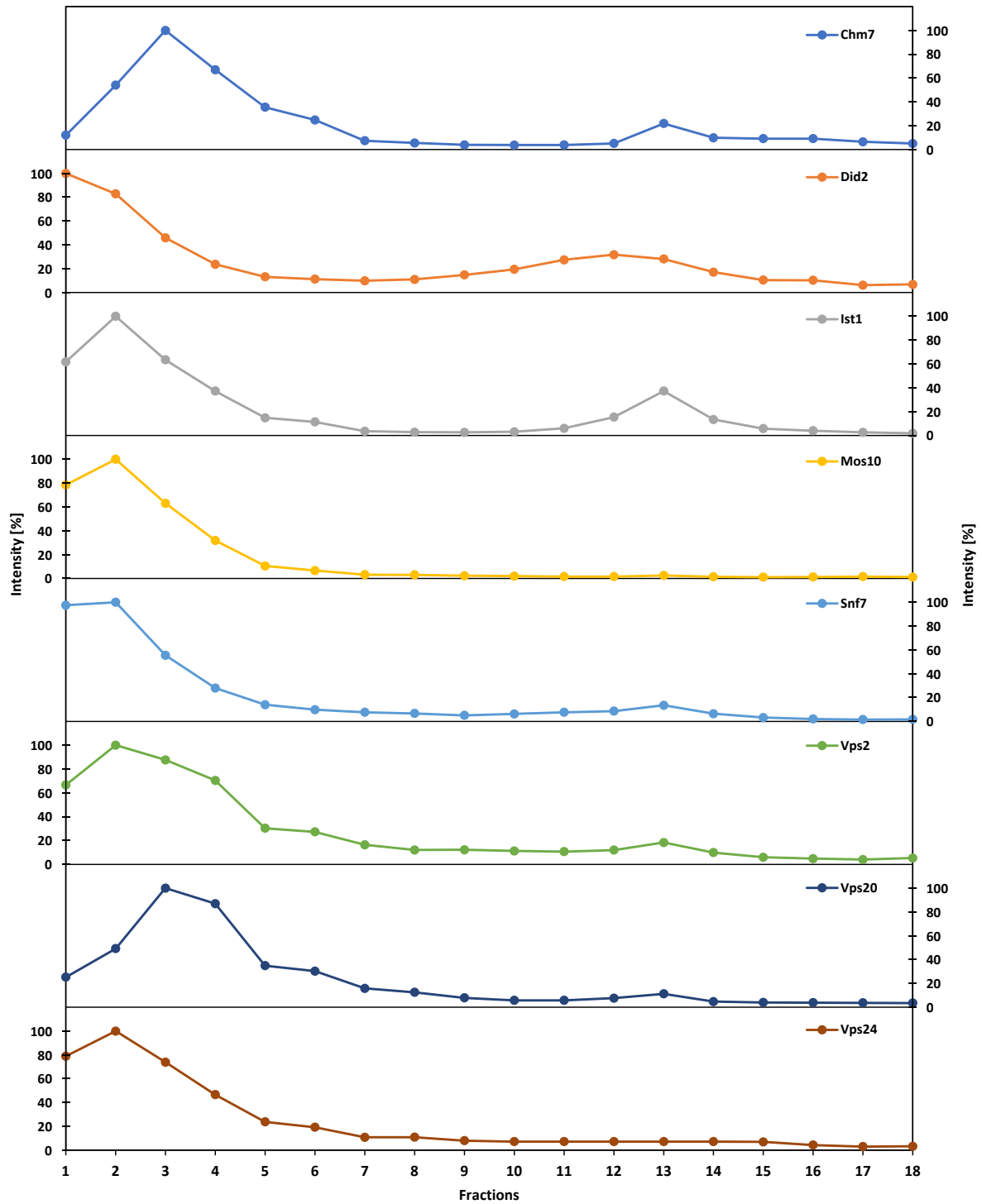


Figure S 42: ESCRT-III proteins sucrose profiles in the Vps68 deletion strain RKY3222.

Sucrose density fractionation into 18 fractions based on the sedimentation rate of all ESCRT-III proteins after in SPBS10 buffer.

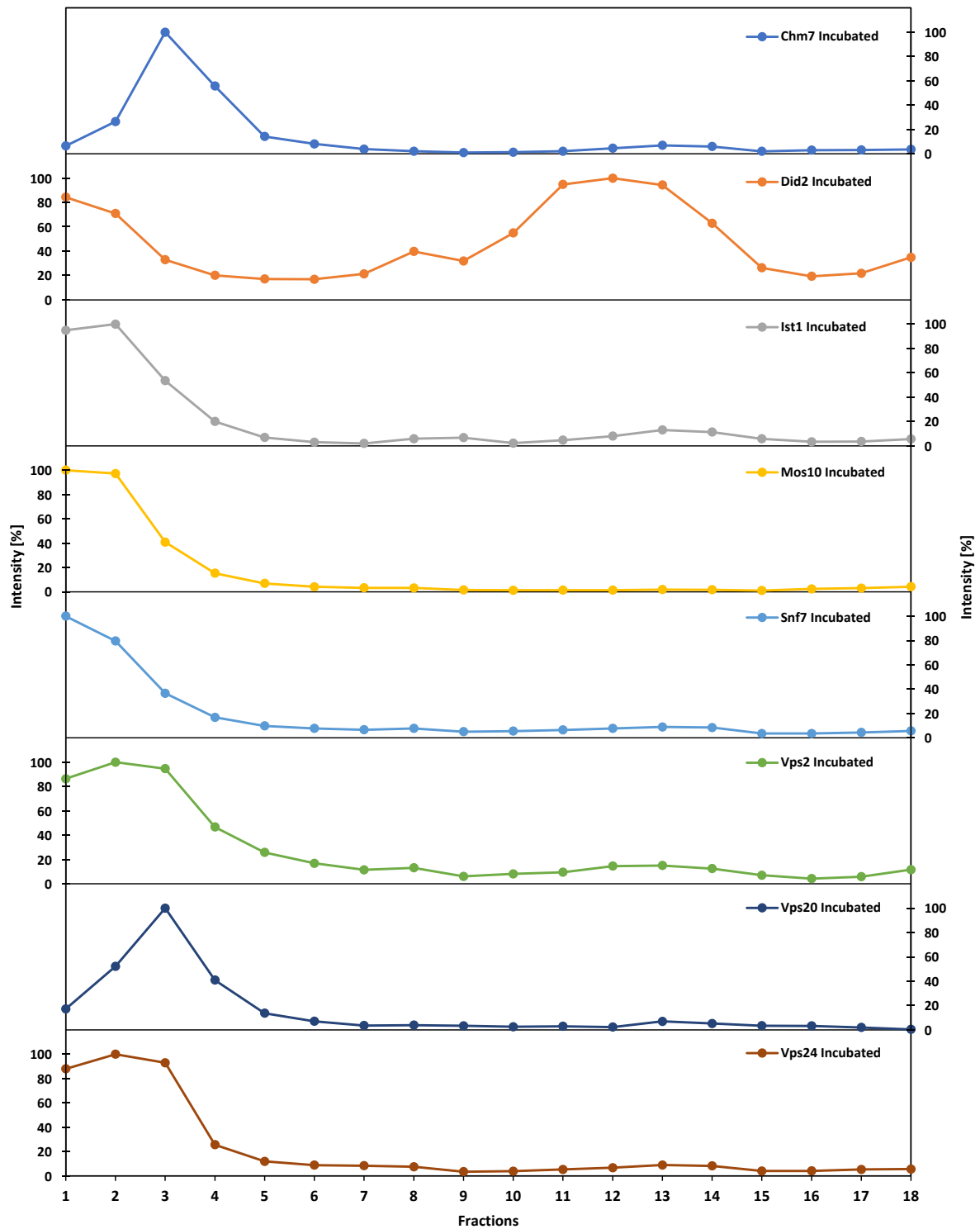


Figure S 43: ESCRT-III proteins sucrose profiles in the *Vps68* deletion strain RKY322 after incubation.

Sucrose density fractionation into 18 fractions based on the sedimentation rate of all ESCRT-III proteins after incubation for 30 min at 37 °C in SPBS10 buffer.

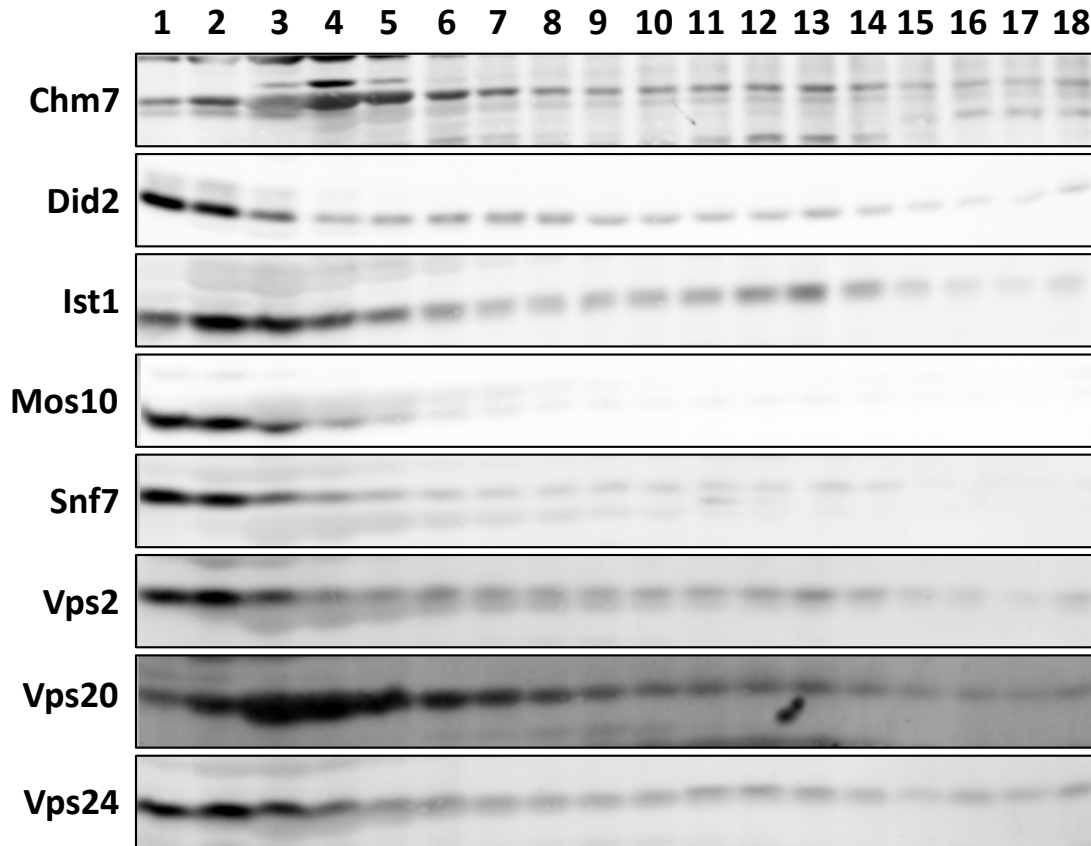


Figure S 44: WB results of the sucrose gradient from the WT strain RKY1558.

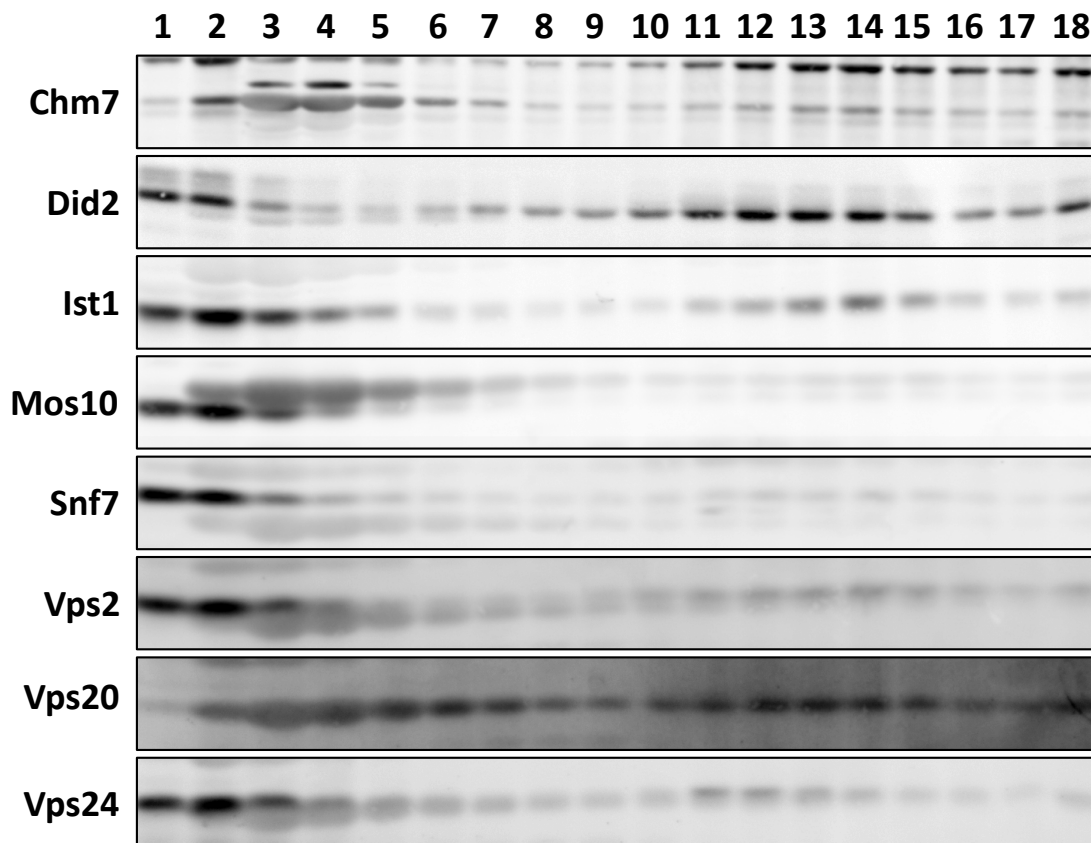


Figure S 45: WB results of the sucrose gradient from the WT strain RKY1558 after incubation.

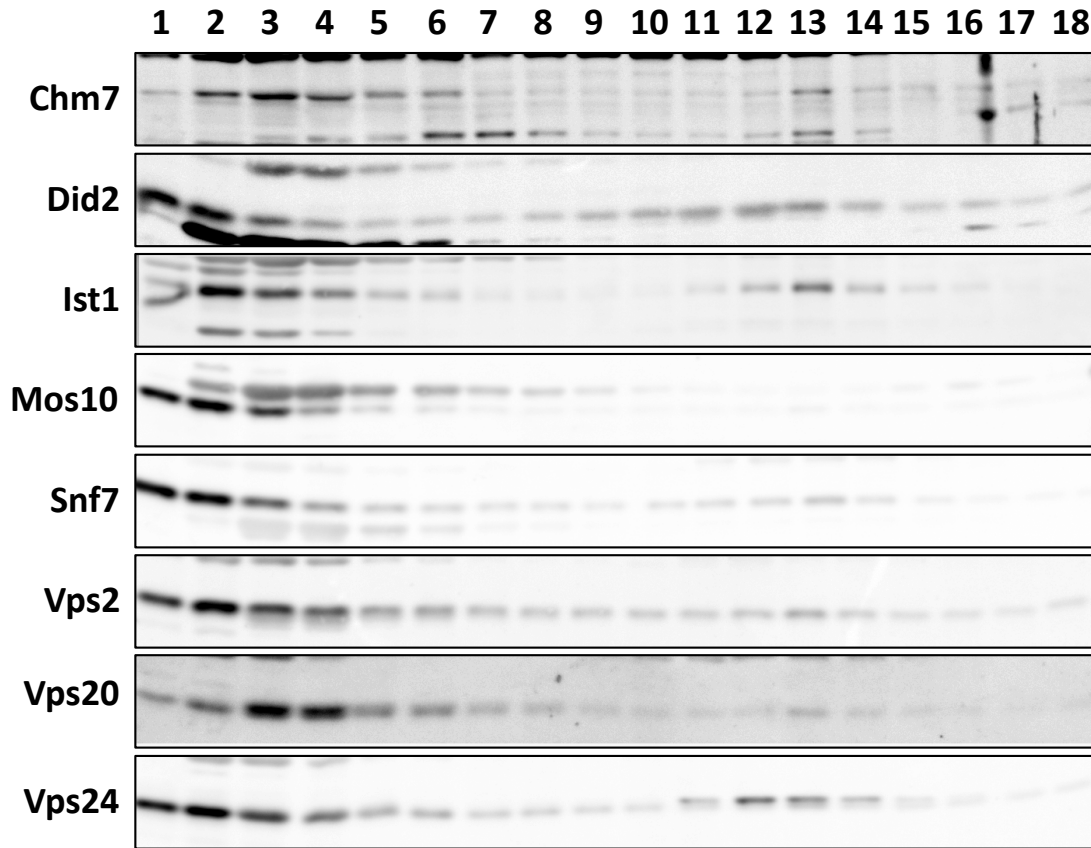


Figure S 46: WB results of the sucrose gradient from the $\Delta vps68$ strain RKY3222.

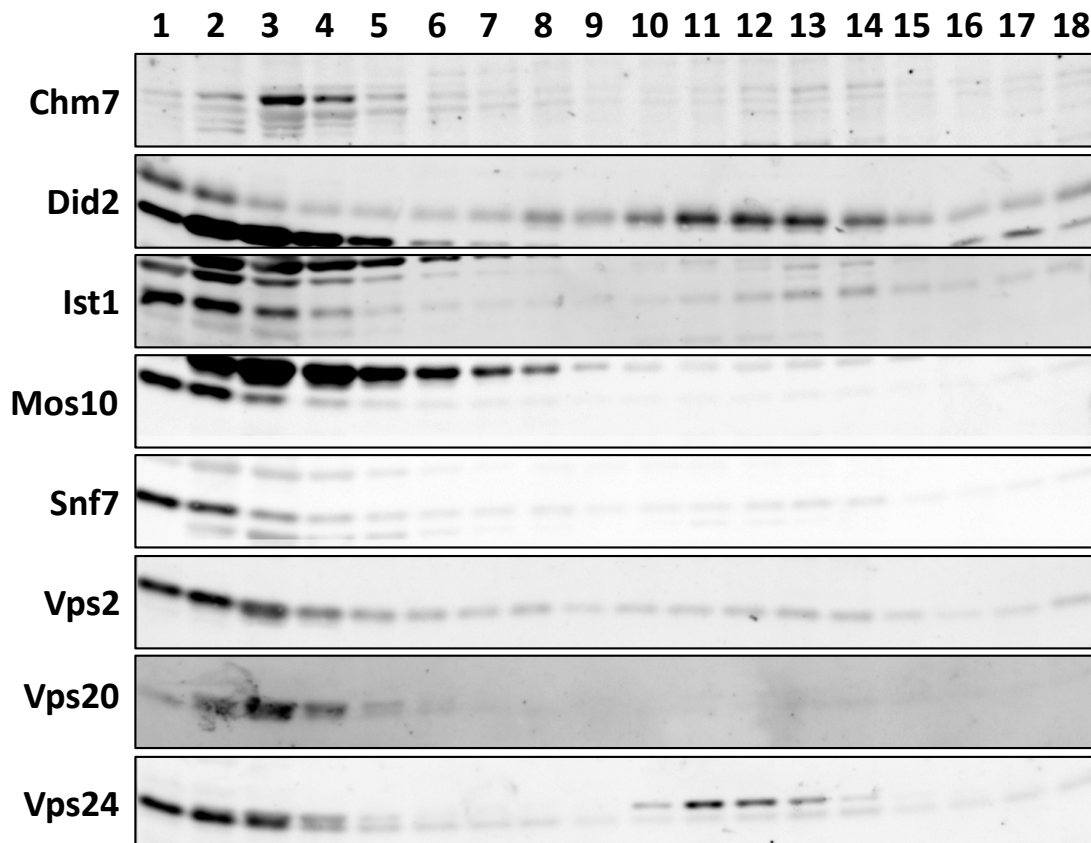


Figure S 47: WB results of the sucrose gradient from the $\Delta vps68$ strain RKY3222 after incubation.

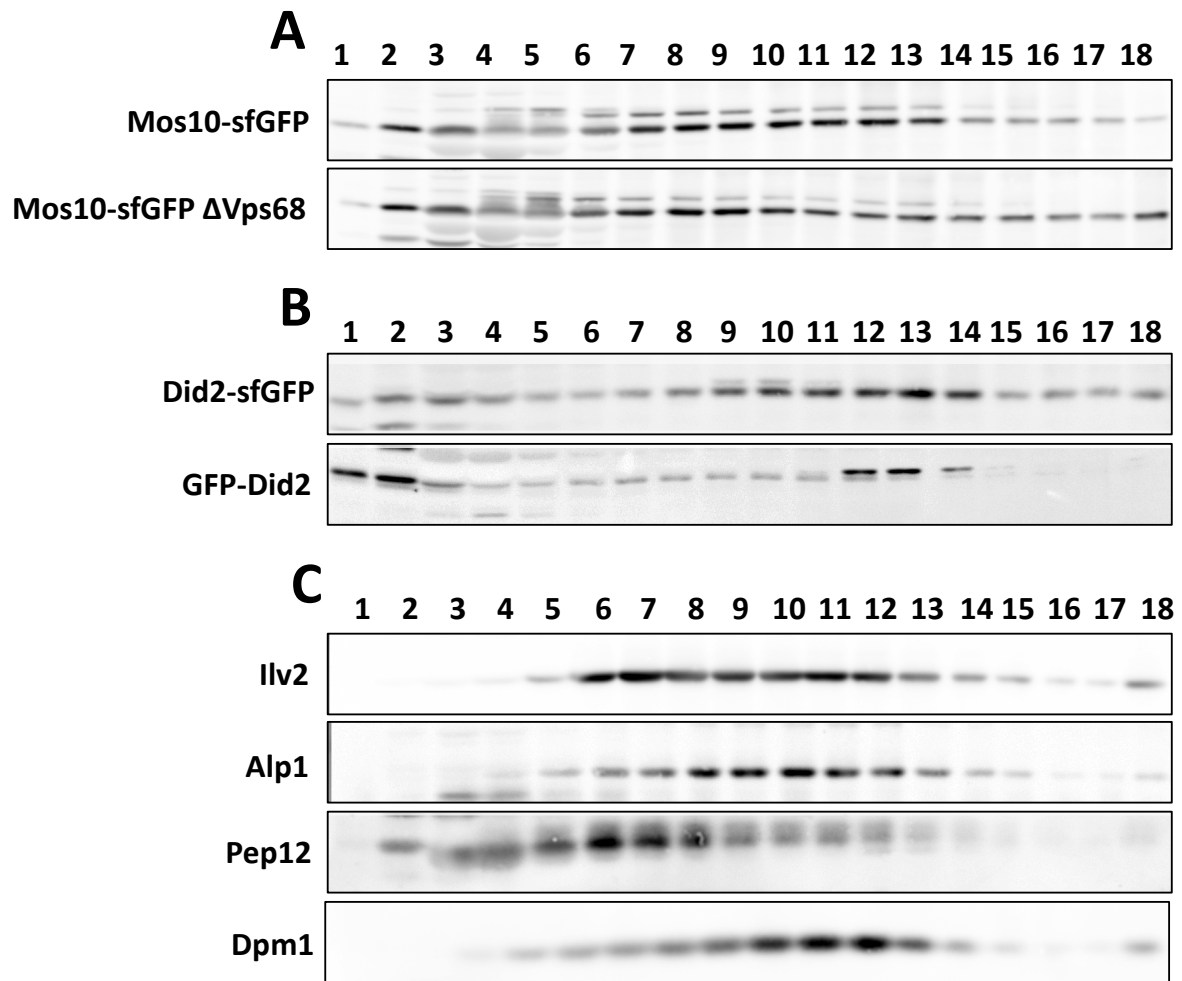


Figure S 48: Sucrose profiles of marker and tagged proteins.

A: WB results of the Mos10-sfGFP tagging in the WT and $\Delta vps68$ background. **B:** WB results of n-terminal and c-terminal tagged Did2 by sfGFP and GFP. **C:** WB results of the marker proteins Ilv2 (mitochondria), Alp1 (vacuole), Pep12 (late endosome), and Dpm1 (ER).

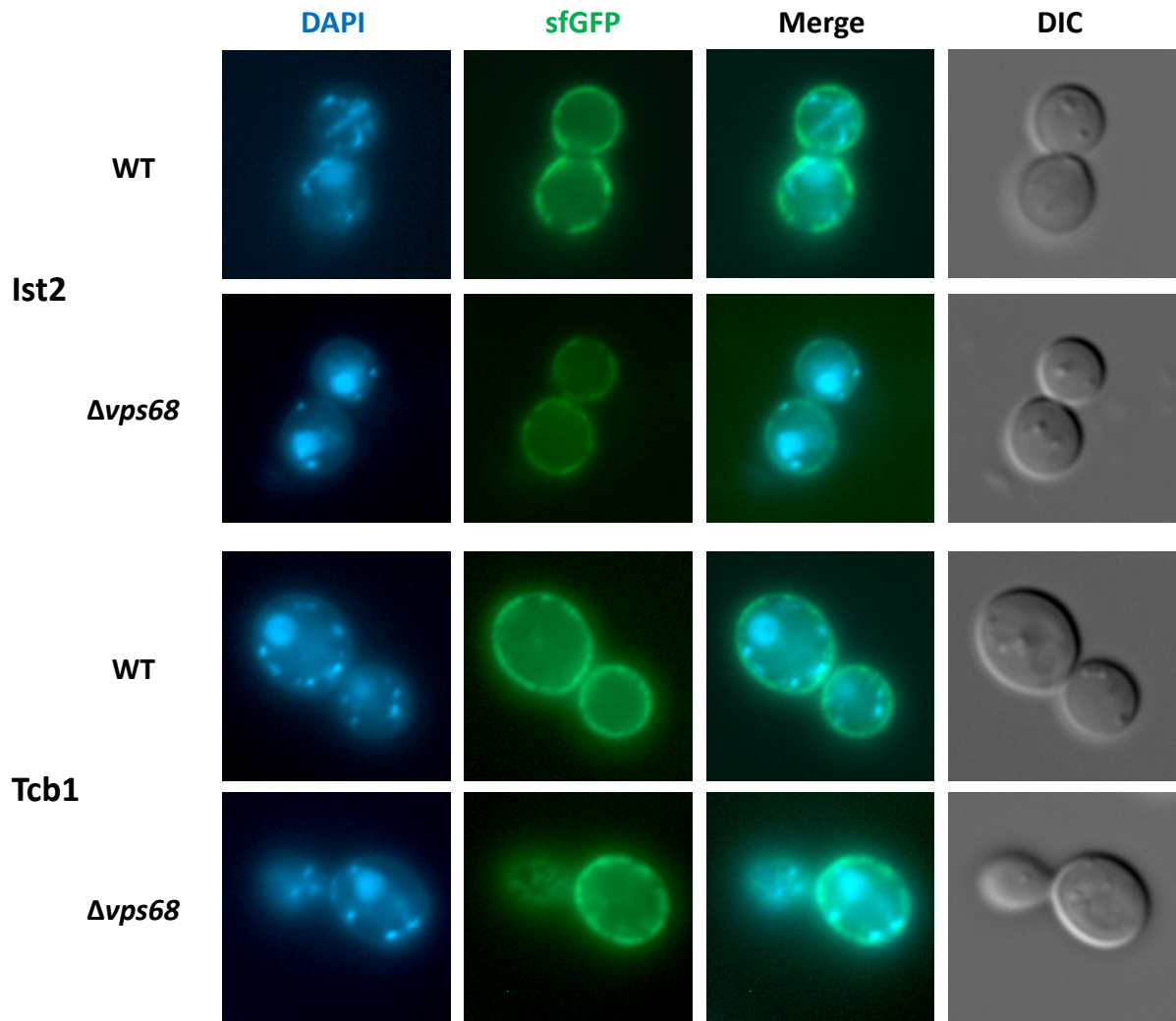


Figure S 49: Evaluating Vps68 induced alterations in ER-PM tethering visualized by Ist2- & Tcb1-sfGFP.
 The marker proteins Ist2 and Tcb1 are ER proteins involved in ER to PM tethering shown by the sfGFP tagged variants of each protein in the WT strain RKY1558 and $\Delta vps68$ strain RKY3222 background.

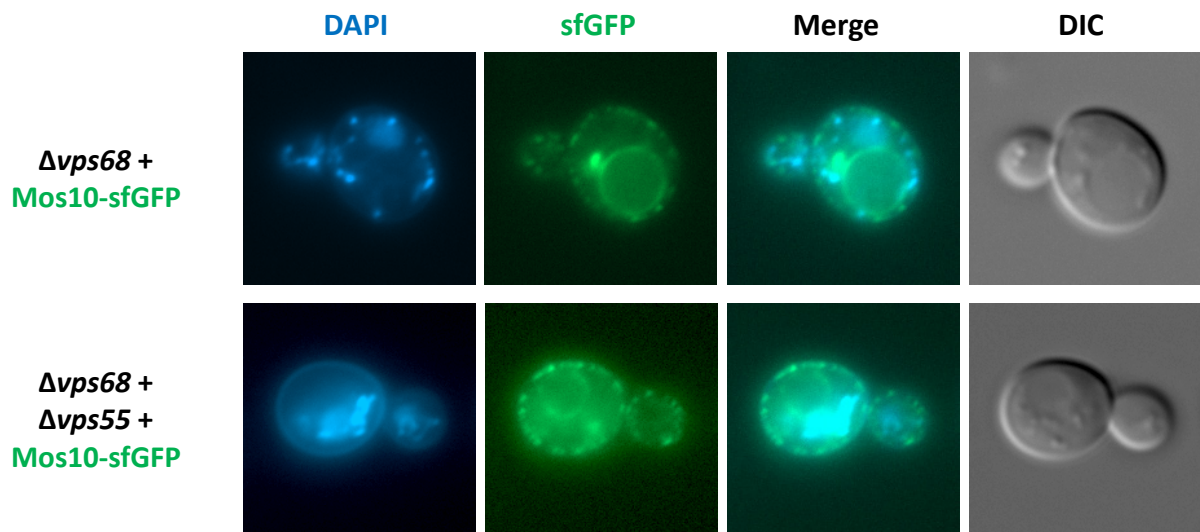


Figure S 50: Alterations in Mos10-sfGFP distribution by Vps68 and Vps55 single and double deletions.

SUMMARY

The endosomal sorting complex required for transport (ESCRT) is a part of the heteromeric complex machinery consisting of ESCRT-0, -I, -II, and -III ensuring functional protein traffic of endocytic and biosynthetic cargo. Stepwise sorting of labeled cargo material inside the lumen of the endosome by invagination and abscission of the endosomal membrane to form intraluminal vesicles (ILV's) is mediated by the ESCRT-III complex. The complex consists of eight members of which Vps20, Snf7, Vps2, and Vps24 are considered ESCRT-III essential subunits, and Chm7, Did2, Ist1, and Mos10/Vps60 are commonly labeled as complex associated proteins. The correct interplay between the proteins ensures cargo sorting into the MVB (multivesicular body) pathway and transport from the late endosome into the vacuolar lumen for degradation. Besides the initial function of vacuolar protein sorting (vps), the complex is involved in a multitude of cellular processes like cell abscission, virus budding, autophagy, and remaining nuclear envelope integrity.

The step-wise assembly of the ESCRT-III complex is mediated after the cascade-like ESCRT-0 to ESCRT-II complex formation at the membrane budding site, collecting cargo protein for invagination into the endosomal lumen. ESCRT-III Vps20 is recruited to the membrane by the ESCRT-II member Vps25, then nucleating Snf7 association and oligomerization. Additional assembly of ESCRT-III members like Vps24 and Vps2 further drives membrane bending away from the cytosol to the final abscission event, before being recycled back to cytosolic monomers by Vps4. Although Mos10 has been implicated in the recycling step of the ESCRT-III units by interacting with the Vps4/Vta1 complex, the protein's function remains poorly characterized.

This thesis tried to find new insights in Mos10 functionality by finding yet uncharacterized interacting partners, thus connecting the protein to new putative non-endosomal functions or understanding its role in the established ESCRT-III complex. For this purpose, a series of crosslinking experiments with tagged variants of Mos10 were performed. Purification was achieved by IMAC (Immobilized Metal Ion Affinity Chromatography) after adding a poly-his sequence to the protein and by immunoprecipitation of sfGFP tagged Mos10. Both methods revealed a multitude of putative Mos10 interacting partners by MS analysis to be further reduced by applying the SILAC (stable isotope labeling with amino acids in cell culture) technique. After selecting possible Mos10 interacting partners, IP and Co-IP experiments of tagged candidate variants were used to identify an interaction between the two proteins. An interaction between Mos10-6His and Vps68-13myc besides native Mos10 and Vps68-fGFP could be verified by purification of Vps68 and co-precipitating Mos10.

The influence of Vps68 on the assembly and composition of the ESCRT-III complex was examined. After Vps68 depletion, an enrichment of the core subunits Snf7, Vps2, and Vps24 in the complex was detected with a reduced number of Did2, Ist1, and Mos10 molecules. Thus, it appears that ESCRT-III disassembly is blocked in $\Delta vps68$ mutant. The influence of *VPS68* deletion on the intracellular localization of ESCRT-III proteins was examined by fluorescence microscopy with sfGFP-tagged variants. While the localization of most ESCRT-III proteins was not significantly altered, a marked relocation was observed for Mos10. In wildtype, Mos10-sfGFP was localized at the vacuolar membrane, while in $\Delta vps68$ it was dispersed into vesicular structures enriched at the cell cortex.

Further, the impact of *VPS68* deletion on the sorting of the endocytic cargo protein Ste6 was investigated. By cycloheximide chase experiments, it could be shown that Ste6 is strongly stabilized in a $\Delta vps68$ mutant. This indicates that the transport of the protein to the yeast vacuole for degradation is blocked. The $\Delta vps68$ block in endocytic trafficking was compared with other mutants of the *vps*-pathway, whose site of action has been established. These experiments show that the *VPS68* deletion neither leads to a class D phenotype, as in $\Delta vps21$, nor to a class E phenotype, as in $\Delta snf7$. The Ste6-GFP distribution in the $\Delta vps68$ mutant rather resembles wildtype with more pronounced accumulation of endosomal dots. The data taken together suggest that Vps68 acts after the formation of the ESCRT-III complex and is required for cargo delivery from the late endosome to the vacuolar lumen.

ZUSAMMENFASSUNG

Der für den endosomalen Protein-Transport erforderliche ESCRT (endosomal sorting complex required for transport)-III Komplex ist ein Teil der heteromeren Komplexmaschinerie, die aus ESCRT-0, -I, -II und -III besteht und die Sortierung von endozytischem und biosynthetischem Cargo in intraluminäre Vesikel (ILVs) bewerkstelligt. Der ESCRT-III Komplex besteht aus acht Mitgliedern, von denen Vps20, Snf7, Vps2 und Vps24 als essentielle Untereinheiten des ESCRT-III-Komplexes angesehen werden, während Chm7, Did2, Ist1 und Mos10/Vps60 gemeinhin als komplexassoziierte Proteine bezeichnet werden. Das korrekte Zusammenspiel der Proteine gewährleistet die Sortierung des Cargos in den MVB (multivesicular body)-Weg und den Transport aus dem späten Endosom in das vakuoläre Lumen zur Degradation. Neben der ursprünglichen Funktion der vakuolären Proteinsortierung (vps) ist der Komplex an einer Vielzahl von zellulären Prozessen wie Zellteilung, Virusknospung, Autophagozytose und Aufrechterhaltung der Kernhüllenintegrität beteiligt.

Der schrittweise Aufbau des ESCRT-III-Komplexes erfolgt kaskadenartig beginnend mit ESCRT-0- bis zu ESCRT-II an der Knospungsstelle der Membran und sammelt das Cargo-Protein für die Einschleusung in das endosomale Lumen. Das ESCRT-III Protein Vps20 wird durch die ESCRT-II-Untereinheit Vps25 an die Membran rekrutiert, wodurch die Assoziation und Oligomerisierung von Snf7 ausgelöst wird. Weitere ESCRT-III-Mitglieder wie Vps24 und Vps2 sorgen dafür, dass sich die Membran bis zur endgültigen Abtrennung der ILVs vom Zytosol zum Lumen hin verbiegt. Sodann wird der Komplex durch Vps4 wieder aufgelöst. Mos10 wird eine Funktion bei der Auflösung der ESCRT-III Komplexe über den Vps4/Vta1 Komplex zugesprochen, doch ist die Funktion des Proteins nach wie vor unzureichend geklärt. In dieser Arbeit wurde durch Identifizierung bislang nicht charakterisierter Interaktionspartner versucht, neue Einblicke in die Funktionalität von Mos10 zu gewinnen, um einerseits Verbindungen zu neuen nicht-endosomalen Funktionen herzustellen oder auch, um andererseits seine Rolle im etablierten ESCRT-III Komplex besser zu verstehen. Dazu wurden eine Reihe von Quervernetzungsexperimenten mit markierten Varianten von Mos10 durchgeführt. Die Reinigung erfolgte durch IMAC (Immobilisierte Metallionen-Affinitäts-Chromatographie) nach Hinzufügen einer Poly-his-Sequenz zum Protein und durch Immunpräzipitation von sfGFP-markiertem Mos10. Beide Methoden ergaben eine Vielzahl von möglichen Interaktionspartnern von Mos10 durch MS-Analyse, die durch Anwendung der SILAC-Technik (Stable Isotope Labeling with Amino Acids in Cell Culture) weiter reduziert werden konnte. Nach der Auswahl möglicher Mos10-Interaktionspartner wurden IP- und Co-IP-Experimente an markierten Kandidatenvarianten durchgeführt, um eine Interaktion zwischen

den beiden Proteinen zu identifizieren. Eine Interaktion zwischen Mos10-6His und Vps68-13myc konnte neben nativem Mos10 und Vps68-fGFP durch Aufreinigung von Vps68 und Ko-Präzipitation von Mos10 nachgewiesen werden.

Der Einfluss von Vps68 auf den Aufbau und die Zusammensetzung des ESCRT-III Komplexes wurde untersucht. Es zeigte sich, dass in der *VPS68* Deletionsmutante die Core-Untereinheiten Snf7, Vps2 und Vps24 im Komplex angereichert waren, während die ESCRT-III assoziierten Protein Did2, Ist1 und Mos10 abgereichert waren. Das deutet darauf hin, dass die Auflösung des ESCRT-III Komplexes in der $\Delta vps68$ -Mutante blockiert ist. Der Einfluss der *VPS68*-Deletion auf die intrazelluläre Lokalisierung der ESCRT-III-Proteine wurde durch Fluoreszenzmikroskopie mit sfGFP-markierten Varianten untersucht. Während die Lokalisation der meisten ESCRT-III-Proteine nicht signifikant verändert war, wurde für Mos10 eine deutliche Relokalisation beobachtet. Im Wildtyp war Mos10-sfGFP an der Vakuolenmembran lokalisiert, während es in $\Delta vps68$ in vesikulären Strukturen verteilt war, die am Zellkortex angereichert waren.

Außerdem wurde untersucht, wie sich die Deletion von *VPS68* auf die Sortierung des endozytischen Cargo-Proteins Ste6 auswirkt. Durch Cycloheximid-Chase-Experimente konnte gezeigt werden, dass Ste6 in einer $\Delta vps68$ -Mutante stark stabilisiert ist. Dies deutet darauf hin, dass der Transport des Proteins in die Hefevakuole zum Abbau blockiert ist. Die $\Delta vps68$ -Blockade des endozytischen Transports wurde mit anderen Mutanten des *vps*-Wegs verglichen, deren Wirkort bereits bekannt ist. Diese Experimente zeigen, dass die Deletion von *VPS68* weder zu einem Klasse-D-Phänotyp, wie bei $\Delta vps21$, noch zu einem Klasse-E-Phänotyp, wie bei $\Delta snf7$, führt. Die Ste6-GFP-Verteilung in der $\Delta vps68$ -Mutante ähnelt eher dem Wildtyp mit einer ausgeprägteren Akkumulation von endosomalen Punkten. Die Daten deuten darauf hin, dass Vps68 nach der Bildung des ESCRT-III-Komplexes wirkt und dass es für den Transport von Cargo-Proteinen aus dem späten Endosom in das Vakuolen-Lumen benötigt wird.

DANKSAGUNG

Zuallererst möchte ich Herrn Prof. Ralf Kölling danken, mir die Möglichkeit gegeben zu haben, an seinem Lehrstuhl meine Doktorarbeit anfertigen zu können. Ralf, ich danke dir mich all die Jahre mit meinen verrückten Ideen und Vorstellungen unterstützt zu haben. Du hattest stets ein offenes Ohr für mich und ich konnte immer zu dir kommen.

Des Weiteren möchte ich Herrn Prof. Armin Huber danken für die Bereitschaft, die Zweitprüfung meiner Arbeit zu übernehmen. Ich hoffe, die zahlreichen Proteinabkürzungen waren nicht zu sehr verwirrend.

Ein spezieller Dank geht an Herrn Dr. Jens Pfannstiel und Frau Berit Würtz für die Messung meiner Proben am Massenspektrometer und anschließenden Auswertung.

Bedanken möchte ich mich auch beim gesamten Lehrstuhl für Hefegenetik und Gärungstechnologie: bei Oli, Thomas, Nam, Lara, Christian, Dani, Daniel, Luis, Herr Körner und Frau Bühler; für die schöne Zeit im Labor und angenehme Arbeitsatmosphäre. Ein besonderer Dank gilt meinen ehemaligen Mitstreitern Sven und Luana. Mit euch hatte ich eine wundervolle Zeit im Labor, in Hohenheim, in Stuttgart, in Heidelberg und in Bologna. Mit euch war es überall schön und die Jahre mit euch schätze ich sehr.

Ein weiter besonderer Dank gilt Julia. Auch wenn die Pandemie am Anfang 2020 die Welt und auch die Uni Hohenheim ziemlich im Griff hatte, haben wir uns unsere kleine Insel an der Uni geschaffen. Unsere zahlreichen Kochsessions mit guten Gesprächen und guter Laune haben einen immer motiviert weiter zu machen und dafür danke ich dir sehr.

Ich möchte mich auch bei Micha und Sarah bedanken, die sich die Mühe gemacht haben meine Arbeit zu lesen und korrigieren zu wollen. Ich weiß, es war nicht einfach aber vielen Dank für die konstruktive Kritik und Verbesserungen.

An dieser Stelle möchte ich meiner Familie und Freunden danken, die mich während der gesamten Zeit der Arbeit unterstütz und das ein oder andere Mal mitgelitten haben.

APPENDIX

Eidesstattliche Versicherung gemäß §7 Absatz 7 der Promotionsordnung der Universität Hohenheim zum Dr. rer. nat.

Bei der eingereichten Dissertation zum Thema „Influence of the newly identified Mos10 interaction partner Vps68 on ESCRT-III function“ handelt es sich um meine eigenständig erbrachte Leistung. Ich habe nur die angegebenen Quellen und Hilfsmittel benutzt und mich keiner unzulässigen Hilfe Dritter bedient. Insbesondere habe ich wörtlich oder sinngemäß aus anderen Werken übernommene Inhalte als solche kenntlich gemacht. Ich habe nicht die Hilfe einer kommerziellen Promotionsvermittlung oder -beratung in Anspruch genommen. Die Bedeutung der eidesstattlichen Versicherung und der strafrechtlichen Folgen einer unrichtigen oder unvollständigen eidesstattlichen Versicherung sind mir bekannt.

Die Richtigkeit der vorstehenden Erklärung bestätige ich: Ich versichere an Eides Statt, dass ich nach bestem Wissen die reine Wahrheit erkläre und nichts verschwiegen habe.

Ort und Datum

Unterschrift

CURRICULUM VITAE

Personal Data:

Name **Sören Alsleben**
Date of Birth **27.03.1988**
Place of Birth **Mülheim an der Ruhr**
Citizenship **German**



Education/Experience:

01/2017- **University of Hohenheim in Stuttgart**
11/2021 . PhD Student
10/2015- **Leibniz Institute for Natural Product Research and Infection Biology**
12/2016 – **Hans Knöll Institute in Jena**
. Research Associate
10/2011- **Technical University of Dortmund**
09/2015 . Master in Chemical Biology
. Master Thesis at the chair of bio- and chemical engineering
04/2013- **Harvard Medical School in Boston, MA, USA**
10/2013 . Research Associate
. DAAD scholar holder
04/2012- **Max-Planck-Institute of molecular physiology in Dortmund**
09/2012 . Research Assistant
10/2008- **Technical University of Dortmund**
09/2011 . Bachelor in Chemical Biology
. Bachelor Thesis at the MPI in Dortmund
1998- **Karl-Ziegler-Gymnasium in Mülheim an der Ruhr**
2007 . General Qualification for university entrance (Abitur)

Personal:

Languages **German (native), English (excellent)**
Hobbies **Logic puzzle, fitness, games**